

# 低能反电子中微子和相关物理的 实验研究

(申请清华大学理学博士学位论文)

培养单位: 工程物理系

学 科: 物理学

研 究 生: 万 林 焱

指导教师: 陈 少 敏 教 授

二〇一八年十二月



**Experimental Studies on Low Energy  
Electron Antineutrinos and Related  
Physics**

Dissertation Submitted to  
**Tsinghua University**  
in partial fulfillment of the requirement  
for the degree of  
**Doctor of Philosophy**  
in  
**Physics**  
by  
**Wan Linyan**

Dissertation Supervisor : Professor Chen Shaomin

**December, 2018**



# 关于学位论文使用授权的说明

本人完全了解清华大学有关保留、使用学位论文的规定，即：

清华大学拥有在著作权法规定范围内学位论文的使用权，其中包括：（1）已获学位的研究生必须按学校规定提交学位论文，学校可以采用影印、缩印或其他复制手段保存研究生上交的学位论文；（2）为教学和科研目的，学校可以将公开的学位论文作为资料在图书馆、资料室等场所供校内师生阅读，或在校园网上供校内师生浏览部分内容；（3）根据《中华人民共和国学位条例暂行实施办法》，向国家图书馆报送可以公开的学位论文。

本人保证遵守上述规定。

**(保密的论文在解密后应遵守此规定)**

作者签名： \_\_\_\_\_

导师签名： \_\_\_\_\_

日 期： \_\_\_\_\_

日 期： \_\_\_\_\_



## 摘要

能量在数个至数百个 MeV 能段的反电子中微子包括了来自超新星、地球、反应堆以及大气中微子的贡献。这些中微子可作为研究其来源的动力学与寻找超出标准模型新物理的独特探针。这些中微子与物质相互作用的最大反应道之一是与质子的反贝塔衰变 (IBD), 其过程将产生一个正电子和一个中子, 其中对中子的有效探测对实验上区分信号与本底至关重要。本论文针对超新星遗迹中微子 (SRN) 和地球中微子实验的关键问题进行了研究, 并利用与 IBD 信号相似的特点, 测量了大气中微子中性流类弹性散射过程 (NCQE) 的反应截面。

本论文的主要工作与创新点如下:

- 在超级神冈水切伦科夫探测器 (SK) 中使用发光二极管对水的散射与吸收的光学性质进行了刻度研究, 利用放射源对光电倍增管的长期增益变化做出了修正, 并改进了能量重建算法。这些工作降低了 SK 的物理分析的系统误差。
- 使用 2778 天的 SK-IV 数据, 通过探测中子氢俘获信号寻找 SRN。改进了中子探测算法, 利用基于飞行时间的无偏重建和基于正电子产生顶点的有偏重建得到了中子俘获位置与能量的信息, 并通过神经网络进行了优化。SRN 信号探测效率从过去的 8.8% 提高到了 19.3%。利用 525  $\mu\text{s}$  内的快慢信号符合挑选了正电子与中子的候选事例, 同时计算了包括反应堆中微子、宇宙线散裂本底、大气中微子与偶然符合在内的本底数。两者相比较, 统计上符合无信号假设, 由此得出了国际最好的模型无关 SRN 微分通量上限。
- 大气中微子与氧核的 NCQE 事例将产生低能光子和中子, 其中光子会被误判为正电子, 从而成为 SRN 寻找最重要的本底之一。利用其与 SRN 事例在切伦科夫探测器中相似的快慢信号符合特性, 并结合快信号中光子与正电子不同的切伦科夫角分布, 在  $50^\circ$  以上的范围筛选了信号事例。由此测量的 NCQE 截面与理论预期符合。
- 在低于 5 MeV 的能量段, 研究了中微子振荡效应对基线长度关联的地球中微子信号与反应堆中微子本底的影响。计算了中国锦屏地下实验室预期的信号与本底数, 并基于液体闪烁体的性质为地球中微子和铀钍比测量做出了精度预言。利用地球中微子作为放射性核素衰变产物的特点, 给出了地球辐射产热的约束与不同地球模型的测试。

**关键词:** 中微子; 超新星遗迹中微子; 大气中微子; 地球中微子

## Abstract

Electron antineutrinos within the energy range of several to several hundreds of MeV are composed of those from supernovae or past supernovae, the Earth, reactors, and atmospheric neutrinos. They provide a unique probe into the dynamic of sources as well as new phenomena beyond the Standard Model of particle physics. One of the interactions with the largest cross section for neutrino detection in this energy range is inverse beta decay (IBD), which produces a positron and a neutron. The detection of neutron is crucial for the separation between signal and backgrounds. This thesis presents studies based on the analysis of low energy signal and neutron production from neutrino interactions.

- We used LEDs to calibrate the water scattering and absorption properties for the water Cherenkov detector Super-Kamiokande (SK). We employed radioactive sources to correct the bias introduced by the long-term gain increase of PMTs, and implemented a new algorithm to the energy reconstruction process, all of which reduced the systematics as a consequence.
- With SK-IV data of 2,778 days, a search for SRN signal has been performed by detecting the neutron capture signal. We improved the neutron tagging algorithm by reconstructions of the neutron capture vertex based on time-of-flight subtracted PMT hit time and the primary vertex respectively, and optimized the determination of multi-variate cut. The signal-background discrimination power of the algorithm was significantly enhanced, and the signal efficiency was increased from 8.8% to 19.3%. The SRN candidates were compared with the expectations of backgrounds including reactor neutrinos, spallation backgrounds, atmospheric neutrino induced backgrounds, and accidental coincidence. The result was consistent with null signal hypothesis. An upper limit was derived, giving the best limits for the SRN search.
- Atmospheric neutrinos interact with oxygen nuclei in water, producing gammas and neutrons, which imposes an important background for SRN detection by the mis-identification of gammas as positrons. Based on the SRN sample except for Cherenkov angle cut, we obtained NCQE candidates with Cherenkov angle  $> 50^\circ$ . The mean NCQE cross section from atmospheric neutrinos on oxygen was measured to be  $(0.95 \pm 0.12(\text{stat.})_{-0.32}^{+0.49}(\text{sys.})) \times 10^{-38} \text{ cm}^2$ , consistent with the theoretical prediction.



- We performed a calculation on geoneutrinos fluxes generated in the Earth and analyzed the oscillation impact with both vacuum approximation and MSW effect. Considering the backgrounds of reactor neutrinos and  $(\alpha, n)$  interaction, an prediction has been made for the geoneutrino and U/Th ratio sensitivities in a liquid scintillator detector at the Jinping underground lab in Sichuan, China. These measurements will provide powerful constraints on the radiogenic heat budget of the Earth as well as tests on Earth models.

**Key words:** neutrino; supernova relic neutrino; atmospheric neutrino; geoneutrino

## Contents

Chapter 1	Introduction .....	1
1.1	Neutrinos Properties .....	1
1.1.1	Neutrinos in the Standard Model .....	1
1.1.2	Neutrino Oscillation .....	2
1.2	Neutrino Interactions .....	4
1.2.1	The Inverse Beta Decay .....	4
1.2.2	The Neutral Current Quasi-Elastic Scattering.....	6
1.3	Neutrinos from Different Sources and Related Physics .....	7
1.3.1	Overview of Neutrino Sources .....	7
1.3.2	Supernova Relic Neutrinos .....	8
1.3.3	Geoneutrinos .....	22
Chapter 2	The Super-Kamiokande Detector .....	29
2.1	Detector Overview .....	29
2.2	Cherenkov Radiation .....	32
2.3	Photo-Multiplier Tubes .....	33
2.3.1	ID PMTs .....	33
2.3.2	OD PMTs .....	34
2.4	Water and Air System.....	34
2.5	Electronics and Data Acquisition .....	36
2.5.1	Electronic System.....	36
2.5.2	Online DAQ and Trigger .....	37
Chapter 3	Calibration and Reconstruction at SK .....	39
3.1	Detector Calibration .....	39
3.1.1	PMT Response Calibration.....	39
3.1.2	Water Transparency Measurement.....	45
3.1.3	Energy Calibration.....	56
3.2	Detector Simulation.....	60
3.2.1	Cherenkov Photon Production .....	61
3.2.2	Photon propagation .....	62
3.2.3	PMT and Electronics .....	63

3.3	Event Reconstruction .....	64
3.3.1	Vertex Reconstruction .....	64
3.3.2	Direction Reconstruction .....	64
3.3.3	Energy Reconstruction .....	65
3.3.4	Cherenkov Angle Reconstruction .....	68
3.3.5	Muon Fitter .....	69
Chapter 4	Data Reduction at SK .....	71
4.1	First Reduction .....	71
4.2	Spallation Cut .....	72
4.3	External Event Cut .....	76
4.4	Solar Event Cut .....	77
4.5	Cherenkov Angle Cut .....	77
4.6	Multi-Event Cut .....	78
4.6.1	Pre/Post Activity Cut .....	78
4.6.2	Multi-ring Cut .....	80
4.7	Muon/Pion Cut .....	80
4.7.1	Pion Cut .....	80
4.7.2	Charge/Hit Cut .....	81
4.8	Summary of Reduction Efficiency .....	81
Chapter 5	Selection of Correlated Neutrons at SK .....	83
5.1	Neutron Tagging Algorithm .....	85
5.1.1	Pre-selection .....	85
5.1.2	Discriminating Variables .....	87
5.1.3	Multivariate classification .....	102
5.2	Significance Curve .....	103
5.3	Systematic Study with the Am/Be Source .....	105
5.4	Validation with Cosmogenic ${}^9\text{Li}$ Sample .....	108
5.5	Cut Optimization and Efficiency Evaluation .....	109
Chapter 6	SRN Analysis and Result at SK .....	111
6.1	Background Estimation .....	111
6.1.1	Accidental Backgrounds .....	111
6.1.2	Atmospheric NC .....	111
6.1.3	Atmospheric CC .....	112

6.1.4	Spallation Backgrounds .....	114
6.1.5	Reactor Neutrinos .....	114
6.2	Candidate Events .....	114
6.3	Model-Independent Upper Limit .....	115
Chapter 7	NCQE Analysis at SK .....	118
7.1	Introduction and Motivation .....	118
7.1.1	Atmospheric NCQE as the SRN Background .....	119
7.1.2	Further Applications .....	120
7.2	Monte-Carlo Simulation .....	120
7.2.1	Atmospheric Neutrino Flux .....	120
7.2.2	Neutrino Interactions .....	121
7.2.3	Other NC Channels .....	123
7.2.4	MC Reconstruction and Reduction .....	124
7.3	Data Reduction and Neutron Tagging .....	124
7.3.1	Data Reduction .....	124
7.3.2	Neutron Tagging for NCQE Events .....	125
7.4	Analysis .....	129
7.4.1	Candidate Events .....	129
7.4.2	Cross section Calculation .....	132
7.4.3	Systematic Uncertainties .....	132
7.5	Results and Discussion .....	134
7.5.1	Discussion on Future Improvement .....	134
Chapter 8	Geoneutrino Study .....	136
8.1	Geoneutrino Intensity and Energy Spectra .....	136
8.2	Geo $\bar{\nu}_e$ Flux Calculation .....	138
8.2.1	Earth Model .....	139
8.2.2	Oscillation Analysis .....	139
8.3	Liquid Scintillator Detector .....	143
8.3.1	Scintillation Light .....	143
8.3.2	Detector Response Model .....	144
8.3.3	A Proposed Experiment at Jinping .....	147
8.4	Backgrounds .....	148
8.4.1	Reactor Neutrino Background .....	148

## Contents

---

8.4.2	Other Backgrounds .....	150
8.5	Sensitivities .....	151
8.5.1	Predicted IBD Spectrum at Jinping .....	152
8.5.2	Sensitivity for Geoneutrinos .....	153
8.5.3	BSE Model Test .....	154
8.6	Further Discussion .....	156
8.6.1	Requisites for the Detector .....	156
8.6.2	Earth Core Fission Neutrinos .....	156
Chapter 9	Summary and Outlook .....	158
9.1	Summary .....	158
9.2	Outlook .....	159
Reference	.....	161
Acknowledgement	.....	169
Declaration	.....	170
Resume and Publications	.....	171

## Chapter 1 Introduction

This chapter first introduces general properties of neutrinos, then reviews the neutrino interactions, emphasizing on the inverse beta decay and neutral current quasi-elastic scattering. A discussion on different neutrino sources and related physics is presented, focusing on supernova relic neutrinos and geoneutrinos, including the dynamics of supernovae and Earth, and the present experimental status.

### 1.1 Neutrinos Properties

Less than a century from its discovery, neutrinos are nowadays significantly pushing forward the progress of fundamental physics governing our universe. Named by their electrical neutrality and tiny masses, neutrinos were first postulated by Wolfgang Pauli in 1930 to explain the continuous electron energy spectrum in nuclear  $\beta$ -decay. His neutrino solution to the energy and momentum crisis was to propose that the  $\beta$ -decay of the nucleus is a three-body process involving the nucleus, the electron, and the neutrino<sup>[1]</sup>. This postulation was confirmed experimentally by C. Cowan and F. Reines in 1956 with the discovery of electron anti-neutrinos from the nuclear reactor<sup>[2]</sup>.

#### 1.1.1 Neutrinos in the Standard Model

Neutrinos are only subject to weak interaction. It is experimentally well-established that there are 3 generations of neutrinos,  $\nu_e, \nu_\mu, \nu_\tau$ , coupling to the corresponding 3 generation leptons  $e, \mu, \tau$ . Experiments on Large Electron-Positron Collider (LEP) reported the final electroweak measurements performed with data taken at the Z resonance, which constrained the number of light neutrino species to be  $2.9840 \pm 0.0082$ <sup>[3]</sup>. This result requires only 3 generations of active neutrinos, and any further generation of neutrinos has to be non-conventional neutrinos, for example, sterile neutrinos which do not have electroweak interaction.

The absolute value of neutrino mass remains unknown so far, though the upper limits of  $\nu_e$  have been obtained by  $\beta$ -decay measurements at eV level<sup>[4]</sup>. Still, the non-zero mass of at least 2 generations of neutrinos along with neutrino mixing can be derived from the fact that neutrinos oscillate among the 3 generations<sup>[5,6]</sup>. This contradicts the

massless prediction within the Standard Model<sup>[7]</sup>, marking neutrinos as the only particle showing deviation from SM so far.

### 1.1.2 Neutrino Oscillation

Experiments provide compelling neutrino oscillation evidences compatible within the present frame work of 3-generation neutrino mixing, although there are some experimental hints for the hypothetical sterile neutrinos that interact only via gravity and do not interact via any of the fundamental interactions<sup>[8-10]</sup>.

#### 1.1.2.1 Vacuum Oscillation

Neutrino mixing indicates that the mass eigenstates are not flavor eigenstates, i.e., the neutrino mixing matrix  $U$  is not diagonal. Denoting the mass eigenstates as  $\nu_1$ ,  $\nu_2$ , and  $\nu_3$ , and the flavor eigenstates as  $\nu_e$ ,  $\nu_\mu$ , and  $\nu_\tau$ , the matrix  $U$  is parameterized by three mixing angles between different generations of neutrinos and the CP phase,

$$\begin{aligned}
 U &= \begin{pmatrix} 1 & & \\ & c_{23} & s_{23} \\ -s_{23} & c_{23} & \end{pmatrix} \times \begin{pmatrix} c_{13} & s_{13}e^{-i\delta_{cp}} & \\ & 1 & \\ -s_{13}e^{-i\delta_{cp}} & & c_{13} \end{pmatrix} \times \begin{pmatrix} c_{12} & s_{12} & \\ -s_{12} & c_{12} & \\ & & 1 \end{pmatrix} \\
 &= \begin{pmatrix} c_{12}c_{13} & s_{12}c_{13} & s_{13}e^{-i\delta} \\ -s_{12}c_{23} - c_{12}s_{13}s_{23}e^{i\delta} & c_{12}c_{23} - s_{12}s_{13}s_{23}e^{i\delta} & c_{13}s_{23} \\ -s_{12}c_{23} - c_{12}s_{13}c_{23}e^{i\delta} & c_{12}s_{23} - s_{12}s_{13}c_{23}e^{i\delta} & c_{13}c_{23} \end{pmatrix}, \quad (1-1)
 \end{aligned}$$

where  $s_{i,j}$  and  $c_{i,j}$  represent the sine and cosine of a mixing angle between the  $i$ -th and  $j$ -th generations respectively.

The survival probability of an electron antineutrino  $\nu_e$  with energy  $E$  propagating over a baseline  $L$  can thus be written as

$$P_{\alpha\beta}(E, L) = \sum_i \sum_j e^{-i\tilde{M}_{i,j}} \times U_m(i, \alpha)^\dagger U_m(\beta, i) U_m(\alpha, j) U_m(j, \beta)^\dagger, \quad (1-2)$$

where  $\alpha$  and  $\beta$  indicate the initial state and the final state respectively,  $\tilde{M}_{i,j} = \Delta M_{ij}^2 L/2E$ , with the oscillation distance  $L$  and the energy  $E$ , and  $\Delta M_{ij}$  is the neutrino mass difference between the  $i$ th and  $j$ th generations.  $U_m$  is the eigenmatrix of neutrino mass mixing matrix  $A = U \times M \times U^\dagger$ , where  $M$  is the neutrino mass matrix,  $M_{ij} = \delta_{ij} \times \Delta M_{ij}$ , and  $U$  is the neutrino oscillation matrix.

### 1.1.2.2 Matter Effect

The presence of propagating medium can change drastically the pattern of neutrino oscillations due to the weak but existing interaction between neutrinos and the particles forming the medium. In case of matter oscillation, the Hamiltonian of the neutrino system in matter  $H_m$  differs from the Hamiltonian in vacuum  $H_0$ ,  $H_m = H_0 + H_{int}$ , with  $H_{int}$  describing the interaction of neutrinos and particles such as the electrons, protons and neutrons in the medium matter. The effect of matter in neutrino oscillations is usually called Mikheyev-Smirnov-Wolfenstein (MSW) oscillation effect, or matter effect<sup>[11]</sup>.

The mixing matrix for the MSW oscillation of neutrinos changes from vacuum oscillation as

$$A'_{11} = A_{11} + V, \quad (1-3)$$

with the additional term  $V$  representing the chemical potential,

$$V = 2\sqrt{2}G_F n_e E_\nu, \quad (1-4)$$

where  $G_F$  is the Fermi constant,  $n_e$  is the electron density, and  $E_\nu$  is the neutrino energy. Therefore, the neutrino mixing angle in matter can be written as

$$\sin 2\theta_m = \frac{\tan 2\theta}{\sqrt{\left(1 - \frac{N_e}{N_e^{\text{res}}}\right)^2 + \tan^2 2\theta}}, \quad (1-5)$$

where  $N_e^{\text{res}}$  is the effective density, referred to as resonance density,

$$N_e^{\text{res}} = \frac{\Delta m^2 \cos 2\theta}{2E\sqrt{2}G_F}. \quad (1-6)$$

If  $N_e \ll N_e^{\text{res}}$ , Eq. (1-5) reduces to vacuum oscillation, and  $\theta_m \approx \theta$ . On the contrary, if  $N_e \gg N_e^{\text{res}}$ , the presence of matter greatly suppresses neutrino oscillation,  $\theta_m \approx \pi/2$ . Based on this effect, neutrino tomography is feasible with a high luminosity source and a high electron density environment. Typical examples include using solar neutrinos propagating through the Sun to probe solar interior, or using geoneutrinos to probe the Earth.





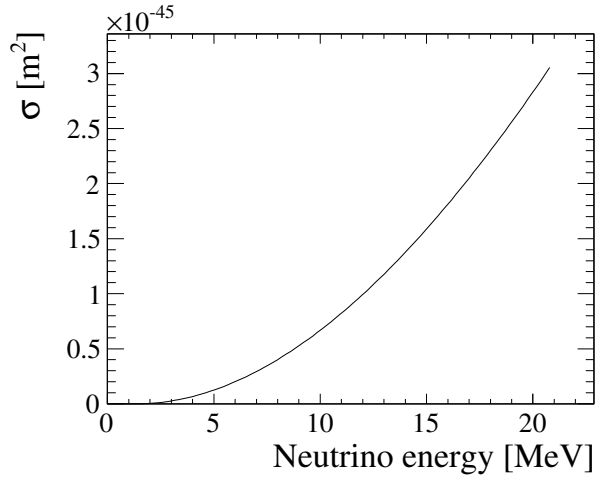


Figure 1.2 Cross section for IBD interaction as a function of incident neutrino energy.

Inverse beta decay is the simplest neutrino nuclear interaction, in which an electron antineutrino  $\bar{\nu}_e$  scattered on a proton  $p$ , producing a positron  $e^+$  and a neutron  $n$ ,



In a typical Cherenkov or scintillation detector, the positron is detected immediately by Cherenkov radiation or scintillation light and is referred to as the primary event, or prompt event, and the neutron is detected by its capture after thermal propagation, referred to as the delayed event. If the capture occurs on a hydrogen nucleus, a 2.2 MeV  $\gamma$  ray will then be emitted with a lifetime of  $\sim 200\mu s$ ,



In the MeV level of low energy range, the energy of the out-going positron of an IBD event can be written as a function of incident neutrino energy approximated to the 0th order,

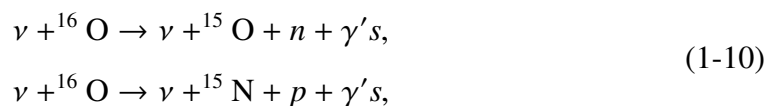
$$T_{e^+} = E_{\bar{\nu}_e} + m_p - m_n - m_{e^+}. = E_{\bar{\nu}_e} - 1.8\text{MeV}. \quad (1-9)$$

In IBD events, antineutrinos are usually detected by identifying  $e^+$ , or sometimes by a time-correlated signal between a prompt signal and a delayed signal. This feature provides a distinct signature against backgrounds, and will thus increase the sensitivity for IBD

signals. In some cases where a 2.2 MeV  $\gamma$  does not exceed the energy threshold and will not trigger a signal, for example a water Cherenkov detector, the neutron capture signal can be selected by associating the prompt signal through neutron tagging, as to be discussed in Chapter 5.

### 1.2.2 The Neutral Current Quasi-Elastic Scattering

Neutral current quasi-elastic interaction (NCQE) with  $^{16}\text{O}$  is found to be one of the major channels in water based neutrino detectors for neutrinos with several hundred MeV energy<sup>[15]</sup>. The interaction processes can be written as



in which neutrinos knock out one or multi-nucleons from oxygen, and the residual nuclei de-excites, emitting  $\gamma$ 's. The number and energies of these  $\gamma$ 's depend on the final states of excitation energy levels and corresponding branching ratios. The produced  $\gamma$  ray then propagates in water and can be detected by the Cherenkov light of the secondary electron or positron mainly through Compton process and pair production. The recoil proton is usually below the Cherenkov threshold and becomes invisible, while the recoil neutron can be captured on hydrogen, releasing a 2.2 MeV photon that can be tagged, and mimicking an IBD signal.

Theoretical predictions have been given for both low energy case and high energy case, the latter of which applies to T2K neutrino beam and atmospheric neutrino with energy of GeV or sub-GeV<sup>[15]</sup>, as shown in Fig. 1.3. This cross section has been measured from T2K neutrino beam, reporting a result in agreement with the theoretical prediction<sup>[16]</sup>. Still, the cross section on oxygen from atmospheric neutrinos has not yet been studied before, which remains as a backgrounds for many rare signal searches in water Cherenkov detectors.

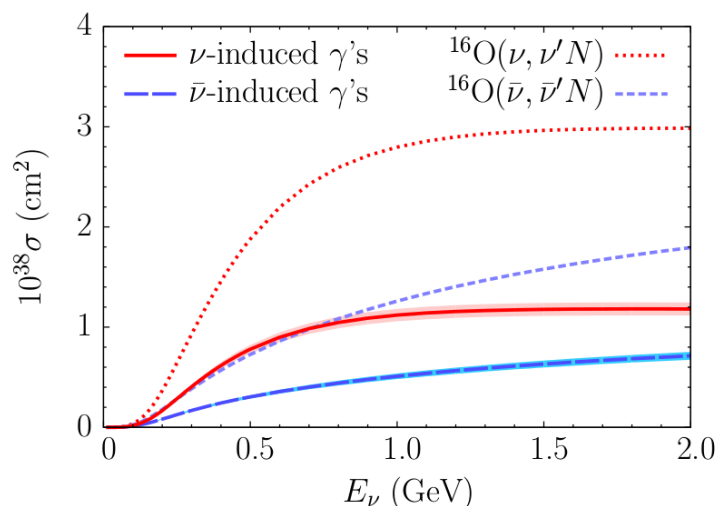


Figure 1.3 Cross section for NCQE interaction as a function of incident neutrino energy, cited from Ankowski's model<sup>[15]</sup>.

### 1.3 Neutrinos from Different Sources and Related Physics

Neutrinos are generated in various physics processes and come from a variety of sources. In this section, we first briefly review the neutrino sources, and then focus on both the supernova relic neutrinos and the geoneutrinos with IBD signature.

#### 1.3.1 Overview of Neutrino Sources

Neutrinos originate from various sources, including cosmic relic neutrinos from the relic of the Big Bang<sup>[17]</sup>, supernova neutrinos from the collapsed supernova explosions, solar neutrinos from the Sun, atmospheric neutrinos from the cosmic-ray interactions in the air, accelerator neutrinos from accelerators, reactor neutrinos from nuclear reactors, and geoneutrinos from the decay-chain of  $^{238}\text{U}$  and  $^{232}\text{Th}$  inside the Earth.

These neutrinos have very different properties on energy spectra, flavor composition, and directional distribution, and thus can be distinguished in most cases. The energy of neutrinos ranging from several eV for the cosmic relic neutrinos<sup>[18]</sup> to several PeV from some extra terrestrial neutrino source<sup>[19]</sup>.

Owing to the fact that neutrino interaction with matter is very weak, neutrinos can be used as a probe into the dynamics of these neutrino sources, especially when the sources are far away or heavily shaded.

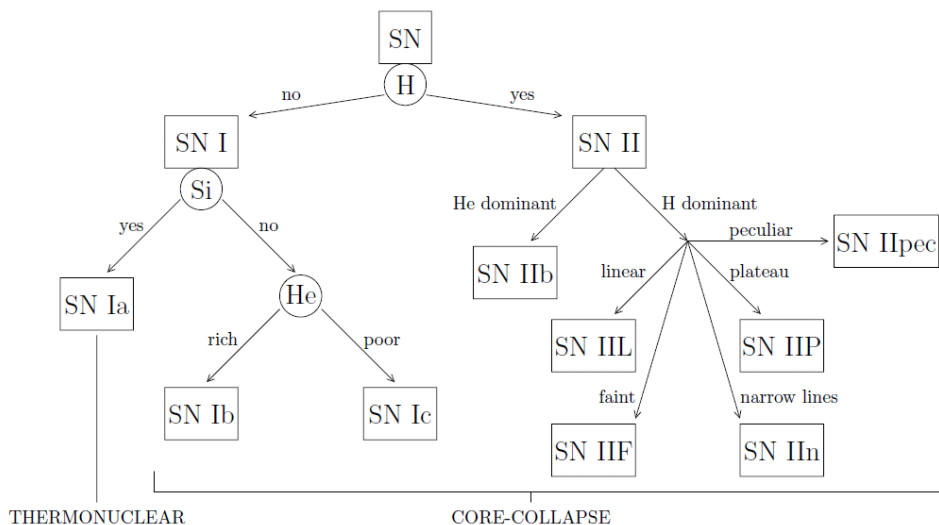
### 1.3.2 Supernova Relic Neutrinos

Supernova relic neutrinos (SRNs) are the neutrinos emitted from past supernova bursts everywhere in the universe. In this section, we will first introduce supernova bursts, especially core-collapse supernovae, and the dynamics driving them. Then we discuss on supernova neutrinos and supernova relic neutrinos, emphasizing on the neutrino spectra and flux predicted by different models. Finally the present status of SRN search in different experiments is covered.

#### 1.3.2.1 Supernova Overview

For historical reasons, supernovae are classified into type I and II by their light spectroscopic characteristics instead of their trigger scheme, as shown in Fig. 1.4. To remedy for that, supernova categories are further divided into sub-categories, where Type Ia supernovae are believed to be triggered by the thermonuclear disruption of white dwarf stars in binary systems, and Type Ib, Ic and II supernovae are generated by the gravitational collapse of the core of massive stars.

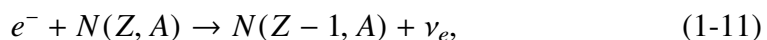
Core-collapse supernova burst is an important topic in supernova astronomy and star evolution as well as in neutrino physics. The progenitors of core-collapse supernovae are typically with larger mass than type Ia. When the mass of a progenitor satisfies  $M \gtrsim 8M_{\odot}$ , where  $M_{\odot}$  denotes one solar mass, after its burning out, a gravitational collapse will be triggered. Most of energy from a core-collapse supernova burst is carried away by the emission of a large number of neutrinos. The term supernova in the following context refers to core-collapse supernovae unless otherwise explained.


 Figure 1.4 The classification scheme of supernovae<sup>[20]</sup>.

Core-collapse supernova bursts can be driven by different causes dependent on the progenitor mass and metallicity, but the early phases of the burst producing neutrinos are quite similar<sup>[21]</sup>. The explosive processes related to the neutrino emission can be summarized as below<sup>[20,22,23]</sup>.

- Photo-disintegration.

As the density and the temperature in the core climbs during the star collapse, electron capture on nucleus



becomes favorable, further reducing the electron degeneracy pressure in support of the gravitational force inside the iron core and accelerating the core collapse. Though some  $\nu_e$ 's are generated in this stage, the amount is negligible compared to the total emission. These neutrinos, together with the neutrinos emitted in the pre-supernova stage through pair production, can escape freely from the core, possible to be used as an early warning for a close-by supernova burst, but the amount of neutrinos is not significant in supernova relic neutrino analysis.

- Neutrino trapping.

The inner and outer parts of star core begin to evolve differently. In the inner part, the collapse is homologous, with the collapsing velocity  $v \propto r$ , and it takes the same time for all parts collapse, while the density increases at the same rate everywhere. In the outer part, however, the collapse is quasi-free fall,  $v \propto 1/r^2$ . When the density

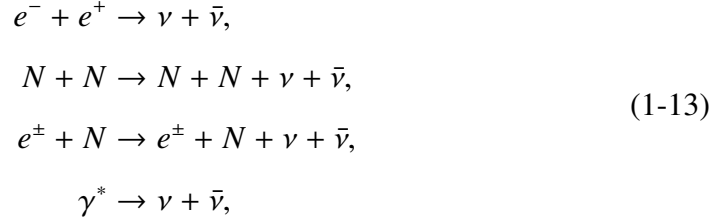
of the inner part of the core reaches  $10^{11} - 10^{12} \text{ g}\cdot\text{cm}^{-3}$ , electron neutrinos begin to be trapped in a so-called neutrinosphere by the nuclei through coherent scattering, the cross section of which follows  $\sigma_{\text{coh}} \propto A^2$ . This neutrinosphere is defined by radius as

$$R_\nu \approx 1.0 \times 10^7 \text{ cm} \left( \frac{E_\nu}{10 \text{ MeV}} \right). \quad (1-12)$$

- Neutrino burst.

The inner core continues to collapse until the density exceeds the nuclear limit ( $\sim 10^{14} \text{ g}\cdot\text{cm}^{-3}$ ), enabling the repulsive nuclear pressure to halt the collapse and to drive a shock wave outwards. Nuclei are then dissociated into free protons and neutrons by the shock wave, emitting a huge number of electron neutrinos through the process of electron capture on protons  $e^- + p \rightarrow n + \nu_e$ , enabling the previously trapped  $\nu_e$ 's to decouple from the nuclei. This process of electron neutrinos emission and free is called the prompt electron neutrino burst, with the peak luminosity exceeding  $10^{53} \text{ erg}\cdot\text{s}^{-1}$  for a few ms.

Besides, neutrinos of all flavors are produced thermally in the collapsed region via both neutral current (NC) and charged current (CC) processes,



and additional  $\nu_e/\bar{\nu}_e$ 's are produced by CC interactions,



- Delayed explosion.

The shock wave loses energy, and calculations show that it will not be able to reach the star surface in most cases. Instead, it is generally supposed that the explosion is relayed by neutrinos depositing energy through a so-called delayed explosion mechanism  $\sim 1$  second later than a prompt explosion.

Finally after cooling down, what remains of the progenitor will form either a neutron star or a black hole, depending on the its mass and metallicity.

### 1.3.2.2 Supernova Relic Neutrinos

Supernova bursts with neutrino observations are rare, expected at the rate of 2~3 per century<sup>[24]</sup>, while the accumulated supernova relic neutrinos throughout the history of universe can make a sensible probe into the dynamics of supernova burst as well as many other topics. To shed light on the supernova explosion mechanism, other than waiting for the burst neutrinos from the centennial supernova within our galaxy, SRNs from past supernovae should be thoroughly studied. Since 1987A, many calculations of SRN flux have been available, giving different results based on different hypotheses for the explosion mechanism<sup>[25–34]</sup>.

A general SRN spectrum prediction at the observatory can be given by<sup>[35]</sup>,

$$\frac{dN}{dE_\nu}(E_\nu) = c \int_0^\infty R_{SN}(z)(1+z) \frac{dN(E_\nu(1+z))}{dE_\nu} \left| \frac{dt}{dz} \right| dz, \quad (1-15)$$

where  $dN/dE_\nu$  is the energy spectrum from one supernova explosion, assumed to be universal in supernovae of different masses,  $R_{SN}$  is the core-collapse supernova rate at redshift  $z$ , the detected energy  $E_\nu$  from a neutrino is  $E_\nu(1+z)$  at production due to the redshift, and  $t$  is the cosmic time following the Friedmann equation,

$$\frac{dz}{dt} = -H_0(1+z)\sqrt{\Omega_m(1+z)^3 + \Omega_\Lambda}, \quad (1-16)$$

where  $H_0$  is the Hubble constant,  $\Omega_m$  is the cosmic matter density, and  $\Omega_\Lambda$  is cosmological constant.

#### **Rate of Core-collapse Supernovae**

The rate of core-collapse supernovae used to be calculated from the cosmochemistry<sup>[25,26]</sup> and the time variance used to be given by the cosmochemical evolution<sup>[27–29]</sup>. In recent SRN models<sup>[30–34]</sup>, however, the estimation of supernova rate is based on the star formation rate (SFR) with a rather good accuracy compared to other parameters in SRN spectra prediction.



The core-collapse supernova rate as a function of SFR can be written as<sup>[32]</sup>

$$R_{SN}(z) = \dot{\rho}_*(z) \frac{\int_8^{50} \Phi(m) dm}{\int_{0.1}^{100} m \Phi(m) dm}, \quad (1-17)$$

where  $R_{SN}(z)$  is the supernova rate at redshift  $z$ ,  $\dot{\rho}_*(z)$  is the SFR density,  $\Phi(m)$  is the initial mass function. The integral limits are the mass ranges of stars that lead to core collapse. Below  $8M_\odot$ , the progenitor tends to evolve into a dwarf, while above  $50M_\odot$ , the progenitor tends to form a black hole directly without an explosion<sup>[21]</sup>.

### Supernova Neutrino Spectra

The supernova neutrino emission flux and spectra remain a mystery, with many models proposed but none of them providing very high precision or has been verified. The average of neutrino energy can be estimated by the total amount of gravitational binding energy liberated in a supernova explosion

$$E_{\text{bind}} \sim \frac{3}{5} \frac{GM_{NS}^2}{R_{NS}} \sim 3 \times 10^{53} \left( \frac{M_{NS}}{1.4M_\odot} \right)^2 \left( \frac{R_{NS}}{10\text{km}} \right)^{-1} \text{ erg}, \quad (1-18)$$

where  $M_{NS}$  is the mass of a neutron star and  $R_{NS}$  is the radius. Energy estimations based on the only available neutrino data from a supernova so far, the SN 1987A in the Large Magellanic Cloud  $\sim 50$  kpc away, showed consistency with the above calculation<sup>[36,37]</sup>. However, due to the small statistics, where only 11 neutrinos have been detected from SN 1987A by Kamiokande II<sup>[38]</sup> and 8 by IMB<sup>[39]</sup> experiments, the explosion mechanism has not yet been well-established with SN neutrino data. An example of neutrino luminosity and average energy from a numerical simulation in a supernova explosion with the delayed explosion mechanism by Totani *et al.* is shown in Fig. 1.5<sup>[40]</sup>.

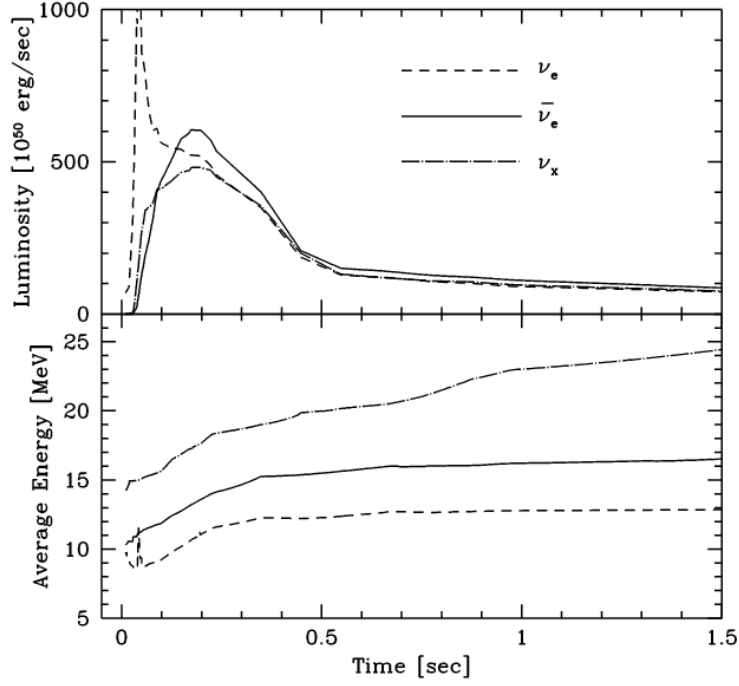


Figure 1.5 The first 1.5 s evolution of neutrino luminosity and average energy from a numerical simulation<sup>[40]</sup>.

As Eq. (1-13) indicates, most neutrinos are emitted in pairs, presumably carrying equivalent amount of energy among neutrino flavors. However, only some simulation results show equal partitions for the luminosities of all flavors<sup>[40]</sup>, while significant deviations are seen in others<sup>[41]</sup>. A commonly accepted hierarchy on the average neutrino energy among the species is

$$\langle E_{\nu_e} \rangle < \langle E_{\bar{\nu}_e} \rangle < \langle E_{\nu_x} \rangle, \quad (1-19)$$

with the average energy<sup>[40,42]</sup>,

$$\begin{aligned} \langle E_{\nu_e} \rangle &\approx 13\text{MeV}, \\ \langle E_{\bar{\nu}_e} \rangle &\approx 16\text{MeV}, \\ \langle E_{\nu_x} \rangle &\approx 23\text{MeV}. \end{aligned} \quad (1-20)$$

The energy spectrum of supernova neutrinos for each flavor is assumed to follow the Fermi–Dirac (FD) distribution with different temperatures and a zero potential<sup>[29]</sup>,

$$\frac{dN}{dE} = L \frac{120 E^2}{7\pi^4 T^4} \frac{1}{e^{E/T} + 1}, \quad (1-21)$$

where  $T \approx \langle E \rangle / 3.1514$  is the effective neutrino temperature and  $L$  is the total luminosity. This requires an approximation that the neutrino emission in a supernova burst is thermal, which is not true due to the energy dependence of the interaction cross sections. Figure 1.6 shows the energy spectrum from the same simulation as Fig. 1.5 by Totani *et al.* [40], where the zero-potential FD distribution cannot describe the numerical simulation very well.

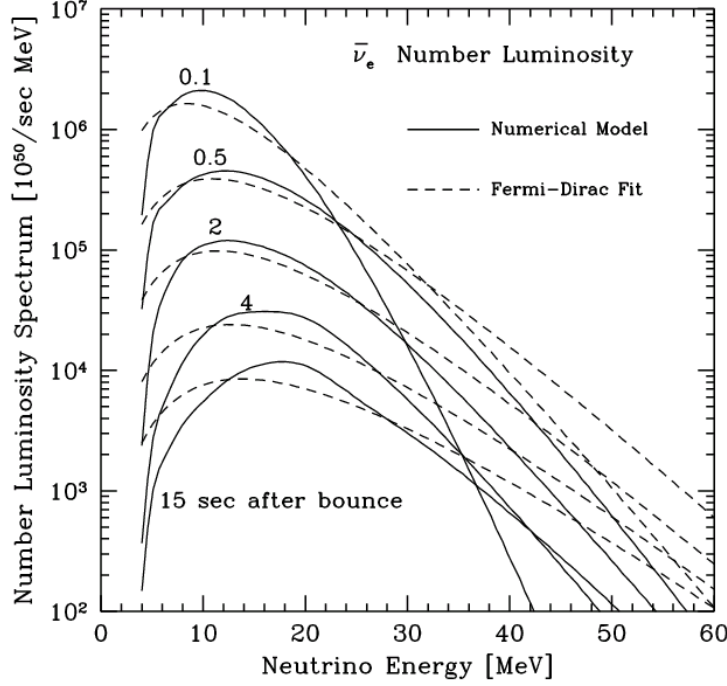


Figure 1.6 Energy spectrum of  $\bar{\nu}_e$  [40].

From Eq. (1-21), a more realistic pinched Fermi–Dirac (FD) distribution can be extended to parameterize the supernova neutrino spectrum for a given flavor predicted from most models [41],

$$\frac{dN}{dE} = L \frac{1}{F(\eta)} \frac{E^2}{T^4} \frac{1}{e^{E/T-\eta} + 1}, \quad (1-22)$$

where  $\eta$  is the pinching parameter and  $F(\eta)$  is a normalization function. The neutrino emission can then be characterized by the total flux  $L_\nu$ , the thermal temperature of emission  $T_\nu$ , and the pinching parameter  $\eta$ . Of these three parameters, no one depends sensitively on the supernova mass, thus enabling the assumption in SRN calculation Eq. (1-15) that SN spectra are not sensitive to the core-collapse supernova properties. Some recent SRN models also take into consideration the change of neutrino spectrum of a certain generation during its propagation through the universe because of oscillation [31,32].

Future detections of a nearby core collapse supernova by the present large neutrino detectors including Super-Kamiokande, IceCube, SNO+, *etc* will greatly enhance our knowledge on the supernova explosion mechanism and the supernova neutrino spectrum<sup>[43,44]</sup>.

### **SRN Models**

Some representative SRN models and predictions are summarized in Ref.<sup>[45]</sup> and Ref.<sup>[46]</sup>. The predictions for supernova relic neutrino rate and emission spectrum from the various models differ due to their assumptions on the supernova rates, the modifications on FD distribution, whether oscillation effect is considered or not, and the processes of supernova explosions.

In late 20th century, the discussion has been focused on the estimation of supernova rate, when constant SN rate model<sup>[25]</sup>, cosmic gas infall model<sup>[27]</sup>, chemical evolution model<sup>[28]</sup>, and population synthesis model<sup>[26]</sup> were proposed. Totani and his collaborators first assumed in the constant SN rate model in 1995 that the supernova rate was a constant, then updated with the population synthesis model that the supernova rate was time-dependent, derived from galaxy evolution based on the population synthesis method. Malaney *et al.* proposed that the supernova rate should be calculated from the redshift evolution of cosmic gas, and Hartmann *et al.* proposed the calculation of SFR from cosmic chemical evolution. Later, with the experimental search on SRN, a star formation rate constraint model<sup>[33]</sup> was proposed by Kawasaki *et al.* to obtain the supernova rate from SFR constrained by the SRN result from Super Kamiokande<sup>[47]</sup>.

Another concern on the insufficient FD-distribution-based description of the emission spectrum resulted in the heavy metal model<sup>[29,30]</sup> proposed by Kaplinghat *et al.*, in order to describe the spectrum by the universal metal enrichment history. Later in 2008, Horiuchi *et al.* proposed the HBD 6 MeV model<sup>[32]</sup>, predicting the neutrino emission spectrum with a pinched FD distribution with effective temperatures between 4-6 MeV This is further extended to a universal emission model for different temperatures<sup>[48]</sup>.

Large mixing angle (LMA) model<sup>[31]</sup> by Ando *et al.* in 2002 is the first SRN model to introduce the neutrino oscillation effect. In 2009, Lunardini *et al.* proposed the failed SN model<sup>[34]</sup>, in which the flux was more significant and the neutrino spectra were harder considering the failed supernova explosions.

## 1.3.2.3 Experimental Search

Supernova relic neutrinos contain all species of either neutrinos or anti-neutrinos. The largest cross section for neutrino experiments in this  $\sim 10$  MeV region is inverse beta decay, which produces a positron and a neutron. In this section, we concentrate on the search for SRN signal in a large water-Cherenkov detector, together with the present status of SRN search from different experiments in the world.

**Cherenkov Radiation**

Charged particles with a speed exceeding the light speed in medium emit Cherenkov radiation. The Cherenkov threshold is determined by the refractive index of a medium. For electrons in pure water, the threshold is 0.76 MeV, while for muons, it is 157 MeV. Cherenkov photons are usually ultra-violet, decreasing as the wavelength increases.

Compared to scintillation light, which is also widely employed in low energy neutrino experiments, Cherenkov radiation has a lower light yield, but retains the directional information, which is important for solar neutrino detection *etc.* For an IBD event, the direction of the incident neutrino is already lost in the positron production stage. Still, the directional information can help to suppress backgrounds such as solar neutrinos in SRN detection.

A typical light yield with regard to the electron kinetic energy is shown in Fig. 1.7. This process will be described in detail in Section 3.2.1 with quantitative explanation.

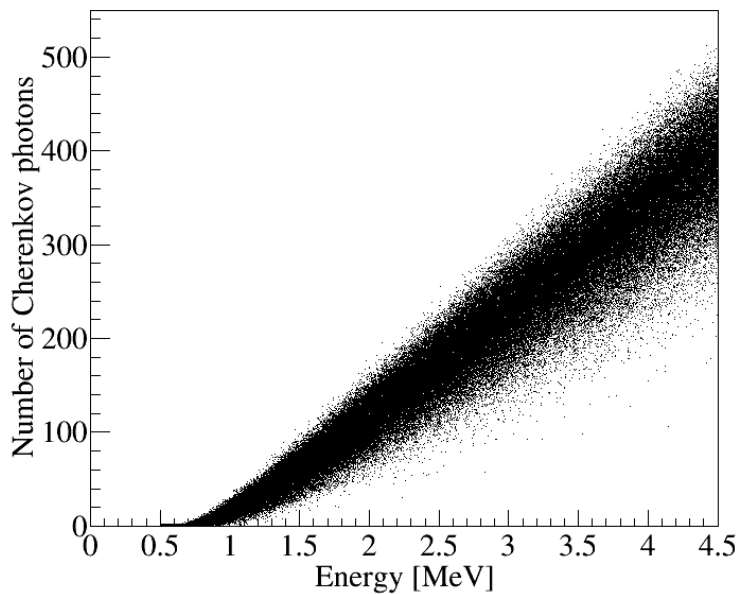


Figure 1.7 Typical Cherenkov Yield for electrons in water versus electron energy.

### Backgrounds for SRN

Backgrounds for the SRN search in Super Kamiokande include the atmosphere neutrinos, neutral current events, the spallation backgrounds induced by the incident cosmic muons, and reactor neutrinos.

#### Atmosphere $\nu_\mu/\bar{\nu}_\mu$ 's CC

Atmospheric  $\nu_\mu/\bar{\nu}_\mu$ 's can interact with water via the CC process

$$\nu_\mu + n \rightarrow \mu^- + p, \quad (1-23)$$

and

$$\bar{\nu}_\mu + p \rightarrow \mu^+ + n. \quad (1-24)$$

In this analysis, the first process does not contaminate the data sample due to the absence of direct neutron and the negligible yield of secondary neutron in low energy region. Similarly, the atmospheric  $\nu_e$  background does not produce neutrons and will not be tagged.

In the second process, however, the daughter electron from the Michel decay of the muon and neutron may fake an IBD signal. The muons as reaction products here may have energy below the Cherenkov threshold, and is called invisible muons. These muons decay to positrons mimicking the primary signal<sup>[49]</sup>, and may coincide with the neutron produced to form an irreducible background at Super Kamiokande even with the neutron tagging technique.

#### Atmosphere $\bar{\nu}_e$ 's CC

The very low end of atmospheric  $\bar{\nu}_e$  spectrum overlap with the SRN detection window, and the CC background from atmospheric  $\bar{\nu}_e$ 's has exactly the same signature as the SRN signal, forming another irreducible background in this analysis. Atmospheric  $\bar{\nu}_e$  within the energy range of SRN sample is believed to be very low and is predicted by some theoretical models. However, the spectrum in lower end is not clearly studied and no experimental result is available, introducing additional systematic uncertainty to the SRN search.

#### Neutral current events

The dominant NC process in this energy region is mainly the NC quasi-elastic scattering with nuclei, knocking out nucleons from the nuclei and leaving excited nuclei

which may emit low energy  $\gamma$ 's. An example of quasi-elastic scattering process can be written as:



where the actual interaction takes place between the neutrino and a nucleon bounded in the nuclei in the initial state. The nucleon in the final state is freed and continues to propagate in water, sometimes triggering secondary processes in water. Most of the NC events can be removed by a Cherenkov angle cut while the residual become background in our SRN sample. This background will be discussed in detail in Chapter. 7.

### **Reactor neutrinos**

Reactor neutrinos are  $\bar{\nu}_e$ 's overlapping the lower end of the SRN energy spectrum, producing exactly the same signal as SRN IBD. After the Fukushima Daiichi nuclear disaster<sup>[50]</sup> in 2011, nuclear power plants in Japan were shut down and only some of them resumed operation from 2016. The reactor neutrinos from these nuclear reactors and also from the nearby South Korea reactors become irreducible backgrounds in the data sample. The energy of reactor neutrinos is known to be below 10 MeV. However, some reactor neutrino events may still leak into the SRN signal region via the energy resolution effect.

### **Spallation**

In the energy range of SRN detection, the dominant backgrounds are spallation induced radioactive isotopes, including  ${}^{12}\text{B}$  and  ${}^{16}\text{N}$  with very large yields per day, as well as  ${}^9\text{Li}$  and  ${}^8\text{He}$ , which are accompanied by neutron production. For neutron tagging detection,  ${}^9\text{Li}$  can decay into  $\beta - n$  with a branch ratio of  $(50.8 \pm 0.9)\%$ <sup>[51]</sup>, faking the IBD signal.

Spallation cuts based on the time and spacial separation of the muon precedent in time flow will reduce the spallation backgrounds. The knowledge of the background pattern is important in this reduction, and a precise measurement on the yield of  ${}^9\text{Li}$  in water has been carried in Ref.<sup>[52]</sup>.

### **Accidental backgrounds**

Any single event in the energy window of SRN that does not accompany a neutron signal will be a source of accidental background, especially the remaining solar neutrinos from the solar angle cut, and the radioactive isotopes induced by spallation. The fake neutron signal arises from mis-tagging. The reduction of this backgrounds mostly depends on the improvement in the neutron tagging algorithm.

## Present Status

Supernova relic neutrinos are not observed yet, despite many experimental efforts, mainly from the neutrino experiments KamLAND and Super Kamiokande (SK). Figure 1.8 shows the 90% upper limit for SRN  $\bar{\nu}_e$  flux from KamLAND<sup>[53]</sup>, SK-I/II/III<sup>[49]</sup> and SK-IV results<sup>[54]</sup>, respectively. The predicted flux for SRN from the constant rate model which gives the largest SRN event rate is also plotted for comparison, as shown in shadow in Fig. 1.8. The present analysis results from barely exclude any SRN models.

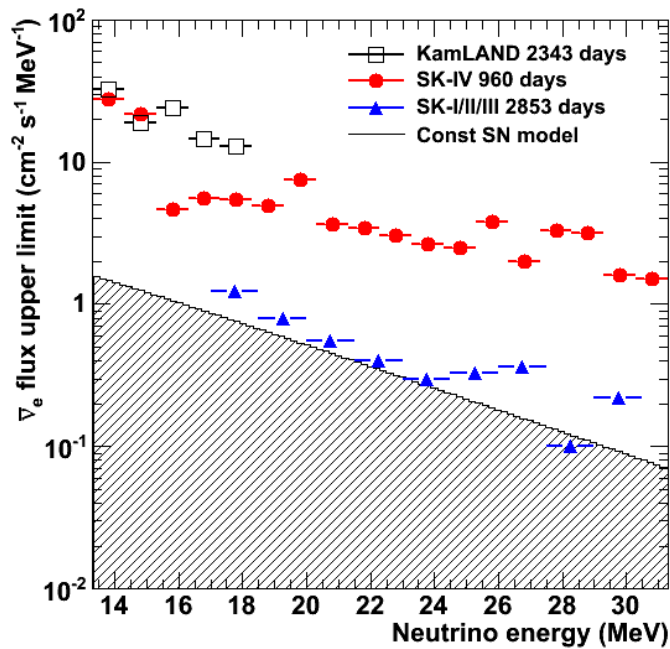


Figure 1.8 The  $\bar{\nu}_e$  flux upper limit from KamLAND<sup>[53]</sup> in black, SK-I/II/III<sup>[49]</sup> in blue and SK-IV results<sup>[54]</sup> in red. The flux of SRN using the constant SN rate model is plotted in shadow.

## KamLAND

KamLAND is a large liquid scintillator detector with 0.6 kiloton fiducial volume, initially designed for the detection of neutrinos, and has recently upgraded to KamLAND-ZEN with a xenon ball inside the scintillator looking for double beta decay<sup>[55,56]</sup>. The relatively high photon yield and the much lower energy threshold of KamLAND enables the direct detection of neutron capture signal, thus sensitive to SRN IBD events. Figure 1.9 shows the positron energy spectrum of the final  $\bar{\nu}_e$  sample in KamLAND<sup>[53]</sup>. The dominant background is the NC events from atmospheric neutrinos. Due to the inability to perform particle identification between electrons and gammas, KamLAND cannot tell the NC events from IBD events. No statistically significant signal is found, and KamLAND gives



the best upper limit of flux below 17.3 MeV.

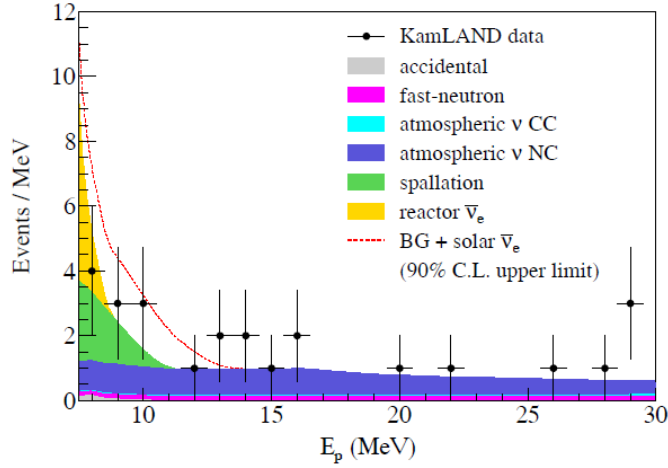


Figure 1.9 The prompt positron energy spectrum for the final  $\bar{\nu}_e$  sample at KamLAND<sup>[53]</sup>.

### SK-I/II/III

Figure 1.10 shows the positron energy spectrum of the final  $\bar{\nu}_e$  sample in SK-III<sup>[49]</sup>, typical for the SK-I/II/III analysis. The energy threshold in SRN detection window was set at 17.3 MeV to reject spallation background. Neutron tagging was not employed in this study due to the limit of the front end electronics and trigger system. As Fig. 1.10 shows, the major backgrounds in this SRN analysis are  $\nu_\mu$  CC,  $\nu_e$  CC,  $\mu/\pi$  and NC events from atmospheric neutrinos, all of which are induced by the atmospheric neutrinos. Among them, the decay electrons/positrons from the invisible muons produced by the  $\nu_\mu$  CC is dominant. A fitting of the four backgrounds and relic signal MC is performed on three data samples of different Cherenkov angle, and no statistically significant signal is found. SK-I/II/III gives the best upper limits for SRN above 17.3 MeV.

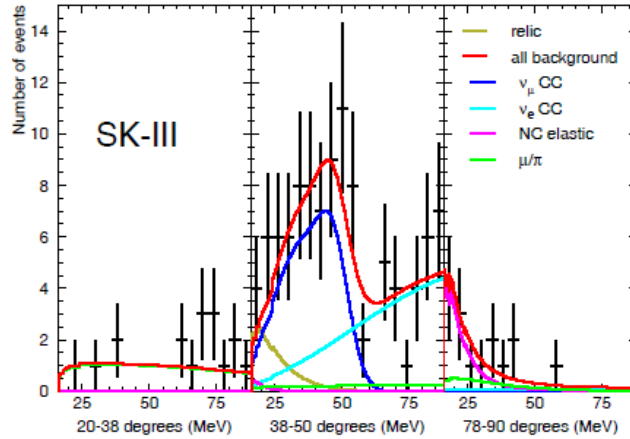


Figure 1.10 The distribution of positron energy for the final  $\bar{\nu}_e$  sample at SK-III<sup>[49]</sup>.

### SK-IV

Figure 1.11 shows the positron energy spectrum of final  $\bar{\nu}_e$  sample in the previous analysis at SK-IV<sup>[54]</sup>. In SK-IV, the DAQ system was changed and the new front end electronics QBEE enabled the software trigger to collect data for the neutron tagging. The SRN analysis SK-IV performed the coincidence events search to identify the IBD signals. With neutron tagging, many of the spallation backgrounds that do not produce neutrons were greatly suppressed, and the energy threshold for this analysis was lowered down to 13.3 MeV. The major backgrounds in this neutron tagging SRN search include the spallation background, atmospheric  $\bar{\nu}_e$  events, and the decay electrons from invisible muons from atmospheric  $\bar{\nu}_\mu$ 's, among which the spallation background dominates. No statistically significant signal was found, and model independent upper limits of flux are extracted for each MeV bin.

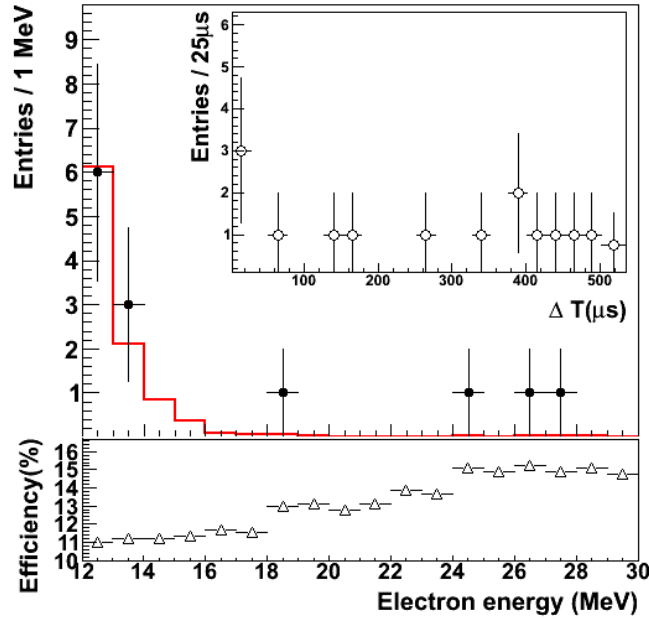


Figure 1.11 The distribution of positron energy for the final  $\bar{\nu}_e$  sample in previous analysis at SK-IV<sup>[54]</sup>.

### 1.3.3 Geoneutrinos

Geoneutrinos are  $\sim$  MeV anti-neutrinos from the Earth interior. In this section, we first introduce the energy budget and bulk silicate Earth models. Then we discuss the mechanism of geoneutrino production and the importance of its detection and measurement. Finally, a review of the present status of geoneutrino studies in different experiments is presented.

#### 1.3.3.1 Energy Budget of the Earth

Understanding the Earth energy budget is crucial, in that it defines the driving power for the Earth activities closely related to the living life, including the mantle convection, plate tectonics, and the geodynamo which describes the magnetosphere protecting the planet from the fatal cosmic radiations<sup>[57]</sup>. For this aim, many fundamental geological questions have to be answered, as they touch on the geological formation, the chemical composition and layering of the Earth.

To begin with, the Earth surface heat flow is currently estimated to be  $46 \pm 3$  TW<sup>[58,59]</sup>. Among them, part of the driving power comes from the initial inheritance of primordial energy since the formation of the planet, released by the accretion as well

as the gravitational differentiation of metal elements sinking to the planet center. The determination of Earth energy budget will answer the question whether this primordial energy is exhausted or not. Besides the primordial energy, the other part of the driving power comes from the radiogenic heat of the natural decay chains of the potassium, thorium and uranium, also known as the heat producing elements (HPE).

HPEs are believed to reside mainly in the silicate shell of the Earth, also known as bulk silicate Earth (BSE). BSE refers to the composition of five reservoirs: the DM(Depleted Mantle), the EM (Enriched Mantle), the CC (continental crust), the OC (oceanic crust), and the LM (lithospheric mantle), as shown in Fig. 1.12<sup>[60]</sup>.

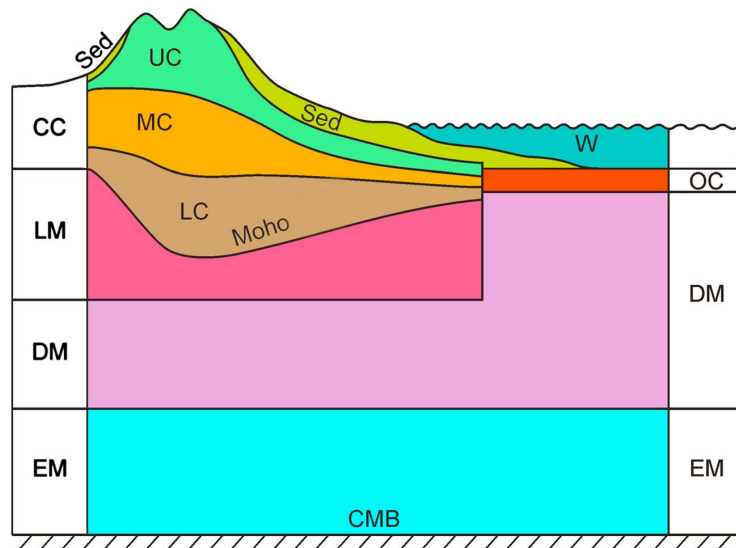


Figure 1.12 A schematic drawing of the structure of the Earth structure<sup>[60]</sup>. The labels are explained in the text.

The predictions for the chemical composition of the BSE are model-dependent. These predictions can be summarized into three classes of distinct predictions for the radiogenic energy ( $Q$ ):

- a) the low- $Q$  models with  $Q \sim 11 \pm 2$  TW, represented by the cosmochemical models<sup>[61]</sup>;
- b) the medium- $Q$  models with  $Q \sim 20 \pm 4$  TW, represented by the geochemical models<sup>[62]</sup>;
- c) the high- $Q$  models with  $Q \sim 33 \pm 3$  TW, represented by traditional geodynamical models<sup>[63]</sup>.

Besides the power budget of primordial energy and radiogenic heat, J. M. Herndon *et al.* also proposed a natural self-sustaining fission reactor mechanism at the core of the

planet to explain for the Earth magnetic field and its long-term variation<sup>[64]</sup>. This is an exotic hypothesis not widely accepted by the community of geologists.

### 1.3.3.2 Geoneutrinos

The abundance of HPEs and their distributions inside the Earth are key ingredients to understand the radiogenic heat from the Earth. One of the methods from the geological side is to drill a deep borehole and measure the chemical composition of the sample taken from it. This method is restricted by the present drilling technique which allows for only  $\sim 13$  km beneath the surface, while the crust typically extends to  $\sim 35$  km. Another approach is from the seismic tomography, which employs surface wave and free oscillation data as well as body wave travel times to resolve the structure of the Earth. However, this approach is sensitive to the density of the Earth layers rather than the abundance of elements.

A direct measurement can be performed by measuring the product of radioactive decays, and the only decay product that can reach from the interior of the Earth to the surface is geoneutrinos. Geoneutrinos are electron antineutrinos  $\bar{\nu}_e$ 's from the decay chain of HPEs. They serve as a unique probe into the interior of the Earth, benefiting from the extremely weak interaction between neutrinos and matter. An example of geoneutrino map from the Earth is shown in Fig. 1.13<sup>[60]</sup>.

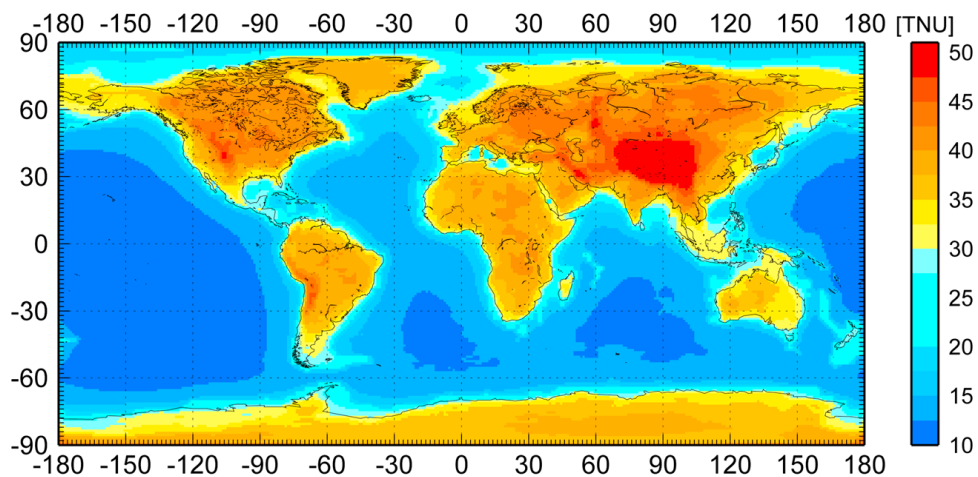


Figure 1.13 Geoneutrino flux at Earth's surface<sup>[60]</sup>. The definition of unit TNU will be covered in Chapter 8.

By detecting the geoneutrino flux, the total amount of HPEs can be derived. The different energy spectrum among geoneutrinos from potassium, uranium, and thorium

can be used to obtain the HPE ratios. Furthermore, taking into account the oscillation effect, a tomography of the BSE using geoneutrinos may be feasible. Present BSE models mainly differ on the description for the Earth mantle. Though lacking the direction information, a precise determination of geoneutrino flux and energy spectrum could allow the identification of mantle geoneutrinos<sup>[65]</sup>, thus discriminating between different BSE models.

The hypothesis of Earth core reactor, or Earth core fission processes<sup>[66]</sup>, will also contribute to the geoneutrino flux. The energy spectra of these neutrinos resembles the spectrum of reactor neutrinos. Since their energy distribution reaches beyond the higher end of the geoneutrinos from radioactive decay, and thus can be distinguished. In following context, we discuss mainly on geoneutrinos from radioactive decay, and refer to them as geoneutrinos. A discussion on Earth core fission neutrinos is included in Section 8.6.2.

### 1.3.3.3 Experimental Search

Geoneutrino detection has become practical with the recent development of neutrino detectors<sup>[67–72]</sup>.

KamLAND performed the first experimental search of geoneutrinos in 2005<sup>[67]</sup>. Assuming a constant Th/U mass ratio at 3.9, the number of geoneutrinos observed at 90% confidence interval was [4.5, 54.2]. Later in 2011, after accumulating 2,135 days of data, KamLAND published a positive observation with higher significance<sup>[68]</sup>. The long-term shutdown of Japanese nuclear reactors from 2011 resulted in a much higher signal to background ratio in KamLAND, and KamLAND claimed to have observed  $116_{-27}^{+28}$  geoneutrino events, as shown in Fig. 1.14<sup>[69]</sup>. The main background is still reactor neutrinos from outside Japan, while other backgrounds include the contribution from  $^{13}\text{C}(\alpha, n)^{16}\text{O}$  and accidental coincidence.

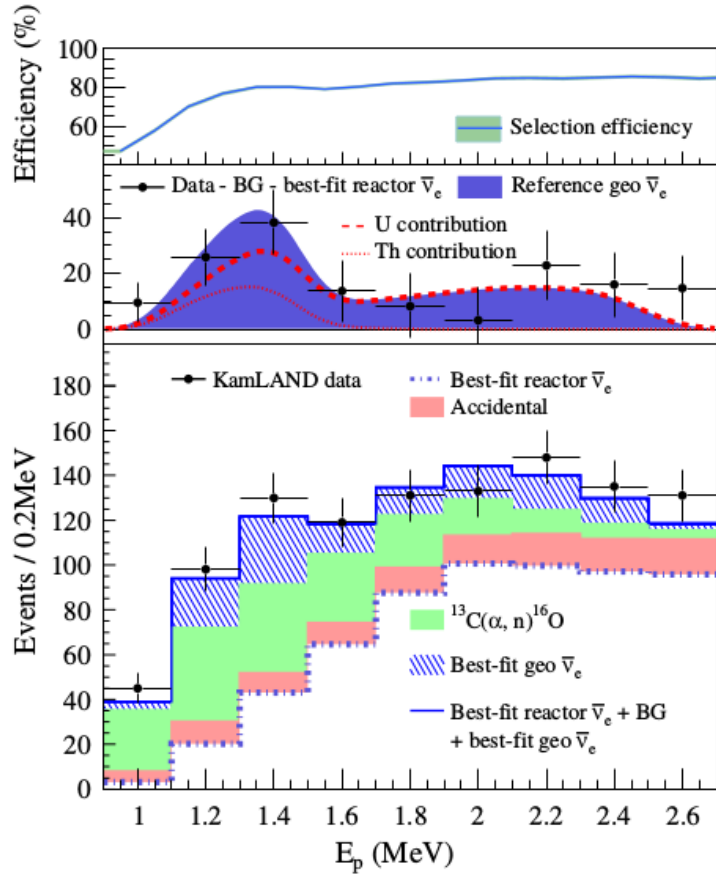


Figure 1.14 Final geoneutrino data sample observed by KamLAND in 2013<sup>[69]</sup>.

Borexino is another liquid scintillator detector that performed experimental studies on geoneutrinos<sup>[73,74]</sup>. In 2010, Borexino published the first observation of geoneutrinos at more than  $3\sigma$  confidence level<sup>[70]</sup>. A following up paper in 2013 attempted to fit the uranium and thorium components individually, though the result was not statistically significant<sup>[71]</sup>. In 2015, Borexino reported geoneutrino observation by  $5.9\sigma$  exclusion of null hypothesis, as shown in Fig. 1.15<sup>[72]</sup>.

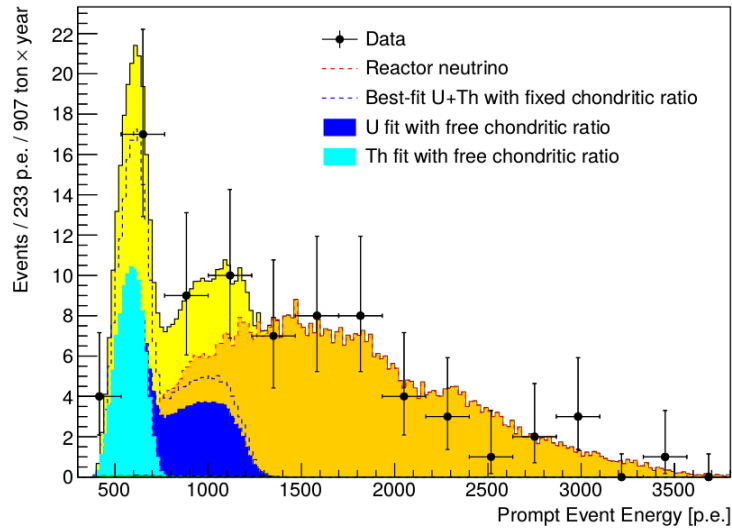


Figure 1.15 Final geoneutrino data sample observed by Borexino in 2015<sup>[72]</sup>.

Geoneutrino measurements should be interpreted with input from geology community to provide information inaccessible by conventional methods<sup>[57]</sup>. Figure 1.16 shows the observation from KamLAND and Borexino compared to the expectations from different BSE models. Both studies disfavor the exhausting of primordial energy (the intercept point at the y-axis), yet cannot distinguish among BSE models due to the large uncertainty.

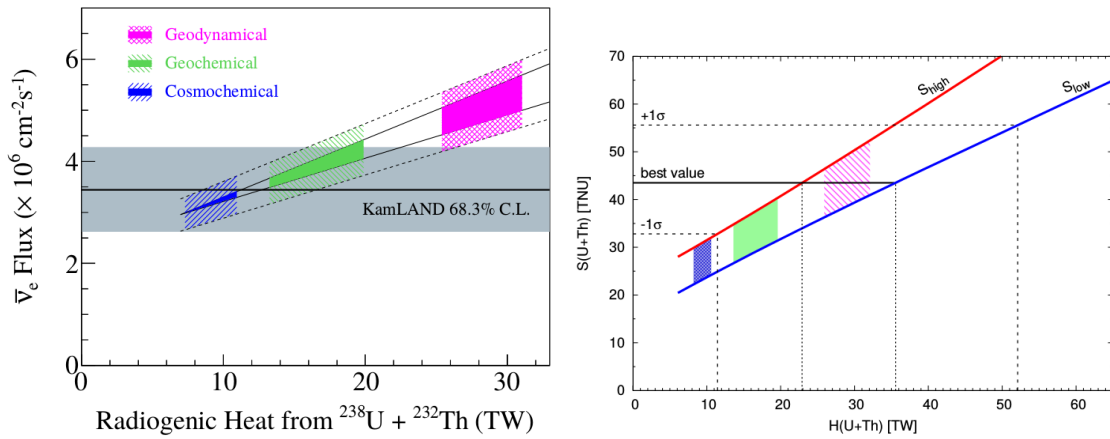


Figure 1.16 The horizontal bands show the geoneutrino observation from KamLAND (left) and Borexino (right). The oblique lines show the expected geoneutrino signal as a function of radiogenic heat. The colored oblique bands show the expectations from different BSE models<sup>[69,72]</sup>.

The uncertainties in both experiments are dominated by statistical uncertainty, contributed mainly by the low statistics and the high reactor neutrino background. In addition, the ratio of uranium and thorium in geoneutrinos is a nother critical issue that should be resolved. All the present measurements assumed a fixed chondritic U/Th ratio, and no



measurement of this value has ever been successful. Future large experiments such as SNO+<sup>[75]</sup>, JUNO<sup>[76,77]</sup>, HANOANO<sup>[78]</sup>, and Jinping<sup>[79]</sup> will push forward the solution for these issues.

## Chapter 2 The Super-Kamiokande Detector

This chapter discusses the Super-Kamiokande detector, including the detector overview, the mechanism to detect signal, and the key systems related to the operation of the experiment.

The author contributed to the detector maintenance of ID and OD PMTs, the data taking shift, and the preparation work for upgrading.

### 2.1 Detector Overview

Located in a cavity of Kamioka mine in Mt. Ikenoyama, Gifu Prefecture, Japan<sup>[80]</sup>, Super-Kamiokande (SK) is the successor of the famous Kamiokande experiment which endeavored the neutrino observation from supernova SN1987<sup>[38]</sup>.

Inside the Kamioka mine, SK shares with other low-background experiments under 1,000 m overburden of rock (2,700 m.w.e.), which reduces the cosmic ray muons by about 5 orders of magnitude, down to 2.2Hz at SK. To further shield the natural radioactivities from the surrounding rock, reinforced concrete of 40-50/ cm was painted to cover the wall of the experimental hall. Above the hall holding the SK detector tank, a large dome was built for the storage of electronics, with holes on given places that enable in-situ calibration without opening the tank. This area, as well as other experimental places where collaborators are supposed to work within, was painted by a polyurethane material named 'Mineguard' to reduce the radon contamination from the surrounding rock in the air. Figure 2.1 shows the schematic view of the detector.

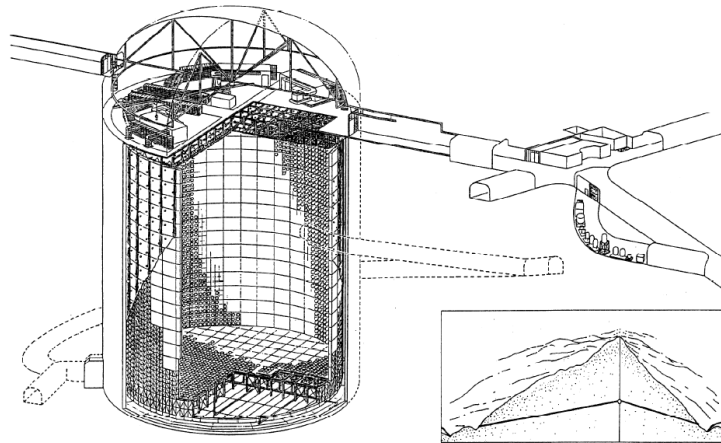


Figure 2.1 A schematic layout of Super-Kamiokande detector and its position inside the Ikenoyama mountain.

The Super-Kamiokande detector tank is a cylinder 41.4 m in height and 39.3 m in diameter, holding 50 kiloton pure water. A layer of black sheet at 2 m from the tank wall separates optically the detector into two concentric cylinders of an inner detector (ID) and an outer detector (OD), leaving 32 kiloton water in ID. The ID is currently viewed by 11,129 20-inch photomultiplier tubes (PMTs) distributed with an interspace of 70 cm as the main detection part, while the OD has a looser distribution of 1,885 8-inch PMTs to veto the cosmic ray muons. These PMTs and their cables are housed by the same supporting frame at ID edge covered with black polyethylene terephthalate sheets, or simply called black sheet, to prevent optical leak between ID and OD, as shown in Fig. 2.2.

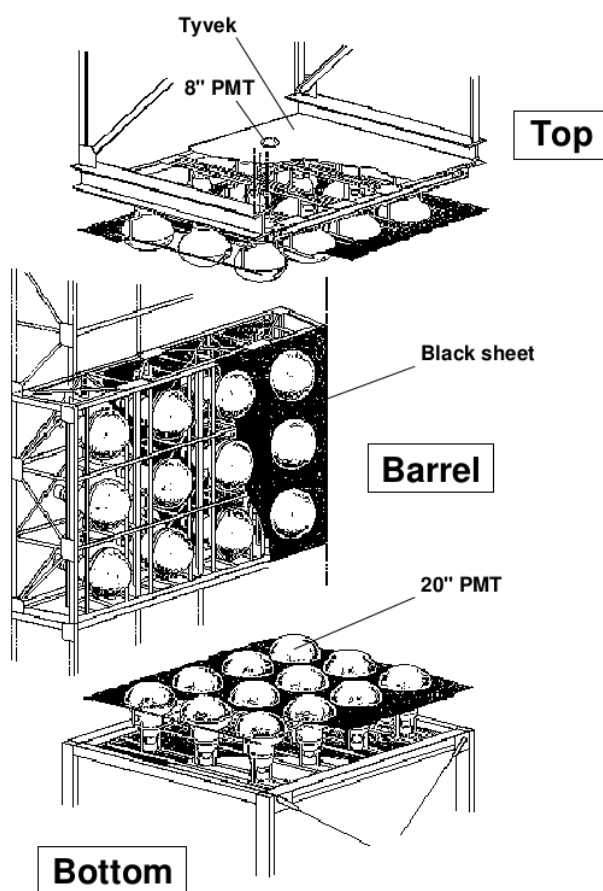


Figure 2.2 The frame structure of the PMT support system in the SK tank.

Inside the SK tank, neutrinos are detected through the interaction in water, producing charge particles or secondary charged particles which emit detectable Cherenkov photons. SK is the largest water-Cherenkov detector with energy threshold down to several MeVs, allowing for various purposes of studies to be performed, including atmospheric neutrinos, solar neutrinos, supernova (relic) neutrinos, and neutrinos from man-made sources such as accelerators or nuclear reactors. SK is also competitive in its initial design purpose of nucleon decay, as well as indirect dark matter search.

The running period of SK can be divided into four phases, from SK-I to SK-IV. The detector first began operation in April, 1996, with 11,146 PMTs in ID forming a photon coverage of  $\sim 40\%$ . This operation continued till July, 2001, when the detector was stopped for maintenance such as faulty PMT replacement, and the time between is referred to as SK-I. During the water re-filling in tank after the maintenance, an accident in which one of the ID PMTs imploded resulted in a chained reaction with a shock-wave that destroyed all the ID PMTs underwater then. In 2002, SK resumed operation after a

Table 2.1 A summary of SK running periods.

SK Period	SK-I	SK-II	SK-III	SK-IV
Begin	Apr. 1996	Oct. 2002	Jul. 2005	Sep. 2008
End	Apr. 2001	Oct. 2005	Aug. 2008	-
Livetime (days)	1489.2	798.6	518.1	1775.6
No. ID PMTs	11,146	5,182	11,129	11,129
No. OD PMTs	1,885	1,885	1,885	1,885
Photocoverage	40%	19%	40%	40%
Front-end Electronics	ATM	ATM	ATM	QBEE
Trigger	Hardware	Hardware	Hardware	Software

redistribution of the remaining ID PMTs above water to allow even coverage of the tank with a photon coverage of merely  $\sim 19\%$ . To prevent the catastrophe of implosion, every PMT was protected with an acrylic cover and a fiberglass reinforced plastic (FRP) case. In Oct. 2005, SK opened its tank again to mount the new PMTs produced during SK running in the tank, and the running period between is referred to as SK-II. After the installation, SK continued operation with a coverage of  $\sim 40\%$  till Jul., 2008, called SK-III. In Aug., 2008, after calibration and upgrading of the electronics and the data acquisition system, SK started to run again and continues till today. This phase is referred to as SK-IV. A summary of livetime and differences between SK-I - SK-IV periods is included in Tab. 2.1.

## 2.2 Cherenkov Radiation

When the speed of a charged particle is greater than the speed of light in medium, it radiates Cherenkov photons in the forward region within a cone pattern of Cherenkov angle  $\theta_c$  along its path. For a charged particle with relative speed  $\beta$  and the medium refractive index  $n(\lambda)$  dependent on the Cherenkov photon wavelength  $\lambda$ , the Cherenkov angle  $\theta_c$  can be calculated as:

$$\cos \theta_c = \frac{1}{\beta n(\lambda)}, \quad (2-1)$$

The refractive index of SK water is about 1.33 at 589 nm, therefore, for ultra relativistic particles with  $\beta \approx 1$ , the Cherenkov angle  $\theta_c \approx 42^\circ$ . The energy threshold for Cherenkov

light  $E_{thr}$  is calculated by

$$E_{thr} = \frac{m}{\sqrt{1 - (1/n)^2}}, \quad (2-2)$$

where  $m$  is the mass of the charged particle. For the physics event of interest, electrons with their small mass are usually ultra-relativistic and their Cherenkov angles peak at  $42^\circ$ , while heavier particles such as  $\mu$ 's and  $\pi$ 's tend to have lower Cherenkov angles. Further discussion is included in Section 3.2.1.

### 2.3 Photo-Multiplier Tubes

#### 2.3.1 ID PMTs

The ID PMTs are 20-inch PMT (R3600)<sup>[81]</sup> developed by Hamamatsu Photonics, the structure of which is shown in Fig. 2.3.

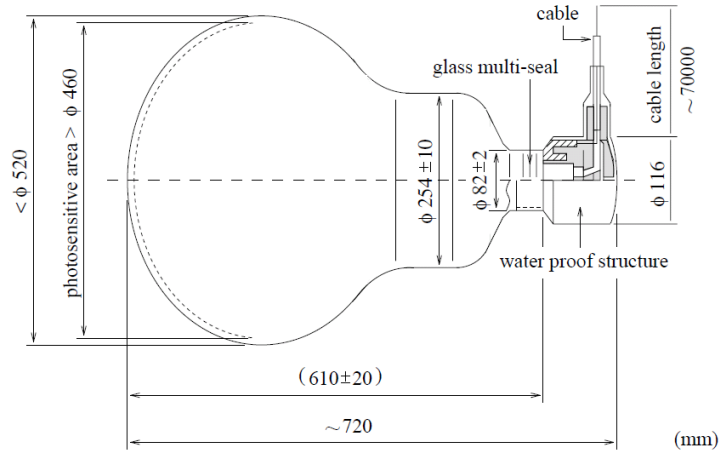


Figure 2.3 An overview of the Hamamatsu R3600 PMT.

The photo-cathode is made of baikkali (Sb-K-Cs). The sensitive wavelength region is between 300 ~ 600 nm, with the maximum quantum efficiency ~ 20%, as shown in Fig. 2.4.

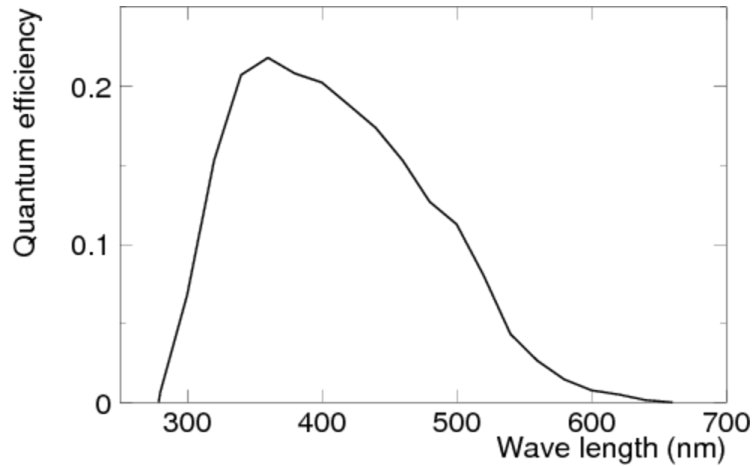


Figure 2.4 The quantum efficiency of the Hamamatsu R3600 PMT as a function of wavelength<sup>[81]</sup>.

Photons collected by the photo-cathode emit single or multiple photo-electrons (p.e.) via the photoelectric effect, and these p.e.'s are then amplified with a gain factor  $\sim 10^7$  by the 11 chain dynodes.

During the propagation from the cathode to the first dynode, p.e.'s are driven by the electrical field and are easily diverted out of the way by the Earth's geomagnetic field. To compensate this effect, 26 Helmholtz coils were deployed surrounding the detector wall, reducing the external magnetic field from 450 mG to 50 mG.

The PMT dark noise in SK-I was  $\sim 3.5$  kHz at a threshold of 0.25 p.e. and has now increased to  $\sim 5.2$  kHz, partially due to radioactivity from the additional acrylic cover and the FRP case applied from SK-II on.

### 2.3.2 OD PMTs

The OD PMTs are covered by a wavelength shifting acrylic plate. The incoming photons are absorbed and re-emitted with a longer wavelength to better match the peak quantum efficiency of the PMT, increasing overall collection efficiency by 50%. This compensates the relatively low coverage but impairs the time resolution due to the absorption and re-emission mechanism. Fortunately, since the OD PMTs are used as a veto counter only, the worse time resolution does not affect its functionality.

## 2.4 Water and Air System

### Water System

It is crucial to maintain the SK tank water at a constant and high level of purity for the propagation of photons. The absorption and scattering in the tank water must be kept as low as possible to ensure both sufficient photon statistics and good time response. Radioactive isotopes in water may form a significant background in low energy detection and should also be eliminated. Besides, the water quality has to be stable and constantly monitored, so as not to contaminate the data sample with any detector-level abnormality.

The fresh water to be purified and filled into the tank comes from two streams inside the Kamioka mine, supplied by the natural rain and snow melt in the mountain. The water is then pumped through a purification system and is continuously circulated through a purification system with a flow of  $\sim 60$  tons/hour, as shown in Fig. 2.5<sup>[82]</sup>.

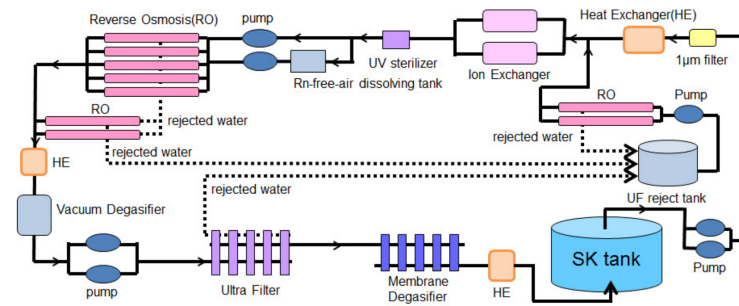


Figure 2.5 A schematic of the water purification system in SK<sup>[82]</sup>.

Various filters and systems are employed to remove contaminants, including an ion exchanger, a vacuum degasifier and membrane degasifier to remove the radon gas, a size specific filters and an ultra filter (UF), and a reverse osmosis (RO) filter. Water entrance in the bottom of the tank and removal points in the top of tank have been calculated and carefully chosen to reduce convection as much as possible, keeping water uniformity. To further reduce convection driven by thermodynamics, heat exchangers (HE) are used to maintain the supply water at a constant temperature of  $\sim 13$  °C, with a variation of 0.01 °C<sup>[82]</sup>. This low temperature, as well as a UV sterilizer, suppress any potential bacterial growth. Still, nonuniformity of water temperature is observed, indicating better water quality in the tank bottom, as shown in Fig. 2.6.



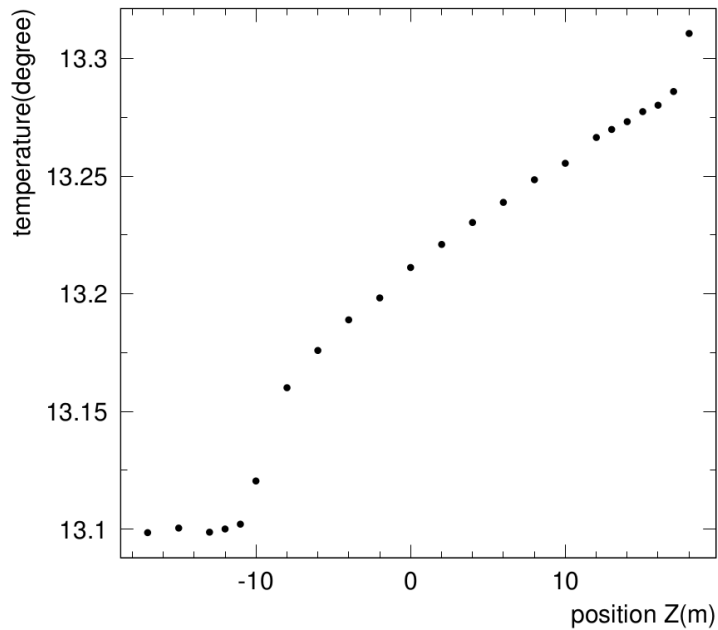


Figure 2.6 Water temperature in SK tank.

### Air Purification

The natural mine air is radon-rich from the surrounding rocks produced by natural uranium decays, imposing a background for low energy detection and also potential health risk due to inhalation. The air flow has a seasonal variation, which causes the different radon contamination level of  $\sim 30 \text{ Bq/m}^3$  in winter and  $\sim 1500 \text{ Bq/m}^3$  in summer<sup>[83]</sup>.

A special air supply system consisting of a large air blower, air filters and a heat exchanger is installed at the entrance of the mine to supply fresh air from outside with a rate of  $70 \text{ m}^3/\text{min}$ , thus keeping the radon (Rn) concentration as low as  $\sim 50 \text{ Bq/m}^3$ . To further reduce Rn concentration in the tank, a special Rn free air system was developed to keep the input Rn concentration to the tank at  $0.06 \pm 0.05 \text{ mBq/m}^3$ <sup>[82]</sup>.

## 2.5 Electronics and Data Acquisition

Atop the SK tank in the experimental dome, there are four electronic huts hosting the high voltage power supplies and the electronic system, and a central hut hosting the trigger system and the control electronic.

### 2.5.1 Electronic System

In 2008, Super-Kamiokande experiment installed a new electronic system which tend to remove the use of hardware trigger<sup>[84]</sup>. In this system, all the data recorded by

the PMTs are output. A more sophisticated software trigger is implemented in the online data acquisition system. The front-end electronics uses new QBEE system (QTC-Based Electronics with Ethernet), where QTC refers to an ASIC developed as a high-speed charge (Q)-Time converter. One QBEE module takes input from 24 PMTs at most with stable observance and fast digitization, which allows a software-based trigger system with a merger PC located in the central hut, as shown in Fig 2.7.

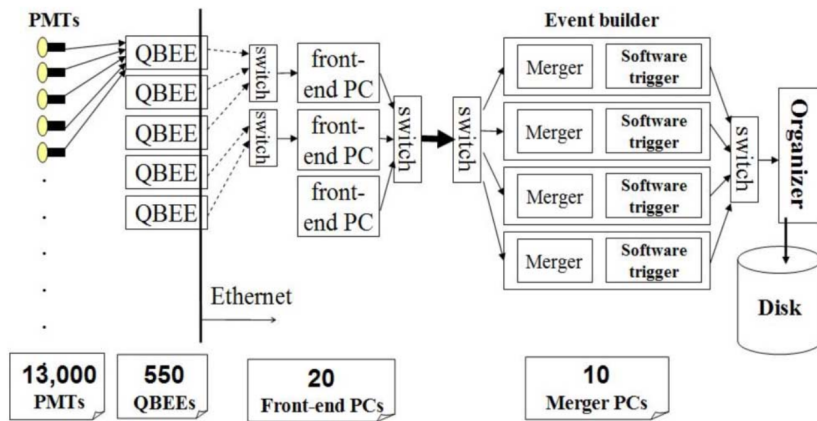


Figure 2.7 A schematic showing the trigger system used in SK-IV.

During the digitalization in QBEE, the PMT charge is still integrated but with three input channels of different gains 1,  $1/7$ , and  $1/49$ , thus to improve the charge resolution for a wider range of 0.2 to 2500 pC. The output from the QTC modules is then sent to the TDCs to measure the pulse width and digitalized later by an FPGA with the charge and timing information, before being sent to the front-end PCs which pass the hit information onto the merging PCs. Finally, the merge PC applies the software trigger thresholds to every event with different trigger width and determines whether to store or remove the selected event on disk.

### 2.5.2 Online DAQ and Trigger

Different trigger thresholds drive the classification of signal: Super Low Energy (SLE), Low Energy (LE) and High Energy (HE) triggers. The thresholds for these types depend on different SK periods, and the thresholds in SK-IV are shown in Table 2.2. The minimum threshold of SLE at 31 PMT hits approximately defines the SK energy threshold at 3 MeV for electrons.

The trigger threshold as well as trigger time is different from previous periods in

Table 2.2 A summary of QBEE triggers.

SK-IV triggers	Hits/200ns Threshold	Event Width ( $\mu$ s)
OD	22	
SLE	34→31	[-0.5, 1.0]
LE	47	[-5, 35]
HE	50	[-5, 35]
SHE	70→58	[-5, 35]
AFT	SHE w/o OD	[35, 535]

SK-IV. Different trigger types do not share the same trigger width to efficiently use the disk space, as SLE triggers are too frequent to expand their time width, while HE trigger are rare enough and related pre- or post-activities are of interest in atmospheric neutrino analysis. The time window is 40  $\mu$ s for LE or HE triggers. For SLE triggers, it is 1.5  $\mu$ s. Besides, a special high energy (SHE) trigger was first introduced in SK-IV to enable the neutron capture signal tagging, with relative high threshold (lowered to 58 hits in Sep. 2011). If an SHE trigger does not accompany an OD trigger, i.e., it's not an apparent muon event, an additional 'After Trigger' (AFT) is issued. The 500  $\mu$ s of data following the AFT trigger will saved for future analysis of neutron captures. The corresponding trigger thresholds and trigger window widths are shown in Table 2.2.

## Chapter 3 Calibration and Reconstruction at SK

This chapter covers the detector calibration, simulation, and reconstruction. For each section, we will introduce the global picture of the system in the SK collaboration, while emphasizing on the contributions from the author.

### 3.1 Detector Calibration

Calibration quantitatively measures the detector performance, providing crucial parameters and systematic uncertainty for data analysis. Depending on the level of measured items, the calibration performed at SK can be split into three categories: PMT calibration, water transparency calibration, and energy scale calibration.

On detector calibration, the author was responsible for the nickel related analysis of QE update and top bottom asymmetry estimation, as well as the water transparency measurements by laser and by decay electron. The author also took part in related hardware work.

#### 3.1.1 PMT Response Calibration

PMTs provide timing and charge information, which are used in both energy and position reconstructions.

PMT charge is usually parameterized as the product of two factors: the PMT gain and quantum efficiency. Gain refers to the conversion factor from the generated number of p.e.'s on the cathode to the charge output of the PMT in pico Coulomb (pC). Quantum efficiency (QE) by definition refers only to the ratio of p.e.'s emitted from the cathode to the number of incident photons. However, since the first-dynode collection efficiency can not be isolated from the measurement of QE, we define the QE here as the ratio of p.e.'s collected by the first dynode to the number of incident photons on the cathode.

For the low-energy events, most PMT hits are single p.e., and the QE calibration is critical, while for the high energy events, where charge information is required to get the exact number of p.e.'s on a single PMT, gain calibration is also crucial. Since the PMTs used at SK are mostly from the same model with only the difference in production batches and the fluctuations PMT by PMT, an 'absolute gain' is defined as the average amplification factor for all PMTs, while a 'relative gain' is used for the individual PMT

difference. The overall QE is absorbed in a ‘COREPMT’ parameter to be mentioned in LINAC calibration, and the ‘QE table’ refers to a normalized QE factor PMT by PMT.

### 3.1.1.1 High Voltage

PMTs must work under proper and relatively uniform high voltage to produce similar output charge for the same incident photons. At SK, this high voltage value is adjusted by the response to an isotropic light source: scintillation light.

A scintillator ball is placed at the center of SK tank as a permanent fixture, and is triggered by the light produced from a xenon (Xe) lamp passes through an optical fibre, as shown in Fig. 3.1.

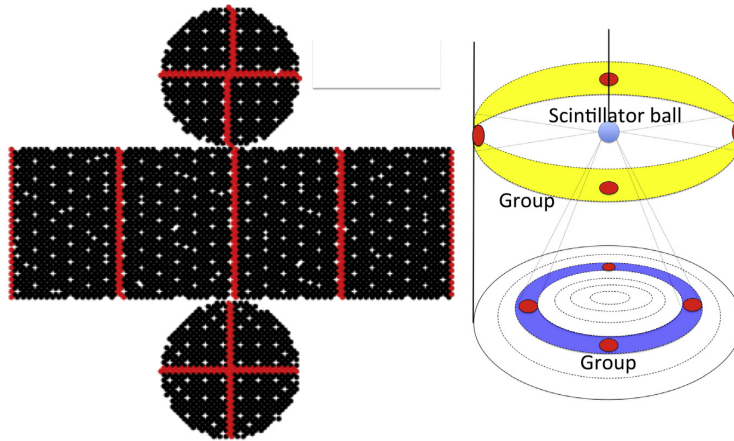


Figure 3.1 A sketch of the high voltage calibration by a scintillator ball triggered by a Xe lamp. The red dots illustrate positions of the pre-calibrated reference PMTs.

To compensate for the geometric acceptance, 420 reference PMTs were calibrated one by one before the PMT installation into the tank and distributed uniformly as shown in Fig. 3.1. The HV input for each PMT was adjusted to match its charge output with the pre-calibrated PMT’s in the same geometrical location.

### 3.1.1.2 Relative Gain

The normalized ‘relative gain’ is determined by a laser system with two setups generating flashes of different intensity. The light source is a nitrogen laser emitting photons whose wavelengths are shifted by a dye to match the PMT response spectrum. The emitted photons then pass through an optical fiber to a diffuser ball near the tank center, as shown in Fig. 3.2.

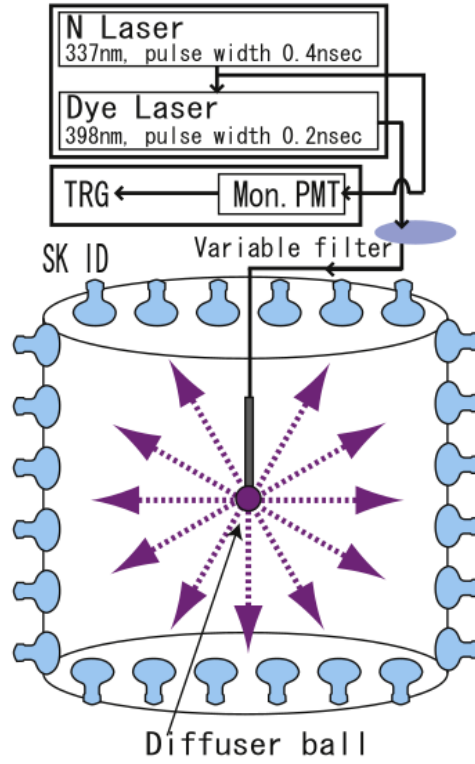


Figure 3.2 The overview of the timing calibration system.

The two intensities give different different hit patterns. The high-intensity flash illuminates every PMT with multiple photons and the low-intensity flash fires only several PMTs, and thus enabling a reasonable assumption of a single photon hit. Denoting the PMT id as  $i$ , the high-intensity flash gives the charge  $Q_{obs}(i)$  and low-intensity flash gives the number of events that records an over threshold hit  $N_{obs}(i)$ , i.e., the hit frequency. The geometrical acceptance and QE are therefore cancelled out:

$$\begin{aligned} Q_{obs}(i) &\propto I_s \times a(i) \times \epsilon_{qe}(i) \times G(i) \\ N_{obs}(i) &\propto I_w \times a(i) \times \epsilon_{qe}(i) \end{aligned} \quad (3-1)$$

where  $I_s$  and  $I_w$  are the average intensities of high and low intensity flashes, respectively,  $a(i)$  is the acceptance of ID-PMT  $i$ ,  $\epsilon_{qe}$  is the QE, and  $G(i)$  is the PMT gain. The overall ‘gain’  $G(i)$  relies on the precision of laser intensity, but the relative gain can be directly derived as,

$$G(i) = \frac{Q_{obs}(i)}{N_{obs}(i)F_{norm}}, \quad (3-2)$$

where  $F_{\text{norm}}$  is a normalization factor. The distribution of relative gain at SK is shown in Fig. 3.3.

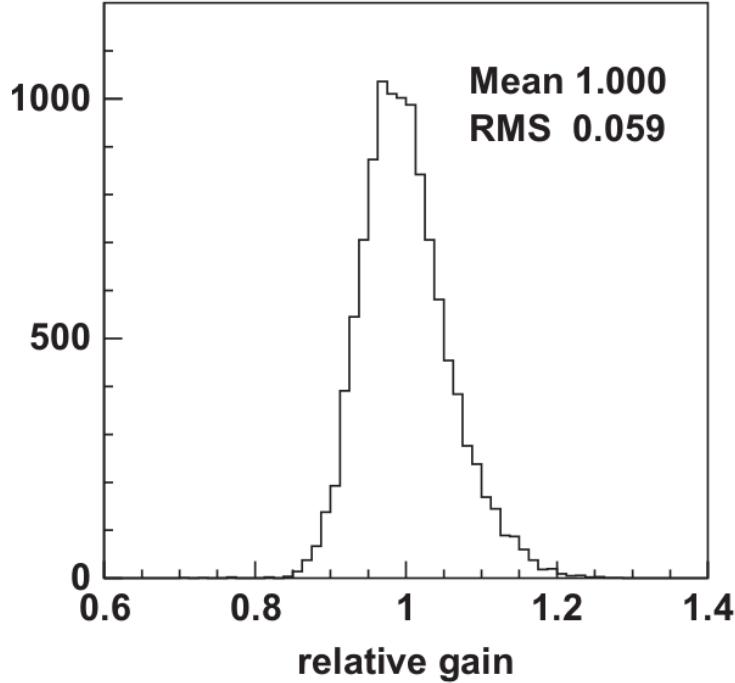


**Fig. 10.** Distribution of relative gain of PMTs.

Figure 3.3 Distribution of the relative gain of PMTs at SK.

### 3.1.1.3 Absolute Gain

The calibration of the absolute gain value is carried with a nickel (Ni) source emitting isotropic  $\gamma$ 's of 9 MeV from the neutron capture  $^{58}\text{Ni}(n, \gamma)^{59}\text{Ni}$ , where the neutrons are emitted from a  $^{252}\text{Cf}$  source<sup>[85]</sup>. For uniformity, the Ni-Cf source is shaped as a spherical melon ball, and deployed at the tank center for the absolute gain calibration. The  $\gamma$ 's intensity and energy is so low that the average charge produce by every event is only 0.004 p.e./PMT, and thus ensure with Poisson statistics that more than 99% of the hits produce only single p.e. on a PMT.

The relative gain value and dark hits effect should be corrected before deriving the absolute gain. The first item is corrected by dividing the charge with the relative gain obtained as described in Section 3.1.1.2. To account for dark hits, an on- and off-time windows are defined by the expectation whether a PMT could possibly be hit by the source, and the data in the off-time window is considered as dark noise to be subtracted from the on-time data. The charge distribution from all ID PMTs after correction is shown

in Fig. 3.4, where a linear extrapolation is applied to represent the region below the 0.3 pC threshold.

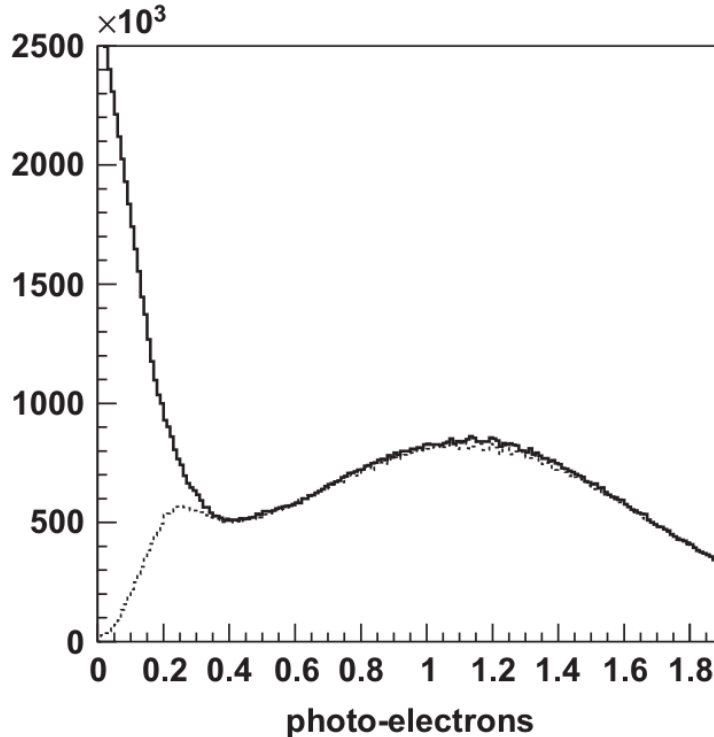


Figure 3.4 The single p.e. distributions with a linear extrapolation under 0.3 pC.

Averaging from this single charge distribution gives the conversion factor from pC to single p.e. as 2.658 pC / p.e. in SK-IV. A long-term gain increase has been observed at SK as well as many other experiments using PMT as photo sensor. No clear reason has been identified, and a correction is included in data analyses run by run to account for this effect.

#### 3.1.1.4 Quantum Efficiency

The normalized QE table is crucial for the reconstruction of low energy events. QE is measured by the Ni-Cf used in the absolute gain calibration so that the intensity of light source is low enough to satisfy Eq. (3-1). This time the acceptance as well as the solid angle has to be corrected. While the latter can be directly calculated, a Monte-Carlo (MC) simulation is used to predict the number of photons arriving at each PMT. The QE table is calculated by counting the number of observed hits in data and taking the ratio between the observed hits to the predicted number of hits from MC, with an overall normalization to remove the dependence of the absolute light intensity.



The setup for MC is important to obtain a proper QE table, and it should take into consideration the water transparency and the nonlinearity of the transparency to reproduce the acceptance in data. In SK-IV, the water transparency variation inside the tank is modeled by a piecewise linear function established by measuring the temperature profile throughout the ID. Details will be covered in Section 3.1.2.4. Previously in SK-IV, the QE table was produced using SK-III data during the water convection period, when the nonuniformity of water was believed to be zero. However, a recent study showed that the QE table had a  $\phi$  direction nonuniformity, which is related to the convection and circulation of water, as shown in Fig. 3.5.

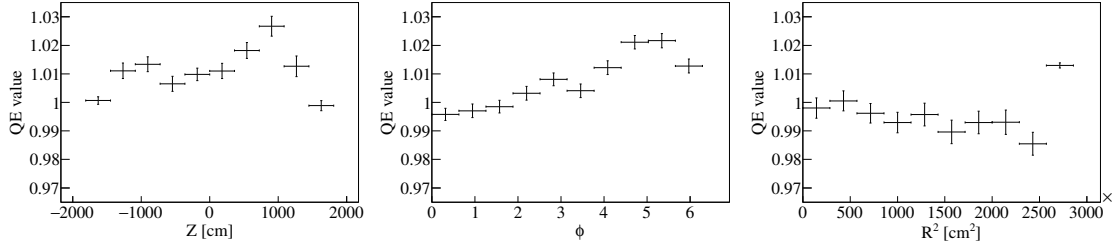


Figure 3.5 Previous QE table used in SK-IV in  $z$  (left),  $\phi$  (middle),  $r$  (right) direction. Systematic nonuniformity was observed.

Now a new QE table has been calculated using the nickel data without water convection, so as to avoid the nonuniformity in  $\phi$  direction. The expected nonuniformity in  $z$ -direction is included in MC to compare with data, while the solid angle is directly corrected analytically for both data and MC,

$$N' = N_{obs}(i) \times R(i)^2 / \alpha(\theta(i)), \quad (3-3)$$

where  $N_{obs}(i)$  is the observed hit in  $i$ -th PMT,  $R(i)$  is the distance from the  $i$ -th PMT to the event vertex,  $\theta(i)$  is the incidence angle of a photon to the PMT and  $\alpha$  is the corresponding solid angle. Some position dependence remains even after this acceptance correction, including the angular acceptance on the PMT surface, the reflection from neighboring surfaces, the scattering and absorption by the water, *etc.* These effects are compensated in MC. Finally after normalization, the relative QE of the ID PMTs is obtained as shown in Fig. 3.6. This quantity is tabulated and used in the MC simulations.

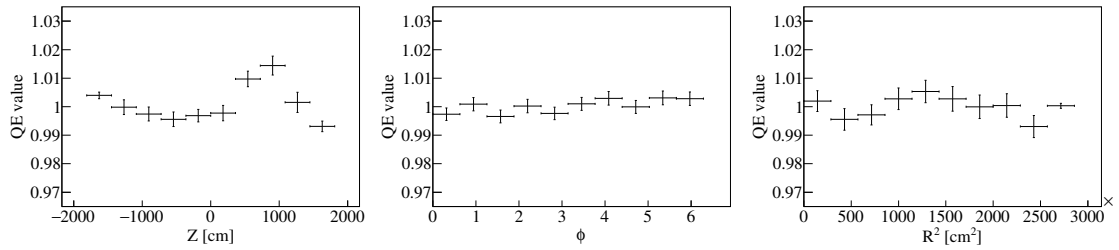


Figure 3.6 Present QE table used in SK-IV in  $z$  (left),  $\phi$  (middle),  $r$  (right)-direction. Good uniformity is observed except for the  $z$ -direction, where the water quality nonuniformity is still not well-understood.

### 3.1.1.5 Timing Calibration

Hit time is the only information used in the vertex and direction reconstructions of the low energy events. The response time of a readout channel depends mainly on the PMT transit time, the length of a PMT signal cable, the processing time of electronics, and the time-walk effect due to the dependence of rise time on the pulse amplitude.

In the timing calibration, the light source is the same nitrogen laser as that used in the relative gain calibration shown in Fig. 3.2. The diffuser ball is again placed near the center of the tank. The directional nonuniformity of the photon emission time is measured and observed to be within 0.2 ns.

Due to the correlation between the time response and pulse height, i.e., charge, the calibration gives a 2-dimensional table. The time of flight (ToF) must be subtracted from the recorded hit time, which introduces an uncertainty of  $\pm 50$  ns. The timing distribution in every of the 180 bins on the charge axis is parameterized as an asymmetric Gaussian function and evaluated with the same data set. The smoothed 2-dimensional TQ distribution is then fitted by a piecewise polynomial function. The function with fitted parameters is then used in MC.

### 3.1.2 Water Transparency Measurement

Three kinds of water transparency measurements are performed at SK, namely the water laser measurement for the scattering and absorption of photon in water, the through-muon measurement for the effective total attenuation length in the high energy physics group, and the decay-electron measurement for the effective total attenuation length in the low energy physics group.

This section discusses the water laser measurement and the decay-electron measurement only, since the topics for this thesis are concentrated on the low energy physics.

Also discussed is the water transparency nonuniformity in the  $z$ -direction, i.e., top-bottom asymmetry in water.

### 3.1.2.1 Water Laser Measurement

The attenuation length in water is obtained by combining the measurements on the scattering and absorption of the optical photons. By definition, the scattering coefficient is measured by the hits scattered off the direction of the input light, and the absorption coefficient can be measured by the total light intensity. However, this is not practical for an in-situ monitoring. At SK, using several mono-direction light sources with well-known wavelengths, we compared the timing and spatial distributions of the light with those from MC, and extracted the light absorption and scattering coefficients as functions of wavelength.

#### **Experimental setup**

The light source in this measurement referred to as the water laser system, is a combination of dye and N<sub>2</sub> lasers of wavelengths 337, 375, 405, 445 and 473 nm. The laser beam is directed into SK tank via the optical fibers connected to injectors in different positions, as shown in Fig. 3.7. There are 7 injection positions for the laser beam, with 2 on the top endcap and 5 on the barrel region in a vertical line. The present water laser analysis uses only data from one of the top injectors (called new-top) beaming down. Data from other injectors, especially from the position on the barrel beaming horizontally, have the potential to resolve the top-bottom asymmetry in SK tank water, and recently a new group starts to analyze the horizontal laser data.

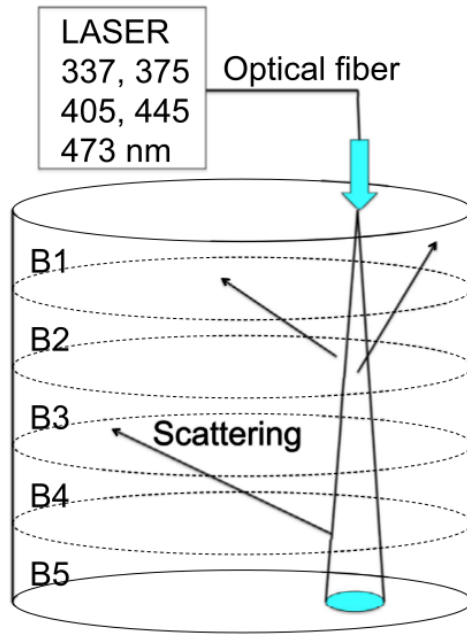


Figure 3.7 Schematic view of the water laser system.

### Analysis method

In the water laser analysis, the SK tank is divided into 7 sections, namely, the top endcap, barrel 1 through 5 from top to bottom, and the bottom endcap. After the water laser event selection by the calibration trigger attached, PMT hits are extracted from the data file with charge and hit time information. To avoid the inclusion of saturated PMTs, the hits in the cluster region facing the beam are rejected, which, for the new-top injector, is in the bottom endcap. The remaining hits are then corrected for the ToF and filled with a weight of PMT charge in 7 hit-time histograms, which correspond to the 7 sections of the SK tank.

The laser intensity is a nuisance parameter which impacts the sensitivity of this study. However, it is not easy to measure the laser intensity. Although a measurement of total charge in the cluster region facing the light beam can provide a reference value to tune the water laser intensity in MC, this value is affected by the saturation effect of PMTs. Besides, it is not realistic to reproduce MC for every intensity measured. To eliminate the fluctuation of laser intensity in the water laser analysis, the 7 hit-time histograms should be normalized to remove the impact of laser intensity. Consequently, this water laser measurement is not very sensitive to the absorption parameter.

Many MC samples are generated with different sets of scattering and absorption parameters. The deviation of these 7 histograms between data and a MC sample is

calculated by a  $\chi^2$  test. To ensure sufficient statistics, the range for calculation in the histogram is changed for each region. The input parameter set for the MC sample with the minimum  $\chi^2$  is determined to be the measured water scattering coefficients. An example of the fitting histograms is shown in Fig. 3.8.

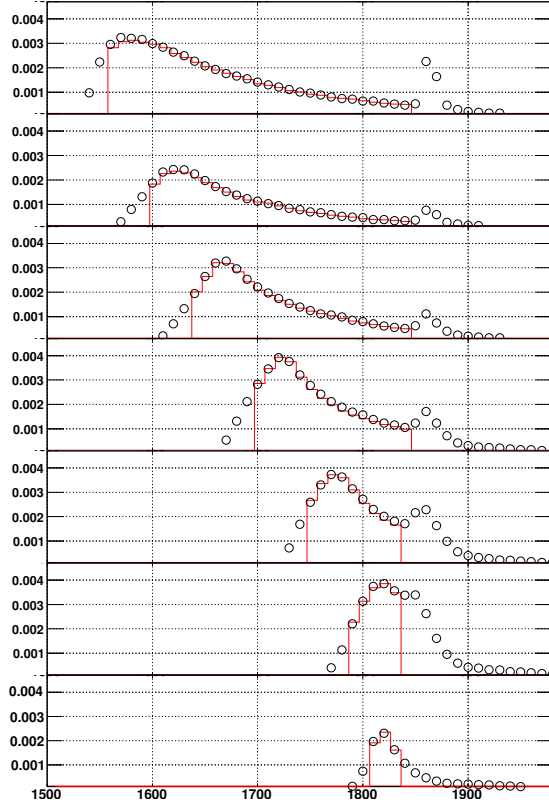


Figure 3.8 An example of water laser data (black points) and MC (red line) fit.

### 3.1.2.2 Calibration result

At SK, the input parameters are defined as those for the absorption  $\alpha_{\text{abs}}(\lambda)$ , the symmetric scattering  $\alpha_{\text{sym}}(\lambda)$  described by  $1 + \cos^2 \theta$ , and the asymmetric scattering  $\alpha_{\text{asy}}(\lambda)$  described by  $1 + \cos \theta$ , where  $\theta$  defines the angle between the incident direction and the reflected direction. The water transparency can be obtained as

$$L(\lambda) = \frac{1}{\alpha_{\text{abs}}(\lambda) + \alpha_{\text{sym}}(\lambda) + \alpha_{\text{asy}}(\lambda)}. \quad (3-4)$$

For the 5 wavelengths available in water laser data, these three parameters are fit with polynomials of  $\lambda^{-1}$  to obtain the wavelength dependent curves,

$$\begin{aligned}
 \alpha_{\text{abs}} &= P_0 \times \frac{P_1}{\lambda^4} + C, \\
 \alpha_{\text{sym}} &= \frac{P_1}{\lambda^4} \times \left(1 + \frac{P_5}{\lambda^2}\right), \\
 \alpha_{\text{asy}} &= P_6 \times \left(1 + \frac{P_7}{\lambda^4} \times (\lambda - P_8)^2\right), \\
 C &= P_0 \times P_2 \times (\lambda/500)^{P_3}, \quad \lambda \leq 464\text{nm},
 \end{aligned} \tag{3-5}$$

where  $P_0 \sim P_8$  are the fitting parameters. These polynomial function definitions are empirical and do not exactly represent real physical properties<sup>[86]</sup>. The functions used in present SK simulation were calibrated in 2009 and are shown in Fig. 3.9

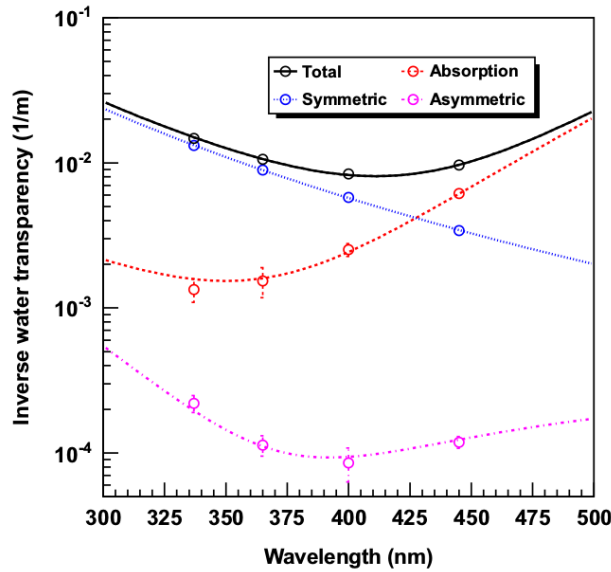


Figure 3.9 The calibration of water scattering parameters in 2009<sup>[86]</sup>.

As shown in Fig. 3.10, the symmetric scattering parameter shows a good stability over time, while the sensitivity is relatively poor for the absorption parameter and the asymmetric scattering parameter. The slight increasing trend of water parameter is due to the uncorrected threshold effect in hits due to the gain increasing as described in Section 3.1.1.3.

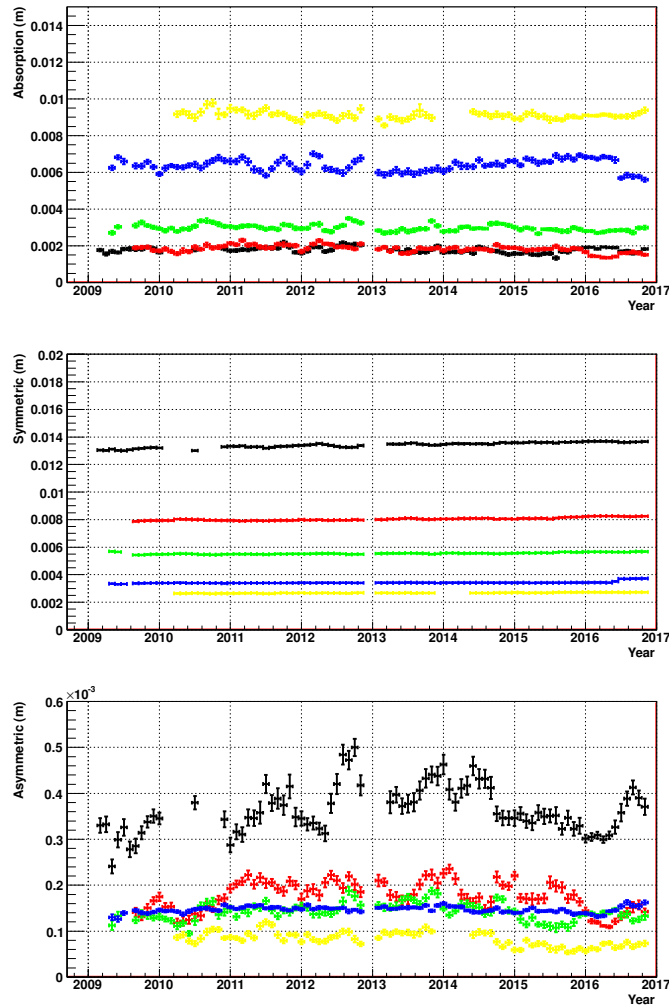


Figure 3.10 Water parameter stability over time.

### 3.1.2.3 Decay-electron Measurement

Although the water laser calibration can provide 5 different water transparency values for the 5 available different wavelengths, it is desired to measure the effective water transparency directly for Cherenkov photons. Since water transparency keeps changing inside the SK tank on a daily basis due to the water circulation, *etc.*, a daily sample with sufficient statistics is necessary for the calibration. The 2.2 Hz muon rate indicate that many muons are stopped inside the SK tank, and quickly decay to produce Michel electrons. These decay-electrons radiate Cherenkov photons with the well-known Michel spectrum and is therefore suitable for the water transparency calibration.

#### Data selection

Unlike the water laser data where events are selected directly by the calibration trigger, decay-electron events have to be selected with certain criteria to remove the backgrounds:

1.  $3.0 \mu\text{sec} \leq \Delta t \leq 8.0 \mu\text{sec}$ , where  $\Delta t$  represents the time difference between the parent muon and the daughter decay-electron candidate;
2.  $L_{\text{wall}} > 2 \text{ m}$ , where  $L_{\text{wall}}$  is the distance between the reconstructed vertex of the decay electron candidate event and the ID wall, i.e., the fiducial volume for decay-electron events is 22.5 kiloton;
3.  $|\vec{x}_\mu - \vec{x}_e| < 250 \text{ cm}$ , where  $\vec{x}_\mu$  is the reconstructed stopping point of cosmic ray muon and  $\vec{x}_e$  is the reconstructed decay electron candidate vertex.

### Analysis method

After the event selection, the distance  $r$  between the  $i$ th PMT and the decay electron candidate is calculated. All the ID PMTs are grouped by  $r$  and divided into 60 bins. An effective hit for every PMT  $N_{\text{eff}}^i$  is calculated as

$$N_{\text{eff}}^i = (X_i + \epsilon_{\text{tail}} - \epsilon_{\text{dark}}) \times \frac{N_{\text{all}}}{N_{\text{normal}}} \times \frac{R_{\text{cover}}}{S(\theta_i, \phi_i)} \times \frac{1}{QE_i}, \quad (3-6)$$

where  $X_i$  is the gain corrected occupancy of a PMT to account the effect of multiple photoelectrons,  $X_i = \log(\frac{1}{1-x_i})/x_i$ , and  $x_i$  is the ratio of the number of hit PMT's to the total number of PMT's in a  $3 \times 3$  patch around the  $i$ -th PMT;  $\epsilon_{\text{tail}}$  and  $\epsilon_{\text{dark}}$  are correction factors respectively for the tail effect and dark noise;  $N_{\text{normal}}$  accounts for the bad tubes and dead channels;  $R_{\text{cover}}$  corrects the acceptance of the candidate vertex to the  $i$ -th PMT, i.e., solid angle;  $QE_i$  is the QE table value for the  $i$ -th PMT. More details are explained in the context of Eq. (3-21). Then the average of  $N_{\text{eff}}^i$  is calculated for every  $r$  bin, and  $\ln(N_{\text{eff}}^i)$  is plotted against  $r$ , as shown in Fig. 3.11. This histogram is fitted by a linear function within the range from 1,200 cm to 3,500 cm. The inverse of the fitted slope by definition is the attenuation length.



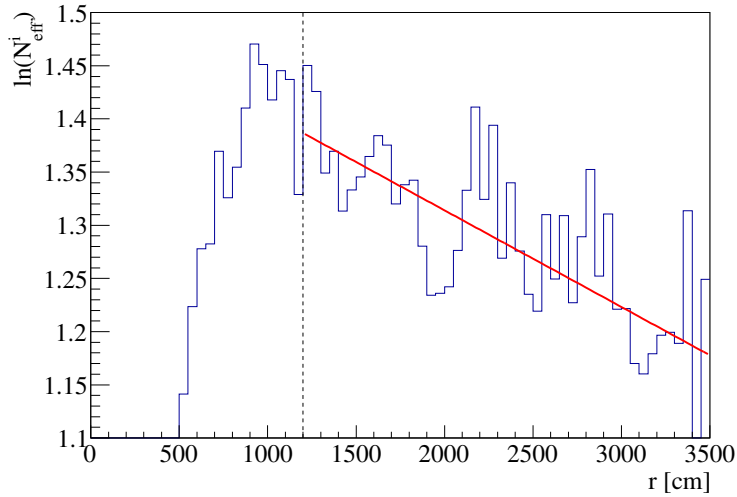


Figure 3.11 A typical histogram of  $N_{\text{eff}}^i$  versus  $r$  (blue solid), fitted by a linear function within the range from 1,200 cm to 3,500 cm (red solid). The fitting range is indicated by a black dotted line.

### Result and validation

Since SK is under a rock shielding of 2,700 m.w.e., the number of decay-electron events from muons per day are still limited. To ensure the stability of fitting, two methods have been adopted. The first is to fix the intercept on the y-axis, which used to cause a problem in obtaining the water transparency due to the gain increase in SK-IV, but has been fixed by tuning the conversion factor  $C$ , which describes the threshold effect, and converts the gain increase into the hit increase. The calculation of  $C$  will be covered in Section 3.3.3.2. After the fix, the y-intercept is so stable that can be regarded as a constant 1.499, as shown in Fig. 3.12. The second method is to take a  $\pm 7$ -day running average of water transparency. Figure 3.13 shows the water transparency evolution with time. The variation of the water transparency is observed within 10% throughout the SK-IV period.

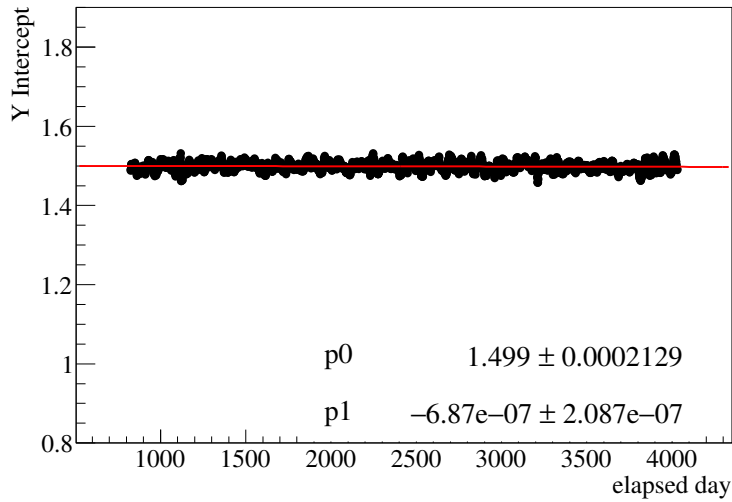


Figure 3.12 Stability of fitted y-intercept after the threshold effect correction. X-axis is the elapsed day from the beginning of SK-IV. A good stability over SK-IV period is observed.

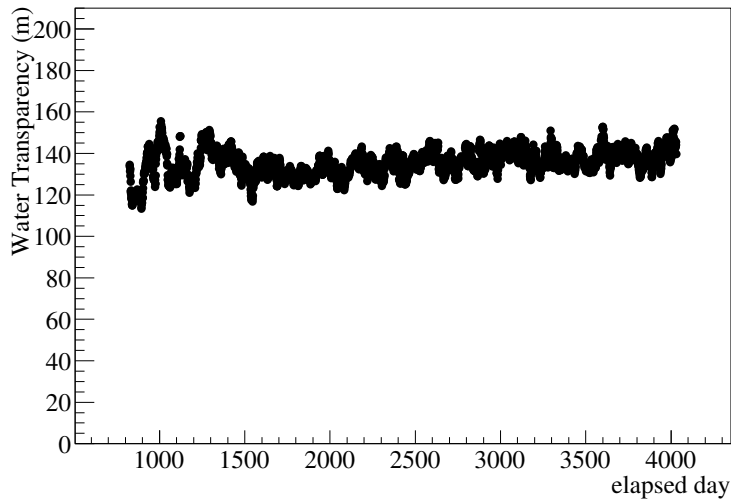


Figure 3.13 Water transparency evolution with time. A  $\pm 7$ -day average is used in this figure. X-axis is the elapsed day from the beginning of SK-IV. Water transparency varies within 10%.

The sum of  $N_{\text{eff}}^i$ ,  $N_{\text{eff}}$ , is a direct indicator of event energy, as will be discussed in Section 3.3.3.1. The calculation of  $N_{\text{eff}}$  is sensitive to the water transparency, and thus a stable  $N_{\text{eff}}$  in some sense verifies the estimation of water transparency. Figure 3.14 shows the average  $N_{\text{eff}}$  of the decay-electron spectrum with a good stability.

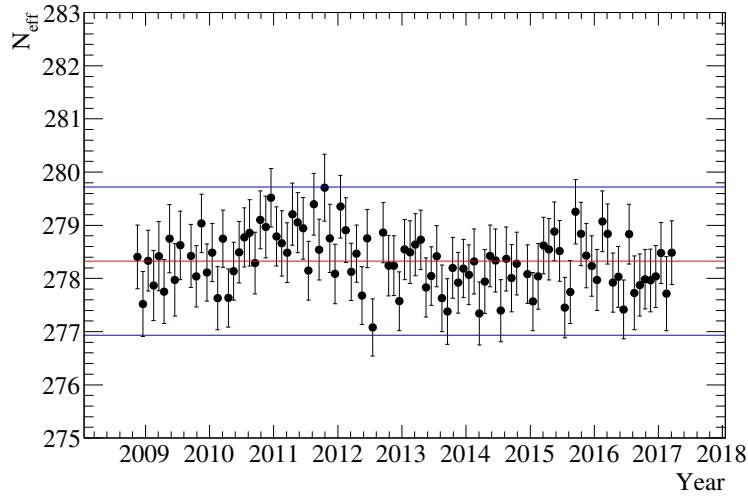


Figure 3.14  $N_{\text{eff}}$  evolution with time. Blue lines indicate 0.5% deviation from average value (red line).

#### 3.1.2.4 Top-bottom Asymmetry

A top-bottom asymmetry (TBA) has been observed in SK data, i.e., after all of the above calibration results corrected in a controlled sample, top PMTs still do not get as many hits as bottom PMTs do. The most possible reason is that the water transparency is not uniform throughout the tank, and the water quality has a  $z$ -dependence, thus causing the TBA effect. As shown in Fig. 2.6, the water temperature is varying along the  $z$ -axis. A  $z$ -dependent water transparency model is constructed to accommodate this effect,

$$\begin{aligned}\alpha_{\text{abs}}(\lambda, z) &= \alpha_{\text{abs}}(\lambda) \times (1.0 + \beta z) & (z \geq -1, 100\text{cm}), \\ \alpha_{\text{abs}}(\lambda, z) &= \alpha_{\text{abs}}(\lambda) \times (1.0 - 1, 100\beta) & (z \leq -1, 100\text{cm}),\end{aligned}\tag{3-7}$$

where  $\beta$  is the slope in the unit of  $\text{cm}^{-1}$ , an indicator for the top-bottom asymmetry level. This  $z$ -dependent water transparency is shown in Fig. 3.15, in three different parameter sets. Only  $\alpha_{\text{abs}}$  is modelled with  $z$ -dependence, while both scattering parameters are assumed to be constant.

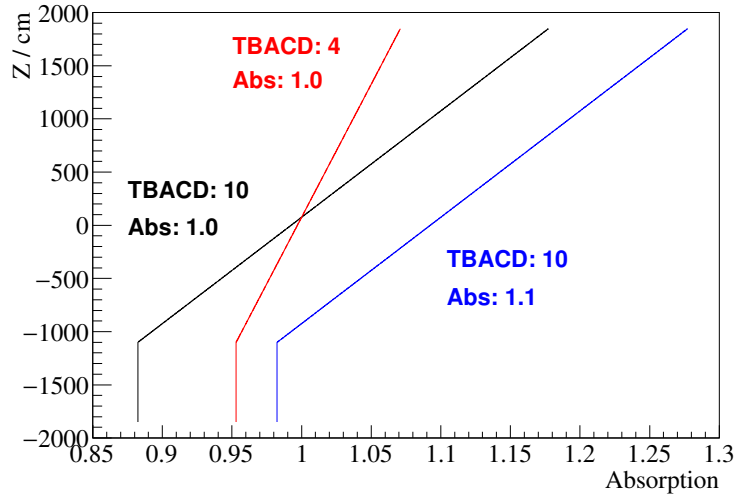


Figure 3.15 Three examples of  $z$ -dependent water model parameter sets. Labels and the corresponding models are in the same color. The scattering component is assumed to be constant, while the absorption component stays as a constant below -11 m and increases linearly above.

A top-bottom asymmetry parameter (TBA) is constructed as

$$\text{TBA} = \frac{\langle \text{top} \rangle - \langle \text{bottom} \rangle}{\langle \text{barrel} \rangle}, \quad (3-8)$$

where  $\langle \text{region} \rangle$  represents the mean hit rate of PMTs in each region corrected by acceptance and gain increasing only, without any relative QE, water transparency or dark noise correction. TBA is monitored by the Xe laser data discussed previously in the high voltage calibration and the Ni-Cf source data used in absolute gain calibration and QE calibration. The time variation of TBA over the SK-IV period is shown in Fig. 3.16, with blue points measured by the Xe lamp and red points measured by the monthly Ni-Cf calibration. Both show a good agreement.

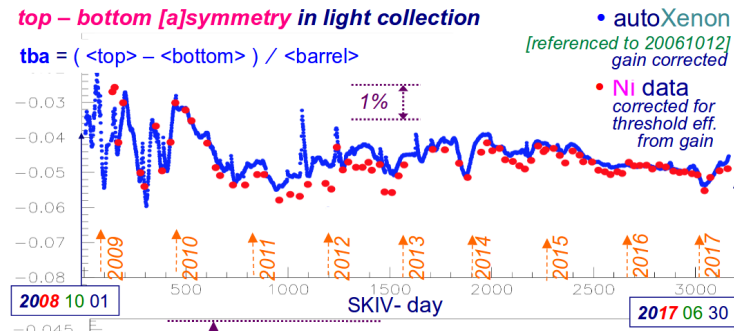


Figure 3.16 TBA time variance in SK-IV. Blue points are measured by the Xe lamp and red points measured by the monthly Ni-Cf calibration. Both show a good agreement.

To relate this phenomenal TBA parameter to the water slope  $\beta$ , the hit map from the nickel data is fitted by different  $\beta$  values in MC, where the hit number is again corrected by acceptance only. This  $\chi^2$  fitting was carried with 10 randomly chosen runs in 2009-2010 and a conversion function from TBA to  $\beta$  was constructed as

$$\beta = (-0.163 \times \text{TBA}^2 - 3.676 \times \text{TBA}) \times 0.01. \quad (3-9)$$

A validation with recent run data was done and the result agreed with the previous function.

### 3.1.3 Energy Calibration

The calibration of absolute energy scale directly determines the energy for low energy events at SK. To calibrate the absolute energy scale, a linear accelerator for single electron energy calibration (LINAC) and a deuterium-tritium neutron generator (DT) are regularly performed on SK.

#### 3.1.3.1 LINAC Calibration

LINAC is short for the LINear ACcelerator installed above the SK tank, with which data are taken at various positions inside the fiducial volume, tracking detector response in the variables relevant to physics studies<sup>[87]</sup>.

##### **LINAC overview**

This accelerator was initially designed for medical purposes in 1978 and later modified and installed at SK in 1996. Figure 3.17 shows the present setup, where LINAC is fixed in a tunnel near the dome above the SK tank. The electron beam generated by the accelerating gun is tuned in direction by the steering magnet D1-4 before reaching different positions in the tank. The electron energy is calibrated by a germanium detector with keV-level resolution. To exclude multi-electron events, besides software-level cuts, a special collimator is used to control the number of electrons entering the transportation tube. The beam intensity is tuned to very low level, with only 10% triggers containing any electrons. This ensures  $\sim 1\%$  multi-electron event ratio.

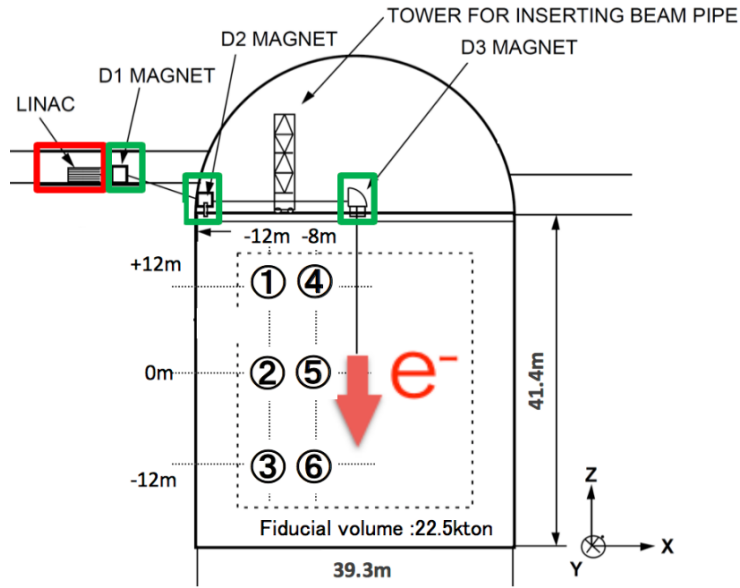


Figure 3.17 The LINAC and its beam line at the SK detector. The 22.5 kiloton fiducial volume is indicated by a dashed line. Circled numbers mark the positions for the previous calibration in 2016.

### Data taking

During SK-IV, LINAC calibrations were performed 5 times, in 2009, 2010, 2012, 2016, and 2017, respectively. The beam positions are limited by the length and conjunction of the beam pipes as well as the calibration hole locations. An arbitrary combination of three calibration holes along the x-axis at -12 m, -6 m and -4 m, and three depths along the z-axis at -15 m, 0 m and 15 m are used in sequence for the calibration data taking. The electron energy ranges from 4.4 MeV to 18.0 MeV.

### Analysis result

To analyze the LINAC calibration data, Monte Carlo samples with most of the parameters measured by other calibration sources were produced to tune the overall energy response factor, or COREPMT. COREPMT is determined by a comparison of the peak positions in the  $N_{\text{eff}}$  distributions between data and MC.

LINAC calibration in 2016 determined this COREPMT to be  $\sim 0.87$ . The differences of  $N_{\text{eff}}$  between data and MC with the tuned COREPMT in different positions were treated as the systematic uncertainty introduced by position dependence, as shown in Fig. 3.18. This energy scale variation is below 1%.

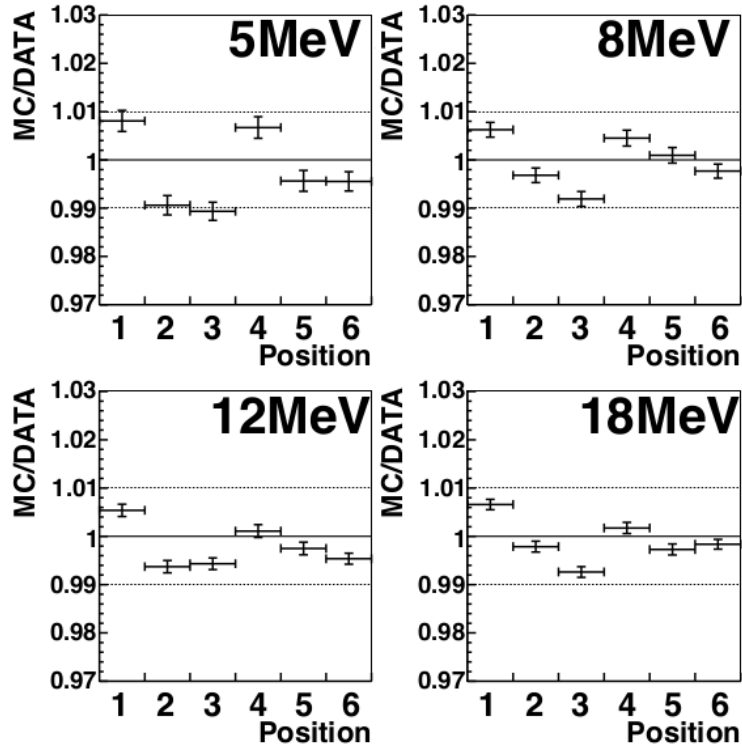


Figure 3.18 Data and MC differences in 2016 LINAC calibration for various positions and energies.

### 3.1.3.2 DT Calibration

Though different injection positions are possible, electrons produced by the LINAC are still limited in direction: the beam goes only downward, thus unable to accommodate the angular dependence which is calibrated by the DT calibration<sup>[88]</sup>.

#### DT overview

The DT generator emits 14.2 MeV neutrons via



This neutron interacts with oxygen to produce  ${}^{16}\text{N}$  by



The  ${}^{16}\text{N}$  then decays to  ${}^{16}\text{O}$ , producing a 6.1 MeV  $\gamma$  ray and a 4.3 MeV  $\beta$  (66%), or a 10.4 MeV  $\beta$  (28%),



The half-life of  $^{16}\text{N}$  is 7.13 seconds.

Since the beta energy is not monochronic, these beta rays cannot be directly used for the absolute energy calibration. However, the flexibility of the DT device and the uniform direction of  $\beta$ 's and  $\gamma$ 's from the  $^{16}\text{N}$  decay provide a unique measurement on the directional and positional dependence of energy scale, which allows a systematic study of low energy analysis.

### Data taking

A sketch of the DT calibration is shown in Fig. 3.19<sup>[88]</sup>.

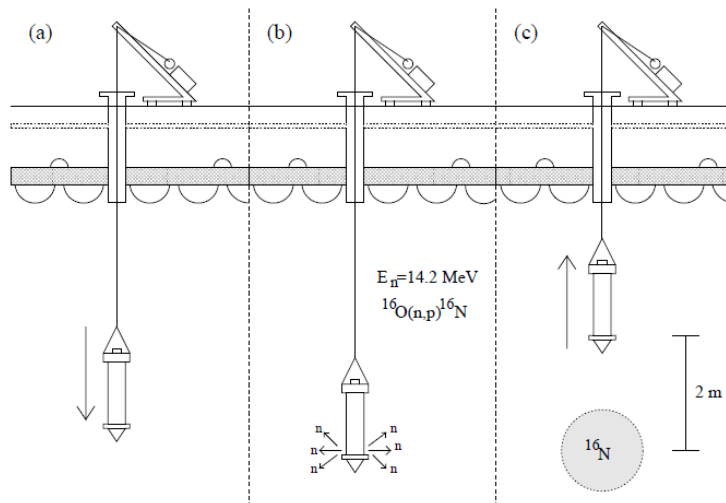


Figure 3.19 The schematic view of DT calibration method<sup>[88]</sup>.

The data taking procedures can be summarized as:

1. As pad a) of Fig. 3.19 shows, the DT generator is first lowered to the assigned position by a crane.
2. Then, as pad b) shows, the generator is fired, producing  $\sim 3$  million neutrons interacting with oxygen.
3. On pad c), the generator is lifted immediately after firing by the crane, 2 m above the initial position where it is filled with  $^{16}\text{N}$  to avoid making any shadow.
4. No data is taken in the above steps until step 3 is completed to avoid electronic noise. This data taking lasts for 40 seconds.

The above cycle is repeated  $\sim 25$  times at a single location to accumulate  $\sim 300,000$   $^{16}\text{N}$  events for further analysis with reconstruction tools and MC comparison.

### Analysis result

The position and directional dependence of the energy scale calibrated by the DT



data is shown in Fig. 3.20.

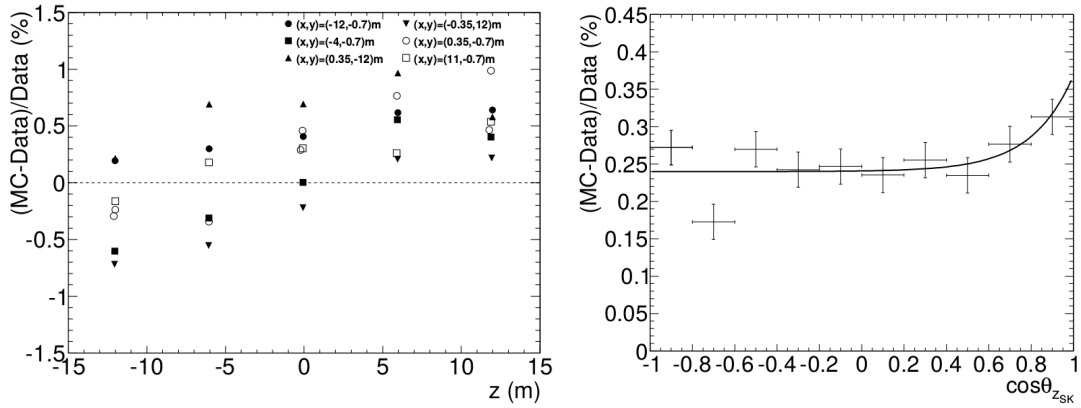


Figure 3.20 The position (left) and direction (right) dependence of the difference of effective hit ( $N_{\text{eff}}$ ) peak between the data and MC simulation. Left: The horizontal axis shows the  $z$ -position [m]. Right: The horizontal axis shows the cosine of the zenith angle.

Figure 3.21 shows the stability of energy scale from the DT data set in SK-IV. The fluctuation is within 0.3% level during the SK-IV phase.

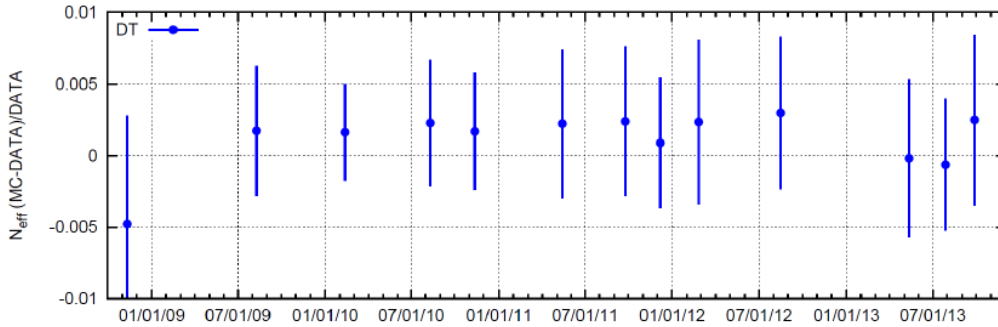


Figure 3.21 The stability of energy scale obtained by the DT calibrations during the SK-IV phase.

### 3.2 Detector Simulation

MC simulation is used for most the analysis and the calibration, as well as the systematic estimation. At SK, MC is separated into the detector- and physics-level. For SK, the official simulation package has a generator for atmospheric neutrino related physics in higher energy range for the interaction calculation, while for low energy physics especially for SRN study, the spectra of positron and neutron produce from IBD interaction are manually set.

The official simulation package at SK is referred to as SKDetSim, which is based on GEANT 3.21. Most physics processes are simulated by GEANT 3 packages, while some of the crucial processes such as photon propagation in water are customized with calibration results.

The author's contribution to the SKDetSim package includes maintenance for photon propagation simulation and unit test with nickel data.

### 3.2.1 Cherenkov Photon Production

Charged particles with energy beyond the Cherenkov light emission threshold

$$E_{\text{thr}} = \frac{m}{\sqrt{1 - (1/n)^2}}, \quad (3-13)$$

generate Cherenkov light in a cone with an open angle  $\theta_c$  as

$$\cos \theta_c = \frac{1}{n\beta}, \quad (3-14)$$

and the differential number of the Cherenkov photons per unit length travelled per unit wavelength is

$$\frac{d^2N}{d\lambda dx} = \frac{2\pi z^2 \alpha}{\lambda^2} \left(1 - \frac{1}{\beta^2 n^2(\lambda)}\right) = \frac{2\pi z^2 \alpha}{\lambda^2} \sin^2 \theta_c, \quad (3-15)$$

where  $n$  is the refractive index in SK water,  $m$  is the mass of the charged particle,  $\beta$  is the velocity of the charged particle in unit of vacuum light speed  $c$ ,  $z$  is the particle charge in unit of  $e$ ,  $\alpha$  is the fine structure constant, and  $dx$  is the infinitesimal range of traveling length.

The refractive index  $n$  is determined with considerations including water temperature, water pressure, *etc.* For a typical  $n$  value at SK, the thresholds of the Cherenkov emission for common charged particles in physics analysis are summarized in Table 3.1.

For faster simulation, the actual number of photon generated is less than  $N$  (typically  $N/3$ ), thus to save the simulation time of photons which will not arrive on PMTs due to coverage *etc.*

Table 3.1 Thresholds of Cherenkov radiation for charged particles at SK.

Particle	Energy threshold [MeV]
$e^\pm$	0.767
$\mu^\pm$	157.4
$\pi^\pm$	207.9

### 3.2.2 Photon propagation

Some of generated Cherenkov photons will be reflected or absorbed by water itself and impurities inside even after purification and cooling. The overall attenuation effect can be written as

$$I(x) = I_0(\lambda) \exp(-x/L(\lambda)), \quad (3-16)$$

where  $I(x)$  is the light intensity after a travel length of  $x$ ,  $I_0(\lambda)$  is the initial light intensity, and  $L(\lambda)$  is the attenuation length of the medium. The attenuation length representing the water transparency is parameterized at SK with three wavelength-correlated water coefficients: absorption coefficient  $\alpha_{\text{abs}}$ , Rayleigh scattering  $\alpha_{\text{ray}}$  and Mie scattering  $\alpha_{\text{mie}}$ . Mie scattering only differs from Rayleigh scattering by the target molecule size and mechanism rather than the behavior, and thus is difficult to distinguish. At SK, these two scattering components are combined and divided into a symmetric scattering coefficient  $\alpha_{\text{sym}}$ , including mainly the Rayleigh scattering and also the contribution from the symmetric part of Mie scattering, and an asymmetric scattering parameter  $\alpha_{\text{asy}}$  including the asymmetric part of Mie scattering. Therefore, the total attenuation length in MC simulation can be defined as

$$L_{MC}(\lambda) = \frac{1}{\alpha_{\text{abs}} + \alpha_{\text{sym}} + \alpha_{\text{asy}}}, \quad (3-17)$$

corresponding to the calibration explained in Eq. (3-4).

The reflection of Cherenkov photons by the detector structure such as the surface of PMT, the black sheet and so on, was also measured and accommodated in the MC simulation<sup>[86]</sup>.

### 3.2.3 PMT and Electronics

In SKDetSim, when a photon reaches the PMT surface, it is either reflected, or transmitted through, or absorbed by the cathode. The probability for each process depends on the incident angle as well as the wavelength, and is accounted in SKDetSim. The photon can generate a photoelectron only when it is absorbed by the cathode. Figure 3.22 illustrates these three processes on a PMT surface.

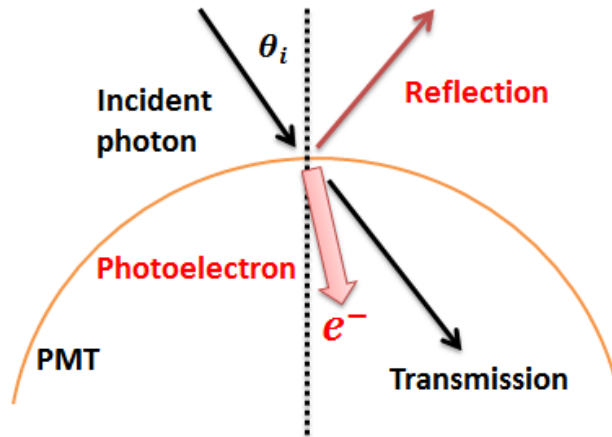


Figure 3.22 A sketch of the PMT response for an incident photon in SKDetSim.

The probability of the  $i$ -th PMT to absorb an incident photon and emit a p.e. is defined as

$$\text{Prob}_i(\lambda) = \text{Eff}(\lambda) \times \text{Prob}_{\text{obs}}(\lambda, \theta) \times \text{COREPMT} \times \text{QE}_i, \quad (3-18)$$

where  $\text{Eff}(\lambda)$  is the overall quantum efficiency of the 20-inch PMT with wavelength dependence,  $\text{Prob}_{\text{obs}}(\lambda, \theta)$  is the probability of absorption process for a given incident angle  $\theta$ ,  $\text{COREPMT}$  is the overall scale factor to correct the average quantum efficiency, and  $\text{QE}_i$  is the relative QE for the  $i$ -th PMT. The dependence of quantum efficiency on the position of incident photon on PMT surface is not included in the current version of SKDetSim, though a relevant study is still ongoing.

Finally, when the number of p.e.'s are determined, the corresponding charge is calculated and compared with the threshold of the electronics.

### 3.3 Event Reconstruction

At SK, low energy events are defined as the events with less than 1,000 hit PMTs. Unlike high energy reconstruction tools which consider both time and charge information, low energy reconstruction tools use mainly timing information and hit patterns. This is due to the fact that most low energy events only produce single p.e. on each hit PMT.

In this section, we will first introduce vertex reconstruction and direction reconstruction, then focus on the energy reconstruction and the correction of threshold effect in it. Cherenkov angle reconstruction is an important tool for particle identification in Cherenkov detectors, and we will describe its algorithm. Finally, the muon reconstruction tool, which is used to identify incoming muons and following spallation events, is also presented. The author was responsible for the threshold effect correction of the energy reconstruction analysis.

#### 3.3.1 Vertex Reconstruction

The typical travel distance for 10 MeV electrons and positrons in water is  $\sim 10$  cm, less than the corresponding vertex resolution  $\sim 50$  cm. Therefore, the electron or positron can be assumed to radiate Cherenkov light at a still point.

In the low energy analysis, BONSAI<sup>[89]</sup> is the mostly adopted vertex reconstruction tool, since it can give the best vertex resolution. The ToF-subtracted time residual  $\Delta t_i$  on the  $i$ -th PMT is defined as

$$\Delta t_i = t_i - \text{ToF}(\vec{x}) - t_0, \quad (3-19)$$

where  $t_i$  is the original hit timing on the  $i$ -th PMT,  $\vec{x}$  and  $t_0$  are the candidate pair of vertex and Cherenkov light emission time, and ToF is the time of flight for photons from the candidate vertex to the hit PMT. The probability density function (PDF) for  $\Delta t$  for signal is obtained from LINAC. The PDF for PMT dark noise is assumed to be flat. BONSAI looks for the best-fit  $\vec{x}$  and  $t_0$  pair by maximizing the likelihood function constructed from the time residuals of given hits and gives an evaluation of the fit.

#### 3.3.2 Direction Reconstruction

Direction reconstruction in water Cherenkov detectors is based on the Cherenkov ring pattern. For relativistic electrons, the Cherenkov angle distribution peaks at  $42^\circ$ . Due

to the multi-scattering effect, this angle is diluted, especially for charged particles with energies close to the Cherenkov threshold.

Direction reconstruction at SK requires a vertex reconstruction result as an input. A likelihood function  $L(\vec{d})$  is constructed as:

$$L(\vec{d}) = \sum_i^{N_{20}} \log(f(\cos \theta_{\text{dir},i}, E)) \times \frac{\cos \theta_i}{a(\theta_i)}, \quad (3-20)$$

where  $N_{20}$  refers to the number of hits satisfying  $-20 \text{ ns} < \Delta t < 20 \text{ ns}$ ,  $\theta_{\text{dir},i}$  refers to the angle between the incident particle direction  $\vec{d}$  and a vector pointing from the reconstructed vertex to the  $i$ -th hit PMT,  $f(\cos \theta_{\text{dir},i}, E)$  refers to the expected distribution of  $\theta_{\text{dir},i}$  dependent on the particle energy  $E$  due to multi-scattering,  $\theta_i$  is the solid angle of the  $i$ -th PMT's surface to the reconstructed vertex, and  $a(\theta_i)$  corrects for the acceptance. We obtain the distribution of  $f(\cos \theta_{\text{dir},i}, E)$  by MC simulation. This reconstruction looks for the best-fit of  $\vec{d}$  by maximizing the likelihood function.

The typical angular resolution at SK for a 10 MeV electron is  $\sim 25^\circ$ .

### 3.3.3 Energy Reconstruction

For the Cherenkov process in low energy region, number of Cherenkov photons follows a monotonic response to the incident particle energy, as shown in Fig. 1.7. Due to the low photon yield for low energy events, single p.e. is assumed for most of PMT hits. The incident particle energy can thus be approximated to be proportional to the number of PMT hits.

#### 3.3.3.1 $N_{\text{eff}}$ Calculation

As Eq.( 3-6) suggests, several corrections are needed to obtain the corresponding 'effective hit' value of a PMT hit. The effective hits within a 50 ns residual time window are then summed up with a correction of water transparency to obtain a variable named  $N_{\text{eff}}$ , which will be converted to energy,

$$N_{\text{eff}}^i = (X_i + \epsilon_{\text{tail}} - \epsilon_{\text{dark}}^i) \times \frac{N_{\text{all}}}{N_{\text{normal}}} \times \frac{R_{\text{cover}}}{S(\theta_i, \phi_i)} \times \frac{1}{QE_i}, \quad (3-21)$$

$$N_{\text{eff}} = \sum_{i=1}^{N_{50}} \left\{ N_{\text{eff}}^i \times \exp\left(\frac{r_i}{\lambda(\text{run})}\right) \right\},$$

in which the variables are:

- Occupancy  $X_i$

It's not easy to decide whether the  $i$ -th hit PMT generates a single p.e. or more, even with charge information, due to the resolution. To account for the case of multiple p.e.'s, the hit information from PMTs in a  $3 \times 3$  patch surrounding this candidate PMT  $i$  is also collected. Assuming the same hit probability for these 9 PMTs, we define an occupancy  $X_i$  to estimate the number of p.e.'s generated by the  $i$ -th PMT based on the Poisson statistics as

$$\begin{aligned} X_i &= -\log(1 - x_i)/x_i, & x_i < 1 \\ X_i &= 3.0, & x_i = 1 \end{aligned} \quad (3-22)$$

where  $x_i$  is the ratio of hit PMTs surrounding the  $i$ -th hit PMT. This occupancy needs further correction for the gain increase, as will be addressed in Section 3.3.3.2.

- Tail hits correction  $\epsilon_{\text{tail}}$

Scattering, absorption/re-emission, and reflection dilute the time resolution, leaving some tail hits behind the 50 ns window. These tail hits are corrected by the term  $\epsilon_{\text{tail}}$ .

- Dark noise correction  $\epsilon_{\text{dark}}^i$

As discussed in Section 3.1.1.3, dark noise is estimated by the hits in the off-time window, and  $\epsilon_{\text{dark}}^i$  corrects the dark noise on a run-by-run and PMT-by-PMT basis.

- Bad PMTs  $N_{\text{all}}/N_{\text{normal}}$

Though the 11,146 PMTs ( $N_{\text{all}}$ ) were initially installed in the tank in SK-I, the number of properly operating PMTs now in SK-IV is only 11,129 ( $N_{\text{normal}}$ ). This term is corrected for consistency with previous SK periods.

- Photocoverage  $R_{\text{cover}}/S(\theta_i, \phi_i)$

The acceptance and photocoverage is corrected by this term, where  $\theta_i$  and  $\phi$  represent the incident angle and azimuth angle, respectively.  $S$  is the photocathode coverage of  $i$ -th PMT, and  $R$  is the overall photo-coverage.

- PMT quantum efficiency  $\text{QE}_i$

This QE has the same definition as discussed in Section 3.1.1.4.

- Water transparency  $\lambda(\text{run})$

From  $N_{\text{eff}}^i$  to  $N_{\text{eff}}$ , the exponential term  $\exp(r_i/\lambda(\text{run}))$  applies the correction for the water transparency. Here,  $r_i$  refers to the distance between the reconstructed

event vertex and the  $i$ -th hit PMT, and  $\lambda(\text{run})$  refers to the water transparency as a function of run number. The measurement of  $\lambda$  is described in Section 3.1.2.3.

### 3.3.3.2 Threshold Effect Correction

Due to the long-term increase of PMT gain mentioned in Section 3.1.1.3,  $N_{\text{eff}}$  is observed to have an increasing trend for all the calibration data sets. This is due to the ‘threshold effect’ where the increase of gain results in more hits which exceed a fixed threshold. To correct this threshold effect, we parameterize the gain increase and assign a conversion factor  $C$  between the gain increase and hit increase,

$$\begin{aligned} F_G(k, \text{run}) &= (G_t(k, \text{run}) - G_0)/G_0, \\ F_N(k, \text{run}) &= (N_t(k, \text{run}) - N_0)/N_0, \\ F_N(k, \text{run}) &= F_G(k, \text{run}) \times C, \end{aligned} \tag{3-23}$$

where  $G_0$  is the gain for the reference run at the beginning of SK-IV,  $G_t$  is the PMT gain for the current run, estimated by the off-time window charge from an independent study. PMTs are grouped by production year and denoted by  $k$  to tag their batch. The conversion factor  $C$  is assumed to be uniform over time and for different PMT batches, even though the gain increasing amplitudes vary. Since the gain increase does not exceed 20% throughout the SK-IV period, the correlation of hit increase and gain increase can be treated as linear.

The occupancy  $X_i$  in the  $N_{\text{eff}}$  calculation is modified as

$$X_i(x_i) \rightarrow X_i(x_i(QE_j))/(1 + F_G \times C), \tag{3-24}$$

where  $x_i$  is corrected for the QE of  $j$ -th PMT in the  $3 \times 3$  patch surrounding  $i$ -th PMT, and the threshold effect is quantified as  $F_G \times C$ , where  $G$  is the relative gain increase and  $C$  is a conversion factor. Similarly,  $\epsilon_{\text{dark}}$  is also corrected by

$$\epsilon_{\text{dark}} = \epsilon_{\text{dark}}/(1 + F_G \times C) \tag{3-25}$$

This conversion factor is estimated by tuning the y-intercept of Fig. 3.11 to a constant over time. As a crosscheck,  $N_{\text{eff}}$  for different calibration data samples (decay electron, nickel, DT, LINAC) is recalculated and confirmed to be stable, an example of which is



shown in Fig. 3.14. The stability of  $N_{\text{eff}}$  grouped by PMT batches is also confirmed, validating the assumption of uniform  $C$  over time and over different PMT batches. The  $C$  value in SK-IV is finally determined to be 0.226 for the data.

### 3.3.3.3 Energy Calculation

The energy of the incident particle is reconstructed as a polynomial function of  $N_{\text{eff}}$  to the 4th order for  $E < 25$  MeV and to the 2nd order for  $E > 25$  MeV,

$$\begin{aligned} E_{\text{rec}} &= \sum_{i=0}^4 a_i (N_{\text{eff}})^i, & E_{\text{rec}} < 25\text{MeV} \\ E_{\text{rec}} &= \sum_{i=0}^2 a_i (N_{\text{eff}})^i, & E_{\text{rec}} > 25\text{MeV} \end{aligned} \quad (3-26)$$

where  $E_{\text{rec}}$  is the reconstructed energy and  $a_i$  is the  $i$ -th order coefficient determined by LINAC calibration. For 10 MeV electrons, the energy resolution is about 14%.

In principle, the  $N_{\text{eff}}$  based energy reconstruction method will also work for events below the detection threshold of  $\sim 4$  MeV, though with much worse resolution due to the nonlinearity of Cherenkov radiation.

### 3.3.4 Cherenkov Angle Reconstruction

The removal of the non-electron/positron backgrounds in SRN samples requires particle identification information. At SK, due to the mass difference of charged particles and the mechanism of Cherenkov light emission, particle identification is done by the Cherenkov angle. In the energy range of SRNs, the positrons of IBD candidates are ultra-relativistic with a Cherenkov angle at  $42^\circ$ , while for muons and pions it becomes smaller due to their heavier mass. The PMT hits induced by  $\gamma$ -rays are isotropically across the detector, thus showing a much different hit pattern and cannot fake a  $42^\circ$  Cherenkov ring.

Hits from a candidate event within a residual time window of 15 ns are combined in 3-hit sets so that every set uniquely defines a cone with an opening angle. These opening angles are filled to a histogram and forms a distribution, which does not have a well-defined shape. A 7-bin sliding sum is calculated and the maximum center bin is taken as the peak of this distribution, and thus defines the Cherenkov angle of this event. This Cherenkov angle is used to reject non-electron/positron backgrounds such as muons,

pions and  $\gamma$ 's.

### 3.3.5 Muon Fitter

The main backgrounds for the SRN search are spallation products induced by the cosmic ray muons. These events are correlated with precedent muons in space and time, and can be rejected by likelihood construction dependent on the muon type and track. A precise reconstruction of muon events is crucial in suppressing the spallation backgrounds.

#### 3.3.5.1 Muboy

A muon reconstruction tool named Muboy<sup>[90,91]</sup> is applied to fit the events with more than 1,000 p.e.'s, since these events are very likely to be cosmic ray muons. Cosmic ray muons at SK are classified into 4 categories, namely single through-going muons, stopping muons, multiple muons and corner clipper muons. Muboy can fit multiple tracks simultaneously and find the most likely category for the muon candidate. It also evaluates the quality of the fit by goodness. All of the above information is used in the spallation likelihood calculation.

The muon rate at SK is 2.2 Hz, while the time window for HE events is 40  $\mu$ s. If an HE time window is already open, for the time being, another incoming muon will be not registered as a trigger again. The rate of the un-registered second muon is found to be  $\sim$  100 / day. To get back these untagged muons, a software trigger in Muboy is implemented to check the already found muon candidates.

#### 3.3.5.2 Brute Force Fitter

As indicated by the goodness value, Muboy may give a poor fit due to exotic hit patterns or extremely low/high number of hits. These cases account for 1.4% of the total fit. A brute force fitter (BFF) is developed as an alternative to refit these muons which failed the Muboy fit (goodness < 0.4). It performs a grid search for the entry and exit points in the ID surface.

Even though BFF is extremely slow and can only fit the single-through muons due to the algorithm, about 75% of the failed muons from Muboy can be successfully reconstructed by BFF.

## 3.3.5.3 Energy Loss

Energy loss per track length ( $dE/dx$ ) for energetic muons may have peaks along the path, and may thus be closely related to the spatial distribution of spallation events. To calculate the energy loss for a given muon, the muon track is first reconstructed. Binned by 50 cm along this track, for every bin, the ToF-timing information of every hit PMT is calculated to look for the hits whose incident photons are most likely to be emitted from this bin, as shown in the left panel of Fig. 3.23. Recently, a likelihood calculation method is employed to smooth the  $dE/dx$  spectrum, as shown in the right panel of Fig. 3.23. This new method is expected to improve the spallation reconstruction.

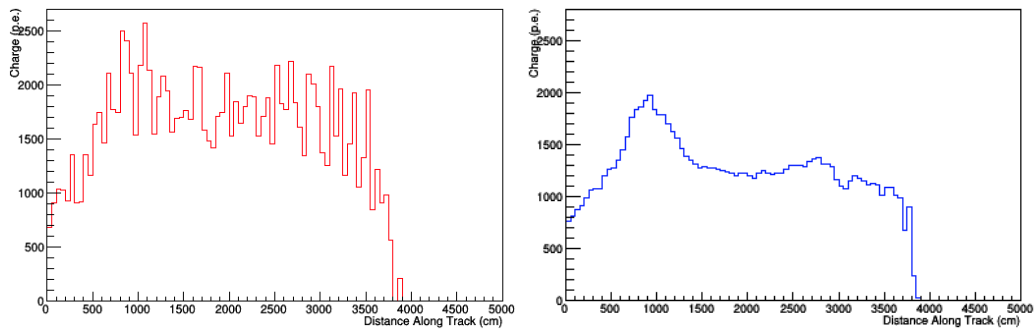


Figure 3.23 Energy loss binned along the same muon track using the old (left) and new (right) calculation method respectively.

## Chapter 4 Data Reduction at SK

As discussed in Section 1.3.2.3, the search for SRN can use IBD events because of its large cross section. To select IBD events, in the absence of a 100 % detection efficiency of neutrons due to the SK detector properties, a careful and efficient reduction of the prompt events is required. For an easier demonstration, the term energy  $E$  in this chapter is limited to reconstructed energy  $E_{rec}$ . For SRN signal, it is the positron kinetic energy plus the annihilation energy.

The author performed the data reduction for the data collected in 2014 – 2018 during SK-IV, improved the multi-event cut, and re-calculated the estimated efficiency for an SRN spectrum.

### 4.1 First Reduction

First reduction, or precut, is a series of basic requirements to select the physics events against non-physics events, such as those due to PMT flashers and detector calibrations. This cut reduces the sample size significantly, facilitating further studies.

#### **Bad Run Cut**

A typical run at SK contains 24-hour data, with ~80,000 subruns which last for 1-minute each. During the data taking, runs are labelled as normal run or test run, the later of which is usually during the calibration or with a hardware problem.

At the offline stage, normal runs are further examined on a subrun basis by eye scan of low energy analysis group members and experts. If a normal run has either of the following problem:

- run time < 5 min,
- beginning of run < 15 min after a high voltage (HV) recovery,
- hardware problems recorded by shift person or expert,
- evident distortion in event distribution tracing back to a change recorded by shift person or expert,

it is tagged as a bad run. Generally, only the good run data are used in physics analysis.

#### **Fiducial Volume Cut**

Most radioactive backgrounds is from the surrounding rock and detector wall (steel frame and PMT surfaces), and are likely to be reconstructed close to the tank wall.

In addition, the nonuniformity is enormous at the tank edge even after the acceptance correction, due to the reflection on surfaces and the much larger time resolution of PMT for extreme incident angles. To eliminate these effects, a fiducial volume cut of 200 cm from the tank wall is applied.

### Goodness Cut

Primary events are reconstructed by BONSAI, as described in Section 3.3. BONSAI evaluates the goodness of fit by  $G_V$  and DirKS, which represent the quality of vertex reconstruction and direction reconstruction respectively. Based on these goodness values, ovaQ (One dimensional variable of Vertex and Angular reconstruction Quality) is constructed as  $ovaQ = G_V^2 - \text{DirKS}^2$ . The first reduction requires  $G_V > 0.4$  and  $ovaQ > 0.25$ .

### Calibration Events Cut

Some calibration data requires test runs, such as the nickel calibration and DT calibration as discussed in Section 3.1. Other calibration data, however, are taking during normal runs with periodical calibration triggers. By rejecting events tagged with the calibration triggers, we eliminated the possible contamination from calibration data into the SRN search sample.

### Noise Events Cut

PMT noises tends to have lower charges than those for the true hits. By requiring  $N(Q < 0.5 \text{ p.e.})/N_{all} < 0.55$ , a large fraction of noise events are removed.

### OD Cut

An OD trigger indicates an incoming muon, thus the event cannot be a SRN candidate. In case the OD trigger does not function properly, events with OD hits  $> 19$  are removed.

### Muon Time Cut

The muon rate at SK is  $\sim 2$  Hz. Energetic muon deposits energy inside the tank, with a large number of secondary tracks and hits, which are likely to be reconstructed as low energy events. To eliminate these backgrounds, all the events within  $50 \mu\text{s}$  after a muon event are rejected.

## 4.2 Spallation Cut

Spallation products form the main background in lower energy range for SRN search at SK, both in the spectrum analysis, and in the neutron tagging analysis. The background in neutron tagging analysis originates from  ${}^9\text{Li}$  production and the mis-tagged accidental coincidence from cosmic ray induced spallations. Previous studies<sup>[49]</sup> used four variables

to construct a likelihood to reject the spallation-like events.

### Spallation Backgrounds

Cosmic-ray muon induced spallation backgrounds in the detectable energy range at SK are listed in Table. 4.1. The imperfect energy reconstruction could smear the endpoint of spallation energy distribution, thus contaminating higher energy SRN samples up to 24 MeV, below which spallation cuts are applied.

Table 4.1 Summary of cosmic-ray muon induced spallation radioactivities at SK<sup>[51,92]</sup>.

Isotope	Mean life [s]	Decay mode	$E_{\text{kin}}$ [MeV]	Primary process
${}^{11}_4\text{Be}$	19.9	$\beta^-$	11.51	(n, $\alpha$ + 2p)
		$\beta^- \gamma$	9.41+2.1( $\gamma$ )	
${}^{16}_7\text{N}$	10.3	$\beta^-$	10.44	(n,p)
		$\beta^- \gamma$	4.27+6.13( $\gamma$ )	
${}^{15}_6\text{C}$	3.53	$\beta^-$	9.77	(n,2p)
		$\beta^- \gamma$	4.51+5.30( $\gamma$ )	
${}^8_3\text{Li}$	1.21	$\beta^-$	$\sim 13.0$	( $\pi^-$ , $\alpha$ + ${}^2\text{H}$ +p+n)
${}^8_5\text{B}$	1.11	$\beta^+$	$\sim 13.9$	( $\pi^+$ , $\alpha$ + 2p+2n)
${}^{16}_6\text{C}$	1.08	$\beta^-$ +n	$\sim 4$	( $\pi^-$ ,n+p)
${}^9_3\text{Li}$	0.26	$\beta^-$	$\sim 13.6$	( $\pi^-$ , $\alpha$ + 2p+n)
		$\beta^- \gamma$	$\sim 10$	
${}^9_6\text{C}$	0.18	$\beta^+$ +p	3~5	(n, $\alpha$ + 4n)
${}^8_2\text{He}$	0.17	$\beta^- \gamma$	9.67+0.98( $\gamma$ )	( $\pi^-$ , ${}^3\text{H}$ +4p+n)
		$\beta^-$ +n		
${}^{12}_4\text{Be}$	0.034	$\beta^-$	11.71	( $\pi^-$ , $\alpha$ +p+n)
${}^{12}_5\text{B}$	0.029	$\beta^-$	13.37	(n, $\alpha$ +p)
${}^{13}_5\text{B}$	0.025	$\beta^-$	13.44	( $\pi^-$ ,2p+n)
${}^{14}_5\text{B}$	0.02	$\beta^- \gamma$	14.55+6.09( $\gamma$ )	(n,3p)
${}^{12}_7\text{N}$	0.016	$\beta^+$	16.38	( $\pi^+$ ,2p+2n)
${}^{13}_8\text{O}$	0.013	$\beta^+$ +p	8~14	( $\mu^-$ , $\mu^-$ + $\pi^-$ +p+2n)
${}^{11}_3\text{Li}$	0.012	$\beta^-$	20.62	( $\pi^+$ ,5p+ $\pi^0$ + $\pi^+$ )
		$\beta^-$ +n	$\sim 16$	

### Spallation Likelihood

The spallation cut is constructed by the following procedures.

First, as described in Section 3.3.5.1, muons are classified into four categories of single through muons, stopping muons, multiple muons, and corner clipper muons.

Then, four variables are constructed to describe the correlation between the incoming

muon and the primary event of an IBD candidate:

- $d_t$ , the time difference between the primary event and the preceding muon;
- $l_t$ , the transverse distance between the primary event and the preceding muon track;
- $l_n$ , the longitude distance between the primary event and peak position of the  $dE/dx$  distribution along the muon track.
- $Q_{\text{peak}}$ , the peak value of  $dE/dx$  binned by 50 cm along the muon track.

Third, a spallation sample and a random sample are prepared by setting a cut on the time difference  $dt$ . The spallation sample requires  $0 > dt > -30$  s preceding the primary event and random sample requires  $0 < dt < 30$  s after the primary event. The spallation sample distribution is then subtracted by the random sample. For different samples, different distribution of the four discrimination variables can be observed and the likelihood function can be constructed, thus evaluating the possibility of the primary event to be spallation-like or signal-like. Typical distributions for spallation events and non-spallation events for the single through muons are shown in Fig. 4.1.

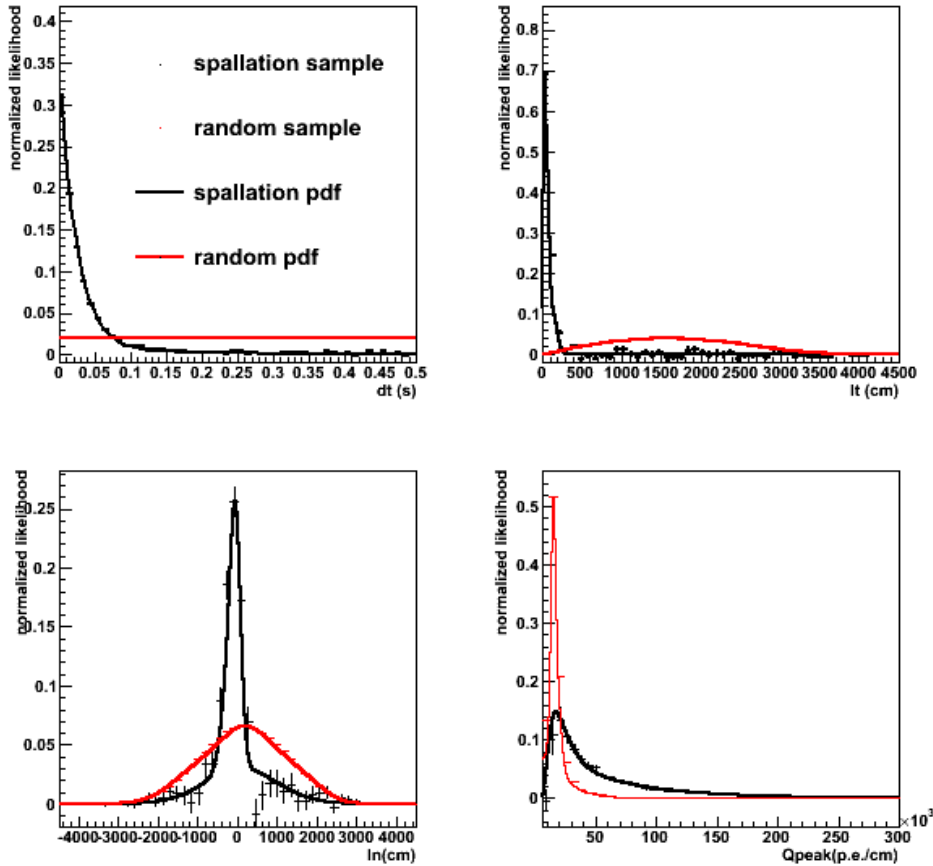


Figure 4.1 Distributions of  $d_t$ ,  $l_t$ ,  $l_n$  and  $Q_{\text{peak}}$  using the single through muon<sup>[45]</sup>.

A spallation likelihood  $L_{\text{spall}}$  is thus constructed as:

$$L_{\text{spall}} = \sum_i \log \frac{\text{PDF}_{\text{spall}}^i}{\text{PDF}_{\text{random}}^i}, \quad (4-1)$$

where  $i$  represents one of the four discriminating variables. The distribution of the spallation likelihood for both the spallation data sample and the random sample is shown in Fig. 4.2.

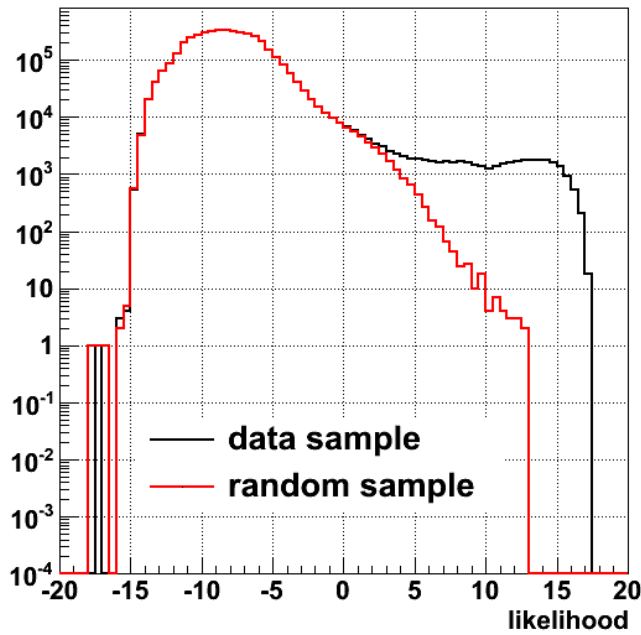


Figure 4.2 Distributions of the spallation likelihood using the single through-going muons<sup>[46]</sup>.

### Performance

The spallation cut is performed on the output of likelihood function, and is changed for different muon categories and primary event energy. A random event sample is generated by randomly choosing vertex, adverting the sign of  $dt$ , while keeping the other information of the SRN sample with regard to muons. This random sample is used to evaluate the effect of the spallation cuts on the SRN signals. The efficiency for SRN signal in different energy ranges for the spallation cuts are listed in Table 4.2.



Table 4.2 SRN efficiency with spallation cuts.

Energy range	Efficiency in SK-IV	Efficiency in SK-I/III
18-24 MeV	89.8%	89.7%
14-18 MeV	80.5%	80.3%
12-14 MeV	72.1%	
11-12 MeV	61.2%	
8-11 MeV	51.3%	

### 4.3 External Event Cut

Higher energy  $\gamma$ 's from radioactive backgrounds outside the tank or from the tank wall can travel further into FV, contaminating the data sample even after applying the FV cut. The distance between the reconstructed vertex and the point of entry on the tank wall calculated from the reconstructed vertex and inverted direction is called as effwall. The distributions of effwall for the data and MC SRN signal are shown in Fig. 4.3.

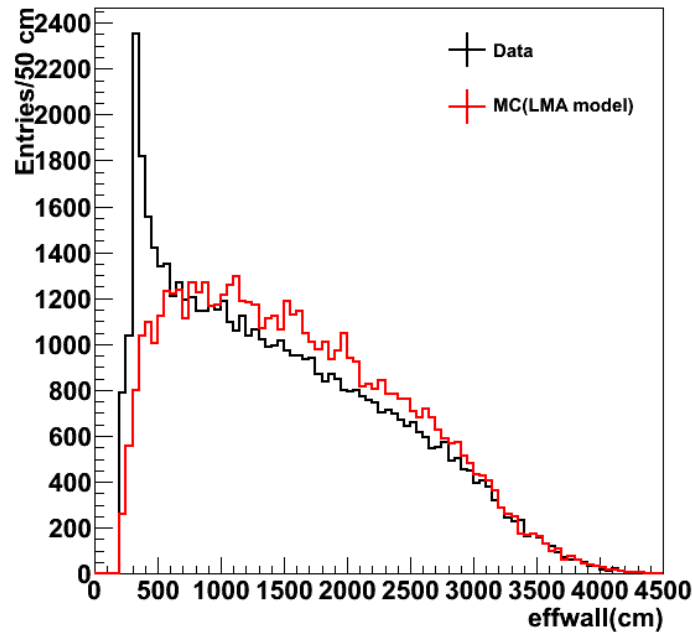


Figure 4.3 Distributions of effwall for the data (black line) and the SRN signal (red line)<sup>[46]</sup>.

The incoming event cut is therefore set at 300 cm for  $E > 22$  MeV, 450 cm for  $12 \text{ MeV} < E < 22$  MeV, and 600 cm for  $E < 12$  MeV.

#### 4.4 Solar Event Cut

Solar neutrinos are detected at SK by the electron scattering on electrons  $\nu + e \rightarrow \nu + e$ . Though without a neutron, the higher energy solar neutrinos can still leak into our final SRN sample through accidental coincidence with its relatively high luminosity. The angle between the reconstructed direction of an event to the sun direction at the time of the event is called  $\theta_{\text{sun}}$ . The distribution of  $\theta_{\text{sun}}$  for solar neutrinos at  $\sim 10$  MeV quite stands out from the flat distribution of the SRN signals, providing an easy way to tag and reject solar neutrinos, as shown in Fig. 4.4.

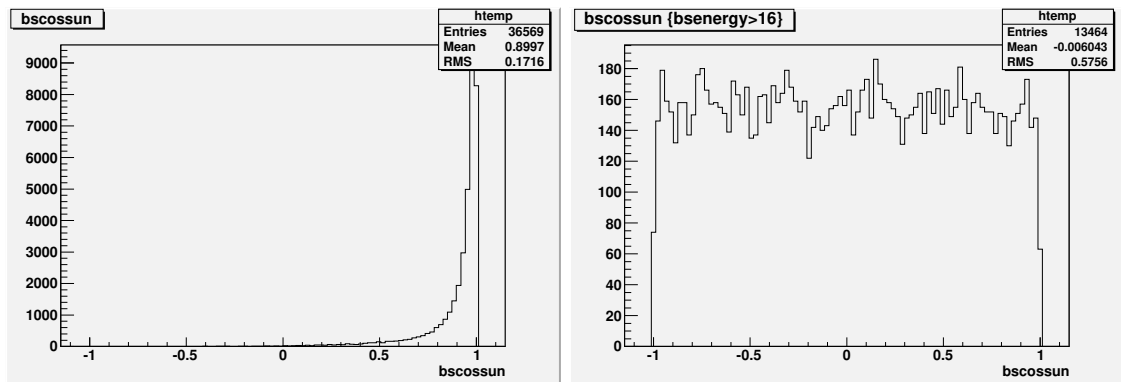


Figure 4.4 Distributions of  $\cos\theta_{\text{sun}}$  for the solar MC (left) and the SRN MC (right).

Since the energy of the solar neutrinos is below 16 MeV, we reject events with  $\cos\theta_{\text{sun}}$  greater than 0.9 and energy lower than 16 MeV. Remaining solar neutrino background due to the resolution effect is expected to be removed by the neutron tagging.

This cut will be one of the main different cut between the neutron tagging analysis and spectral analysis of SRN search. For the neutron tagging analysis, this cut can be loosened because solar neutrinos do not have neutrons and contribute to the final sample only by accidental coincidence.

#### 4.5 Cherenkov Angle Cut

Atmospheric  $\nu_{\mu}/\bar{\nu}_{\mu}$  will generate muons via charged current interaction, which can be mis-reconstructed as electrons in the energy range of several tens of MeV, when the muon energy is around 100-500 MeV. For relativistic  $e^{\pm}$ 's  $\sim 10$  MeV, the Cherenkov angle is  $\sim 42^{\circ}$ , while for these muons, the Cherenkov angle tends to be lower.

On the other hand, background events with multiple  $\gamma$ 's, or an electron and a  $\gamma$ , as many spallation events do, usually have larger Cherenkov angles for the isotropic light

emission of  $\gamma$ 's.

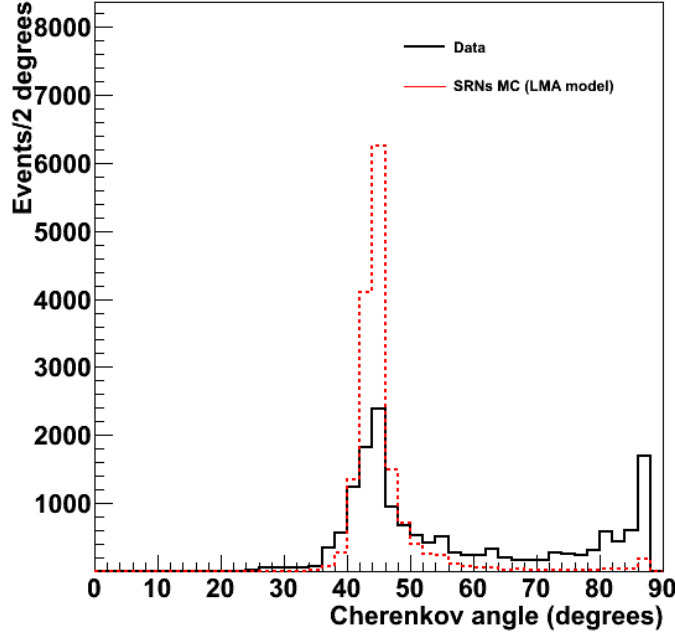


Figure 4.5 Distributions of Cherenkov angle for the data (black line) and LMA MC (red line)<sup>[46]</sup>.

Figure 4.5 shows the Cherenkov angle for the data and the simulated SRN signal, from which the Cherenkov cut is determined to be  $38^\circ < \theta_C < 50^\circ$ .

## 4.6 Multi-Event Cut

The prompt signal in an IBD event should be a single event in a  $1.3 \mu\text{s}$  time interval, while the CC backgrounds from atmospheric neutrinos tend to be multi-events, for instance, a decay electron from a muon. To remove these events, we apply multi-event cuts from the aspects of both space and time.

### 4.6.1 Pre/Post Activity Cut

Invisible muons with energy lower than the Cherenkov threshold can not be detected at SK, and the following decay electrons or induced spallations will escape from the muon or spallation cuts. Cosmic-ray muons are unlikely to have such low energy with the rock overburden of SK. Instead, invisible muons are more likely to be produced by atmospheric  $\nu_\mu/\bar{\nu}_\mu$ 's. Decay electrons from these invisible muons can be removed if the atmospheric neutrino generates a prompt gamma when interacting with an oxygen. For the  $[-5, 0] \mu\text{s}$

precedent time range covered by an SHE trigger, the distribution of number of hits within a 15 ns sliding time is shown in the left panel of Fig. 4.6. Events with  $N_{15} > 11$  are called pre-activity events, and are removed from the final sample.

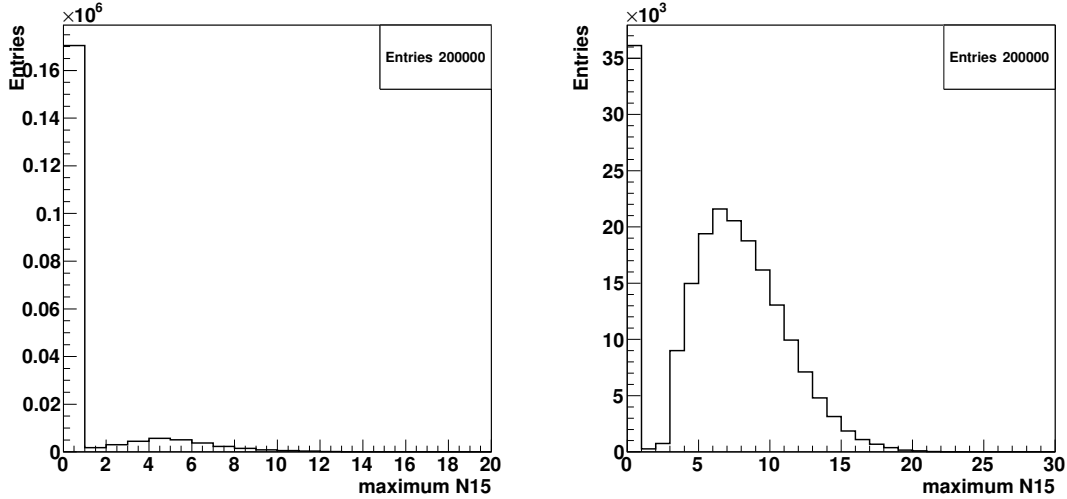


Figure 4.6 Distributions of  $N_{15}$  in  $5\mu\text{s}$  random trigger (left) and in  $35\mu\text{s}$  trigger. The latter has wider distribution due to the existence of  $2.2\text{ MeV } \gamma$ .

Visible muons produced by atmospheric  $\nu_\mu/\bar{\nu}_\mu$ 's can be mis-reconstructed with Cherenkov angle  $> 38^\circ$ , leaking into the SRN sample. The decay electron signal from such muons produces a second peak, which is used to tag these muons after the primary event in the time range  $[0, 35] \mu\text{s}$  recorded by the SHE trigger. Using a similar number of hit in a 15 ns sliding window, the distribution of  $N_{15}$  after the primary event is shown in the right panel of Fig. 4.6. Due to the existence of  $2.2\text{ MeV } \gamma$ , this distribution is shifted to the right and spread wider than the left panel. Post-activity events are thus defined by  $N_{15} > 19$ , and are removed from the SRN sample.

The event displays of a pre-activity and a post-activity event example are shown in Fig. 4.7.

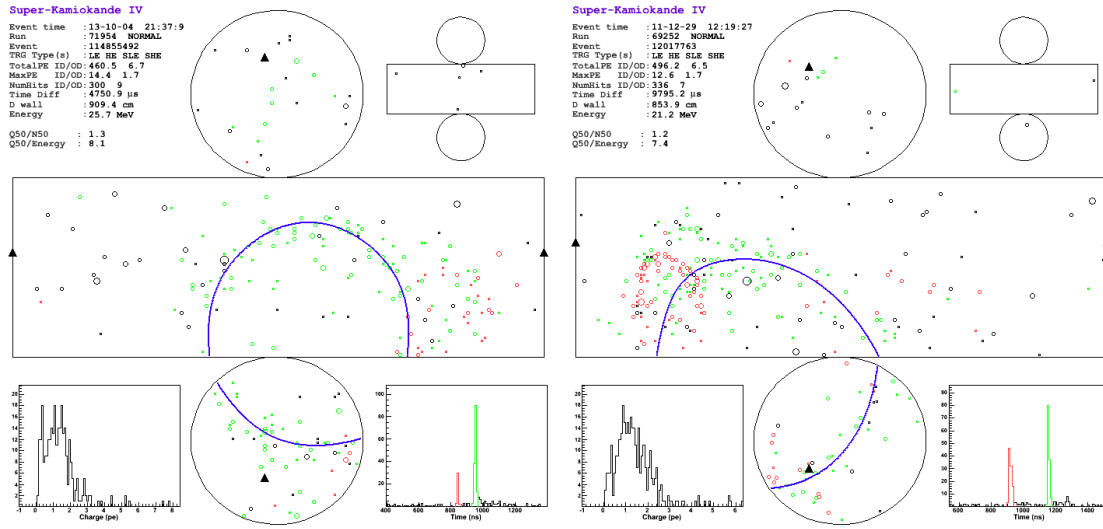


Figure 4.7 Event display for an example of a pre-activity event (left) and a post-activity event (right) [45].

#### 4.6.2 Multi-ring Cut

A positron only generates one Cherenkov ring in the tank while backgrounds from atmospheric neutrinos tend to undergo multi-processes and produce multiple charged particles, thus producing multiple rings. A simple ring counting will cause signal efficiency loss due to some poor reconstructed positron ring and the fuzziness in ring pattern itself for low energy positrons. Instead of counting ring numbers, the angle between rings are taken as the cut parameter, requiring  $\theta_{\text{ring}} < 60^\circ$  for any two rings inside an event, using the ring counting tool in Ref<sup>[93]</sup>.

### 4.7 Muon/Pion Cut

The residual muon and pion events after the Cherenkov angle cut will remain in the data sample, and further reduction is required.

#### 4.7.1 Pion Cut

The Cherenkov angle cut removes most non-electron backgrounds by the relativity of the particle. However, this cut does not reject high energy pion. The Cherenkov angle distribution of these pions tends to peak at  $42^\circ$  with a sharper than SRN positrons due to the higher energy and less multi-scattering. To account for the width of Cherenkov angle distribution, the ratio of hits number within  $\pm 3^\circ$  around the Cherenkov angle peak over

the number within  $\pm 10^\circ$ , called  $\pi_{\text{like}}$ , is constructed. Events with  $\pi_{\text{like}} > 0.58$  are regarded as pion-like events, and are removed from the SRN sample.

#### 4.7.2 Charge/Hit Cut

In addition to the above non-electron particle cut, muons and pions are further rejected by the charge and hit distribution within 50 ns as a function of reconstructed energy  $E$ <sup>[45]</sup>. Such distributions for  $e$ 's,  $\mu$ 's and  $\pi$ 's are shown respectively in Fig. 4.8. Events with  $Q_{50}/N_{50} \geq 2.0 + 0.0025 \times E$  are tagged as  $\mu/\pi$ 's, and are removed from the SRN sample.

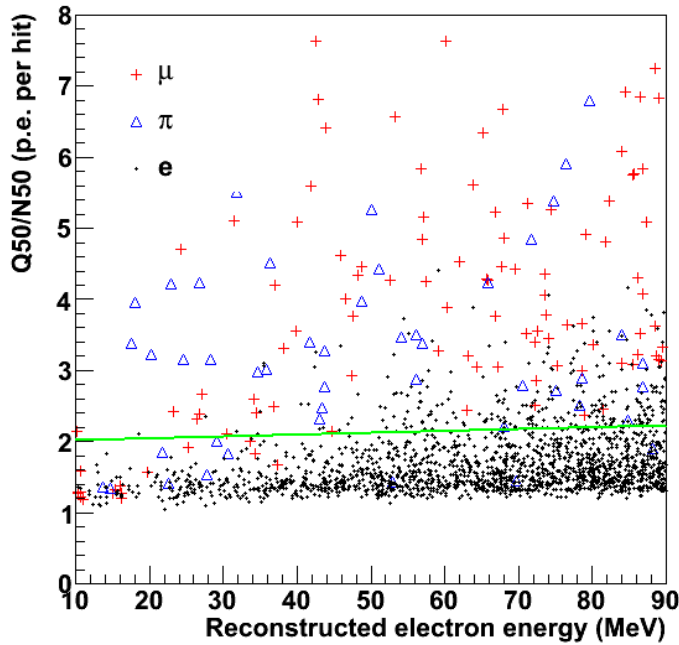


Figure 4.8 The distribution of  $Q_{50}/N_{50}$  as a function of the reconstructed energy  $E$  for  $e$ 's,  $\mu$ 's and  $\pi$ 's obtained from the simulated atmospheric neutrinos<sup>[46]</sup>.

## 4.8 Summary of Reduction Efficiency

The reduction efficiency is evaluated by SRN MC sample, and the efficiency value may vary slightly according to the energy profile of the SRN model. Table 4.3 shows the efficiencies evaluated by the LMA model. It should be noted that these efficiencies are evaluated in sequence as listed in Table 4.3. The accumulated signal efficiency is the product of individual efficiencies.

Table 4.3 Data reduction efficiencies evaluated by LMA model. Detailed calculations explained in the text.

Reduction	Efficiency
First reduction	>99%
Spallation cut	77.1%
External event cut	92.8%
Solar cut	97.2%
Cherenkov angle cut	88.6%
Pre/post activity cut	99.8%
Multi-ring cut	99.5%
$\pi$ cut	99.2%
Charge/hit cut	99.8%

## Chapter 5 Selection of Correlated Neutrons at SK

For antineutrinos in the SRN search window, the neutron energy from IBD is usually lower than 1 MeV. The energy and angular distribution can be explicitly calculated to first order as P. Vogel and J. F. Beacom demonstrated<sup>[14]</sup>. The convolved neutron energy distributions for different SRN model are shown in Fig. 5.1. These neutrons propagating in water are quickly thermalized and eventually captured by the oxygen or hydrogen nucleus.

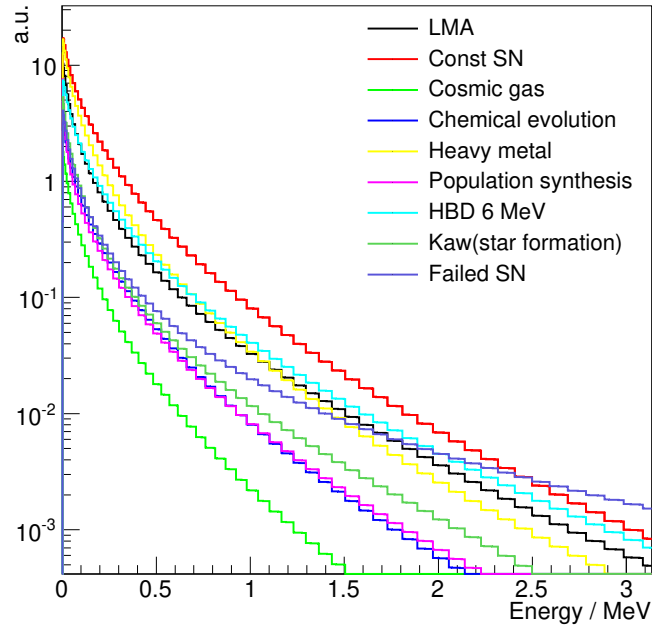


Figure 5.1 Energy of neutrons produced in IBD events.

In the above energy range, neutron capture on hydrogen has a cross section of  $\sim 0.33$  bars, much larger than the  $\sim 0.19$  millibar cross section on oxygen. Therefore, we assume the neutrons are  $\sim 100\%$  captured by hydrogen as Eq. (5-1).



The neutron capture lifetime is measured to be  $204.8 \mu\text{s}$ <sup>[94]</sup>. Before being captured, neutrons are constantly losing energy and changing directions by scattering. The distance between the capture vertex of a thermal neutron and the primary vertex where the neutron



is generated is usually negligible compared to the vertex resolution in SK ( $\sim 50$  cm). Figure 5.2 shows the typical distance between the capture vertex and the primary vertex in the direction of neutron emission for different incident antineutrino energy model simulated using Geant4.9.6<sup>[95]</sup>.

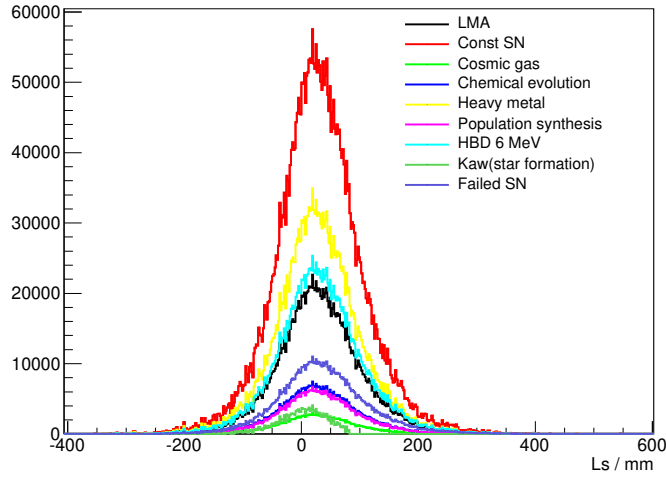


Figure 5.2 Distance between the capture vertex and the primary vertex.

The 2.2 MeV  $\gamma$  emitted from a neutron capture on hydrogen can be used to tag neutrons, giving a power to discriminate IBD signals over the background of radioactive isotopes and spallations. Since the 2.2 MeV  $\gamma$  is below the trigger threshold of SK, a special trigger scheme is adopted to record their information. As introduced in Section 2.5.2, for 2.2 MeV  $\gamma$ 's outside the usual  $35 \mu\text{s}$  HE time window, a  $500 \mu\text{s}$  time window of the AFT trigger is opened right after an HE trigger without an OD trigger. After extracting the AFT data and combining with the preceding HE data, we developed a neutron tagging technique to look for the associated 2.2 MeV  $\gamma$  signals.

The neutron tagging technique, also known as Ntag, was first introduced to SK in 2009 by H. watanabe and H. Zhang<sup>[96]</sup>, and further developed by Y. Zhang<sup>[46]</sup> and T. Irvine<sup>[97]</sup> towards higher signal efficiency and purity either in the low neutrino energy data sample to search for SRN signals or in the high energy atmospheric neutrino interactions to distinguish anti-neutrinos from neutrinos. This section presents the author's work in developing neutron tagging technique for the SRN search with 2.2 MeV  $\gamma$  vertex reconstruction, the tuning of the neural network, validations with different samples, as well as the optimization of the cut value for the SRN sample.

The four-vector momenta and vertex positions for both the 2.2 MeV  $\gamma$  and the

prompt positron are obtained from toy-MC. Then the generator-level information is sent to SKDetSim for the detector-level simulation. Dark noise is only simulated to  $5 \mu\text{s}$  after the primary trigger, and afterwards dummy trigger, i.e., a constant calibration trigger that does not coincide with any physics events, is used as backgrounds to add into the pure data sample from MC, thus unbiased from the actual backgrounds in the experiment.

## 5.1 Neutron Tagging Algorithm

To distinguish 2.2 MeV  $\gamma$  signals from backgrounds, a comprehensive understanding of signal and background characteristics is crucial. For signal, a 2.2 MeV  $\gamma$  is expected to produce all the PMT hits within a narrow timing (ToF-subtracted) window, and these hits are expected to be anisotropic. The neutron capture vertex should be close to the neutrino vertex, and the energy of the hits, though difficult to fully reconstruct, should correspond to  $\sim 2.2$  MeV. Dominant backgrounds in this energy range include natural radioactivities from the surrounding rock and detector material, radon contamination in tank water, PMT dark noise, etc. These background sources have different characteristics, as natural radioactivities from the surrounding usually produce hit clusters, and dark noise tends to produce isotropic hits in random patterns.

In searching for the 2.2 MeV  $\gamma$ 's, we first look for timing peaks within the trigger data right after the primary event. Then we calculate a set of 22 variables for each candidate. These variables are then sent into a neural network, where the output is used to determine the likelihood of the neutron capture signal.

### 5.1.1 Pre-selection

First, all the PMT hits within the given certain time range are ToF-subtracted to the primary vertex, as introduced in Section 3.3. This time range is constrained by the AFT trigger time of  $535 \mu\text{s}$  as well as after pulses from the primary event, which contaminate the time range close to the primary event. Therefore, a time range from  $0.05 \mu\text{s}$  to  $535 \mu\text{s}$  is chosen to select 2.2 MeV  $\gamma$  candidates at a cost of  $\sim 7\%$  efficiency loss. Figure. 5.3 shows the time distribution with ToF-subtraction for the 2.2 MeV  $\gamma$ 's<sup>[45]</sup>. From this distribution, we chose a 10 ns window to search for the candidate cluster hits.

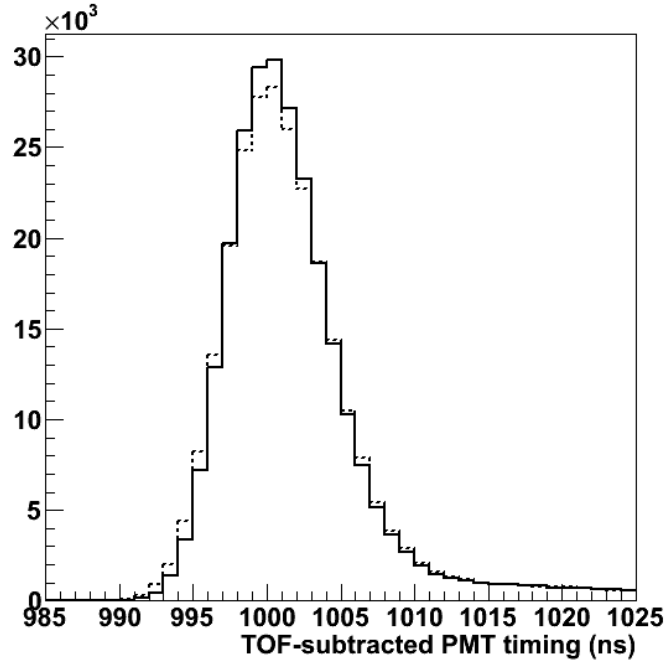


Figure 5.3 Time distributions for 2.2 MeV  $\gamma$  candidates with ToF subtracted for true primary vertex (solid line) and reconstructed primary vertex (dashed line)<sup>[45]</sup>.

Figure 5.4 shows the distribution of number of hits within a 10 ns sliding window for 2.2 MeV  $\gamma$  and background noise. In this figure, we required

$$N_{10} > 7 \quad (5-2)$$

where  $N_{10}$  is the number of hits in the 10 ns sliding window. The candidate time  $t_0$  is defined as the timing of the first hit in  $N_{10}$ . To avoid double counting of the same neutron capture event and maximizing the discrimination over background, the candidate needs a further check for a wider window to  $t_0 + 20$  ns. The hits within this 20 ns window is regarded as from the same neutron, and the set of hits with the max  $N_{10}$  sliding within the 20 ns window is taken as the 2.2 MeV  $\gamma$  candidate. Outside the  $t_0 + 20$  ns, hits are treated as separate candidates.

To remove energetic backgrounds in the SHE+AFT trigger range, an upper limit on the number of hits is applied as

$$\begin{aligned} N_{10} &\leq 50, \\ N_{200} &\leq 100, \end{aligned} \quad (5-3)$$

where  $N_{200}$  is the number of hits in  $\pm 100$  ns around  $t_0$ .

There are 35.4% of true neutron capture events remaining the above cuts, with 1.6 background events tagged on average for each neutrino event.

### 5.1.2 Discriminating Variables

After the pre-selection, candidates are processed to calculate 22 variables. These variables are chosen to cover most of the distinctive differences between signals and backgrounds, and can be classified into hit pattern ( $N_{10}$ ,  $N_{300}$ ,  $N_c$ ,  $N_{low}$ ,  $N_{highQ}$ ,  $N_{low\theta}$ ,  $N_{back}$ ,  $\phi_{rms}$ ,  $\theta_{mean}$ , and  $\theta_{rms}$ ), charge information ( $Q_{rms}$  and  $Q_{mean}$ ), time information ( $T_{rms}$ ,  $minT_{rms}(3)$ , and  $minT_{rms}(6)$ ), and reconstruction related ( $NF_{wall}$ ,  $\delta T_{rms}$ ,  $\delta N_{10}$ ,  $BS_{wall}$ ,  $BS_{energy}$ ,  $FP_{dist}$ ,  $BF_{dist}$ ). Later in this subsection we will show the signal-background comparison for each variable. To make figures easier to read, we scaled background to  $22\% = 35.4\%/1.6$  so that the total number of signals and backgrounds is the same in each figure.

#### 5.1.2.1 Number of hits in 10 ns: $N_{10}$

This variable is required to be above 7 and used as a cut in the pre-selection. Figure 5.4 shows a comparison of  $N_{10}$  between signal and background. Unlike those for the accidental background,  $N_{10}$  tends to have a larger number for signal.

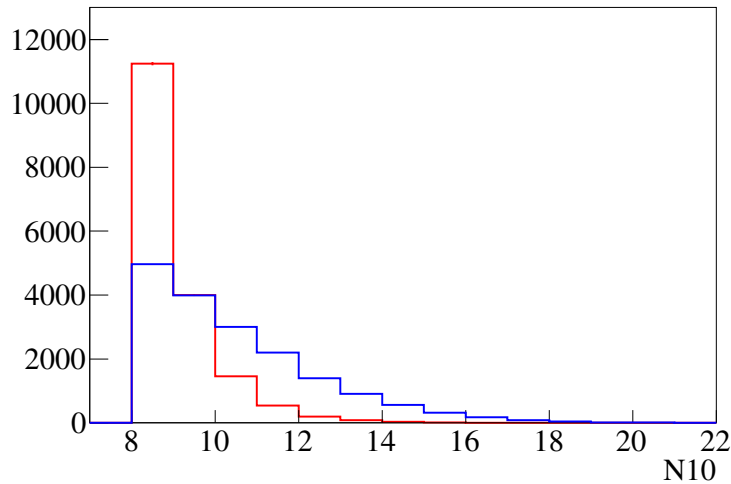


Figure 5.4  $N_{10}$  distributions for both the neutron capture signal (blue) and the background (red). See text for more details.

5.1.2.2 Number of clustered hits:  $N_c$ 

Due to the spatial distribution around the detector wall, hits from many backgrounds, such as radioactive contaminants in the PMT glass, or PMT flashings, are found to have a cluster pattern, both in time and space. For 2.2 MeV  $\gamma$  signals, however, the fiducial volume cut for the primary events requires the vertex to be more than 2 m away from the tank wall. The neutron capture vertices are therefore rarely close to the tank wall to cause a set of clustered hits, as shown in Fig. 5.5.

The direction of a hit is defined by a vector pointing from a vertex to a hit PMT. However, due to the less hits, the neutron vertex is poorly or even not reconstructed, and we use the primary vertex instead to calculate the direction of hits.

For all  $N_{10}$  hits in a 2.2 MeV  $\gamma$  candidate, if the angle between a pair of hit vectors is less than  $14.1^\circ$ , these hits form a cluster of  $N_c = 2$ . If an additional hit is within  $14.1^\circ$  of any hit in a cluster, it adds up to the cluster hit count  $N_c$ . We expect the number of hits in a cluster  $N_c$  for the background to be larger than that for signal.

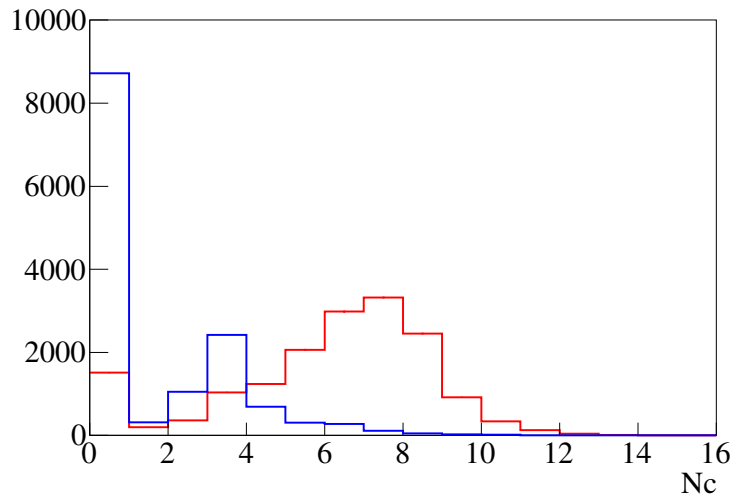


Figure 5.5  $N_c$  distributions for both the neutron capture signal (blue) and the background (red). See text for more details.

5.1.2.3 Number of hits on low probability PMTs:  $N_{low}$ 

For a neutron capture vertex, even though the direction of emitted  $\gamma$  is not predictable, the geometric acceptance and attenuation can still give different hit probabilities for the PMTs. If most of the hits in a candidate have very low hit probability, this candidate is

very likely to be a background event. The hit probability for the  $i$ -th PMT is calculated as

$$A_i \propto \frac{F(\theta_i)}{R_i^2} e^{R_i/L} \quad (5-4)$$

where  $F(\theta_i)$  is the acceptance of  $i$ -th PMT for the incident angle  $\theta_i$  (collection efficiency and quantum efficiency assumed to be uniform on  $\theta_i$ ),  $R_i$  is the distance from the vertex to the  $i$ -th PMT, and  $L$  is the light attenuation length in water. Similar to the calculation of  $N_c$ , instead of neutron capture vertex, the primary vertex is employed in determination of  $R_i$ .

The number of hits with low hit probability  $N_{low}$  is obtained by first defining a group of high hit probability PMTs for each primary event, which consist of PMTs totaling the top  $x\%$  of hit probabilities for all PMTs listed from high to low. If a hit PMT is not included in this group, this hit is counted as low probability hit.

However, this cut causes a position nonuniformity. When a primary event is relatively close to the tank wall, the distribution of high hit probability PMTs is highly concentrated, while for a primary vertex in the tank centre, all PMTs will be assigned a similar hit probability. To compensate for this nonuniformity, the percentage of hit probability ranking required to be high probability,  $x\%$ , varies throughout the tank, as shown in Fig. 5.6.  $N_{low}$  assuming random distribution of primary vertices inside the fiducial volume is shown in Fig. 5.7. We expect a smaller  $N_{low}$  for 2.2 MeV  $\gamma$  signals.

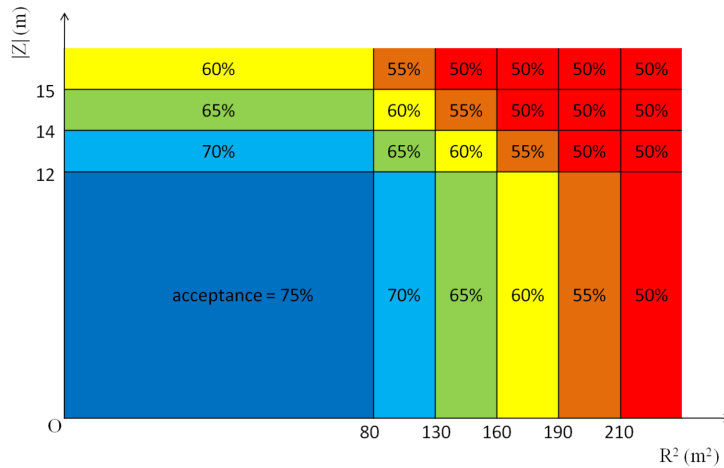


Figure 5.6 A map of required total hit probability ( $x\%$ ) based on the primary vertex position in tank<sup>[45]</sup>.

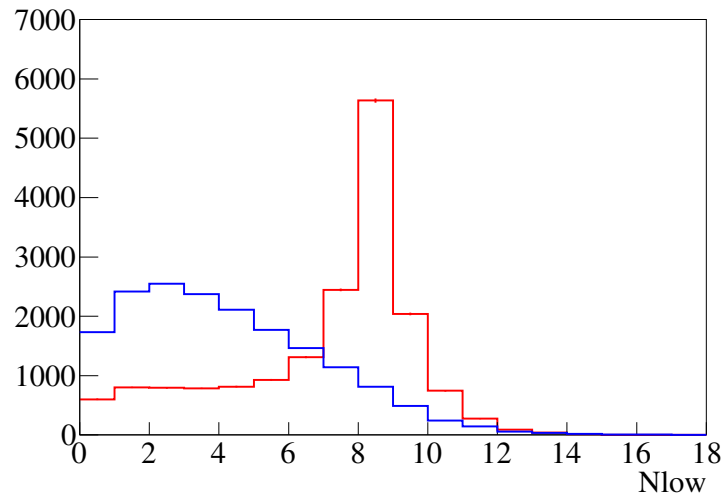


Figure 5.7  $N_{low}$  distributions for both the neutron capture signal (blue) and the background (red). See text for more details.

#### 5.1.2.4 Number of hits in 300 ns: $N_{300}$

The  $N_{10}$  cut removes many low energy backgrounds. However, for high energy backgrounds, such as the PMT flashing or high noise channels,  $N_{10}$  can be large and may contaminate the signal sample. The crucial feature to distinguish signal from these backgrounds will be the number of hit in a wider time window,  $N_{300}$ . The hits of a neutron capture event are usually fully contained within a 10 ns window, while for these high energy backgrounds, the noise effect will continue in a longer time range, thus forming a larger, more disperse pattern, as shown in Fig. 5.8.

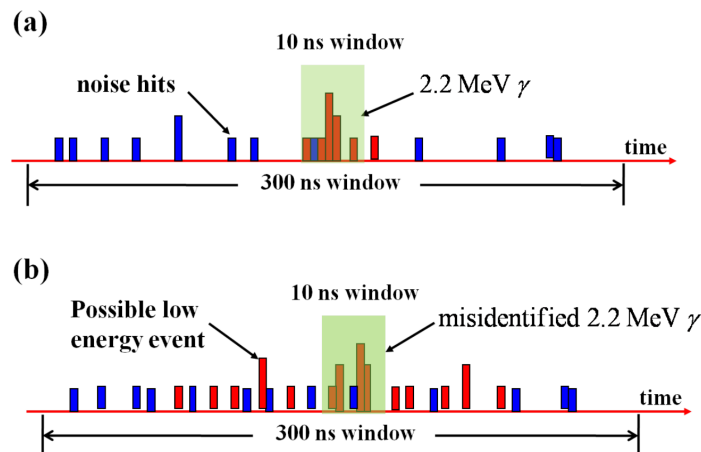


Figure 5.8 Upper figure shows a typical neutron capture event, and lower figure shows a hypothetical background signal to be rejected. The blue markers correspond to the PMT dark noise, and the red markers represent a signal or a PMT flasher<sup>[45]</sup>.

We expect a smaller  $N_{300}$  for signals, as shown in Fig. 5.9.

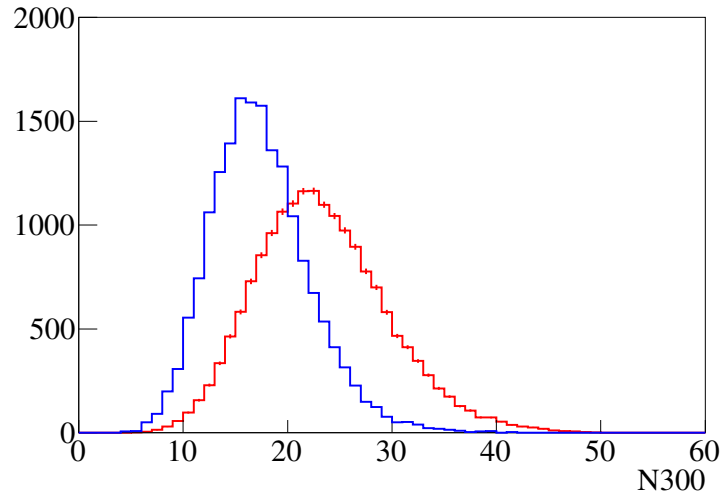


Figure 5.9  $N_{300}$  distributions for both the neutron capture signal (blue) and the background (red). See text for more details.

#### 5.1.2.5 Hit vector RMS: $\phi_{rms}$

We calculate the RMS of the azimuthal angle of the hit vectors  $\phi_{rms}$  for each 2.2 MeV  $\gamma$  candidate. Unlike neutron capture on gadolinium or lithium, the neutron capture on hydrogen emits only a single 2.2 MeV  $\gamma$ . This single  $\gamma$  is expected to deposit most of its energy in one direction, though the actual hits will spread as the  $\gamma$  interacts with water. On the contrary, the PMT dark noise tends to form a random hit pattern, and have a larger  $\phi_{rms}$ , as shown in Fig 5.10.

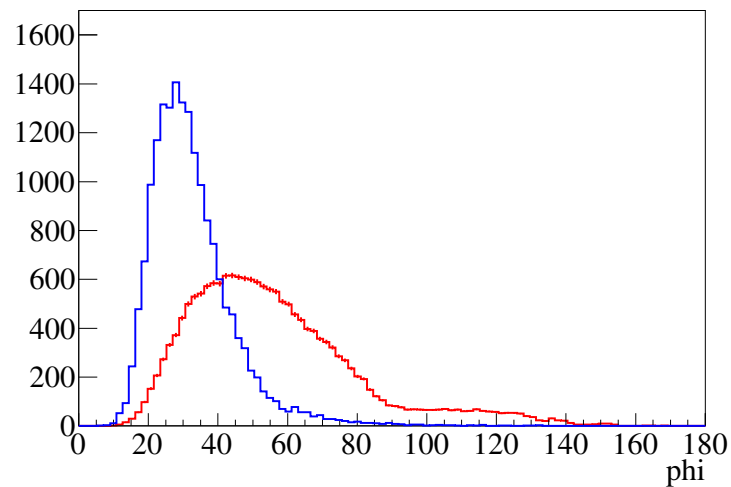


Figure 5.10  $\phi_{rms}$  distributions for both the neutron capture signal (blue) and the background (red). See text for more details.



5.1.2.6 The mean value and RMS of the opening:  $\theta_{mean}$  and  $\theta_{rms}$ 

Here we define an opening angle  $\theta_i$  to describe the angle between the  $i$ -th hit vector and the sum of all hit vectors for a candidate.  $\theta_{mean}$  is the mean value of the opening angle  $\theta_i$ . For the 2.2 MeV  $\gamma$  induced Compton electrons,  $\theta_{mean}$  should peak around  $42^\circ$ , while background events are more likely to have a clustered hit pattern and a smaller  $\theta_{mean}$ , as shown in Fig. 5.11. On the other hand,  $\theta_{rms}$ , the RMS of the opening angle  $\theta_i$ , can tell a cluster faked  $N_{10}$  peak from a true 2.2 MeV  $\gamma$  peak by its unreasonably narrow distribution against the wider multiple-scattering induced distribution, as shown in Fig. 5.12.

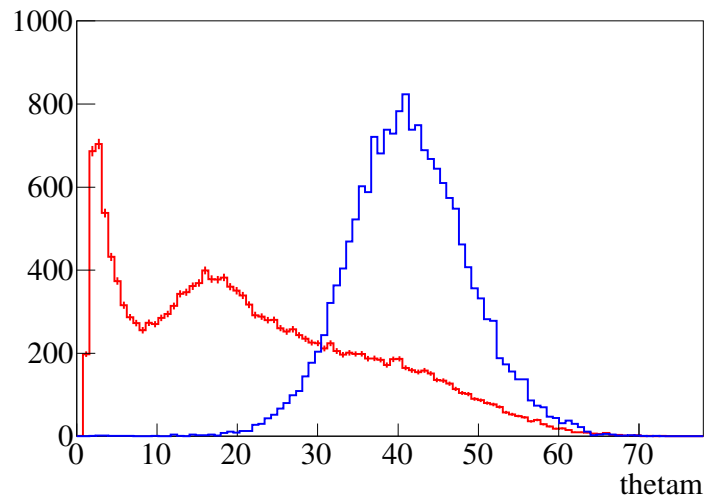


Figure 5.11  $\theta_{mean}$  distributions for both the neutron capture signal (blue) and the background (red). See text for more details.

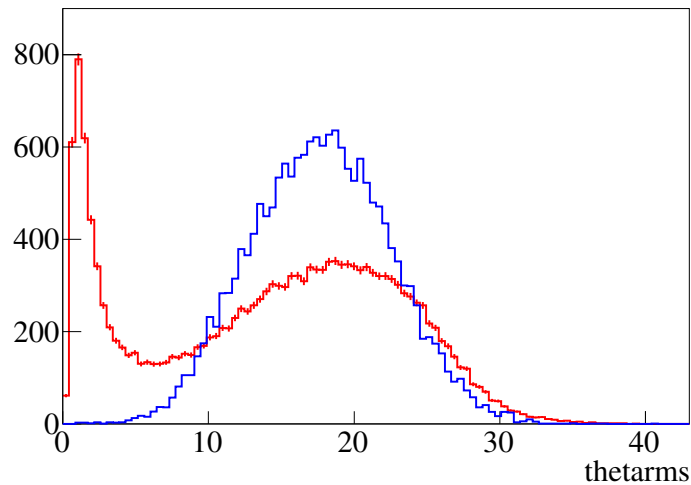


Figure 5.12  $\theta_{rms}$  distributions for both the neutron capture signal (blue) and the background (red). See text for more details.

5.1.2.7 Number of backward hits:  $N_{back}$ 

The 2.2 MeV  $\gamma$  tends to lie mostly in the forward direction, since Compton electrons emitted Cherenkov light with the directional information, while for dark noise the hits tend to be uniformly distributed. The number of PMT hits with  $\theta_i > 90^\circ$  is referred to as  $N_{back}$ . We expect  $N_{back}$  to be smaller for signal, as shown in Fig. 5.13.

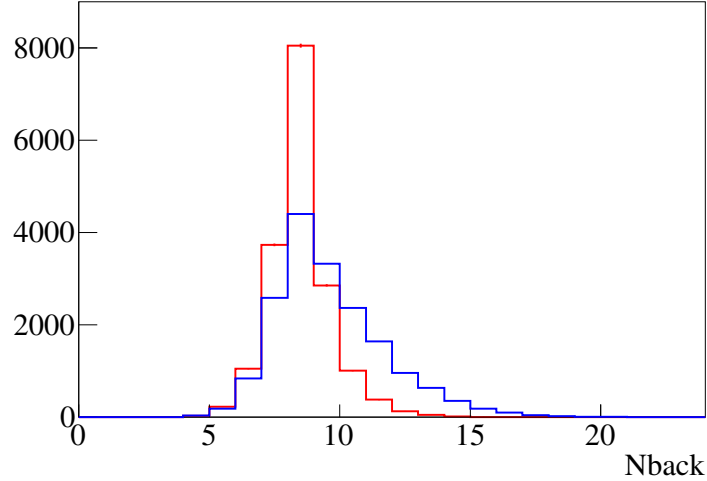


Figure 5.13  $N_{back}$  distributions for the neutron capture signal (blue) and the background (red). See text for more details.

5.1.2.8 Number of hits with low  $\theta$ :  $N_{low\theta}$ 

Similar to the situation of  $N_{back}$ , the Cherenkov hits from Compton electrons scattered by true 2.2 MeV  $\gamma$ 's are also unlikely to have really low number  $\theta_i$ 's, while radioactive backgrounds on PMT windows or from the tank wall tends to form a cluster, producing hits with much lower  $\theta_i$ 's. The number of hits with  $\theta_i < 20^\circ$  is defined as  $N_{low\theta}$ . We expect  $N_{low\theta}$  to be smaller for signal, i.e.,  $N_{10} - N_{low\theta}$  to be larger, as shown in Fig. 5.14.

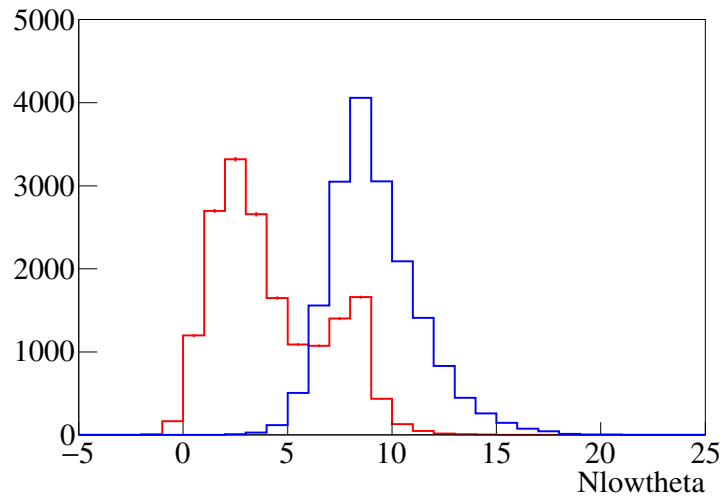


Figure 5.14  $N_{10} - N_{low\theta}$  distributions for both the neutron capture signal (blue) and the background (red). See text for more details.

#### 5.1.2.9 Charge mean and RMS: $Q_{mean}$ and $Q_{rms}$

Though for low energy analysis in SK, PMT charge usually cannot provide much information, in neutron tagging processes where we take into consider the actual performance of every PMT channel, the charge distribution may still give a hint on the possibility of a hit to be from signal or from electronic noises.  $Q_{mean}$  and  $Q_{rms}$  are defined respectively as the mean and the RMS of the number of p.e.'s for a candidate. For noisy channels or PMT sparkling events which produce enough hits to mimic a 2.2 MeV  $\gamma$  events, it is very likely that these channels have higher gain than usual PMTs and thus have higher  $Q_{mean}$  and wider  $Q_{rms}$ , as shown in Fig. 5.15 and Fig. 5.16.

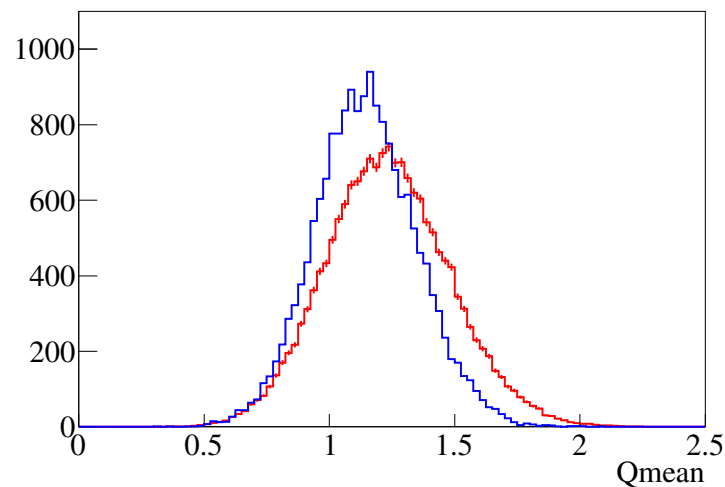


Figure 5.15  $Q_{mean}$  distributions for both the neutron capture signal (blue) and the background (red). See text for more details.

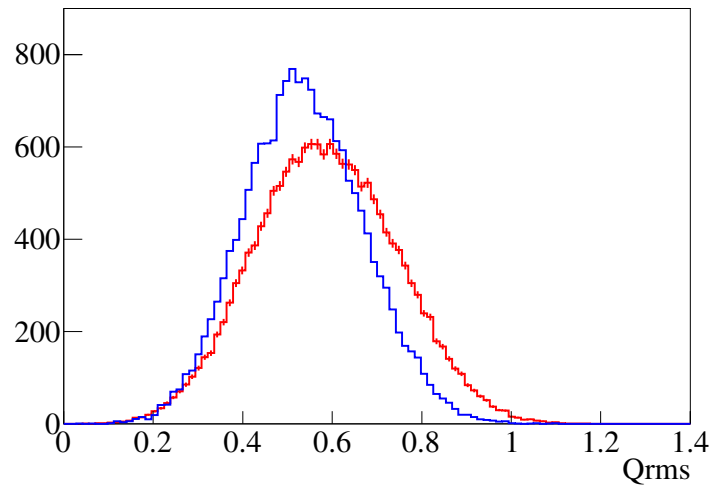


Figure 5.16  $Q_{rms}$  distributions for both the neutron capture signal (blue) and the background (red). See text for more details.

#### 5.1.2.10 Number of hits with high charge: $N_{highQ}$

The number of hits with more than 3 p.e.'s for a candidate is defined as  $N_{highQ}$ . Due to the same reason as mentioned above, noisy channels tend to have a higher gain and thus if a PMT gets unreasonably high charge, it's more likely to be from a noisy channel than that from a signal event. The distribution of  $N_{highQ}$  is shown in Fig. 5.17.

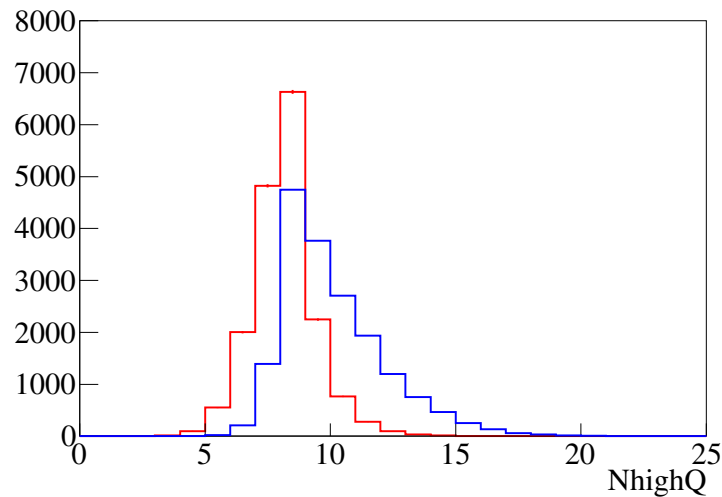


Figure 5.17  $N_{highQ}$  distributions for both the neutron capture signal (blue) and the background (red). See text for more details.

#### 5.1.2.11 Hit time RMS: $T_{rms}$

Though the timing information has been used in the pre-selection to select 2.2 MeV  $\gamma$  candidates at a 10 ns cut, hits from true 2.2 MeV  $\gamma$ 's tend to concentrate in this 10 ns

time window. Without scattering, hits from 2.2 MeV  $\gamma$ 's are expected to arrive on PMTs at exactly the same ToF-subtracted time, and thus the width of the time distribution is simply determined by the PMT timing resolution, which is  $\sim 3$  ns for those with charge  $\sim 1$  p.e. at SK<sup>[80]</sup>. Variable  $T_{rms}$  is the RMS of the timing of all  $N_{10}$  hits, as shown in Fig. 5.18. We expect a smaller  $T_{rms}$  for 2.2 MeV  $\gamma$  signals.

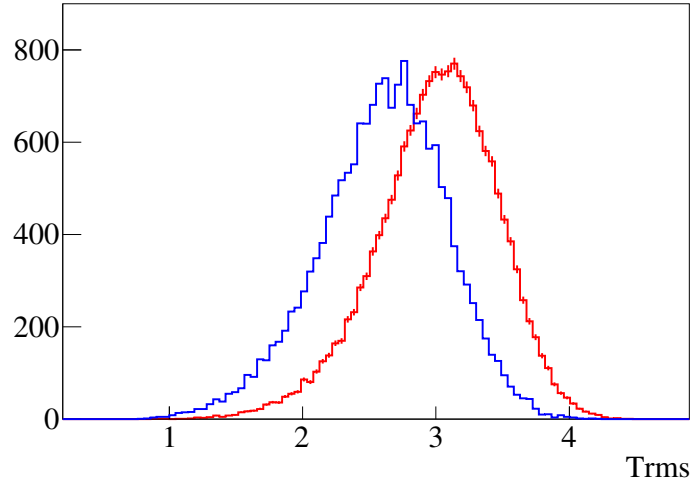


Figure 5.18  $T_{rms}$  distributions for both the neutron capture signal (blue) and the background (red). See text for more details.

#### 5.1.2.12 Minimum RMS of hit time: $minT_{rms}(3)$ and $minT_{rms}(6)$

Due to the inevitable PMT dark noise, even when a candidate originates from a 2.2 MeV  $\gamma$ , it may still have several hits from the noise and result in a smeared  $T_{rms}$ . To eliminate the influence from these noisy hits, a minimal  $T_{rms}$  based on only part of the candidate hits is reconstructed as  $minT_{rms}(x)$ , where  $x$  is the considered number of hits from the total  $N_{10}$ , as shown in Fig. 5.19.

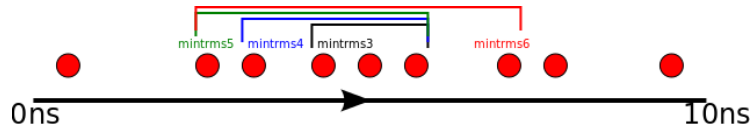


Figure 5.19 A scheme for the construction of  $minT_{rms}$ . Clusters of 3-6 hits with minimal  $T_{rms}$  are shown for a candidate with  $N_{10} = 9$ . Possible background in this candidate will not contaminate the  $minT_{rms}$ <sup>[97]</sup>.

Among possible  $x$  choices from 2 to 7, we use  $minT_{rms}(x)$  with  $x = 3$  and  $x = 6$  for the neural network inputs, as shown in Fig. 5.20 and Fig. 5.21.

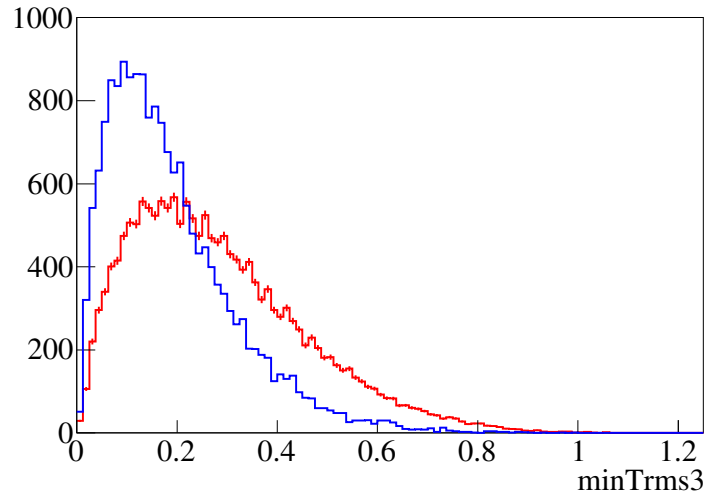


Figure 5.20  $\min T_{rms}(3)$  distributions for both the neutron capture signal (blue) and the background (red). See text for more details.

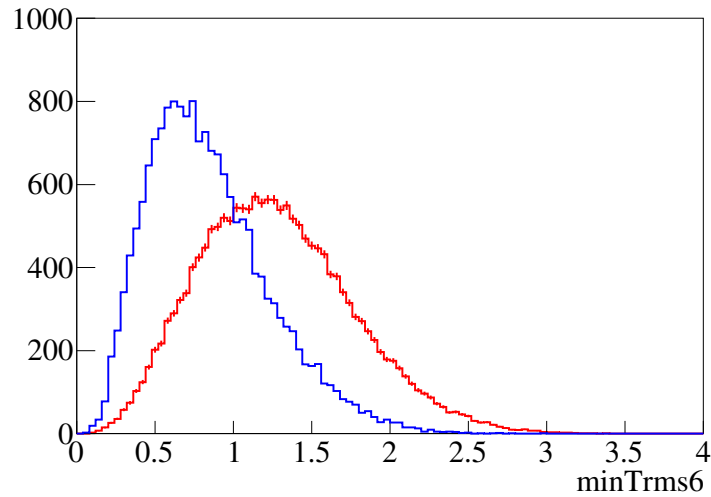


Figure 5.21  $\min T_{rms}(6)$  distributions for both the neutron capture signal (blue) and the background (red). See text for more details.

#### 5.1.2.13 Neut-Fit variables: $NF_{wall}$ , $\delta N_{10}$ and $\delta T_{rms}$

Neutron Fit (Neut-Fit) is a vertex fitter developed by Tristan Irvine<sup>[97]</sup>. This fitter performs a grid searching for the best vertex which minimize the  $T_{rms}$  for all the hits from a candidate,

$$T'_{rms} = \sqrt{\frac{\sum_i^{N_{10}} (t_i - t_{mean})^2}{N_{10}}}, \quad (5-5)$$

where  $t_{mean} = \sum_i^{N_{10}} t_i / N_{10}$ , and  $t_i$  is the hit timing on the  $i$ -th PMT after the ToF subtraction to the grid vertex. This process repeats with a finer precision until 0.5 cm. The Neut-Fit reconstructed vertex is heavily biased towards the primary vertex due to the initial choice of the  $N_{10}$  hits, which is determined by the ToF subtracted time to the primary vertex.

With Neut-Fit, the reconstructed neutron capture vertex and the goodness of the fit can be used to discriminate the 2.2 MeV  $\gamma$  signal from background. The distance between the Neut-Fit vertex and the nearest tank wall is defined as  $NF_{wall}$ . The neutron vertex is more likely to be close to its primary vertex, and Neut-Fit tends to be biased towards the primary vertex. Therefore, for 2.2 MeV  $\gamma$ 's, the reconstructed vertex should satisfy the fiducial cut applied to the primary vertex, i.e., the candidate should not be reconstructed near the ID wall, as shown in Fig. 5.22.

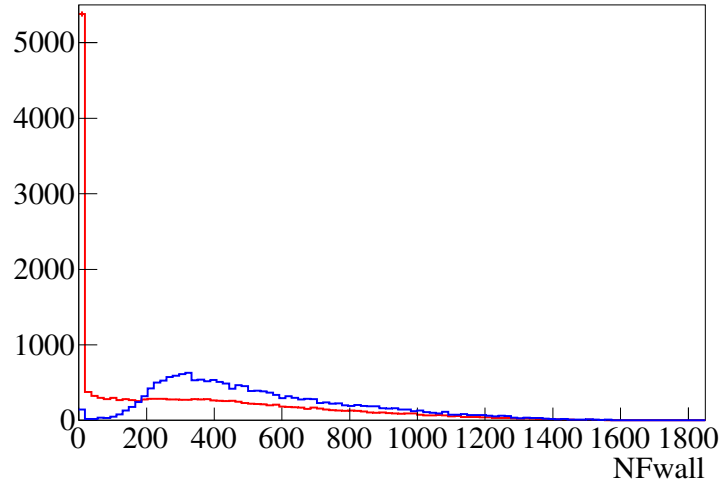


Figure 5.22  $NF_{wall}$  distributions for both the neutron capture signal (blue) and the background (red). See text for more details.

The minimal  $T'_{rms}$  Neut-Fit obtained for the best vertex tends to be smaller than  $T_{rms}$  for the primary vertex for neutron capture signal events. For backgrounds, however, they usually do not originate from a single source or a source outside the fiducial volume, thus having larger  $T'_{rms}$  values. Comparing  $T_{rms}$  from different vertices, the variable  $\delta T_{rms} = T_{rms} - T'_{rms}$  is constructed to discriminate between signals and backgrounds, as shown in Fig. 5.23.

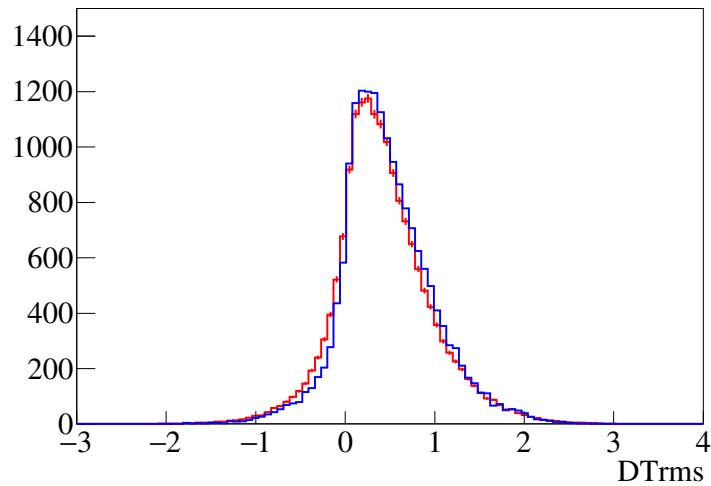


Figure 5.23  $\delta T_{rms}$  distributions for both the neutron capture signal (blue) and the background (red). See text for more details.

As shown in Fig. 5.3, we can find that with ToF subtracted to the reconstructed primary vertex, some hits from the 2.2 MeV  $\gamma$  may still spread outside the 10 ns window. Sliding another 10 ns window in 40 ns around the neutron candidate, and re-performing the ToF subtraction with regard to the Neut-Fit vertex, a new variable  $\delta N_{10} = N'_{10} - N_{10}$  is constructed, as shown in Fig. 5.24. For the 2.2 MeV  $\gamma$  signal, this  $N'_{10}$  should be smaller than  $N_{10}$ , while for backgrounds without a single source,  $N'_{10}$  should not have such a improvement from  $N_{10}$ .

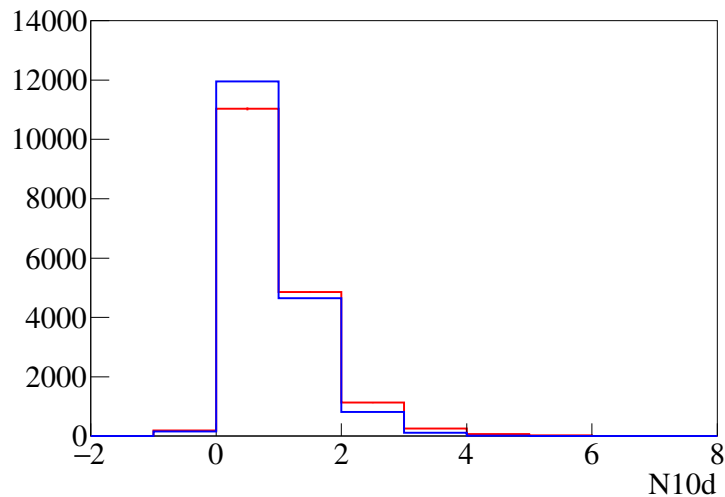


Figure 5.24  $\delta N_{10}$  distributions for both the neutron capture signal (blue) and the background (red). See text for more details.



5.1.2.14 BONSAI fit variables:  $BS_{wall}$  and  $BS_{energy}$ 

BONSAI fit is an unbiased low energy fitter as described in Section 3.3. It is optimized for low energy events, but requires at least 10 hits to perform the vertex fitting, and is extremely slow when the input hits exceeds 1000 hits. To account for that, for each 2.2 MeV  $\gamma$  candidate, BONSAI fit is performed on the surrounding  $1.3\mu\text{s}$  of data; if the number of hits in a  $1.3\mu\text{s}$  time window exceeds 1000, the selection window is narrowed to 325 ns surrounding the 10 ns candidate; if the number is still exceeding, the event is too noisy to be a good neutron capture event, and is dropped.

$BS_{wall}$  is the distance between the reconstructed BONSAI vertex and the nearest ID wall. Similar to  $NF_{wall}$ ,  $BS_{wall}$  removes backgrounds reconstructed near the ID wall, and is independent of  $NF_{wall}$  due to the difference in reconstruction algorithm, as shown in Fig. 5.25.

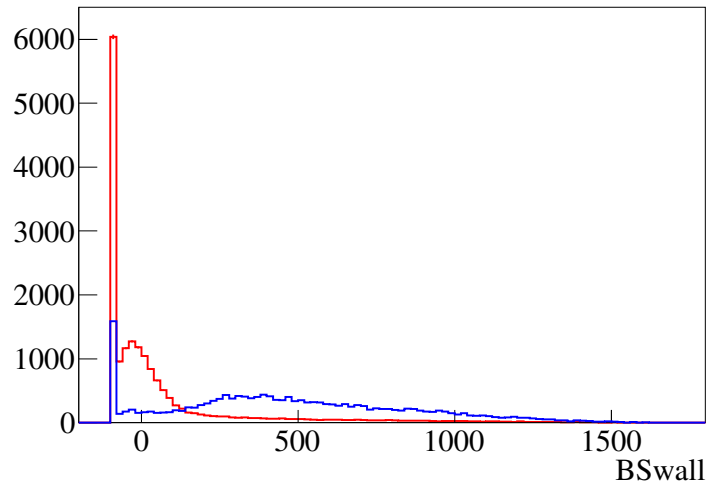


Figure 5.25  $BS_{wall}$  distributions for both the neutron capture signal (blue) and the background (red). See text for more details.

$BS_{energy}$  is the effective number of hits for the candidate event, representing the energy. As explain in Section 3.3, the energy of low energy events are first reconstructed by the effective number of hits, and then converted to energy (MeV) by an energy scaling function. For 2.2 MeV  $\gamma$  events, however, the energy scaling function under 3 MeV is not properly calibrated at SK. In this case, a variable  $BS_{energy}$  is defined to be the effective number of hits, to represent the energy of a candidate event. The mono-energetic 2.2 MeV  $\gamma$  is expected to have a sharper peak in the  $BS_{energy}$  distribution, as shown in Fig. 5.26.

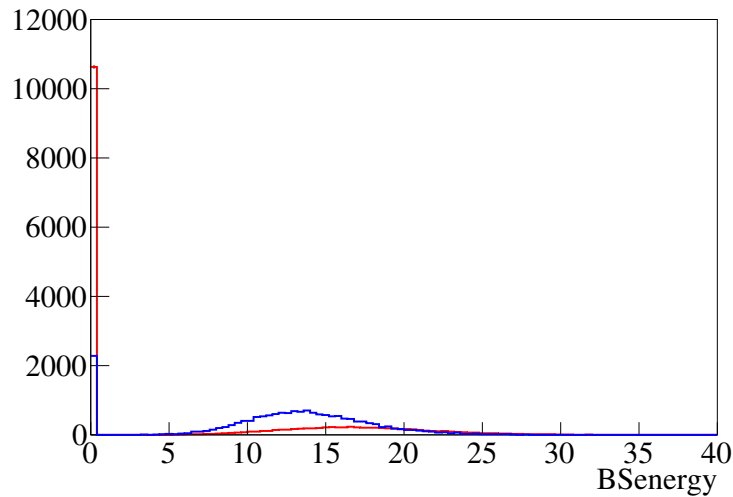


Figure 5.26  $BS_{energy}$  distributions for both the neutron capture signal (blue) and the background (red). See text for more details.

#### 5.1.2.15 Fit agreement variables: $FP_{dist}$ and $BF_{dist}$

The difference between vertices reconstructed by different methods can be used to evaluate the goodness of neutron fit and the likelihood for the hits within a candidate to originate from the same source.

$FP_{dist}$  is the distance between the Neut-Fit neutron vertex and the primary vertex reconstructed by BONSAI. As we have shown in Fig. 5.2, SRN IBD neutrons do not travel far from the neutrino interaction point before being captured. The primary vertex reconstructed by BONSAI is proved to be more reliable for the higher energy and more apparent Cherenkov ring<sup>[89]</sup>. If a Neut-Fit reconstructed neutron vertex is close to its BONSAI reconstructed primary vertex, the candidate is more likely to be a 2.2 MeV  $\gamma$  signal, as shown in Fig. 5.27.

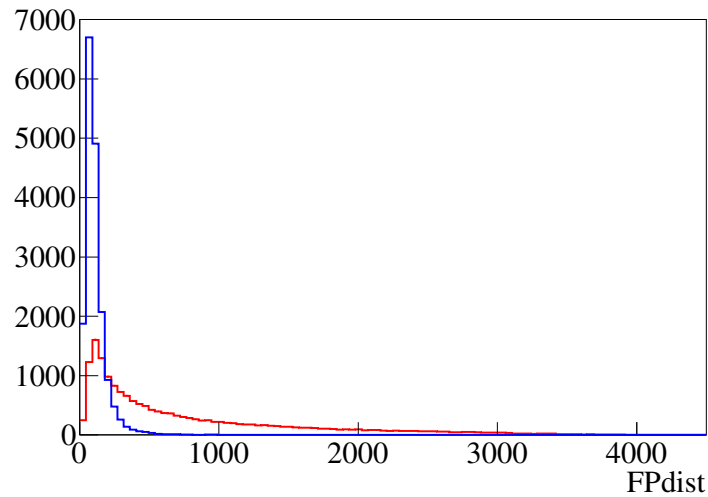


Figure 5.27  $FP_{dist}$  distributions for both the neutron capture signal (blue) and the background (red). See text for more details.

$BF_{dist}$  is the distance between neutron vertices reconstructed by BONSAI and Neut-Fit. Due to the difference of algorithm and input hit set where BONSAI takes  $1.3 \mu s$  and Neut-Fit takes a set biased 10 hits, these two reconstructions will differ if the candidate is accidentally chosen from longer-lived backgrounds, as shown in Fig. 5.28.

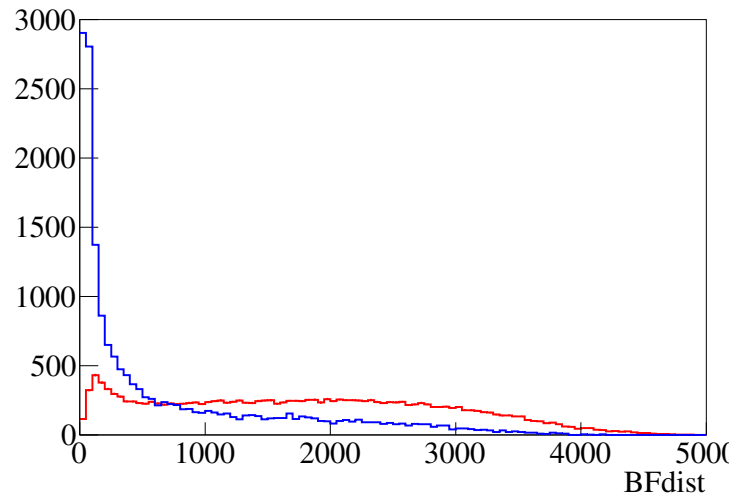


Figure 5.28  $BF_{dist}$  distributions for both the neutron capture signal (blue) and the background (red). See text for more details.

### 5.1.3 Multivariate classification

Multivariate classification is a machine learning based technique for pattern recognition. Derived from the training events separated in both classes or even events from a single class, a classifier can determine the mapping function describing a decision bound-

ary. A Toolkit for Multi-Variate Analysis TMVA has been implemented in the widely used in high energy physics area analysis framework ROOT<sup>[98]</sup>. In this analysis, after comparing several classifier, we decided to use a feed-forward Multi-Layer Perceptron (MLP) in TMVA to maximize the separation between signal and backgrounds.

In this analysis, MLP was trained with 10,000,000 events hybrid with both the MC simulated 2.2 MeV  $\gamma$  signal and the dummy trigger backgrounds. There were 20,458,451 candidates selected, in which 3,507,630 candidates were true 2.2 MeV signals, and 16,950,821 were backgrounds. To avoid over-training, this sample was split randomly into a training sample with 3/4 of the candidates and a testing sample with 1/4 of the candidates. The tunable parameters in a MLP include signal and background weight (fixed at 1), number of iteration cycles, and the node pattern. After several trials and considering the time consumed, the number of cycles was determined at 1,000 and the node pattern was chosen as 22:18:8:1 (input variables : hidden layer 1 : hidden layer 2 : output). The output node represents the MLP calculated similarity of a candidate to a training 2.2 MeV  $\gamma$  signal or a training background, to be used as a cut in latter stage.

## 5.2 Significance Curve

The efficiency of 2.2 MeV  $\gamma$ -ray selection is defined to be

$$\epsilon = \frac{\text{True neutrons that are tagged as candidates}}{\text{All neutron captures}}, \quad (5-6)$$

And the background rate as

$$R = \frac{\text{Dummy triggers tagged as candidates}}{\text{All dummy triggers}}. \quad (5-7)$$

The pre-selection is a rigid cut and its efficiency is calculated from MC simulation and the dummy trigger data, as shown in Table 5.1.

Table 5.1 Neutron tag pre-selection efficiency

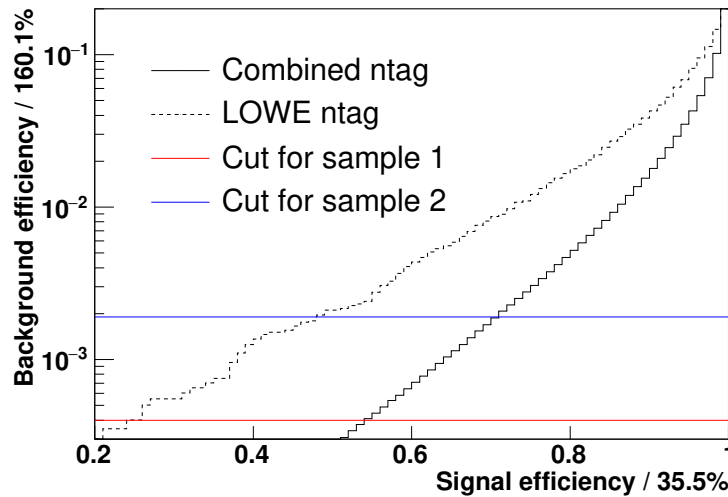
Signal (MC) / event	Background (dummy trigger) / event (500 $\mu$ s)
35.4%	160.1%

In the neural network selection, however, these efficiencies are dependent on the

1-dimensional MLP cut. To compare with the previous neutron tagging study in LOWE group, this MLP cut is set at a point that the background level is the same as the previous study, as shown in Table 5.2. Two different energy regions are separated by the level of backgrounds, where below 14.3 MeV the spallation backgrounds dominate and the cut must be set tighter to remove the backgrounds. A significant improvement on the neutron tagging efficiency is observed. The efficiency in the low-energy region is nearly doubled, while it also increased by  $\sim 40\%$  in the high-energy region. A comparison for the improved and the previous neutron tagging method versions can be directly observed in Fig. 5.29. For  $E_{\bar{\nu}_e} > 14.3$  MeV, the neutron tagging with a loose cut ( $\sim 25\%$  signal efficiency and  $\sim 0.3\%$  accidental background level) was applied, while for  $E_{\bar{\nu}_e} < 14.3$  MeV, the neutron tagging with tight cut ( $\sim 19\%$  signal efficiency and  $\sim 0.065\%$  accidental background level) was applied.

Table 5.2 A comparison of neutron tag efficiency with the previous study<sup>[46]</sup>

NTag version	Signal (MC) / event		Background (dummy trigger) / event (500 $\mu$ s)
	Improved	Old	
$E_{\bar{\nu}_e} < 14.3$ MeV	19.1%	10.2%	0.065%
$E_{\bar{\nu}_e} > 14.3$ MeV	25.2%	18.1%	0.3%

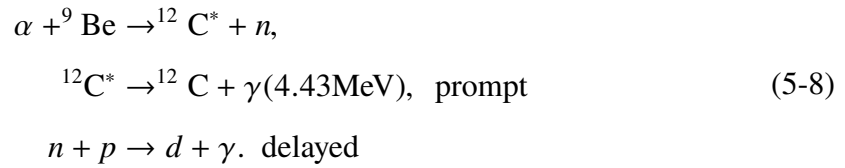
Figure 5.29 A comparison of neutron tag efficiency with the previous study<sup>[46]</sup>

### 5.3 Systematic Study with the Am/Be Source

To study the systematic uncertainty on the neutron tagging technique, we took neutron capture data in 2009 and 2016 with the neutron emitting calibration source of Am/Be.

#### Experimental Setup

Figure 5.30 shows the Am/Be source embedded in the center of a 5 cm cube of bismuth germanate oxide (BGO) scintillator. The emission of neutron is through the following processes with a prompt  $\gamma$  as the primary event,



where the incident  $\alpha$  is emitted from  ${}^{241}\text{Am}$ . A minor branch directly to the ground state of  ${}^{12}\text{C}$  produces a neutron without time correlation and is counted as background. The prompt  $\gamma$  triggers SHE signal, after which the AFT will cover 93% probability range of a neutron capture. On one hand, the existence of BGO compensated the low Cherenkov photon yield for 4.43 MeV  $\gamma$ 's; on the other hand, it may shade or distort the propagation and capture of neutron in water.

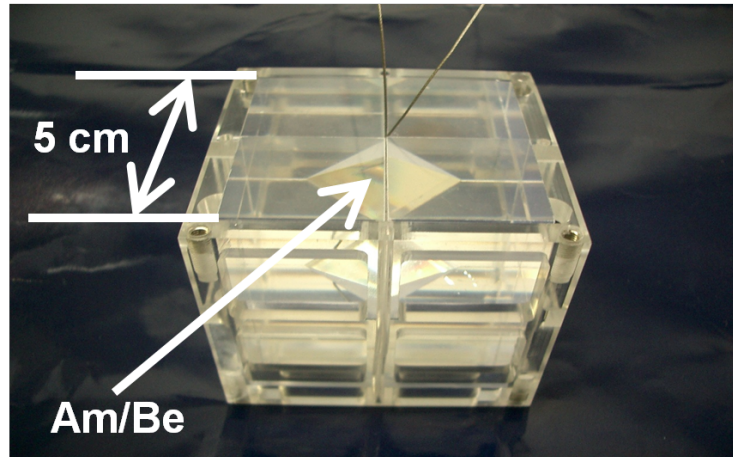


Figure 5.30 A photo of the Am/Be source.

The Am/Be source is placed via 2 different calibration holes into 3 different locations during the calibration data taking to study the position dependence of neutron tagging efficiency. Table 5.3 lists the detailed positions. During the data taking at position A, a 10 Hz random trigger data is also taken to evaluate both the source related and the accidental

background levels.

Table 5.3 Am/Be source positions.

Am/Be source	X position (cm)	Y position (cm)	Z position (cm)
A (Center)	35.3	-70.7	0.
B (Y-12)	35.3	-1201.9	0.
C (Z15)	35.3	-70.7	1500.

### Data Selection

This selection caters for the goodness of event, before any neutron selection is applied.

Events passing these selection criteria are counted as Am/Be events.

1. For the primary event:  $750 < \text{total p.e.} < 1,050$  at source A;  $850 < \text{total p.e.} < 1,150$  at source B;  $900 < \text{total p.e.} < 1,150$  at source C;
2. For the AFT event: if  $N_{200} > 50$ , the whole event is rejected;
3. Time difference between any two events is greater than 1.5 ms, to avoid events overlap.

### Efficiency Validation

Am/Be were taken twice in SK-IV, namely 2009 and 2016. SK hardware properties such as water quality and PMT gain, were changed significantly during this period and those differences are considered in MC production. Therefore, the difference between 2009 and 2016 result should be included in the systematic uncertainty.

In the Am/Be data analysis, the number of true 2.2 MeV neutron capture events was calculated by fitting the time distribution of tagged neutrons with an exponential distribution plus a constant component representing the backgrounds. As shown in Fig. 5.31, the time distribution of Am/Be data (black points) in position A (centre) was fitted (red line), with the left panel showing for 2009 Am/Be data and right panel for 2016. The best-fit parameters of  $\tau$  and efficiency are listed in Table 5.4. Similarly, for position B (Y-12) and position C (Z12), the time distributions are shown in Fig. 5.32 and Fig. 5.33 respectively. The best-fit results are listed in Table 5.5 and Table 5.6. The difference of signal efficiency between the MC and the Am/Be source is assigned as the systematic uncertainty of neutron tagging efficiency, which is 10%.

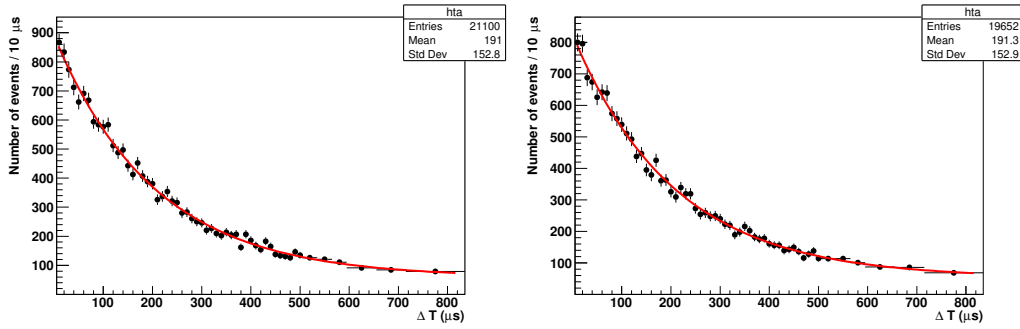


Figure 5.31 The time distribution of Am/Be data (black points) in position A (centre) is fitted (red line), with the left panel showing for 2009 Am/Be data and right panel for 2016 data.

Table 5.4 Comparisons of efficiencies and fit neutron lifetimes between MC simulation, the 2009, and the 2016 Am/Be data at position A.

Position A	MC	2009	2016
$\epsilon_S$	$19.1 \pm 0.2\%$	$18.3 \pm 0.2\%$	$17.9 \pm 0.2\%$
$\tau$		$203.9 \mu\text{s}$	$206.7 \mu\text{s}$

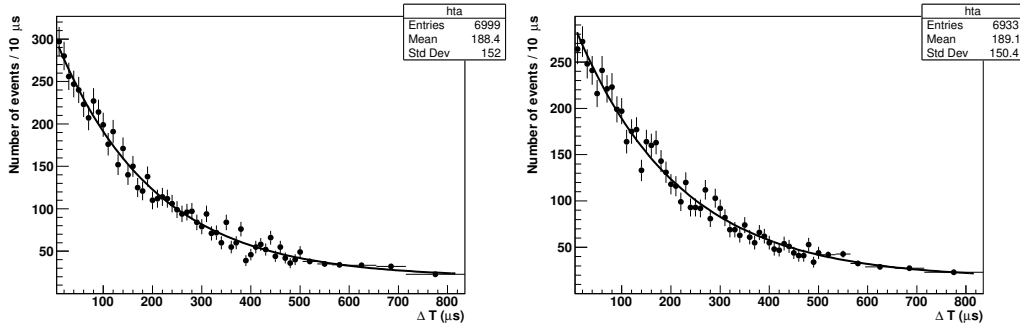


Figure 5.32 The time distribution of Am/Be data (black points) in position B (Y-12) is fitted (red line), with the left panel showing for 2009 Am/Be data and right panel for 2016 data.

Table 5.5 Comparisons of efficiencies and fit neutron lifetimes between MC simulation, the 2009, and the 2016 Am/Be data at position B.

Position B	MC	2009	2016
$\epsilon_S$	$23.4 \pm 0.2\%$	$20.7 \pm 0.4\%$	$20.9 \pm 0.4\%$
$\tau$		$197.7 \mu\text{s}$	$210.7 \mu\text{s}$

Table 5.6 Comparisons of efficiencies and fit neutron lifetimes between MC simulation, the 2009, and the 2016 Am/Be data at position C.

Position C	MC	2009	2016
$\epsilon_S$	$24.6 \pm 0.2\%$	$23.3 \pm 0.5\%$	$22.7 \pm 0.5\%$
$\tau$		$197.2 \mu\text{s}$	$198.9 \mu\text{s}$



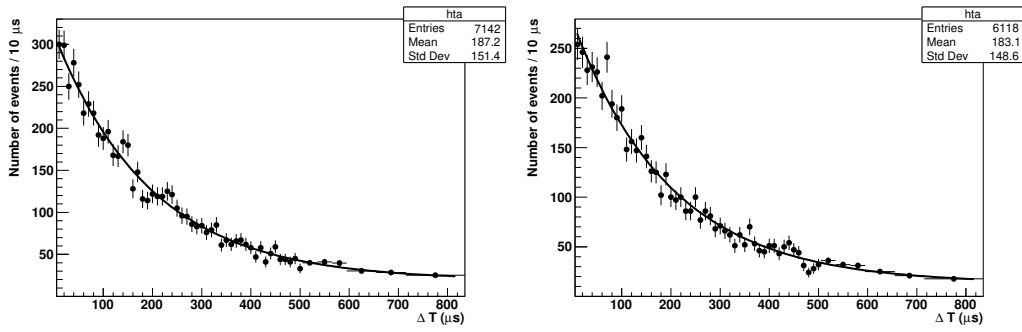


Figure 5.33 The time distribution of Am/Be data (black points) in position C (Z15) is fitted (red line), with the left panel showing for 2009 Am/Be data and right panel for 2016.

#### 5.4 Validation with Cosmogenic ${}^9\text{Li}$ Sample

A  ${}^9\text{Li}$  sample can be obtained by SK normal run data with the same first reduction and neutron tagging as those used in the SRN search. Tagging neutrons in the  ${}^9\text{Li}$  sample not only measures the  ${}^9\text{Li}$  yield at SK, but also validates the neutron tagging technique itself.

We applied the neutron tagging method to the  ${}^9\text{Li}$  sample corresponding to 1886 days live-time. The cut was set at the background level of 0.065% for  $E < 14.6$  MeV. The distribution of time difference between the tagged neutron and the prompt  $\beta$  signal is shown in Fig. 5.34. Also shown is the prompt energy distribution.

Due to the limited statistics in the present  ${}^9\text{Li}$  sample, two different fits were performed, either with a fixed background estimated from accidental level, or with a fixed lifetime of  $\tau = 204.8 \mu\text{s}$ <sup>[94]</sup>. With a fixed background level, the neutron tagging lifetime was fit to be  $\tau = 251.5 \pm 33.1 \mu\text{s}$ , and the number of tagged  $\beta + n$   ${}^9\text{Li}$  events was  $246.6 \pm 23.2$ , as shown in Fig. 5.34. With a fixed neutron lifetime at  $\tau = 204.8 \mu\text{s}$ , the fitted number of tagged  $\beta + n$   ${}^9\text{Li}$  events was found to be  $214.0 \pm 25.6$ , agreeing with the fixed background level result within  $1 \sigma$ . Compared to described in Ref.<sup>[46]</sup>, an obvious improvement from the previous fitting in both the lifetime result of neutron tagging and the uncertainty on the  ${}^9\text{Li}$  yield evaluation.

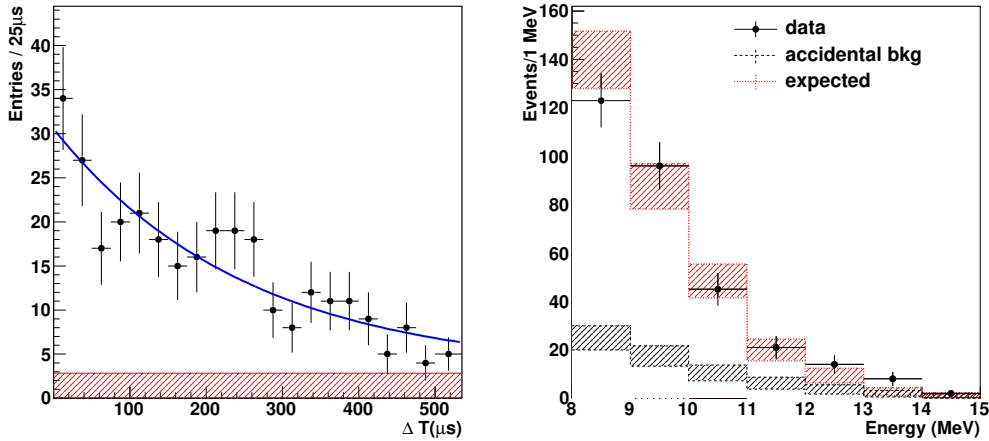


Figure 5.34 Neutron tagging result for  ${}^9\text{Li}$  sample of 1886 days in SK-IV. The left figure shows the time difference between the tagged neutron and the primary event. The right figure shows the energy of primary events with tagged neutrons.

## 5.5 Cut Optimization and Efficiency Evaluation

Previously in this section we applied the neutron cut by two steps: the pre-selection cut and the multi-variable analysis cut, also called the neural network cut, or MLP cut. The pre-selection is a stand-alone cut, while the neural network cut is applied as a step-function, with 2 distinct cuts below and above the energy 13 MeV, or neutrino energy 14.3 MeV. It works under the assumption that the background rates changes drastically below and above 13 MeV. Further optimization is performed to take into consideration the expected backgrounds and signals in each energy bin.

To determine a cut, only MC result can be used to provide efficiency and significance information. Background rates within each energy bin are estimated by MC, with more discussion in Section 6.1. For the signal estimation, due to the very low SRN flux expected from SRN models, and to avoid the model-dependence, we assume null signal here, just to obtain optimized values for the neutron cuts. In this case, the upper limit can be derived as a function of the neural network cut value. Two examples are shown in Fig. 5.35 for the 11 MeV bin and the 17 MeV bin. The optimized MLP cut values are 0.98 and 0.55, respectively.

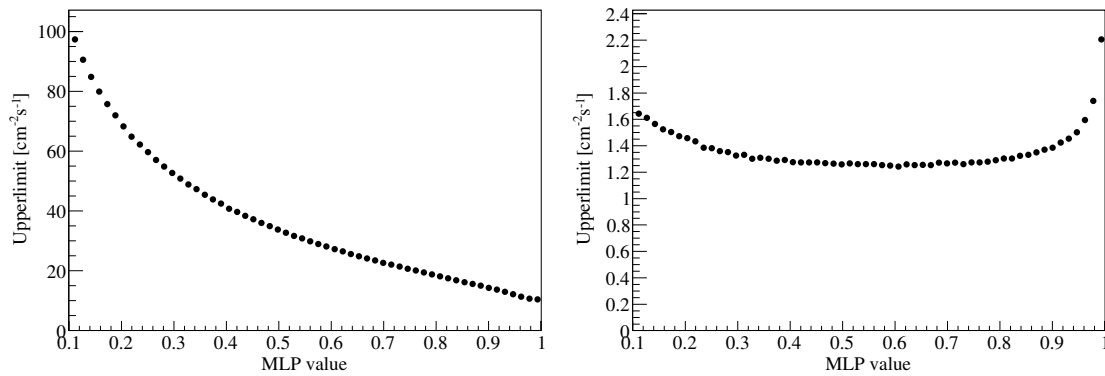


Figure 5.35 The upper limit calculated as a function of the MLP cut value for the 11 MeV bin and the 17 MeV bin.

Using the same method for each energy bin between 8 MeV and 30 MeV, the optimized cut values were obtained, and the efficiency was evaluated from the SRN MC sample, as shown in Fig. 5.36. The previous step function used as the neutron tagging cut is also shown in blue lines on the left figure, with overall signal efficiency at 8.8%<sup>[46]</sup> and 44 events remaining. After optimization, the cut values and efficiencies are shown in black points, with overall signal efficiency at 19.3% and 29 events remaining. The overall signal efficiency and background rejection is significantly improved.

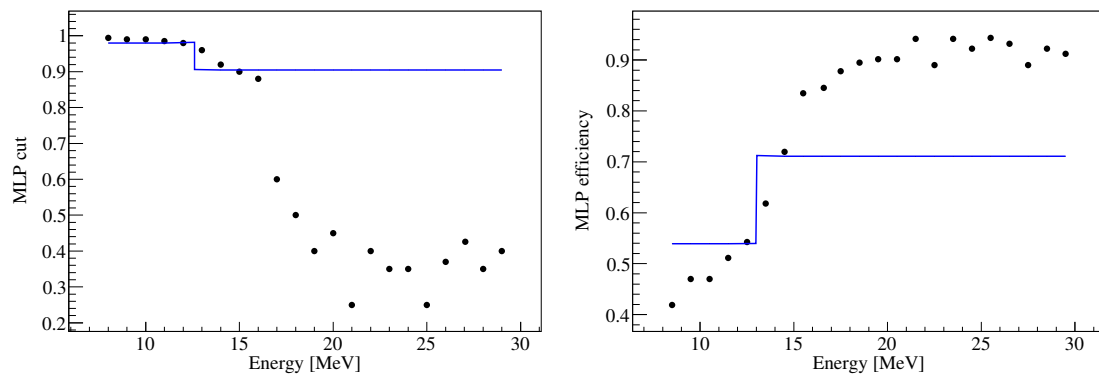


Figure 5.36 The cut values and corresponding efficiencies as a function of energy before and after the optimization.

## Chapter 6 SRN Analysis and Result at SK

This chapter presents the author's work in SRN analysis. We give the background estimation, the SRN candidate events at SK-IV, and the upper limit for SRN flux.

### 6.1 Background Estimation

Table 6.1 summarizes the estimation for each background in the final SRN sample. The method to evaluate the background are also listed. Detailed descriptions will be presented in the following sections.

Table 6.1 Background estimation in the final SRN sample.

Components	Number of Events	Estimation Method
Accidental	$14.2 \pm 1.2$	Ntag algorithm
Atm. NC	$10.0 \pm 4.1$	NC sample
Atm. CC	$5.6 \pm 1.2$	MC
Li9	$3.3 \pm 0.9$	Spallation sample
Reactor	$0.7 \pm 0.2$	KamLAND data
Total	$33.7 \pm 4.6$	

#### 6.1.1 Accidental Backgrounds

Accidental backgrounds are single signals that accidentally form a coincidence pair to mimic the IBD event. This background mainly arises from the low light yield of neutron capture signal in water. To keep a reasonable signal efficiency, we have to tolerate the accidental contamination in the data sample. This background has been explained in detail in Chapter 5.

The systematic uncertainty on the estimation of this background is purely from the neutron tagging method itself, and was evaluated as 10%.

#### 6.1.2 Atmospheric NC

Atmospheric neutrinos contaminate the final data sample through the NC and CC channels, which produce events with similar signatures as IBD events. NC background

can be estimated from MC, as to be discussed in Chapter 7. To reduce the dependence on nuclear interaction models, we employed a data-driven side-band method instead in this analysis.

The mechanism of NC interaction from atmospheric neutrinos on oxygen will be explained in Chapter 7. The signature of NC events is the de-excitation  $\gamma$ 's. The de-excitation  $\gamma$ 's are sometimes accompanied by neutrons knocked out from the oxygen nucleus, forming a coincidence signal mimicking the IBD pair. For the low energy  $\gamma$  events or multi- $\gamma$  events, the Cherenkov angle of the primary event is expected to be reconstructed above  $42^\circ$ , as explained in Section 7.3.1.1. Therefore, the side-band above  $42^\circ$  can be used as a control sample to evaluate the atmospheric NC backgrounds in the data sample. To avoid the resolution effect of Cherenkov angle reconstruction, the side-band used for NC estimation is defined as the Cherenkov angle range  $[78^\circ, 90^\circ]$ . The contamination of atmospheric NC in the SRN data sample is shown in Fig. 6.1.

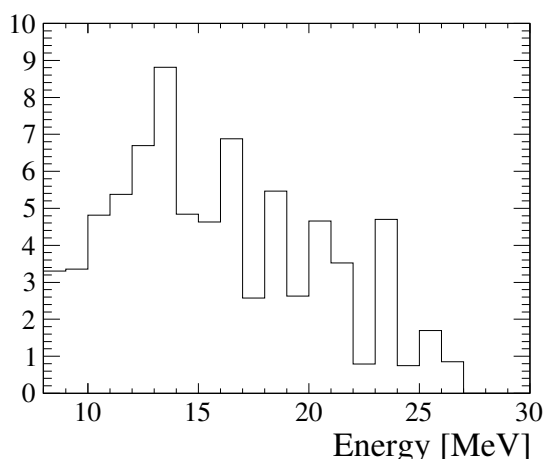


Figure 6.1 The energy spectrum for atmospheric NC events in the SRN sample.

The uncertainty for NC background is 41% as estimated by the NC analysis in Chapter 7, averaging between the upper and the lower uncertainty ranges.

### 6.1.3 Atmospheric CC

The charge current interaction of neutrinos on a proton is rather well understood, and in this case we estimate this background by MC. Atmospheric charged current backgrounds originate from low energy  $\bar{\nu}_e$ 's and  $\bar{\nu}_\mu$ 's in atmospheric neutrinos. For  $\bar{\nu}_e$ 's, this background directly comes from the IBD interaction. The cross section as well as the correlation between the incident neutrino energy and the positron energy follows discussion

in Section 1.2. The contribution of  $\bar{\nu}_e$ 's in the SRN sample is shown in Fig. 6.2. For  $\bar{\nu}_\mu$ 's, however, the prompt signal in the coincidence pair is actually the decay electron from the muon produced via CC. To produce a muon, the neutrino energy  $E_\nu$  must be above 105.7 MeV. Furthermore, if the muon is an invisible muon in water, i.e., its energy is below the Cherenkov threshold of muons in water, it will pass the reduction cuts. In this case, the neutrino energy is required to be less than 160 MeV. The contribution of  $\bar{\nu}_\mu$ 's in the SRN sample is shown in Fig. 6.3.

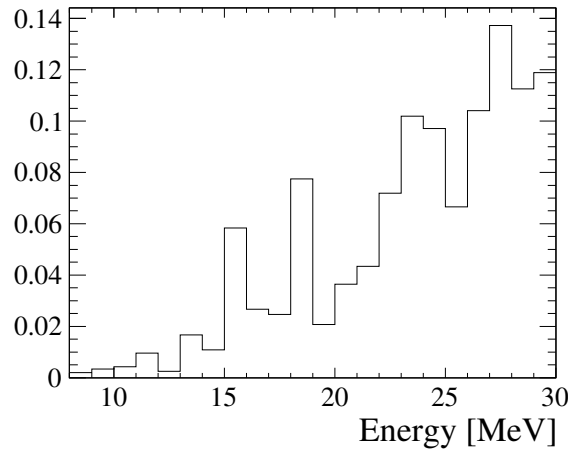


Figure 6.2 The energy spectrum for atmospheric CC from  $\bar{\nu}_e$ 's in the SRN sample.

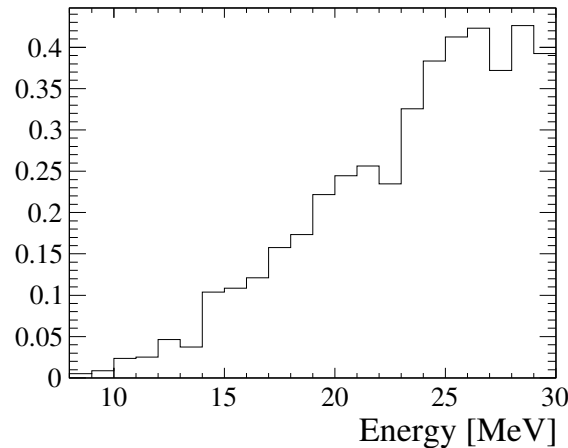


Figure 6.3 The energy spectrum for atmospheric CC from  $\bar{\nu}_\mu$ 's in the SRN sample.

The uncertainties are mainly due to the atmospheric neutrino flux prediction as well as the neutron tagging efficiency evaluation. Above 160 MeV, the atmospheric neutrino energy spectrum is well-described by theoretical models<sup>[99,100]</sup> and constrained

by measurements<sup>[101]</sup>. However, the spectrum below 160 MeV has not yet been measured, and this analysis employs a simulation from FLUKA<sup>[102]</sup>, which give a prediction assuming an approximately flat extension<sup>[103]</sup>.

#### 6.1.4 Spallation Backgrounds

Most spallation backgrounds induced by cosmic ray muons do not produce neutrons, and are thus classified as accidentals. The only spallation background leaking into the final data sample is from  ${}^9\text{Li}$ , which can emit a beta and a neutron, perfectly mimicking the signature of IBD signal.

This background is estimated by a spallation sample as explained in Section 5.4. By tagging the neutron in the spallation sample, and applying the efficiencies of other cuts, we evaluated the number of spallation events in the final sample. More details can be found in Ref.<sup>[52]</sup>. The systematics are mainly from the statistics of the spallation sample as well as the data reduction procedures.

#### 6.1.5 Reactor Neutrinos

Reactor neutrinos originate from nuclear power plants near the Kamioka Observatory. The reactor operation data can be found in the IAEA data base<sup>[104]</sup>. The contribution from reactor neutrinos can be calculated taking into consideration the oscillation effect, as we did in Chapter 8.

To follow the data-driven style of background estimation in this analysis, we estimated the reactor neutrino background by the IBD data provided by KamLAND, another neutrino experiment at the Kamioka Observatory. They can provide the reactor neutrino flux on a daily basis covering the entire SK-IV period. We integrated the flux and scaled it according to the live-time by different energy ranges with different live-times.

The systematic estimation followed the previous analysis<sup>[46]</sup>.

## 6.2 Candidate Events

In this analysis, we employed 2,778 (1,886) days of data from 2008 to 2018 in SK-IV. In the whole 2,778 days of data, events within the energy window [11.3, 31.3] MeV were analyzed. Due to the modification of software trigger system in 2011, the energy threshold for an SHE trigger was lowered from 70 hits to 58 hits, enabling the

neutron tagging analysis for the [9.3, 11.3] MeV region. Therefore, 1,886 days of data were analyzed for this energy range.

After the data reduction and neutron tagging, in the final sample for the SRN analysis, 29 events were observed, in good agreement with the expectation of  $33.7 \pm 4.6$  background events. Figure 6.4 shows the energy distribution of these events against the expectations of backgrounds. The time difference between the primary event and the neutron signal is shown in Fig. 6.5. The statistics is not significant, and the fitted neutron capture lifetime in Fig. 6.5 is  $\tau = 204 \pm 130 \mu\text{s}$ , consistent with the expected neutron capture lifetime in water<sup>[94]</sup>. Therefore we validated the estimation of the number of accidental background in the final SRN sample.

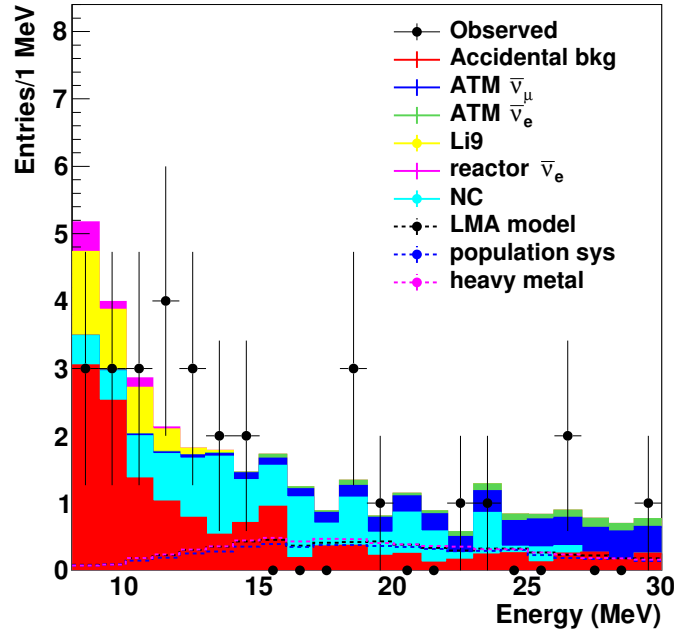


Figure 6.4 The energy spectrum for SRN sample.

### 6.3 Model-Independent Upper Limit

The number of observed events was statistically consistent with the null-signal hypothesis. In the absence of signal, an upper limit of SRN flux was derived. To compare with results from other experiments, we estimated the upper limit for 90% C.L..

Based on present background estimations, this upper limit can be calculated in a model-independent way, setting different limits for different energy bins. The upper limit



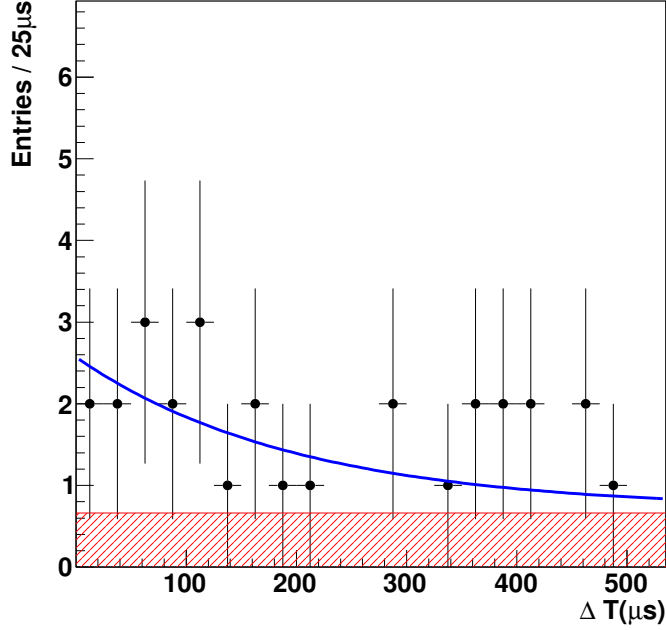


Figure 6.5 The neutron capture time distribution for SRN sample.

in each bin was derived by Rolke method<sup>[105]</sup>. It suits the case of a Poisson distributed signal with a Poisson or Gaussian distributed background, thus caters for the systematics in the background estimation. Moreover, the efficiency was also modeled with a Binomial or a Gaussian distribution. We used the Rolke method implemented in the ROOT toolkit<sup>[106]</sup> in our estimation for the upper limit.

The upper limit for the number of events in each bin was interpreted into the upper limit for the SRN flux by

$$\phi_{90} = \frac{N_{90}}{T \cdot N_p \cdot \bar{\sigma}_{IBD} \cdot \epsilon}, \quad (6-1)$$

where  $\phi_{90}$  refers to the upper limit of the SRN flux and  $N_{90}$  refers to the upper limit of number of events calculated by the Rolke method.  $T$  is the live-time for the data sample used in this bin, either 1,886 days or 2,778 days.  $N_p$  is the number of target protons calculated from the fiducial mass,  $N_p = 1.5 \times 10^{33}$ .  $\bar{\sigma}_{IBD}$  is the IBD cross section, and  $\epsilon$  is the total signal efficiency.

The previous SRN flux upper limit was mainly constrained by KamLAND in the lower energy range below 16 MeV and by SK-I/II/III result above 16 MeV, as shown in Fig. 6.6. Compared to the previous experimental results, this analysis gives a better constraint below 16 MeV, and comparable upper limit with the SK spectrum analysis

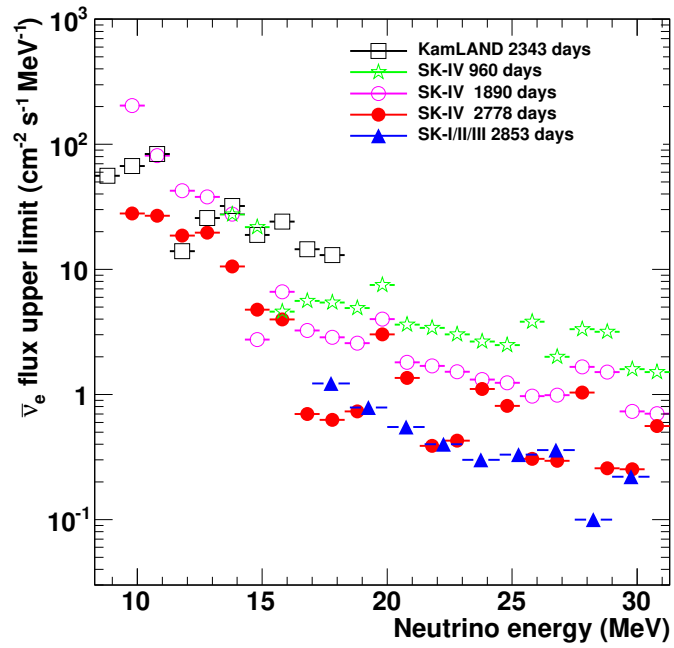


Figure 6.6 Upper limits derived by different experiments and analyses.

above 16 MeV.

## Chapter 7 NCQE Analysis at SK

Neutral current interactions from atmospheric neutrinos on  $^{16}\text{O}$  forms one of the major backgrounds for the supernova relic neutrino search in water Cherenkov detectors like Super-Kamiokande. This background in SRN search is found to be dominated by the quasi-elastic (NCQE) scattering with nucleons inside  $^{16}\text{O}$  nuclei. In this section we first introduce the NC channels including NCQE, and then describe the Monte-Carlo simulation for atmospheric neutrino NC channels. Using the features provided by MC, we can extract the NC sample from data and compare them against MC. Finally we present a measurement of NCQE cross section for atmospheric neutrinos in SK-IV.

### 7.1 Introduction and Motivation

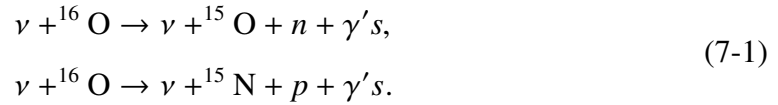
NC signal events in the SRN search window (8-30 MeV) must contain a primary event and a delayed 2.2 MeV neutron capture event. If the neutron capture is absent, it may still form a background by accidental coincidence but will not be classified as NC and will be included in accidental background. The main contribution in NC backgrounds is from NCQE channel. The primary trigger of an NCQE event is typically from a de-excitation gamma of the oxygen nucleus, and leaks into the SRN sample via the resolution effect of Cherenkov angle reconstruction. The delayed neutron is usually a true neutron knocked out by the incident neutrino. This will be further discussed in the section for the event simulation.

The idea of this study came after we tuned the neutron tagging cut bin by bin in the SRN search. By optimizing neutron tagging efficiency to the expected backgrounds for SRN, the efficiency in the lower energy range is decreased and the efficiency in the higher energy range is increased compared to the previous study at SK. The backgrounds in the lower energy range include reactor neutrinos (extending to  $\sim 10$  MeV), cosmogenic spallation  $^9\text{Li}$  (reaching  $\sim 15$  MeV), and accidental backgrounds of which the primary events are spallation singles (spreading the whole region but concentrate in below 15 MeV). The backgrounds in the higher energy range include atmospheric neutrino induced CC ( $\bar{\nu}_e$  and  $\bar{\nu}_\mu$ ) and NC. The physics mechanism of CC is clear, and the uncertainties in estimation are relatively low, while for NC, the previous SRN study at SK assigned 100% uncertainty for its estimation.

NC background was found to be the second largest background source in the search for SRN, next to accidental background, as discussed in Section 6.1. It requires a detailed study in NC and its main contamination channel in SRN sample, i.e., NCQE. This study is also crucial for the future SRN search, especially if SK is going to be loaded with Gadolinium<sup>[107]</sup>. With Gd, the neutron tagging does not introduce as much accidental background as without Gd, while the NCQE backgrounds usually produce true neutrons, thereby not reducible. This measurement will also pave the way for SRN detection in Hyper-K<sup>[108]</sup>. Further possible applications of this measurement are described in the end of this section.

### 7.1.1 Atmospheric NCQE as the SRN Background

Neutral current quasi-elastic interactions of atmospheric neutrinos with  $^{16}\text{O}$  produces de-excitation  $\gamma$ 's and emitted nucleons, which can be used as signatures to identify these events. The process can be written as



For high energy incident neutrinos, the emitted nucleons from the primary process typically have several hundred MeVs of energy and can continue to collide on other  $^{16}\text{O}$  nuclei. This is called as secondary processes, which will produce secondary  $\gamma$ 's and nucleons by the decay of excited  $^{16}\text{O}$ .

Because of the emission of low energy  $\gamma$  rays and the production of neutrons mimicking IBD signal pairs, NCQE events are the major component of NC backgrounds within the "golden" SRN search window of 8-30 MeV. In scintillator detectors, NCQE events will form an irreducible background due to the inability to identify signals of positron and  $\gamma$ 's. In Cherenkov detectors, however, the majority of NCQE  $\gamma$ 's can be distinguished by their larger Cherenkov angles, though a considerable amount of remnant can still leak into the SRN sample through the reconstruction resolution. NCQE  $\gamma$ 's sneak into the SRN sample above 8 MeV through the single high energy de-excitation channels, the energy resolution effect, and multiple  $\gamma$ 's from secondary processes. Based on the Cherenkov angle distribution, we present a study of atmospheric neutrino NCQE events detection and cross section measurement.

### 7.1.2 Further Applications

NCQE channel is also important for the low energy case. With energy region from 20 to 30 MeV, NCQE can be used to detect supernova burst neutrino<sup>[109]</sup>. Because this channel is NC, it provides additional flavor information on SN neutrinos and thereby helps to constrain different SN models<sup>[110,111]</sup>.

## 7.2 Monte-Carlo Simulation

Monte-Carlo (MC) simulation of atmospheric neutrino events was done in two stages. First, an event generator models the interactions of atmospheric neutrinos in water. The atmospheric neutrino flux is taken as the input for this step and the output is a series of final state particles. For example, in the case of NCQE channel, the output could be a de-excited nucleus, a de-excitation  $\gamma$ , and a knocked nucleus. Then, subsequent particle is tracked within ID and the detector response is simulated.

This analysis used the official MC sample by the atmospheric neutrino analysis group at SK. This sample was generated for 500 years of live-time with the SK-IV detector setup, including both the FC (full contained) and the PC (partial contained) events. The UPMU (upward-going muon neutrino) sample is not necessary in this study, since these events enter the tank as muons and will be removed by the OD trigger and spallation reduction.

### 7.2.1 Atmospheric Neutrino Flux

Super-Kamiokande performed a comprehensive study of atmospheric neutrino flux in the energy region from sub-GeV up to several TeV in Kamioka Observatory<sup>[101]</sup>. The measured observables include flux, energy spectrum, and directionality. All these measurements are in good agreement with the theoretical prediction from Honda et.al<sup>[99,100]</sup>. In this thesis, we took the HHKM model as the input for the atmospheric neutrino model, which is also the default atmospheric neutrino model in the MC sample, i.e., no weight is applied. For the systematic study, the flux uncertainty is taken from the previous SK measurement, as shown in Fig. 7.1. The neutrino ratio uncertainty is derived from the theoretical prediction of Honda model. The neutrino-antineutrino ratio used in this study is shown in Fig. 7.2.

We do not consider atmospheric neutrinos above TeV level due to the negligible flux. For atmospheric neutrinos below 160 MeV (the lowest bin in SK atmospheric neutrino

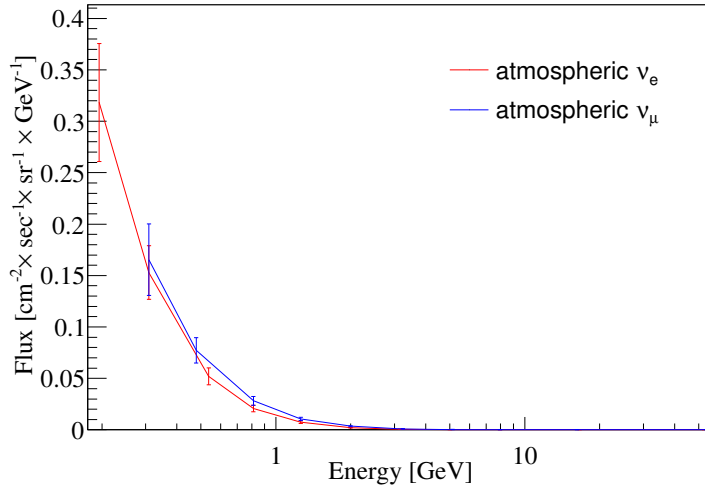


Figure 7.1 Atmospheric neutrino flux measured at SK.

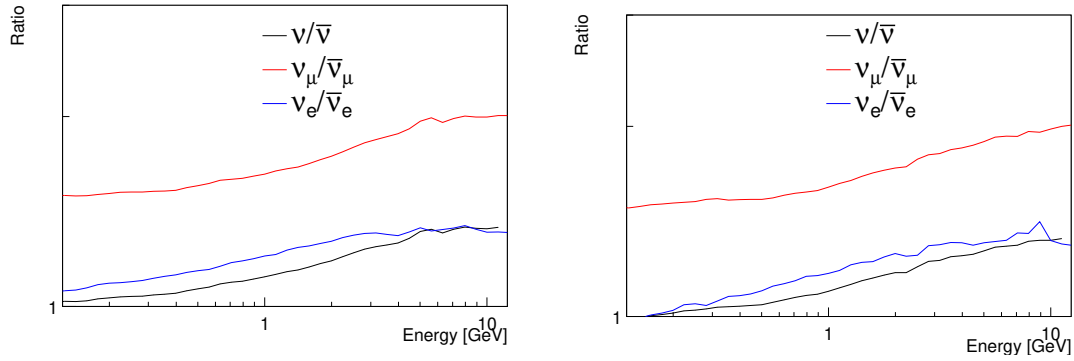


Figure 7.2 Atmospheric neutrino-antineutrino ratios predicted by Honda models HHKM06 (left) and HHKM11 (right).

measurement<sup>[101]</sup>, no experimental data is available, and a simulated result from FLUKA is used<sup>[103]</sup>.

## 7.2.2 Neutrino Interactions

Atmospheric neutrino interactions with constituents of water molecules at SK is simulated by the NEUT generator<sup>[112]</sup>. In general, there is no up-to-date publication or internal technical note for NEUT. The following description of the neutrino interactions is a review based on several previous SK/T2K collaborators' PhD thesis<sup>[113,114]</sup> and a direct contact with NEUT author Hayato<sup>[112]</sup>.

### 7.2.2.1 NCQE Simulation

Based on Ankowski's model<sup>[15]</sup>, the NCQE cross section on oxygen in NEUT is simulated by a oxygen spectral function model<sup>[115]</sup> with the BBBA05 form factor<sup>[116]</sup>,

taking into consideration the Pauli blocking effect at  $pF = 225 \text{ MeV}/c$ . NEUT well reproduces the Ankowski result<sup>[15]</sup>, and also provides additional information on kinematics which cannot be directly subtracted from the model. The nucleon breakdown cross sections as a function of neutrino energy for neutrinos and anti-neutrinos are shown in Fig. 7.3.

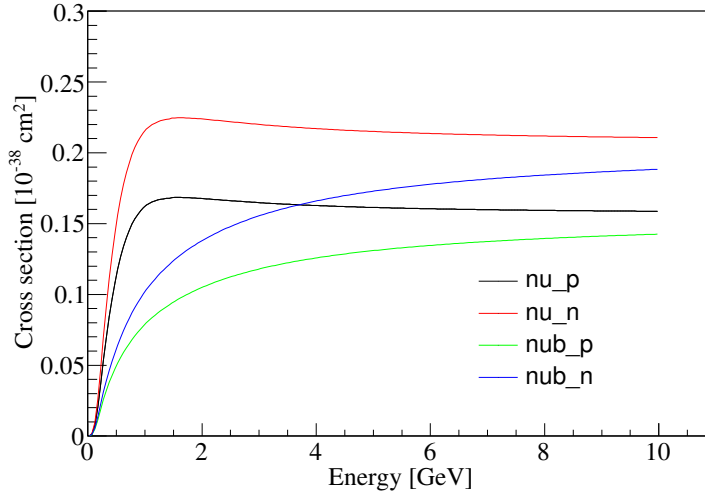


Figure 7.3 Nucleon breakdown cross sections for the NCQE process as a function of neutrino energy.

The remnant excited oxygen nucleus exists with a single hole in  $1p_{1/2}$ ,  $1p_{3/2}$  or  $1s_{1/2}$  state in the simple shell model. Among these final states, the excitation energy levels with gamma emission (and corresponding gamma emission branching ratio) for the state  $1p_{3/2}$  include 6.32 MeV (86.5%) or 9.93 MeV (4.9%) in the case of a proton knock-out, and 6.18 MeV (86.9%) in the case of a neutron knock-out. Therefore, the main signature for NCQE events is a  $\sim 6 \text{ MeV}$  gamma. The de-excitation channels in single-hole states are summarized in Fig. 7.4. Other decay channels include further nucleon emission. The de-excitation from the state  $1s_{1/2}$  is complicated with both de-excitation gamma and additional nucleon emission. We used the data from the  $^{16}\text{O}(p, 2p)^{15}\text{N}$  experiment RCNP-E148<sup>[117]</sup>. Continuum states are assumed to have no gamma emission, while the normal gamma emission assumption is also calculated and included in the systematic study.

#### 7.2.2.2 Detector Simulation

The following processes of transportation, Cherenkov light emission, possible secondary processes, and the detector response are simulated in the GEANT3<sup>[118]</sup> based SK detector simulation package SKDETSIM. In this study, we used the ATMPD group official

Residual isotope	Energy level (MeV)	$J^\pi$	$E_\gamma$ (MeV)	$E_p$ (MeV)	Ratio	$\text{Br}(X_i^* \rightarrow \gamma + Y)$
$^{15}\text{N}$	6.32	$3/2^-$	6.32	—	100%	86.2%
	9.93	$3/2^-$	5.30	—	15.3%	1.1%
			6.32	—	4.9%	0.3%
			7.30	—	2.1%	0.1%
			9.93	—	77.6%	5.4%
10.70	$3/2^-$	—	0.5	—	6.9%	
$^{15}\text{O}$	6.18	$3/2^-$	6.18	—	100%	100%

Figure 7.4 De-excitation modes of  $^{16}\text{O}$  proton hole  $(p_{3/2})_p^{-1}$  and neutron hole  $(p_{3/2})_n$  states<sup>[113]</sup>.

MC. The gain increasing was not implemented in this version, and the gain variation in data was taken into account by the LOWE group reconstruction tool.

The secondary process is illustrated in Fig. 7.5. For the secondary gamma production, there is no available experimental data yet, and the simulation was done by the GCALOR package of GEANT3<sup>[119]</sup>. In the GCALOR, the simulation package NMTC and MICAP are used for hadronic reactions covering the energy of knock-out nucleons in NCQE processes from atmospheric neutrinos. NMTC simulates protons in all energies and neutrons above 20 MeV, while MICAP simulates neutrons below 20 MeV. Some discontinuity is seen at the cutoff and taken as the systematic uncertainty.

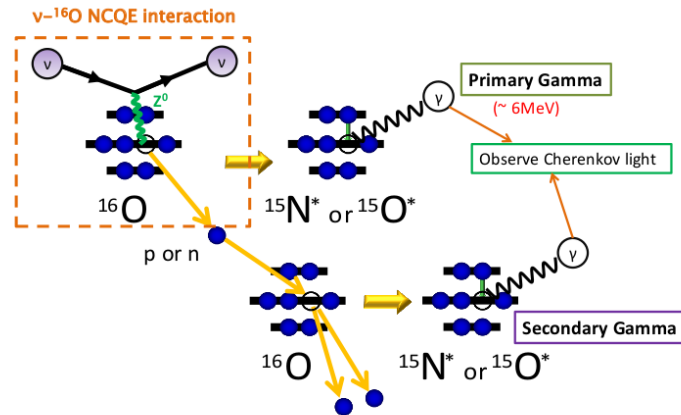


Figure 7.5 An illustration for NCQE primary and secondary processes<sup>[114]</sup>.

### 7.2.3 Other NC Channels

In principal, all the NC channels were included in our MC. The second leading NC channel after NCQE in the MC sample is single pion ( $\text{NC}1\pi$ ), dominated by  $\text{NC}1\pi$  from delta resonance. The third place goes to the multi-pion production channel. The primary signals from these events are de-excitation gamma's after pion absorption on oxygen. If the



produced pion is absorbed before going out of the nucleus, it will be simulated by NEUT. When the produced pion goes out of the nucleus and propagate in water before being absorbed by another oxygen nucleus, it will be simulated in SKDETSIM, i.e., GEANT3 packages.

#### 7.2.4 MC Reconstruction and Reduction

The reconstruction of MC was done by the low group reconstruction tools. BONSAI<sup>[120]</sup> was employed for the vertex reconstruction. The energy reconstruction was performed by calculating the so-called  $N_{\text{eff}}$ , i.e., the effective hits for an event, as discussed in Section 3.3.3.1. Afterwards, the low energy events were processed with the Cherenkov reconstruction tool by combining every 3 hits to derive open angles and to look for the peak of open angle distribution.

The MC reduction was performed in the same way as the data reduction except for the spallation cut and the solar cut. For MC, due to the independence of the atmospheric neutrino MC from muon events, the spallation cut was directly applied as the event weight, i.e., only efficiency was multiplied to calculate the number of events.

### 7.3 Data Reduction and Neutron Tagging

A sample with 2,778 (1,886) days live-time at SK-IV was used in this analysis. The upper bound of energy for the NC sample was set at 30 MeV, where the de-excitation gamma can hardly reach even with the energy resolution effect and where the atmospheric charged current (CC) background also starts to increase as the energy approaches the Michel peak of the decay electrons from muons.

#### 7.3.1 Data Reduction

One of the main motivations for the atmospheric neutrino NC study is to determine the NC events in the SRN search. In SRN study, many strict reductions were applied to remove possible backgrounds, and most of them also worked to make a clean NC sample, as described in Chapter 4. Similarly, these cuts were applied to select NCQE events from the low-energy data sample except for the Cherenkov angle cut.

### 7.3.1.1 Cherenkov Angle Cut

The algorithm of Cherenkov angle reconstruction has been described in Chapter 3.3. The Cherenkov angle of an electron above the threshold is  $42^\circ$ , while for a pion or muons below 30 MeV, the opening angle is less than  $42^\circ$ . On the contrary, the Cherenkov light distribution of NCQE de-excitation gamma's is more uniform, and the corresponding opening angle is consequently reconstructed above  $50^\circ$ , as shown in Fig. 7.6.

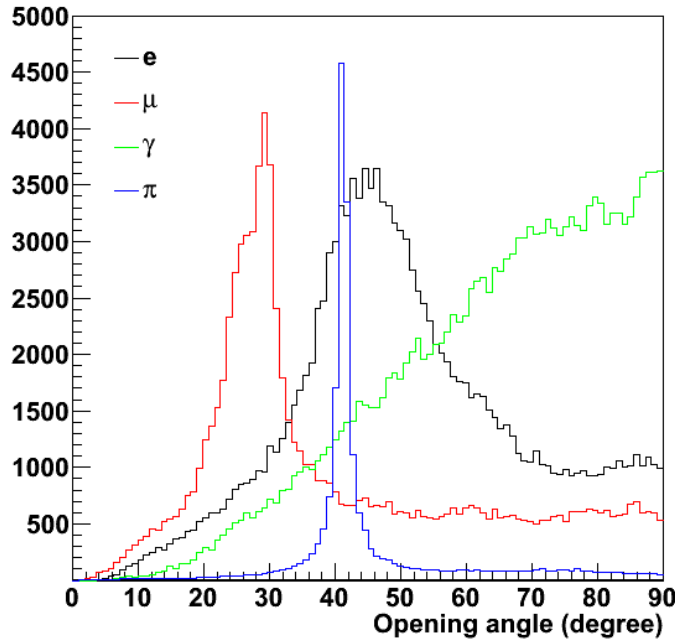


Figure 7.6 The distributions of reconstructed Cherenkov angles for  $e$ 's,  $\mu$ 's,  $\gamma$ 's and  $\pi$ 's.

The angle distribution after the neutron tagging required can be seen in Fig. 7.7, together with MC predictions. Therefore, taking into consideration the resolution effect, we applied a Cherenkov angle cut of  $50^\circ$ , which results in the efficiency of  $\sim 86\%$ .

### 7.3.2 Neutron Tagging for NCQE Events

NCQE events for GeV and sub-GeV neutrinos are likely to knock out a nucleon from the nucleus. Knocked-out neutrons will propagate in water and thermalize. This process is invisible in the sense of Cherenkov light. The thermalized neutrons are then captured on hydrogen, emitting delayed 2.2 MeV gammas, which can be used to tag the NCQE events.

The algorithm for the neutron tagging is the same as the one described in Chapter 5

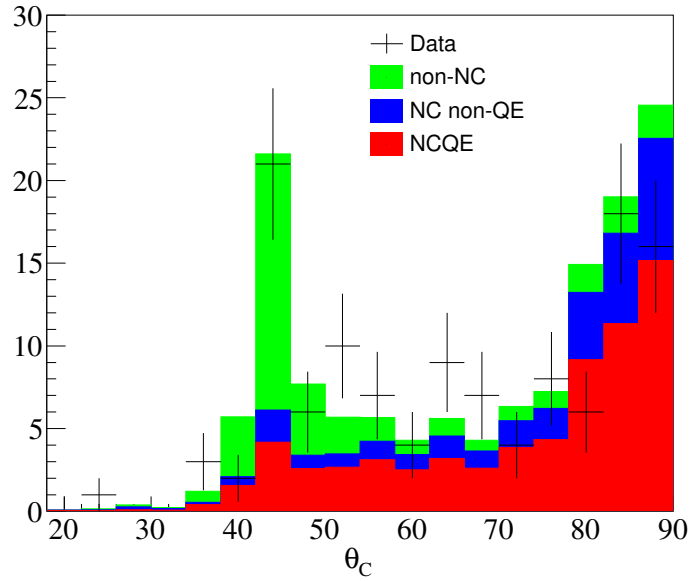


Figure 7.7 Cherenkov angle distributions for both the data and the MC expectation. All cuts are applied, except for the Cherenkov angle cut.

except for the treatment of the neutron travel distance. Since the TOF-subtracted time is corrected with regards to the primary vertex, the distance between primary vertex and neutron capture vertex becomes crucial in the determination of the neutron tagging efficiency. For IBD neutrons from SRN neutrinos, the neutron energy is sub-MeV, and the typical drift distance is less than 5 centimeters away from the primary vertex. However, for neutrons in the NC events, the neutron energy can reach up to several hundreds MeV, as shown in Fig. 7.8. The neutron tagging efficiency was correlated with the simulation of drift distance. Since the present SKDETSIM may not well simulate the neutron propagation process, a comparison between a GEANT4 toy-MC and SKDETSIM was performed, as shown in Fig. 7.8. The neutron tagging efficiencies for different steps in different simulation setups are shown in Table. 7.1. The difference between GEANT4 and SKDETSIM was assigned as the systematic uncertainty.

Table 7.1 Neutron tagging efficiencies for different steps in different simulation setups.

Process	Pre-cut	NN (15 MeV)
SRN	35.4%	71.1%
NC (GEANT4)	29.3%	60.8%
NC (SKDETSIM)	27.7%	57.7%

The neutron capture time for the NC sample after all reductions is shown in Fig. 7.10.

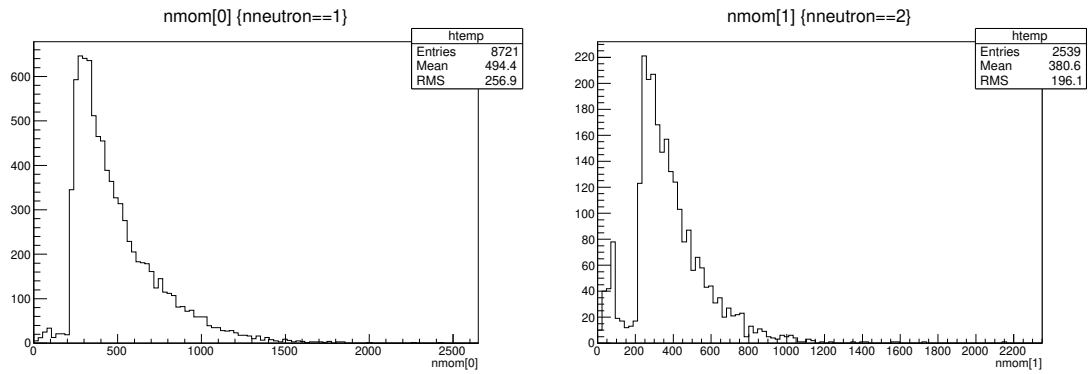


Figure 7.8 Neutron momentum from primary (left) and secondary (right) processes. Bumps in the low energy region is due to the neutrons emitted from the de-excitation of oxygen.

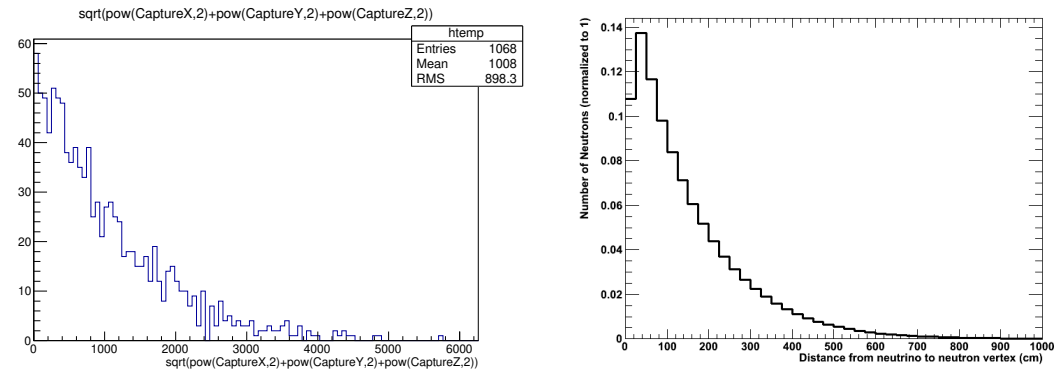


Figure 7.9 Distance from neutron production vertex to capture vertex. Left: toyMC using GEANT4 (primary only, mm, QGSP\_BERT\_HP + NeutronHP); right: skdetsim using GEANT3 (all processes, default, cm).

There are 89 remaining events in total, including true neutron events and accidental background events. The accidental event rate was estimated by using the same tagging criteria on the random trigger sample, and was calculated to be 13.7 events in this NC sample. Fitting the time difference distribution with an exponential signal and a fixed accidental background level, we obtained the total events with neutron as  $75.3 \pm 9.4$  and the life-time as  $219.5 \pm 47.2 \mu\text{s}$ , which is in good agreement with the expectation  $204.7 \mu\text{s}$ <sup>[121]</sup>. Using a fixed  $\tau$  at  $204.7 \mu\text{s}$  and fitting the time distribution again as a cross-check, we obtained  $68.5 \pm 12.1$  events with neutrons, which is statistically consistent with the result from the fixed background fitting. Neutron multiplicity comparison between data and MC is shown in Fig. 7.11. Good agreement is observed.

The total reduction efficiency for NCQE gamma events within [8, 30] MeV scaled to 2,778 days live-time is shown in Fig. 7.12. The main efficiency loss is due to the spallation cut and the neutron tagging. These cuts are tuned bin by bin towards the best significance

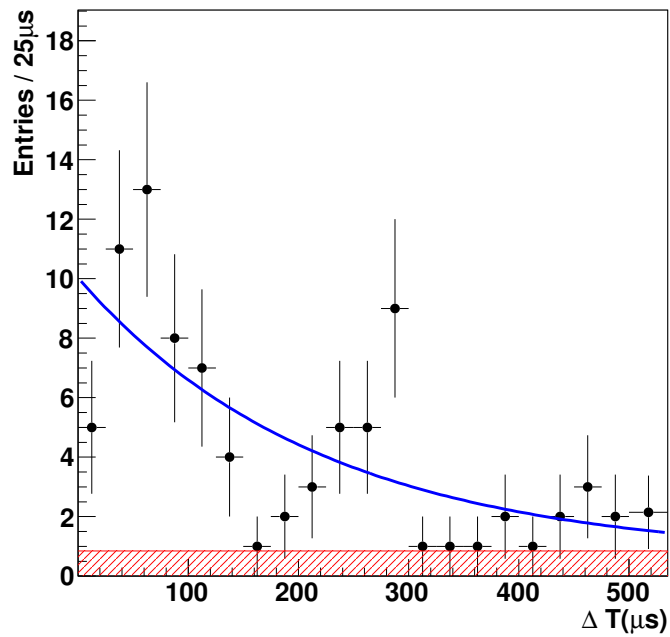


Figure 7.10 Neutron tagging time distribution.

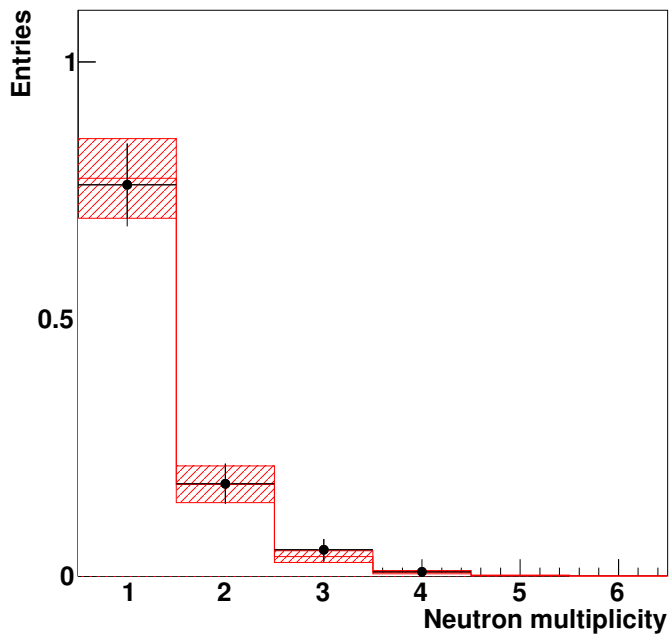


Figure 7.11 Neutron multiplicity in data (black points) and MC (red histogram). The uncertainties assigned to points are statistical while these assigned to histogram are the 10% intrinsic neutron tagging uncertainty.

at the null-signal expectation, putting an energy dependence on the final efficiency.

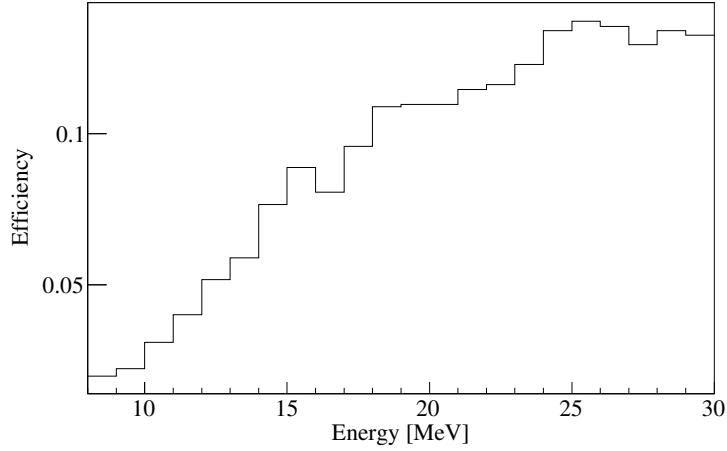


Figure 7.12 Reduction efficiency scaled to 2,778 days livetime. The energy dependence mainly comes from spallation cut (50% to 100%), ntag (4% to 22%), and the livetime difference (72% to 100%).

## 7.4 Analysis

The 89 events in our final data sample are from NCQE, NC other channels, neutron backgrounds including leakage from reactor neutrinos and spallation, and accidental backgrounds. To evaluate the contribution from non-NC and NC non-QE events, and to derive the NCQE cross section, we carried out a further analysis using both the MC and the data from the side-band region in the Cherenkov angle distribution.

### 7.4.1 Candidate Events

The vertex distribution in our NC sample is shown in Fig. 7.13. As expected, a good uniformity is observed. The energy distribution is shown in the upper panel in Fig. 7.14. The energy dependence of the signal efficiency is shown in Fig. 7.12.

In addition to the accidental background, non-NC backgrounds in the data sample include the leakage from spallations, the reactor neutrinos, as well as the atmospheric neutrino CC. The spallation background was estimated using a spallation data sample derived by the local proximity in both time and space<sup>[52]</sup>. The same cuts as in the NC study was then applied on this data sample. Consequently, the spallation background was estimated to be 0.5, mainly contributed by the cosmogenic  ${}^9\text{Li}$  background.

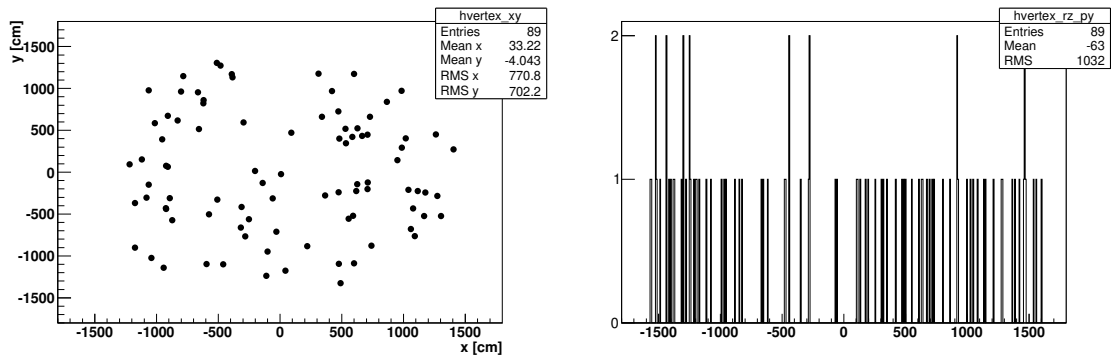


Figure 7.13 Vertex distributions of the NC sample.

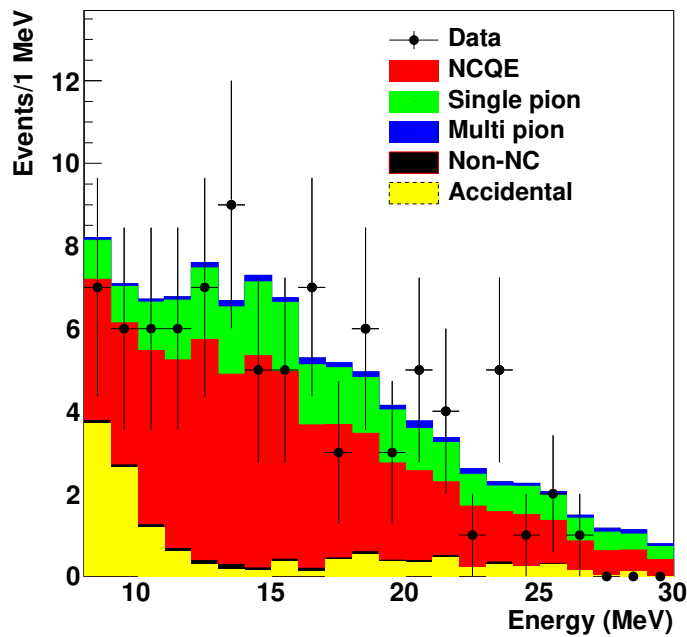


Figure 7.14 Energy distribution of the NC sample. The data is shown in black points with statistical uncertainty. The yellow histogram shows the accidental backgrounds. The red histogram shows the MC expectation of the NCQE events. The green and blue histograms represent the pion channels of NC backgrounds, and the black histogram shows the non-NC background.

Background from the reactor neutrinos are IBD positrons and their Cherenkov angle distribution is well understood. This background leaks into the NC sample through the effect of Cherenkov angle resolution and was estimated to be 0.1 event.

Atmospheric neutrino CC backgrounds include  $\nu_e$  CC and  $\nu_\mu$  CC. Their contribution was evaluated from the same MC batch as that for the NC events. Due to the neutron tagging cut, the leakage into the NC sample must originate from anti-neutrinos. This background was estimated from MC at 0.4 event for  $\bar{\nu}_e$  CC and 0.3 event for  $\bar{\nu}_\mu$  CC. The non-NC backgrounds are summarized in Table. 7.2.

Excluding the non-NC backgrounds, the total NC events in the data sample is estimated as  $74.0 \pm 9.4$ , which can be compared against MC predictions in NCQE and other NC channels, as listed in Table. 7.3.

Table 7.2 Break-down of background sources and contributions in the NC sample.

Components	Events
NC data	74.0
Accidental	13.7
Spallation	0.5
Reactor	0.1
$\bar{\nu}_e$ CC	0.4
$\bar{\nu}_\mu$ CC	0.3
Final sample	89

Table 7.3 Predictions for the processes in MC. A comparison to the NC data is also given.

Components	Events
NCQE	58.0
Single $\pi$	23.1
Multi $\pi$ 's	2.4
DIS	0.0
MC	83.5
NC Data	$74.0 \pm 9.4$



### 7.4.2 Cross section Calculation

The NCQE cross section was measured by comparing the data and the MC expectation. The theoretical prediction  $\langle \sigma_{\text{NCQE}}^{\text{theory}} \rangle$  can be expressed as:

$$\begin{aligned} \langle \sigma_{\text{NCQE}}^{\text{theory}} \rangle &= \frac{\int_{160 \text{ MeV}}^{10 \text{ GeV}} \sum_{i=\nu, \bar{\nu}} \phi_i(E_\nu) \times \sigma_i(E_\nu)_{\text{NCQE}}^{\text{theory}} dE_\nu}{\int_{160 \text{ MeV}}^{10 \text{ GeV}} \sum_{i=\nu, \bar{\nu}} \phi_i(E_\nu) dE_\nu} \\ &= 1.14 \times 10^{-38} \text{ cm}^2, \end{aligned} \quad (7-2)$$

where  $\phi_i(E_\nu)$  is the atmospheric neutrino flux at neutrino energy  $E_\nu$ ,  $\sigma_i(E_\nu)$  is the corresponding theoretical cross section, and  $i$  sums for neutrino and anti-neutrino species. The energy integral was performed between 160 MeV and 10 GeV, above which the atmospheric neutrino flux is trivial, and below which the NCQE gamma cross section with a neutron is negligible. The systematic uncertainty introduced by this energy cutoff was evaluated and included in the systematic analysis in following context. The measured cross section is therefore expressed as:

$$\begin{aligned} \langle \sigma_{\text{NCQE}}^{\text{observed}} \rangle &\approx \frac{N_{\text{tot}}^{\text{obs}} - N_{\text{acc}}^{\text{obs}} - N_{\text{others}}^{\text{obs}} - N_{\text{NCOthers}}^{\text{exp}}}{N_{\text{NCQE}}^{\text{exp}}} \\ &\times \langle \sigma_{\text{NCQE}}^{\text{theory}} \rangle \\ &= (0.95 \pm 0.12_{\text{stat.}}) \times 10^{-38} \text{ cm}^2, \end{aligned} \quad (7-3)$$

where  $N_{\text{tot}}^{\text{obs}}$  refers to the observed number of events in the final reduction sample,  $N_{\text{acc}}^{\text{obs}}$  refers to the accidental background without a true neutron, and was evaluated from the random trigger data.  $N_{\text{others}}^{\text{obs}}$  refers to the non-NC backgrounds, including spallation, reactors, atmospheric CC, *etc.*  $N_{\text{NCOthers}}^{\text{exp}}$  refers to the expected number of NC non-QE backgrounds.  $N_{\text{NCQE}}^{\text{exp}}$  refers to the expected number of NCQE events.

### 7.4.3 Systematic Uncertainties

Atmospheric neutrino flux uncertainty varies for different energy bins, as discussed in Ref.<sup>[101]</sup>. In this paper, a conservative estimation at 18% was taken in the energy range [160 MeV, 10 GeV]. The uncertainty of atmospheric  $\nu/\bar{\nu}$  ratio was estimated at 5% from the theoretical model<sup>[99]</sup>.

The non-QE NC cross sections had 18% uncertainty<sup>[16]</sup>. The spectroscopic factors

and the gamma emission branching ratios determines the uncertainty from the primary simulation<sup>[114]</sup>. By removing and restoring all secondary gamma's from the simulation<sup>[114]</sup>, the uncertainty from the secondary process was estimated to be 13% by the T2K group. Although the atmospheric neutrino energy range is much wider than the T2K beam, the decrease in the flux towards high energy tail is exponential scale. The central value of primary neutrons from atmospheric neutrinos do not essentially tend to be higher than that from T2K  $\nu$ 's. The neutron energy distributions from both study were checked to be in good agreement. In this case, the 13% uncertainty was found to be valid as a conservative estimation.

Data reduction besides neutron tagging imposed a 3% systematic uncertainty, as in the SRN analysis<sup>[46]</sup>. The neutron tagging efficiency had 10% intrinsic uncertainty from calibration (Am/Be) and MC for low-energy neutrons, as discussed in Section 5.3. NC neutron drift distance simulation further introduced 10% uncertainty on the neutron tagging efficiency, as given in Table. 7.1. The cutoff at 10 GeV imposed  $\sim 0.1\%$  uncertainty using simulation with the measured high energy atmospheric neutrino flux<sup>[101]</sup>. The cutoff at 160 MeV introduced less than 0.7% uncertainty, which is estimated by simulation with the theoretical prediction of low energy atmospheric neutrino flux<sup>[103]</sup>. The evaluation of non-NC (reactor,  ${}^9\text{Li}$ , CC, etc) leakage into the NC sample introduced  $\sim 21\%$  to  $N_{\text{others}}^{\text{obs}}$ . However, due to the small ratio of events from the non-NC background, this uncertainty was estimated to be  $\sim 0.2\%$  to the total cross section. All the uncertainties are listed in Table. 7.4.

Table 7.4 Uncertainties in the NCQE measurement

	NCQE	NC others
$\nu_{\text{atm}}$ flux		18%
$\nu/\bar{\nu}$ ratio		5%
Cross section		18%
Primary $\gamma$ 's	10%	3%
Secondary $\gamma$ 's	13%	13%
Data reduction		3%
Neutron drift		10%
Neutron tagging		10%
Others		0.7%

A toy-MC was used to derive the uncertainty envelope for the cross section, and the result is shown in Fig. 7.15. The 68% confidence level region is  $[0.59, 1.49] \times 10^{-38} \text{ cm}^2$ , and the cross section is measured to be  $(0.95 \pm 0.12(\text{stat.})^{+0.49}_{-0.32}(\text{sys.})) \times 10^{-38} \text{ cm}^2$ .

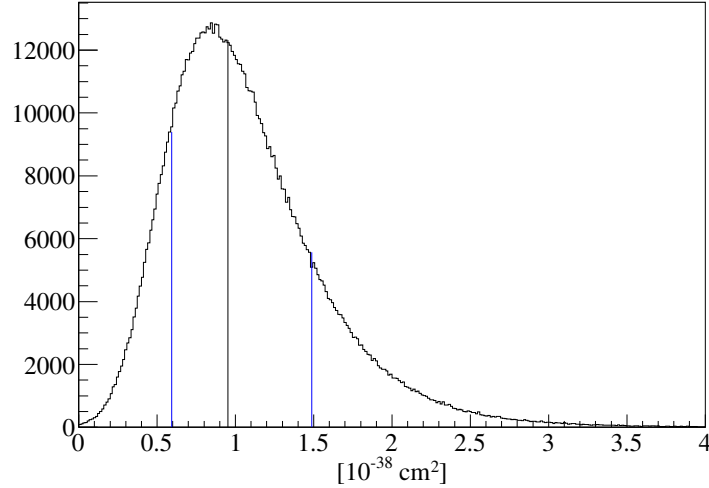


Figure 7.15 The uncertainty envelope for NCQE cross section measurement, as a result of toy MC.

## 7.5 Results and Discussion

We used 2,778 (1,886) days live-time of SK-IV data in a fiducial volume of 22.5 kiloton water detector and applied a strict reduction to remove possible backgrounds from spallation and accidental coincidence. Within the 8-30 MeV energy window, we observed 89 events compared with theoretical prediction of 83.5 events and 15.0 expected non-NC background events of accidental coincidence and spallation. The flux-averaged NCQE cross section measured is  $0.95 \times 10^{-38} \text{ cm}^2$  with a 68% confidence interval of  $(\pm 0.12(\text{stat.})^{+0.49}_{-0.32}(\text{sys.})) \times 10^{-38} \text{ cm}^2$  for atmospheric neutrinos from 160 MeV to 10 GeV. This measurement can be compared with a theoretical prediction of  $1.14 \times 10^{-38} \text{ cm}^2$ .

### 7.5.1 Discussion on Future Improvement

The measurement is affected by systematic uncertainties, including the atmospheric flux, other NC process cross section, primary and secondary process simulation, as well as the neutron tagging efficiency. The flux measurement can be improved with future Cherenkov detectors such as Hyper-Kamiokande<sup>[108]</sup>. The cross section for other NC processes can be improved by the T2K off-axis near detector ND280<sup>[122,123]</sup> and other

nuclear experiments such as MiniBooNE<sup>[124]</sup> and MINERvA<sup>[125]</sup>. For the simulation of primary and secondary processes, the gamma ray emission experiment at RCNP will start to shed light soon when the neutron beam energy is tuned<sup>[126]</sup>

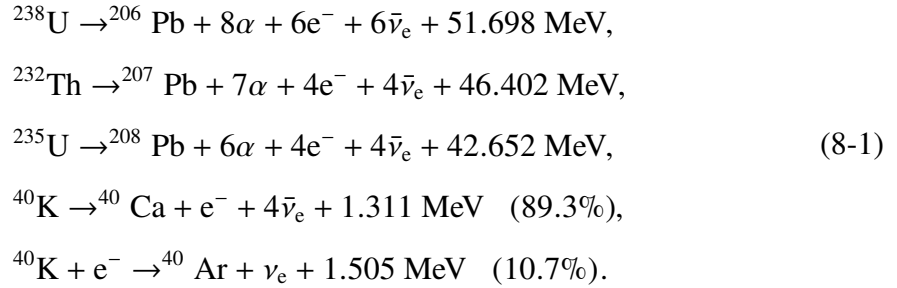
The statistics in this analysis is mainly limited by the neutron tagging efficiency. The present efficiency in pure water is relatively poor and is only  $\sim 20\%$ . When SK is updated to SK-Gd<sup>[107]</sup>, the efficiency is expected to increase to about  $90\%$ , which can reduce the relative uncertainty caused by the neutron tagging efficiency.

## Chapter 8 Geoneutrino Study

This chapter covers a grid-calculation based geoneutrino simulation and the sensitivity study in a liquid scintillator detector, based on a publication by the author of this thesis<sup>[127]</sup>. First we present the simulation of geoneutrino spectra and intensity at the production point, then calculate flux at detection point considering both the Earth model and the oscillation effect of geoneutrinos. An introduction to a proposed liquid scintillator detector follows, based on which we calculate the expected backgrounds and the sensitivity to geoneutrino flux and the Th/U ratio. The interpretation is also included. In the last section, we briefly discuss on the Earth core fission neutrinos.

### 8.1 Geoneutrino Intensity and Energy Spectra

Heat producing elements generate geoneutrinos not only by isotopes themselves, but also by the decay products in the same decay chain, i.e., the decay chain starting from the long-lived isotope  $^{232}\text{Th}$  with  $\tau_{\frac{1}{2}} = 14.0 \times 10^9$  year, from  $^{238}\text{U}$  with  $\tau_{\frac{1}{2}} = 4.47 \times 10^9$  year, and the isotope  $^{40}\text{K}$  with  $\tau_{\frac{1}{2}} = 1.28 \times 10^9$  year:



The  $\nu_e$ 's from the K-shell electron capture of  $^{40}\text{K}$  are difficult to detect due to the smaller cross section of  $\nu - e$  scattering compared to IBD applicable for  $\bar{\nu}_e$ 's. In the following discussion, we consider  $\bar{\nu}_e$ 's from beta decays only.

A general energy formula for the energy spectrum of allowed beta decays can be written as,

$$\begin{aligned}
 dN(E_e) &= \frac{G_F^2 |M|^2}{2\pi^3 \hbar^7 c^5} F(Z, E_e) (E_{max} - E_e)^2 \\
 &\quad \times \sqrt{E_e^2 - m_e^2 c^4} E_e dE_e,
 \end{aligned} \tag{8-2}$$

where  $dN$  refers to the density of event at electron energy  $E_e$ ,  $\frac{G_F^2 |M|^2}{2\pi^3 \hbar^7 c^5}$  is the shape function for allowed decays,  $F(Z, E_e)$  represents the Fermi function describing the electrical field of the isotope nucleus, and  $E_{max}$  is the maximum electron energy allowed by the conservation of total energy. The energy of the emitted geoneutrino  $E_{\bar{\nu}_e}$  is then given by

$$E_{\bar{\nu}_e} = E_{max} - E_e. \quad (8-3)$$

The antineutrinos from all the individual beta decays in a decay chain compose the geoneutrino spectrum for an HPE. The spectra and rates from all the decay branches of the HPEs have to be considered and calculated to estimate the overall geoneutrino intensity and spectrum. Figure 8.1 shows the spectra of geoneutrinos from different HPEs. The spectra are generated with GEANT4<sup>[95]</sup> and checked by different references. A few percent difference is found for  $^{238}\text{U}$  geoneutrino spectrum between the GEANT4 simulation and S. Enomoto's calculation<sup>[128]</sup>. This difference shows up around 1 MeV and will not exceed the 1.8 MeV threshold for IBD, and thus will not influence the detection. Actually, among the  $\bar{\nu}_e$ 's produced from the beta decays of HPEs, only those from the decay chains of  $^{232}\text{Th}$  and  $^{238}\text{U}$  will exceed the reaction threshold of 1.8 MeV for IBD, while the  $\bar{\nu}_e$ 's from  $^{40}\text{K}$  are below 1.5 MeV, unable to be detected through IBD channel.

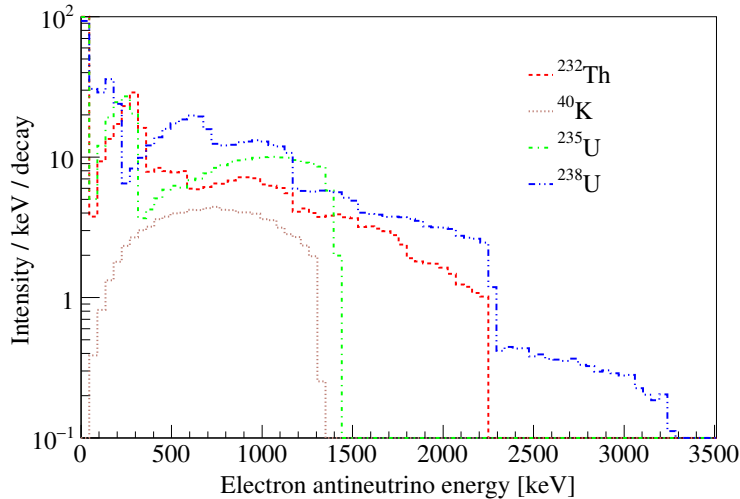


Figure 8.1 The geoneutrino energy spectra produced by HPEs are simulated with Geant4. The  $\bar{\nu}_e$ 's are produced in the decays of  $^{238}\text{U}$ ,  $^{232}\text{Th}$ ,  $^{40}\text{K}$  and  $^{235}\text{U}$ .  $\nu_e$  from  $^{40}\text{K}$  chain are not shown.

Due to the 1.8 MeV IBD threshold, the only contribution to the detectable geoneutrino signal by IBD interaction are from the isotope  $^{214}\text{Bi}$  and  $^{234}\text{Pa}$  from the  $^{238}\text{U}$  decay chain, and  $^{212}\text{Bi}$  and  $^{228}\text{Ac}$  from the  $^{232}\text{Th}$  decay chains<sup>[129]</sup>. The energy spectra of geoneutrinos

from the HPE uranium and thorium have different distributions, with the  $^{238}\text{U}$  geoneutrinos extending to a maximum end point of 3.3 MeV, while the  $^{232}\text{Th}$  geoneutrinos do not exceed the energy of 2.25 MeV. From this difference, the uranium and thorium geoneutrinos can in principal be fitted individually to obtain the Th/U ratio, which in theoretical calculation BSE models give  $m(^{232}\text{Th})/m(^{238}\text{U}) = 3.9$  globally<sup>[60]</sup>.

## 8.2 Geo $\bar{\nu}_e$ Flux Calculation

The calculation of geoneutrino flux and spectrum at the detection site involves the initial energy spectrum at each production point, the distribution of HPEs in the world on a grid basis, the spheric wave propagation, and the oscillation effect. Integrating over the above factors, we derived a general formula of the geoneutrino energy spectrum  $\phi(E)$  as below

$$\begin{aligned} \phi_i(E)dE &= \frac{X_i \lambda_i N_A}{\mu_i} n_\nu(i) \\ &\times \int \frac{A_i(\vec{r}) \rho(\vec{r})}{4\pi L^2} P_{ee}(E, L) f_i(E) d\vec{r} dE, \end{aligned} \quad (8-4)$$

where by sequence  $X$  stands for the natural isotopic mole fraction of the HPE isotope  $i$ ,  $\lambda$  stands for the decay constant of  $i$ ,  $N_A$  refers to the Avogadro constant,  $\mu$  refers to the standard atomic mole mass for  $i$ , and  $n_\nu$  is the average number of  $\bar{\nu}_e$ 's emitted per decay from  $i$ . These parameters are either constants or dependent on the isotope  $i$  only, invariant on the production location.  $A(\vec{r})$  refers to the locally variant abundance for  $i$ , and  $\rho(\vec{r})$  stands for the density, also locally variant. These parameters are taken from the Earth model used.  $L$  stands for the linear distance from the production point to the detection site,  $P_{ee}$  stands for the neutrino survival probability, the calculation of which is included in Section 1.1.2, and  $f(E)$  stands for the normalized  $\bar{\nu}_e$  energy spectrum for the HPE  $i$ , as shown in Fig. 8.1. These parameters are related to the neutrino oscillation.

The total flux  $\phi_i$  is then obtained by integrating the energy spectrum,

$$\begin{aligned} \phi_i &= \int \phi_i(E) dE \\ &= \frac{X_i \lambda_i N_A}{\mu_i} n_\nu(i) \langle P_{ee}^i \rangle \int \frac{A_i(\vec{r}) \rho(\vec{r})}{4\pi L^2} d\vec{r}, \end{aligned} \quad (8-5)$$

where  $\langle P_{ee}^i \rangle$  represents the average  $\bar{\nu}_e$  survival probability, calculated by integrating over

the normalized energy spectrum of HPE  $i$  and its abundance distribution in the Earth.

### 8.2.1 Earth Model

To obtain the locally variant density of the Earth, a reference model describing the BSE is required. A group of geologists built a  $1^\circ \times 1^\circ$  topological map of the Earth crust, named CRUST1.0<sup>[130]</sup>. In CRUST1.0, every  $1^\circ \times 1^\circ$  cell is split in depth into 8 layers of profiles, namely water, ice, upper, middle, and lower sediments, and upper, middle, and lower crusts. Some of the layers may have 0 depth depending on the local structure, whether the cell locates in the ocean or in the mountains. In each layer, CRUST1.0 provides the density  $\rho(\vec{r})$  used in Eqs. (8-4) and (8-5), as well as some other information less relevant to this study. For the mantle however, the determination of boundaries and layers are difficult, not to mention the density and locally variant density distribution. The seismic tomography can be used to obtain these information, and in this analysis we employ the model from Huang *et al*<sup>[60]</sup>. In general, the mantle is divided into three layers of continental lithospheric mantle, depleted Mantle, and enriched mantle. In each mantle layer, the density is assumed to be uniform due to the mantle convection.

The abundance of HPEs  $A_i(\vec{r})$  is assumed to be uniform for every HPE in each geological layer. Different BSE models mainly on this abundance, and in this analysis we take the abundance assumptions from Ref.<sup>[131]</sup>, which employs the medium-Q BSE model.

The Earth model parameters are set at the best precision of  $1^\circ \times 1^\circ$ , but this is still too rough for the  $1/r^2$  propagation of geoneutrinos and the oscillation effect. To facilitate the computation, the  $1^\circ \times 1^\circ$  cell is further divided into grids to calculate the distance  $L$  a neutrino would propagate.

The main uncertainty introduced by this Earth model is from the assumption of HPE abundance, i.e., the uncertainties from the BSE models themselves. From a previous study<sup>[131]</sup>, the uncertainty from Earth model on the total expected geoneutrino flux is  $+12.6\%$ ,  $-12.3\%$ , and  $\pm 15.0\%$  for the crustal geoneutrinos.

### 8.2.2 Oscillation Analysis

Geoneutrinos oscillates following the three generation scheme of neutrino oscillation, as discussed in Section 1.1.2.1. However, it is worth further discussion on the variant propagation length  $L$  for every production point, and on the propagation underneath the



Earth surface.

### 8.2.2.1 Vacuum Oscillation

Following the notations in Section 1.1.2.1, we employ the oscillation parameters  $\theta_{ij}$  and  $\Delta M_{ij}$  from Ref. <sup>[132]</sup>, considering both the central values and uncertainties. The default neutrino mass hierarchy is set as inverted hierarchy, while the case of normal hierarchy is also discussed and included as an uncertainty.

The average survival probability of  $\bar{\nu}_e$ 's, or  $\langle P_{ee}^i \rangle$  as in Eq. (8-5), is obtained by the integral of energy dependent survival probability  $P_{ee}^i(E)$ ,

$$\langle P_{ee}^i \rangle = \int P_{ee}^i(E) f_i(E) dE, \quad (8-6)$$

where  $P_{ee}^i(E)$  is averaged over the HPE distributions in the Earth, considering the oscillation from every grid  $\vec{r}$  to the detection site at the distance  $L$ ,

$$P_{ee}^i(E) = \frac{\int P_{ee}(E, L) \cdot A_i(\vec{r}) \rho(\vec{r}) / (4\pi L^2) d\vec{r}}{\int A_i(\vec{r}) \rho(\vec{r}) / (4\pi L^2) d\vec{r}}. \quad (8-7)$$

The notation is the same as Eq. (8-5). The survival probability  $P_{ee}^i(E)$  as a function of geoneutrino energy is shown in Fig. 8.2.

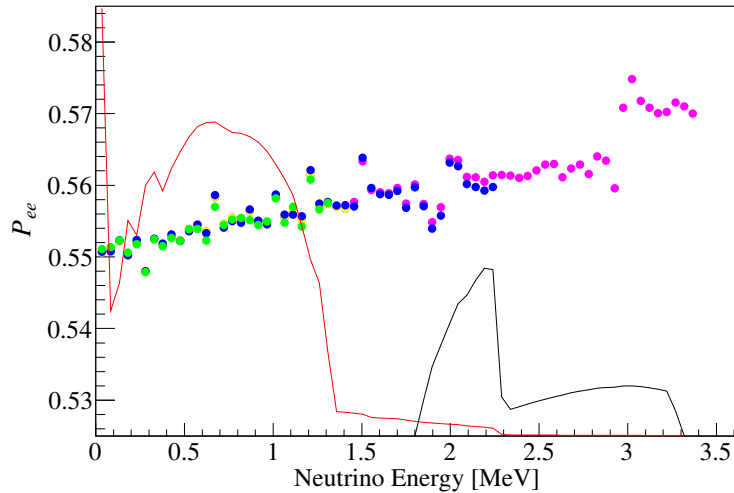


Figure 8.2 Geoneutrino survival probability  $P_{ee}^i$  as a function of geoneutrino energy  $E$ . The magenta points represents for uranium, blue points for thorium, and green points for potassium. The red line shows the total geoneutrino energy spectrum in arbitrary units, and the black line shows the IBD event energy spectrum, also in A.U..

From the calculation, an average survival probability for geoneutrinos  $\langle P_{ee} \rangle$  can be derived by averaging the energy dependent  $P_{ee}^i(E)$  by the HPE energy spectrum. Applying the IBD cross section as a weight, another 'effective' survival probability  $\langle P_{ee}^i \rangle'$  can also be calculated, as listed in Table 8.1.

Table 8.1 The survival probabilities for geoneutrinos of different HPEs averaged  $\langle P_{ee} \rangle$  and effectively averaged  $\langle P_{ee}^i \rangle'$ .

	$^{40}\text{K}$	$^{232}\text{Th}$	$^{235}\text{U}$	$^{238}\text{U}$	Total
$\langle P_{ee} \rangle$	0.554	0.553	0.553	0.554	0.553
$\langle P_{ee}^i \rangle'$	0	0.560	0	0.563	0.562

### 8.2.2.2 Uncertainty Introduced by Oscillation Parameters

The uncertainties from the neutrino oscillation parameters  $\theta_{ij}$ 's and  $\Delta M_{ij}$ 's as cited from Ref. [132] will introduce uncertainties in the expected geoneutrino fluxes. The CP term  $\delta$  and the hierarchy are also taken as uncertainty sources. Table 8.2 gives the estimation of uncertainties propagated from oscillation parameters into the calculation of geoneutrino fluxes.

Table 8.2 The central values, relative uncertainties, and corresponding relative uncertainties propagated to the geoneutrino flux of neutrino oscillation parameters. For  $\Delta M_{ij}$ 's, the unit is eV. For CP term  $\delta$  and mass hierarchy MH, the uncertainty column corresponds to the parameter boundaries.

Parameter	Value	Uncertainty	Flux uncertainty	Crustal uncertainty
$\theta_{12}$	0.584	+2.6%	+1.8%	+1.8%
		-2.4%	-1.7%	-1.7%
$\theta_{13}$	0.149	+2.7%	$\pm 0.2\%$	$\pm 0.2\%$
		-2.8%		
$\theta_{23}$	0.785	$\pm 6.4\%$	$\pm 0.0\%$	$\pm 0.0\%$
$\Delta M_{21}$	$7.53 \times 10^{-5}$	$\pm 2.4\%$	$\pm 0.1\%$	$\pm 0.1\%$
$\Delta M_{32}$	$2.51 \times 10^{-3}$	$\pm 2.4\%$	$\pm 0.0\%$	$\pm 0.0\%$
$\delta$	0	$\pm 1.5$	$\pm 0.0\%$	$\pm 0.0\%$
MH	IH	NH	$\pm 0.0\%$	$\pm 0.0\%$

The total uncertainty introduced by neutrino oscillation parameters is  $^{+1.8\%}_{-1.7\%}$ , mainly

contributed by the uncertainty from  $\theta_{12}$ . It is still negligible compared to the  $^{+12.6\%}_{-12.3\%}$  uncertainty introduced by the Earth model now. However, with the future progress in the theoretical predictions of the BSE models, the uncertainty from the Earth model is likely to be further reduced and this in turn will require a better measurement of  $\theta_{12}$ .

Figure 8.3 shows the correlation between the uncertainty of  $\theta_{12}$  with the propagated uncertainty into the geoneutrino flux. The red solid lines stand for the central value of  $\theta_{12}$  and the corresponding expected geoneutrino flux. The blue dotted lines represent the  $1\sigma$  uncertainty range, as listed in Table 8.2. The precision of measurement on  $\theta_{12}$  is expected to be improved with present and future experiments for solar and reactor neutrinos, including JUNO<sup>[77]</sup> and Hyper-K<sup>[108]</sup>. The sensitivity study of JUNO claims  $\pm 0.3\%$  uncertainty on  $\theta_{12}$  after accumulating sufficient statistics. This prediction is shown in Fig. 8.3 by red dotted dashed lines, and the corresponding uncertainty in the geoneutrino flux is expected to be  $\pm 0.2\%$ .

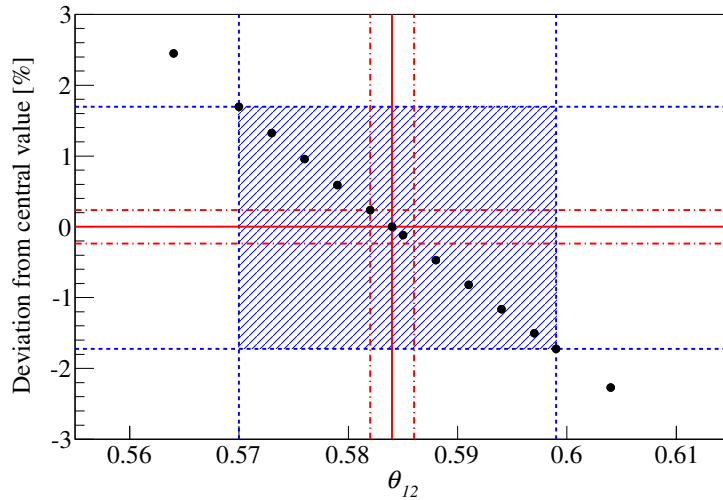


Figure 8.3 The correlation between the predicted geoneutrino flux and  $\theta_{12}$ . The red solid lines stand for the central value of  $\theta_{12}$  and the corresponding expected geoneutrino flux, the blue dotted lines represent the  $1\sigma$  uncertainty range in present experimental measurement, and the red dotted dashed lines stand for the predictions from JUNO<sup>[77]</sup>.

The MSW effect, as discussed in Section 1.1.2.2, is also calculated for the geoneutrinos. Using the same method as described above, we expect  $+0.3\%$  deviation on the geoneutrino flux when considering the MSW oscillation instead of the vacuum oscillation.

### 8.3 Liquid Scintillator Detector

The energy range of geoneutrinos is between 0 to 3.3 MeV. The low energy signal of geoneutrinos requires high light yield to ensure good energy resolution. Also, due to the low cross section of neutrinos, the detector must be large enough to ensure sufficient statistics. Liquid scintillator is a suitable material for the geoneutrino detection, as it is cheap and has relatively high light yield.

Compared to water Cherenkov detectors such as SK, the low light yield will not allow geoneutrinos to trigger any event at SK, while in a liquid scintillator experiment where the trigger threshold is usually below 3 MeV, geoneutrinos can be naturally detected. The deficit of liquid scintillation light compared to water Cherenkov light is that liquid scintillation light does not carry the direction information of the primary particle. In geoneutrino analysis, however, the directional information has already been lost during the IBD process, and thus water will not outperform liquid scintillator.

KamLAND and Borexino have succeeded in performing geoneutrino analysis with liquid scintillator detectors.

#### 8.3.1 Scintillation Light

In a liquid scintillator, a positron with several MeV can generate both scintillation photons and Cherenkov photons. The process of Cherenkov light production has been discussed in Section 3.2.1.

Unlike water Cherenkov photons, scintillation photons are emitted isotropically. The process of scintillation light production can be described by the empirical function called Birks' law<sup>[133]</sup>,

$$\frac{dY_s}{dx} = A \frac{dE/dx}{1 + k_B \cdot dE/dx}, \quad (8-8)$$

where  $dY_s/dx$  refers to the photon yield per distance propagated by the positron,  $A$  stands for a normalization constant,  $k_B$  represents the Birks' constant, which is dependent on the scintillator property.  $dE/dx$  refers to the energy loss of the positron at the energy  $E$ . This dependence causes the nonlinearity of the scintillation light yield, as shown in Fig. 8.4.

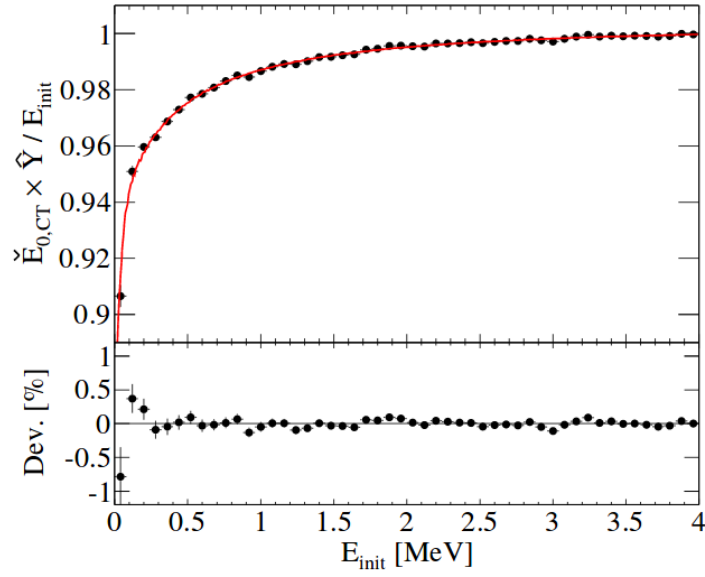


Figure 8.4 The nonlinearity of scintillation light yield as a function of the true energy.

### 8.3.2 Detector Response Model

An energy response model should be able to describe the relation between the incident particle and the output electronic data and reconstruct the incident particle energy from the output, taking into consideration the nonlinearity and nonuniformity of the detector. The energy response of a liquid scintillator detector is important in the reconstruction of neutrino energy, especially in the case of a low-energy neutrino due to the nonlinearity of light emission around 1 MeV.

A generic energy response function can be written as<sup>[134]</sup>

$$E_{\text{obs}}(\vec{x}, E_{\text{init}}, E_{\text{dep}}) = E_0 \sum_{i=1}^N R_i \left\{ O_i \left[ \vec{x}, Y(E_{\text{init}}, E_{\text{dep}}) \right] \right\}, \quad (8-9)$$

where  $E_{\text{obs}}$  refers to the observed energy as a function of the initial energy of the incident particle  $E_{\text{init}}$ , the deposited energy  $E_{\text{dep}}$ , and the scintillation point  $\vec{x}$ .  $E_0$  stands for a scale factor to convert the readout from  $N$  channels of electronics to energy,  $R$  refers to the single channel electronics response,  $O$  refers to the optical response, and  $Y$  refers to the photon yield including Cherenkov photons and scintillation photons.

Some approximations can be applied to simplify Eq. (8-9) in the sense to make it more computationally efficient. First, the wavelength difference between Cherenkov photons and scintillation photons is neglected. Due to the low light yield of Cherenkov photon compared to scintillation photon, this approximation is feasible. Second, the position

dependence of the electronics response is neglected. This is actually not an approximation, but a requirement for the calibration and correction on each channel. Finally, the optical response is decoupled into two parts: photocoverage, and phototransmission. It does not work mathematically, but statistically this decoupling is feasible. The basic idea is the high light yield of scintillator, due to which the yielded photon number actually falls into a Gaussian distribution following the large number law. After these approximations, Eq. (8-9) is modified as

$$E_{\text{obs}}(\vec{x}, E_{\text{init}}, E_{\text{dep}}) = E_0 \cdot R \cdot C(\vec{x})T(\vec{x}) \cdot [Y_s + f Y_C] (E_{\text{init}}, E_{\text{dep}}), \quad (8-10)$$

where  $Y$  is split into  $Y_s$  and  $Y_C$ , namely the scintillation component and the Cherenkov component, the optical response  $O$  is decoupled into photocoverage  $C$  and phototransmission  $T$ , and  $R$  is decoupled from other components to be an independent electronics response term. A schematic view of this model is shown in Fig. 8.5.

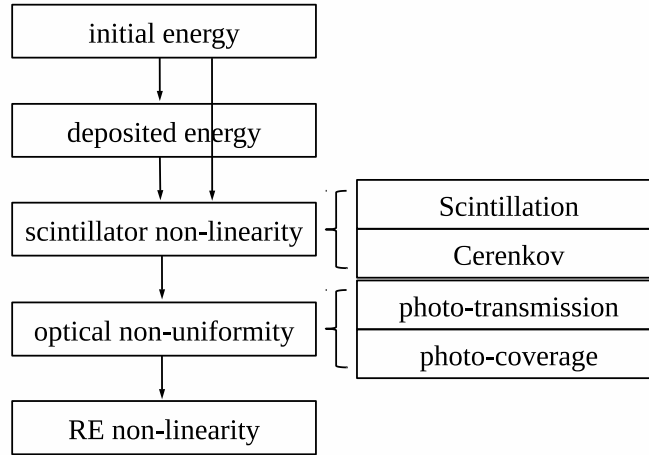


Figure 8.5 A schematic flowchart of the proposed detector response model.

The photon yields  $Y_s$  and  $Y_C$  can be analytically expressed as in Eq. (8-8) and in Section 3.2.1. For the optical responses of phototransmission, first we start with the Beer's law:

$$T(\lambda, l) = \exp(-l/L(\lambda)), \quad (8-11)$$

where  $l$  represents the distance between the scintillation point and the PMT,  $L(\lambda)$  repre-

sents the wavelength dependent attenuation length, and  $T(\lambda, l)$  is the survival probability. Then the phototransmission response  $T(\vec{x})$  can be written as

$$T(\vec{x}) = \frac{1}{n} \sum_{i=1}^n \exp\left(-\frac{l_i(\vec{x})}{L}\right), \quad (8-12)$$

where  $\vec{x}$  is the scintillation point,  $n$  is the number of emitted photons, and  $l_i$  is the distance travelled by the  $i$ -th photon from  $\vec{x}$  to the photosensors, or more precisely, to a continuous surface that contains the photosensor surface. The ratio of the photosensor surface on that continuous surface is defined as the photocoverage. To decouple the phototransmission and the photocoverage, Eq. (8-12) can be expanded and regrouped as

$$T(\vec{x}) = 1 + \sum_{k=1}^{\infty} \left(-\frac{1}{L}\right)^k m_k(\vec{x}), \quad (8-13)$$

$$m_k(\vec{x}) = \frac{1}{n} \cdot \frac{1}{k!} \sum_{i=1}^n [l_i(\vec{x})]^k,$$

where  $m_k(\vec{x})$  is a moment term dependent only on the detector geometry. From Eq. (8-13), the precision of the approximation of finite moment terms is limited by the ratio of  $l_i/L$ . If  $l_i/L$  is small enough, i.e., the case where attenuation does not dominate the photo propagation, the first moment term  $m_1(\vec{x})$  is sufficient to calculate  $T(\vec{x})$ .

The above scheme is summarized into a pseudocode example to explain the procedures for this energy response model.

1. Uniformly place vertices inside the detector volume.
2. For each vertex, generate hypothetical photons isotropically, and trace the distance between it and the continuous surface that contains the photosensor surface. Scattering or absorption should not be included here.
3. Record the portion of photons arriving at photosensors and the total number of photons, and the ratio is the photocoverage.
4. Calculate the moment term  $m_k(\vec{x})$ 's according to Eq. (8-13), and  $m_k(\vec{x})$ 's are sufficient to describe the detector setup and phototransmission.

Since the moment term  $m_k(\vec{x})$ 's are only dependent on the detector geometry, invariant with the photo-properties of the scintillator, they will not require update unless the geometry of the detector is changed, or the reflectivity of some material is modified. Therefore,  $m_k(\vec{x})$ 's can be made into look-up tables, and the application of this scheme

into calibration will be swift, without the need to perform a detector-level simulation.

This energy response model can naturally accommodate multi-volume detectors with different attenuation lengths in different parts. Following the formality of Eq. (8-13), the phototransmission moments for a 2-volume detector can be derived as

$$\begin{aligned}
 T(\vec{x}) &= 1 + \sum_{k=1}^{\infty} \left[ \left( -\frac{1}{L_1} \right)^k m_{1,k}(\vec{x}) + \left( -\frac{1}{L_2} \right)^k m_{2,k}(\vec{x}) \right] \\
 &\quad + \sum_{a,b}^{\infty} \left( -\frac{1}{L_1} \right)^a \left( -\frac{1}{L_2} \right)^b m_{ab}(\vec{x}), \\
 m_{j,k}(\vec{x}) &= \frac{1}{n} \frac{1}{k!} \sum_{i=1}^n [l_{j,i}(\vec{x})]^k, \\
 m_{ab}(\vec{x}) &= \frac{1}{n} \frac{1}{a!} \frac{1}{b!} \sum_{i=1}^n [l_{1,i}(\vec{x})]^a [l_{2,i}(\vec{x})]^b,
 \end{aligned} \tag{8-14}$$

where  $j$  takes the value 1 or 2, and  $l_{1,i} + l_{2,i} = l_i$ . In this case, the  $k$ -th order moment term consists of  $m_{ab}$  where  $a \geq 0$ ,  $b \geq 0$ ,  $a + b = k$ . It is straight forward to expand Eq. (8-14) into more than 2 volume detectors. Eq. (8-14) can also be used to fit a single detector with more than one distinct attenuation terms, i.e., scattering and absorption. Incorporating Eq. (8-14) back into Eq. (8-10), this model can accommodate two volumes with not only distinct attenuation length, but also different yields and electronic scales.

A detailed discussion of the model and its application can be found in Ref.<sup>[134]</sup>. The performance of this energy response model is expected to be less than 0.4% over a course of 5 years for a cylindrical detector of radii and half-height at 5.65 m. This number is sufficiently low compared to the usual statistical energy resolution of liquid scintillator at 1 MeV, which is  $\sim 4\%$ .

### 8.3.3 A Proposed Experiment at Jinping

For the geoneutrino detection, as Fig. 1.14 and Fig. 1.15 shows, the largest background comes from the reactor neutrinos. Therefore, a geoneutrino observation site will have a significant signal background ratio if it locates somewhere far away from the nuclear power plants and reactor sources.

The China Jinping Laboratory (CJPL, latitude at 28.15323°N, longitude at 101.7114°E), is located in a low background experimental site in the Jinping Mountain, Sichuan Province, China. The site is more than 900 km away from the closest



reactors either in operation or under construction. A low-energy neutrino experiment at CJPL will push forward the detection of geoneutrinos greatly.

The Jinping Neutrino Experiment (Jinping) is proposed to be built at CJPL, employing a kiloton-level detector of liquid scintillator or slow liquid scintillator<sup>[135]</sup>. The expected fiducial mass for IBD is 3 kiloton, with a wide range of live-time and energy resolution scanned in a sensitivity study, to be discussed in Section 8.6.1. More sensitivity studies on other physics topics and the assessments of the site as well as detector designs can be found in Ref.<sup>[79]</sup>.

## 8.4 Backgrounds

The backgrounds for geoneutrino detection include electron antineutrino backgrounds which are irreducible due to the exactly same signal signature, and other backgrounds, sometimes can be distinguished by certain features.

### 8.4.1 Reactor Neutrino Background

Reactor neutrinos are electron antineutrinos covering the energy range of geoneutrinos. They form exactly the same signal signature of IBD as geoneutrinos. This background can be fitted by the distinct energy spectrum, extending above the 3.3 MeV geoneutrino energy boundary. Still, the statistical and systematic uncertainties introduced by reactor neutrino background due to its large statistics and spectrum uncertainties can affect the sensitivity of an experiment to the detection of geoneutrinos. The only way to reduce this background is to move the neutrino detector away from the nuclear power plant, and Jinping is the best neutrino observatory site so far in the sense of low reactor neutrino backgrounds.

Reactor neutrinos are electron antineutrinos emitted from the beta decays of the radioactive isotopes in the fission fuel,  $^{235}\text{U}$ ,  $^{238}\text{U}$ ,  $^{239}\text{Pu}$ , and  $^{241}\text{Pu}$ . The neutrino spectrum  $\phi(E_\nu)$  can be calculated by

$$\phi(E_\nu) = \frac{W_{th}LF}{\sum_i f_i e_i} \sum_i f_i S_i(E_\nu), \quad (8-15)$$

where  $W_{th}$  refers to the reactor thermal power and  $LF$  stands for the load factor of the reactor. These parameters can be found in the yearly booklet of the International Atomic Energy Agency (IAEA)<sup>[104]</sup>. As a conservative estimation for geoneutrino sensitivity,

we performed a small over-estimation for the reactor neutrino background by setting the load factor to 1.0 in this study. The fission fraction  $f_i$  for the  $i$ -th isotope should follow  $\sum_i f_i = 1$ . In every fission of the  $i$ -th isotope,  $e_i$  stands for the average energy released, and  $S_i(E_\nu)$  stands for the  $\bar{\nu}_e$  spectrum<sup>[136,137]</sup>. The typical values for these fission parameters can be found in Table 8.3.

Table 8.3 Fission fraction  $f_i$  and average energy  $e_i$  for the fissile isotopes.

Isotope	$f_i$	$e_i$ [MeV/fission]
<sup>235</sup> U	0.58	202.36 ± 0.26
<sup>238</sup> U	0.07	205.99 ± 0.52
<sup>239</sup> Pu	0.30	211.12 ± 0.34
<sup>241</sup> Pu	0.05	214.26 ± 0.33

Reactor neutrinos are also detected by IBD interaction. The event rate  $R(E_\nu)$  can be calculated by the product of the flux  $\phi(E_\nu)$  and the IBD cross section  $\sigma(E_\nu)$ ,

$$R(E_\nu) = \phi(E_\nu) \times \sigma(E_\nu). \quad (8-16)$$

To directly compare between different experiment material, masses, and live-times, a universal geoneutrino unit called Terrestrial Neutrino Unit (TNU) is defined as 1  $\bar{\nu}_e$  events detected by IBD interaction for  $10^{32}$  protons in 1 year live-time. The event rates of reactor neutrinos are shown in the unit of TNU in Table 8.4. Due to the different energy ranges of geoneutrinos and reactor neutrinos, we define [1.8, 10.0] MeV as the Full Energy Range (FER) for whole spectrum of reactor neutrinos, and [1.8, 3.3] MeV as Signal Energy Range (SER) for the reactor neutrinos overlapping with the energy range of geoneutrinos. The uncertainties listed in Table 8.4 are mainly introduced by the oscillation effect<sup>[138]</sup>, evaluated at 1.5% using the same method as in the calculation of geoneutrino oscillation effect. The oscillation parameters and uncertainties are also taken from Ref.<sup>[132]</sup>. Additional deviation from the central value listed can be contributed by considering the MSW oscillation, at the level of 0.5%. This is not considered as an uncertainty source.

The reactor neutrino background is mainly contributed by reactors along the coastline of China, as Fig. 8.6 shows.

Table 8.4 Reactor neutrino rates in different energy ranges at Jinping.

Event rate (TNU)	Constructed		Under construction		Total
	China	Others	China	Others	
FER	$8.9 \pm 0.2$	$10.6 \pm 0.1$	$6.3 \pm 0.1$	$2.0 \pm 0.0$	$27.8 \pm 0.4$
SER	$2.4 \pm 0.1$	$2.3 \pm 0.0$	$1.5 \pm 0.0$	$0.6 \pm 0.0$	$6.8 \pm 0.1$

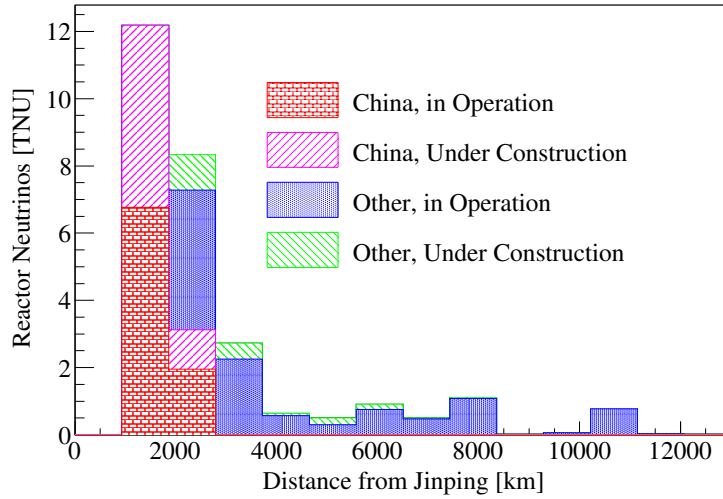


Figure 8.6 Reactor neutrinos from around the world.

#### 8.4.2 Other Backgrounds

Backgrounds other than  $\bar{\nu}_e$ 's may be reducible, but usually cannot be totally removed from the data sample. In the case geoneutrino detection, the backgrounds include the cosmogenic background  ${}^9\text{Li}$  and fast neutron, the natural radioactivity background ( $\alpha, n$ ), and solar neutrinos.

Cosmogenic backgrounds originate to the muons from cosmic rays trespassing the detector. They collide on the carbon nuclei and break them apart. Among these spallation products,  ${}^9\text{Li}$  isotopes decay with a correlated  $\beta - n$  signal, mimicking the IBD signature. Muons from cosmic rays can also produce fast neutrons. These fast neutrons colliding on other nuclei to produce a fast signal, and thermalize before being captured on hydrogen. This process also produces a pair of correlated signals. The rate of cosmogenic backgrounds directly depends on the muon rate at the detector. At Jinping, the 6,720 w.m.e. (water meter equivalent) overburden shielded the detector from the cosmic rays, and the muon rate there is as low as  $(2.0 \pm 0.4) \times 10^{-10}/(\text{cm}^2 \cdot \text{s})$ <sup>[79]</sup>. Assuming a simple veto of 2 s muon veto time window, the live-time loss is expected to be only 1.1%. Benefiting from the extremely low muon rate at Jinping, the  ${}^9\text{Li}$  background is estimated to be  $(0.02 \pm 0.01)/3$  kilotons/1,500 days, while the fast neutron background is calculated

at  $\leq 0.04/3$  kilotons/1,500 days.

The background from natural radioactivity comes from both inside the detector and outside the detector, the latter of which usually comprises of the leakage of MeV  $\gamma$ 's, and can be rejected by a fiducial volume cut. This background leaks into the geoneutrino data sample by  $(\alpha, n)$  reactions and accidental coincidence. Accidental coincidence in large volume detectors are usually negligible after applying a simple fiducial volume cut<sup>[79]</sup>. The  $(\alpha, n)$  reaction however, does mimic the IBD signal by a coincidence of prompt  $\alpha$  and a delayed neutron capture. The  $\alpha$  comes from the natural decays from the long-term decay chains, especially from  $^{210}\text{Po}$ . If we assume the same level of  $^{210}\text{Po}$  contamination as Borexino<sup>[70]</sup>, Jinping is expected to have  $(1.7 \pm 0.1)/3$  kilotons/1,500 days  $(\alpha, n)$  backgrounds.

Solar neutrinos also form a possible background for the detection of geoneutrinos, with the elastic scattering process:

$$\nu + e \rightarrow \nu + e. \quad (8-17)$$

This process has relatively low cross section compared to IBD, and the electron will not coincide with a neutron to form a correlated pair of signals, thus it produces a background only by accidental coincidence, which is negligible compared to the other backgrounds.

To summarize the above discussion, Jinping will have up to  $1.8/3$  kilotons/1,500 days non- $\bar{\nu}_e$  backgrounds in SER, negligible compared to the reactor neutrino background at  $(60.4 \pm 0.9)/3$  kilotons/1,500 days. In the following sensitivity study, we will consider only the reactor neutrino background.

## 8.5 Sensitivities

This section covers the result of simulation, the predictions of sensitivity study, and the implementation on the geological models. In this section, we assume a 3-kiloton liquid scintillator with a 500 p.e./MeV energy resolution (corresponding to  $4.4\%/\sqrt{E_{vis}}$ ). The live-time is taken as 1,500 days, corresponding to 5 years running with some dead-time for calibration. All these parameters have been scanned, and related studies can be found in Section 8.6.1.

## 8.5.1 Predicted IBD Spectrum at Jinping

Figure 8.7 shows the expected IBD events at Jinping. Corresponding numerical results for signal events are included in Table 8.5, in which the geoneutrinos are divided into Th/U and crust/mantle. The comparison between geoneutrino signal and reactor neutrino background is listed in Table 8.6.

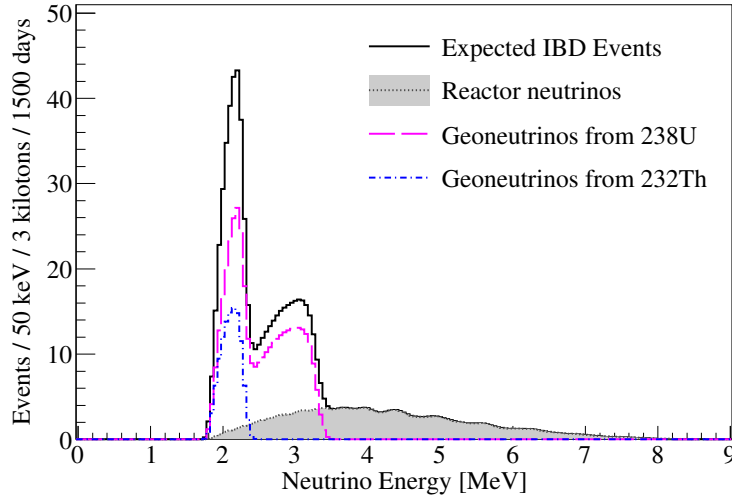


Figure 8.7 The simulation of IBD events at Jinping. The magenta dashed line shows the contribution from  $^{238}\text{U}$ , the blue dotted dashed line shows the contribution from  $^{232}\text{Th}$ , the gray shadow shows the reactor neutrino background, and the black line shows the sum.

Table 8.5 Geoneutrino flux at Jinping in the unit of TNU.

Geo $\bar{\nu}_e$ (TNU)	Crust	Mantle	BSE
Th	$10.6 \pm 0.8$	$2.1 \pm 0.5$	$12.7 \pm 1.0$
U	$38.4 \pm 6.6$	$8.3 \pm 2.3$	$46.7 \pm 6.7$
Th+U	$49.0 \pm 7.3$	$10.4 \pm 2.7$	$59.4 \pm 7.6$

Table 8.6 Geoneutrino signals and reactor neutrino backgrounds expected at Jinping. The setup is a 3-kiloton detector for a live-time of 1,500 days, with an energy resolution at 500 p.e./MeV.

	Geoneutrino			Reactor	
	$^{238}\text{U}$	$^{232}\text{Th}$	Total	FER	SER
Event Rate ( TNU )	46.7	12.7	59.4	27.8	6.8
Total Events	414.5	113.6	527.3	246.8	60.4

### 8.5.2 Sensitivity for Geoneutrinos

To evaluate the sensitivities of geoneutrino flux and Th/U ratios at Jinping, we performed toy Monte Carlo simulations. First, we randomly sampled from the total spectrum in Fig. 8.7 based on the statistics of 3 kiloton  $\times$  1,500 days by 50 keV binning. Next, the spectrum is fitted by the expectations of U, Th and reactor spectra simultaneously using maximum likelihood method. The fitting is limited in the energy range  $E_\nu \in [1.8, 6.8]$  MeV. The procedure of sampling and fitting was repeated 10,000 times to avoid fluctuations. The fitting function is written as

$$N(E) = NR_{geo} \left[ R_U \tilde{f}_U(E) + (1 - R_U) \tilde{f}_{Th}(E) \right] + N(1 - R_{geo}) \tilde{f}_R(E), \quad (8-18)$$

where  $N(E)$  stands for the number of events in the sampled spectrum within the energy bin  $E$ ,  $N$  refers to the total number of IBD events,  $R_{geo}$  is the fraction of geoneutrinos among all the IBD events, and  $R_U$  is the fraction of geoneutrinos from  $^{238}\text{U}$  among the total number of geoneutrinos. The expectations of U, Th and reactor spectra are calculated by the oscillated  $\bar{\nu}_e$  spectra weighted by the IBD cross section, and  $\tilde{f}(E)$ 's stand for the normalized spectra for  $^{238}\text{U}$ ,  $^{232}\text{Th}$ , and reactors respectively, denoted by the subscripts U, Th, and R. The free fitting parameters in this function are  $N$ ,  $R_{geo}$ , and  $R_U$ .

The total number of geoneutrino events is

$$N_{geo} = N \cdot R_{geo}, \quad (8-19)$$

and the Th/U ratio in the measured IBD events at Jinping can be written as

$$R(\text{Th}/\text{U})_{\text{IBD}} = (1 - R_U) / R_U. \quad (8-20)$$

The mass ratio of the HPE thorium and uranium in the BSE can then be derived as

$$R(\text{Th}/\text{U})_m = R(\text{Th}/\text{U})_{\text{IBD}} \cdot \frac{\langle P_{ee}^U \rangle' \tilde{\sigma}_U}{\langle P_{ee}^{\text{Th}} \rangle \tilde{\sigma}_{\text{Th}}} \cdot \frac{X_U \lambda_U n_\nu(\text{U}) \mu_{\text{Th}}}{X_{\text{Th}} \lambda_{\text{Th}} n_\nu(\text{Th}) \mu_U}, \quad (8-21)$$

where  $\tilde{\sigma}$ 's stands for the effective cross section of HPE  $i$ ,

$$\tilde{\sigma}_i = \int \sigma(E) f_i(E) dE / \int f_i(E) dE. \quad (8-22)$$

For the BSE model used in the prediction of geoneutrinos at Jinping<sup>[131]</sup>, the Th/U geoneutrino ratio  $R(\text{Th}/\text{U})_{\text{IBD}} = 0.27$ , and the HPE mass ratio  $R(\text{Th}/\text{U})_m = 4.1$ .

Fixing the reactor neutrino spectrum and set the reactor neutrino rate as a free parameter, we obtained the sensitivities to the geoneutrino flux and the Th/U ratio, as summarized in Table 8.7.

Table 8.7 Geoneutrino sensitivities at Jinping.

Measurement	Precision (%)
$N_{geo}$	4.6%
$R(\text{Th}/\text{U})_{\text{IBD}}$	26.3%

### 8.5.3 BSE Model Test

The BSE models differ on the HPE abundance in mantle and give different predictions for the geoneutrino flux. With the geoneutrino measurement precision at Jinping, the distinguishing power on BSE models is plotted in Fig. 8.8. This figure is difficult to understand due to the cross-over of geological information and the experimental measurement. Basically, the horizontal axis shows the radiogenic heat, the vertical axis shows the expected geoneutrino flux, the oblique lines and bands represent the theoretical prediction on the correlation between  $x$  and  $y$ , and the horizontal structure represents the experimental measurement.

The horizontal solid line stands for the expected geoneutrino measurement at Jinping, and the gray band within the horizontal dashed lines represent the uncertainties. The oblique solid line shows the response between the radiogenic heat and the expected geoneutrino flux under the assumption of a fixed potassium, thorium, and uranium ratio. The starting point of the oblique solid line marks the geoneutrino flux and radiogenic heat from the crust at 49.0 TNU and 7.4 TW. The oblique dashed lines represent the uncertainties introduced by the crustal geoneutrinos. Different colored bands stand for different BSE models, with blue for the low-Q<sup>[61]</sup>, green for the medium-Q<sup>[62]</sup>, and red for the high-Q model<sup>[63]</sup>. The horizontal width of the bands indicates the theoretical uncertainties of these models, and the corresponding intercepts on the  $y$ -axis represent the uncertainties in the prediction of geoneutrino flux. As the geoneutrino flux calculation employs the medium-Q model, the horizontal solid line intercept with the oblique solid line at the center of green band representing medium-Q model.

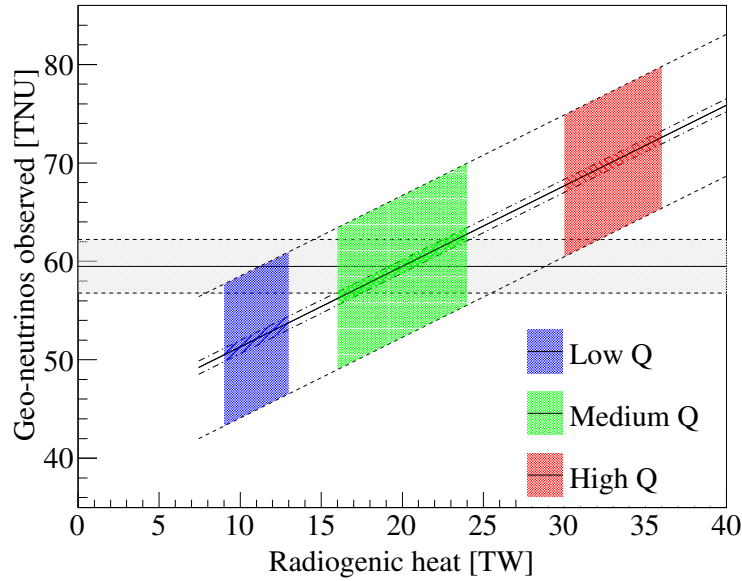


Figure 8.8 The theoretical predictions on the correlation between the radiogenic heat and the expected geoneutrino flux, and the expected experimental measurement precision. Further explanations included in the text.

Besides the experimental measurement uncertainty in the horizontal dashed lines and the model uncertainty, the main uncertainties plotted in Fig. 8.8 actually come from the calculation of crustal geoneutrinos. As mentioned in Section 8.2, the crustal geoneutrino uncertainties are contributed by the Earth model ( $\pm 15.0\%$ ) as well as the oscillation parameters ( $^{+1.8\%}_{-1.7\%}$ ). The Earth model uncertainties originate from the fact that even the crust is not thoroughly understood, due to the limitation of geological data. A more precise global crust model will surely help to reduce of the uncertainty but is not a short-term task.

About half of the geoneutrino events detected at the experiment site actually come within 300 km around the detector<sup>[131]</sup>. A precise crust map of the local environment can reduce the uncertainty on the crustal geoneutrino flux significantly. Seismological and geological data around Jinping are abundant, owing to the studies on the earthquakes. However, the crust around Jinping is very thick as it is located on the Tibetan Plateau, which complicates the construction of a precise local model. A close collaboration between physicist and geoscientists is required towards the aim. For future prospect on the crustal geoneutrino uncertainties, if we expect an optimistic uncertainty of  $\pm 1.0\%$  in the Earth model and  $\pm 1.0\%$  from the oscillation parameters (mainly  $\theta_{12}$ ), the oblique dashed lines will shrink to the oblique dashed dotted lines in Fig. 8.8, significantly increasing the discrimination power of geoneutrinos towards the BSE models.



## 8.6 Further Discussion

In this section, we first discuss on detector requisite for the geoneutrino detection, then presents the test on the hypothesis of the Earth core fission neutrinos.

### 8.6.1 Requisites for the Detector

We scanned the detector parameters including live-time and energy resolution to obtain their influence on geoneutrino flux and Th/U ratio sensitivities. The live-time is expressed in kiloton  $\times$  days, so it is equivalent to target mass.

Figure 8.9 shows the geoneutrino flux and Th/U ratio sensitivities against the resolution and target mass. The left figure shows the sensitivity against energy resolution and the right figure shows the sensitivity against the target mass. The black points show the sensitivity on Th/U ratio, and the blue points show the sensitivity on geoneutrino flux. The lines are simply spline interpolations.

The precisions of both measurements are sensitive to the target mass and less sensitive to the energy resolution as far as this is a kiloton level detector and the light yield is at the level of scintillation light ( $\sim 100$  p.e./MeV). Therefore, on a practical basis, and also to satisfy the requisites of other studies especially for solar neutrinos<sup>[139]</sup>, the detector setup of a liquid scintillator experiment at Jinping is assumed to be 3 kiloton fiducial mass for IBD, 1,500 days live-time, and 500 p.e./MeV resolution.

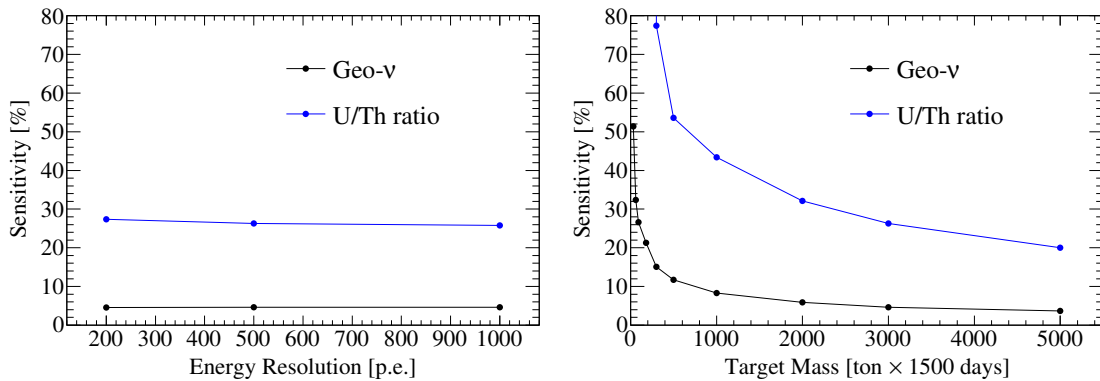


Figure 8.9 Geoneutrino sensitivity and detector requisites. Explanations can be found in text.

### 8.6.2 Earth Core Fission Neutrinos

The hypothesis from J. M. Herndon et al. claims that there are natural fission reactors in the inner core of the Earth. These reactors are also called geo-reactors. Due to the

small size of the inner core compared to other layers of the Earth, the distribution of geo-reactors does not influence the predicted  $\bar{\nu}_e$  flux or spectrum.

To sustain the Earth magnetic field and its variation, the total thermal power of geoneutrinos must be between 3 and 30 TW. Besides, the fuel of such a long-term self-burning reactor should compose of 74.6%  $^{235}\text{U}$  and 24.9%  $^{238}\text{U}$ <sup>[140]</sup>. From this assumption, the energy spectrum of  $\bar{\nu}_e$ 's from geo-reactors should resemble the spectra of reactor neutrinos from nuclear power plants.

Borexino<sup>[71]</sup> and KamLAND<sup>[69]</sup> have set an upper limit of 4.5 TW and 3.7 TW respectively for the thermal power of earth core fission reactors with 95% confidence level. Similarly, at Jinping we performed the analysis and obtained the upper limit by the CLs+b method<sup>[141]</sup>. With the proposed 3 kiloton detector, it takes Jinping only 300 days to excluded the 3 TW geo-reactor hypothesis by setting an upper limit of 1.4 TW at 95% confidence level.

## Chapter 9 Summary and Outlook

This section presents the summaries and discussions on the prospects of the three studies in this thesis.

### 9.1 Summary

Based on the low energy signal and neutron production from neutrino interactions, we presented three studies, namely the SRN search, the atmospheric  $\nu$ -O NCQE interaction measurement, and the geoneutrino sensitivity simulation.

The detection of SRNs will shed light on star formation and supernova burst mechanism as well as the neutrino physics. However, SRNs have not yet been observed. In this thesis, SRNs are searched for in a 2,778-day data sample in SK-IV, a Cherenkov detector via IBD channel. We optimized the neutron tagging technique by two partial reconstruction methods on the neutron vertices and tuned the cut towards the best significance. The total SRN signal efficiency is improved from 8.8% to 19.3%. By tagging the neutron product, we found 29 SRN candidates in the energy range of [9.3, 11.3] MeV, with  $33.7 \pm 4.6$  events expected. This is consistent with null-signal hypothesis, and a model-independent upper limit is derived for every energy bin.

The atmospheric  $\nu$ -O NCQE interaction forms a crucial background to the SRN and other rare signal searches using the IBD channel, due to the  $\gamma - n$  signal it produces, mimicking the IBD  $\beta - n$  pair. This cross section is not well-known, and was first measured by the T2K collaboration, but the T2K neutrino beam profile is different from the atmospheric neutrino profile. This thesis presents a direct measurement of the atmospheric  $\nu$ -O NCQE cross section based on the neutron tagging and the detection of the de-excitation  $\gamma$  from the residual nuclei. The NCQE cross section is measured to be  $(0.95 \pm 0.12(\text{stat.})^{+0.49}_{-0.32}(\text{sys.})) \times 10^{-38} \text{ cm}^2$ , averaged over the atmospheric neutrino energy range between 160 MeV and 10 GeV. This result is consistent within uncertainties with the theoretical prediction of  $1.14 \times 10^{-38} \text{ cm}^2$  by the Ankowski model.

Geoneutrinos are also low-energy  $\bar{\nu}_e$ 's of which the main detection channel is IBD. The detection of geoneutrinos can provide constraint on the Earth heat budget and resolve the BSE HPE abundance which is difficult to derive otherwise. The main background to geoneutrinos is the reactor neutrinos from man-made nuclear power plants, and the loca-

tion of neutrino observatory is a key issue in the signal/background ratio. We simulated a 3-kiloton liquid scintillator detector at Jinping, calculated the expected geoneutrino flux and reactor neutrino backgrounds there. The expected number of geoneutrino IBD events at Jinping for 1,500 days live time is 414.5 and the number of reactor neutrino background within the signal energy window of [1.8, 3.3] MeV is 60.4. The sensitivities is 4.6% towards the geoneutrino flux measurement, and 26.3% towards the Th/U ratio. To achieve such a goal, several requirements on the detector design, including the detector size and the energy resolution, are proposed.

## 9.2 Outlook

The common features of the three studies presented in this thesis include the low energy signal + neutron signature.

Among them, the SRN study is a rare signal search, and the signal-background ratio is important. For the SRN analysis, the background reduction is performed at a cost of the signal efficiency loss. The optimization in the neutron tagging presented in this thesis nearly doubled the signal efficiency of SRN signal. Still, further improvement can be achieved from the hardware level. The SK-Gd project<sup>[107]</sup> plans to load 0.2%  $\text{Gd}_2(\text{SO}_4)_3$  into the water tank of SK. The shorter lifetime and the greater energy of emitted  $\gamma$ 's reaching 8 MeV makes the neutron tagging in Gd loaded water much easier than in pure water. It is estimated that the neutron tagging efficiency will reach 90%<sup>[107]</sup>. The SK tank is now (2018) under refurbishment for the Gd loading. After the upgrading, the SK-Gd project is promising to make an observation of SRN within 10 years of data taking.

The NCQE interaction from the atmospheric neutrinos will still form a strong background for the SRN search even with Gd loaded. Due to the suppression of accidental background in SK-Gd phase, the NCQE background will become the major background, and a precise measurement of its cross section is crucial for the SRN search. The present measurement on the NCQE cross section is mainly limited by systematic uncertainties from the atmospheric neutrino flux, the cross section for other NC processes, the  $\gamma$  emission, and the neutron tagging. Future atmospheric neutrino experiments such as Hyper-Kamiokande<sup>[108]</sup>, the neutrino beam-line detectors<sup>[122–125]</sup>, and related nuclear experiments<sup>[126]</sup> will further constrain the systematic uncertainties.

The geoneutrino observation has been claimed by Borexino experiment<sup>[72]</sup>, and the next goal, precise measurement, can be easily achieved by placing a kiloton level neutrino

experiment at Jinping. Further consideration is about the component of geoneutrinos, from the crust and the mantle. For the BSE model, the crustal abundance of HPEs can be extracted from drills, while for the mantle part, neutrinos are the only probe. In this case, observation of purely mantle neutrinos is a crucial topic. An oceanic neutrino observatory project HANOHANO<sup>[142]</sup>, which removes the crustal geoneutrinos as well as the reactor neutrino backgrounds simply by the distance, was proposed in 2011, but abandoned later due to the difficulty in construction and operation. One alternative solution is to observe the direction of geoneutrinos, thus to perform a tomographic analysis on the components of geoneutrinos. However, the direction information of the incident neutrino in the IBD interaction is carried by the neutron, which is negligible compared to the mass of neutron. Several projects have been pushing forward the detection by loading lithium into liquid scintillator<sup>[143,144]</sup>, but so far none of them has ever succeeded on an event by event basis. Another possible method is to detect the geoneutrinos via elastic scattering on electrons. This channel has smaller cross section compared to IBD, but the direction information is carried by the outgoing electron, which can be detected via for example Cherenkov photon. For this method, the main problem is the low energy of geoneutrinos, which results in the multi-scattering of the electron. Two different approaches have been employed. The first is to reduce the multi-scattering by changing the detection material into gas, with lower density thus lower multi-scattering. This requires the detector to be a segmented TPC<sup>[145]</sup>. The other approach is pattern identification based, which does not require heavy modification on the detector designation of typical liquid scintillation detectors<sup>[146]</sup>. We are looking forward to all of those projects.

## Reference

- [1] Pauli W. Letter to the radioactive ladies and gentlemen. Conference of the District Society in Tübingen. Physical Institute of the Federal Institute of Technology, 1930.
- [2] Cowan C L, Reines F, Harrison F B, et al. Detection of the free neutrino: a confirmation. *Science*, 1956, 124(3212):103–104.
- [3] Schael S, et al. Precision electroweak measurements on the  $Z$  resonance. *Phys. Rept.*, 2006, 427:257–454.
- [4] Kraus C, Bornschein B, Bornschein L, et al. Final results from phase ii of the mainz neutrino mass search in tritium  $\beta$  decay. *The European Physical Journal C - Particles and Fields*, 2005, 40(4):447–468.
- [5] Fukuda Y, et al. Evidence for oscillation of atmospheric neutrinos. *Phys. Rev. Lett.*, 1998, 81:1562–1567.
- [6] Ahmad Q R, et al. Direct evidence for neutrino flavor transformation from neutral current interactions in the Sudbury Neutrino Observatory. *Phys. Rev. Lett.*, 2002, 89:011301.
- [7] Glashow S L. Partial-symmetries of weak interactions. *Nuclear Physics*, 1961, 22(4):579 – 588.
- [8] Aguilar-Arevalo A, et al. Evidence for neutrino oscillations from the observation of anti-neutrino(electron) appearance in a anti-neutrino(muon) beam. *Phys. Rev.*, 2001, D64:112007.
- [9] Aguilar-Arevalo A A, et al. A Search for electron neutrino appearance at the  $\Delta m^2 \sim 1\text{eV}^2$  scale. *Phys. Rev. Lett.*, 2007, 98:231801.
- [10] Aguilar-Arevalo A A, et al. Event Excess in the MiniBooNE Search for  $\bar{\nu}_\mu \rightarrow \bar{\nu}_e$  Oscillations. *Phys. Rev. Lett.*, 2010, 105:181801.
- [11] Bahcall J N, Krastev P I. Does the sun appear brighter at night in neutrinos? *Phys. Rev.*, 1997, C56:2839–2857.
- [12] Formaggio J A, Zeller G P. From eV to EeV: Neutrino Cross Sections Across Energy Scales. *Rev. Mod. Phys.*, 2012, 84:1307–1341.
- [13] Fogli G L, Lisi E, Mirizzi A, et al. Probing supernova shock waves and neutrino flavor transitions in next-generation water-Cherenkov detectors. *JCAP*, 2005, 0504:002.
- [14] Vogel P, Beacom J F. Angular distribution of neutron inverse beta decay,  $\bar{\nu}_e + \vec{p} \rightarrow e^+ + n$ . *Phys. Rev. D*, 1999, 60:053003.
- [15] Ankowski A M, Benhar O, Mori T, et al. Analysis of  $\gamma$ -ray production in neutral-current neutrino-oxygen interactions at energies above 200 MeV. *Phys. Rev. Lett.*, 2012, 108:052505.
- [16] Abe K, et al. Measurement of the neutrino-oxygen neutral-current interaction cross section by observing nuclear deexcitation  $\gamma$  rays. *Phys. Rev.*, 2014, D90(7):072012.
- [17] Lemaître A G. Contributions to a British Association Discussion on the Evolution of the Universe. *Nature*, 1931, 128:704–706.

- 
- [18] Long A J, Lunardini C, Sabancilar E. Detecting non-relativistic cosmic neutrinos by capture on tritium: phenomenology and physics potential. *Journal of Cosmology and Astroparticle Physics*, 2014, 2014(08):038.
- [19] Aartsen M G, et al. Observation of High-Energy Astrophysical Neutrinos in Three Years of IceCube Data. *Phys. Rev. Lett.*, 2014, 113:101101.
- [20] Giunti C, Kim C W. *Fundamentals of neutrino physics and astrophysics*. Oxford: Oxford university press, 2007.
- [21] Takahashi K, Sato K, Burrows A, et al. Supernova neutrinos, neutrino oscillations, and the mass of the progenitor star. *Phys. Rev. D*, 2003, 68:113009.
- [22] Padmanabhan T. *Theoretical Astrophysics: Volume 2, Stars and Stellar Systems*. Cambridge: Cambridge University Press, 2001.
- [23] Kotake K, Sato K, Takahashi K. Explosion mechanism, neutrino burst and gravitational wave in core-collapse supernovae. *Reports on Progress in Physics*, 2006, 69(4):971.
- [24] Cappellaro E, Evans R, Turatto M. A new determination of supernova rates and a comparison with indicators for galactic star formation. *Astron. Astrophys.*, 1999, 351:459.
- [25] Totani T, Sato K. Spectrum of the relic neutrino background from past supernovae and cosmological models. *Astropart. Phys.*, 1995, 3:367–376.
- [26] Totani T, Sato K, Yoshii Y. Spectrum of the supernova relic neutrino background and evolution of galaxies. *Astrophys. J.*, 1996, 460:303–312.
- [27] Malaney R A. Evolution of the cosmic gas and the relic supernova neutrino background. *Astropart. Phys.*, 1997, 7:125–136.
- [28] Hartmann D, Woosley S. The cosmic supernova neutrino background. *Astroparticle Physics*, 1997, 7(1–2):137 – 146.
- [29] Kaplinghat M, Steigman G, Walker T P. The Supernova relic neutrino background. *Phys. Rev.*, 2000, D62:043001.
- [30] Strigari L E, Kaplinghat M, Steigman G, et al. The Supernova relic neutrino backgrounds at KamLAND and Super-Kamiokande. *JCAP*, 2004, 0403:007.
- [31] Ando S, Sato K, Totani T. Detectability of the supernova relic neutrinos and neutrino oscillation. *Astropart. Phys.*, 2003, 18:307–318.
- [32] Horiuchi S, Beacom J F, Dwek E. The Diffuse Supernova Neutrino Background is detectable in Super-Kamiokande. *Phys. Rev.*, 2009, D79:083013.
- [33] Fukugita M, Kawasaki M. Constraints on the star formation rate from supernova relic neutrino observations. *Mon. Not. Roy. Astron. Soc.*, 2003, 340:L7.
- [34] Lunardini C. Diffuse neutrino flux from failed supernovae. *Phys. Rev. Lett.*, 2009, 102:231101.
- [35] Ando S, Sato K. Relic neutrino background from cosmological supernovae. *New J. Phys.*, 2004, 6:170.
- [36] Bethe H A. Supernova mechanisms. *Rev. Mod. Phys.*, 1990, 62:801–866.
- [37] Pagliaroli G, Vissani F, Costantini M L, et al. Improved analysis of SN1987A antineutrino events. *Astropart. Phys.*, 2009, 31:163–176.

- [38] Hirata K, et al. Observation of a Neutrino Burst from the Supernova SN 1987a. *Phys. Rev. Lett.*, 1987, 58:1490–1493. [727(1987)].
- [39] Bionta R M, Blewitt G, Bratton C B, et al. Observation of a neutrino burst in coincidence with supernova 1987a in the large magellanic cloud. *Phys. Rev. Lett.*, 1987, 58:1494–1496.
- [40] Totani T, Sato K, Dalhed H E, et al. Future detection of supernova neutrino burst and explosion mechanism. *Astrophys. J.*, 1998, 496:216–225.
- [41] Keil M T, Raffelt G G, Janka H T. Monte Carlo study of supernova neutrino spectra formation. *Astrophys. J.*, 2003, 590:971–991.
- [42] Takahashi K, Watanabe M, Sato K, et al. Effects of neutrino oscillation on the supernova neutrino spectrum. *Phys. Rev. D*, 2001, 64:093004.
- [43] Abe K, et al. Real-Time Supernova Neutrino Burst Monitor at Super-Kamiokande. *Astropart. Phys.*, 2016, 81:39–48.
- [44] Antonioli P, et al. SNEWS: The Supernova Early Warning System. *New J. Phys.*, 2004, 6:114.
- [45] Zhang H. Study of low energy electron anti-neutrinos at super-kamiokande iv[博士学位论文]. Beijing: Tsinghua University, 2012.
- [46] Zhang Y. Experimental studies of supernova relic neutrinos at super-kamiokande-iv[博士学位论文]. Beijing: Tsinghua University, 2015.
- [47] Malek M, Morii M, Fukuda S, et al. Search for supernova relic neutrinos at super-kamiokande. *Phys. Rev. Lett.*, 2003, 90:061101.
- [48] Bays K R. Search for the diffuse supernova neutrino background at super-kamiokande[博士学位论文]. California: University of California, Irvine, 2012.
- [49] Bays K, et al. Supernova Relic Neutrino Search at Super-Kamiokande. *Phys. Rev.*, 2012, D85:052007.
- [50] Lipsy Y, Kushida E, Incerti T. The fukushima disaster and japan' s nuclear plant vulnerability in comparative perspective. *Environmental Science & Technology*, 2013, 47:6082.
- [51] Tilley D R, Kelley J H, Godwin J L, et al. Energy levels of light nuclei A=8,9,10. *Nucl. Phys.*, 2004, A745:155–362.
- [52] Zhang Y, et al. First measurement of radioactive isotope production through cosmic-ray muon spallation in Super-Kamiokande IV. *Phys. Rev.*, 2016, D93(1):012004.
- [53] Gando A, et al. A study of extraterrestrial antineutrino sources with the KamLAND detector. *Astrophys. J.*, 2012, 745:193.
- [54] Zhang H, et al. Supernova Relic Neutrino Search with Neutron Tagging at Super-Kamiokande-IV. *Astropart. Phys.*, 2015, 60:41–46.
- [55] Eguchi K, et al. First results from KamLAND: Evidence for reactor anti-neutrino disappearance. *Phys. Rev. Lett.*, 2003, 90:021802.
- [56] Shirai J. KamLAND-Zen. *PoS*, 2018, NEUTEL2017:027.
- [57] McDonough W, Sramek O. Neutrino geoscience, news in brief. *Environmental Earth Sciences*, 2014, 71(8):3787–3791.
- [58] Jaupart C, Labrosse S, Mareschal J C. 7.06 - temperatures, heat and energy in the mantle of the earth. In: Schubert G, (eds.). *Treatise on Geophysics*. Amsterdam: Elsevier, 2007: 253 – 303.



- [59] Davies J H, Davies D R. Earth's surface heat flux. *Solid Earth*, 2010, 1(1):5–24.
- [60] Huang Y, Chubakov V, Mantovani F, et al. A reference earth model for the heat-producing elements and associated geoneutrino flux. *Geochemistry, Geophysics, Geosystems*, 2013, 14(6):2003–2029.
- [61] Javoy M, Kaminski E, Guyot F, et al. The chemical composition of the earth: Enstatite chondrite models. *Earth and Planetary Science Letters*, 2010, 293(3–4):259 – 268.
- [62] Jr R A, McDonough W F. Chemical variations and regional diversity observed in {MORB}. *Chemical Geology*, 2010, 271(1–2):70 – 85.
- [63] Boyle A P. *Geodynamics—applications of continuum physics to geological problems* by donald l. turcotte and gerald schubert. wiley, new york, 1982. no. of pages: 450. price: €12.20 (hardback). *Geological Journal*, 1984, 19(3):303–303.
- [64] Hollenbach D F, Herndon J M. Deep-earth reactor: Nuclear fission, helium, and the geomagnetic field. *Proc. Nat. Acad. Sci*, 2001, 98:11085.
- [65] Fiorentini G, Fogli G L, Lisi E, et al. Mantle geoneutrinos in kamland and borexino. *Phys. Rev. D*, 2012, 86:033004.
- [66] Raghavan R S. Detecting a nuclear fission reactor at the center of the earth. *ArXiv e-prints*, 2002..
- [67] Araki T, et al. Experimental investigation of geologically produced antineutrinos with KamLAND. *Nature*, 2005, 436:499–503.
- [68] Gando A, et al. Partial radiogenic heat model for Earth revealed by geoneutrino measurements. *Nature Geo.*, 2011, 4:647–651.
- [69] Gando A, et al. Reactor On-Off Antineutrino Measurement with KamLAND. *Phys. Rev.*, 2013, D88(3):033001.
- [70] Bellini G, et al. Observation of Geo-Neutrinos. *Phys. Lett.*, 2010, B687:299–304.
- [71] Bellini G, et al. Measurement of geo-neutrinos from 1353 days of Borexino. *Phys. Lett.*, 2013, B722:295–300.
- [72] Agostini M, et al. Spectroscopy of geoneutrinos from 2056 days of Borexino data. *Phys. Rev.*, 2015, D92(3):031101.
- [73] Alimonti G, et al. The liquid handling systems for the Borexino solar neutrino detector. *Nucl. Instrum. Meth.*, 2009, A609:58–78.
- [74] Alimonti G, et al. The Borexino detector at the Laboratori Nazionali del Gran Sasso. *Nucl. Instrum. Meth.*, 2009, A600:568–593.
- [75] Andringa S, et al. Current Status and Future Prospects of the SNO+ Experiment. *Adv. High Energy Phys.*, 2016, 2016:6194250.
- [76] Han R, Li Y F, Zhan L, et al. Potential of Geo-neutrino Measurements at JUNO. *Chin. Phys.*, 2016, C40(3):033003.
- [77] An F, et al. Neutrino Physics with JUNO. *J. Phys.*, 2016, G43(3):030401.
- [78] Cicenas B, Solomey N. The HANO HANO Detector and Ongoing Research and Development. *Phys. Procedia*, 2012, 37:1324–1331.
- [79] Beacom J F, et al. Letter of Intent: Jinping Neutrino Experiment. *ArXiv e-prints*, 2016..

- [80] Fukuda Y, et al. The Super-Kamiokande detector. *Nucl. Instrum. Meth.*, 2003, A501:418–462.
- [81] Suzuki A, Mori M, Kaneyuki K, et al. Improvement of 20 in. diameter photomultiplier tubes. *Nuclear Instruments and Methods in Physics Research Section A: Accelerators, Spectrometers, Detectors and Associated Equipment*, 1993, 329(1):299 – 313.
- [82] Nakano Y. 8b solar neutrino spectrum measurement using super-kamiokande iv[博士学位论文]. Tokyo: University of Tokyo, 2016.
- [83] Takeuchi Y, et al. Measurement of radon concentrations at Super-Kamiokande. *Phys. Lett.*, 1999, B452:418–424.
- [84] Yamada S, et al. Commissioning of the new electronics and online system for the Super-Kamiokande experiment. *IEEE Trans. Nucl. Sci.*, 2010, 57:428–432.
- [85] Fukuda S, Fukuda Y, Hayakawa T, et al. The super-kamiokande detector. *Nuclear Instruments and Methods in Physics Research Section A: Accelerators, Spectrometers, Detectors and Associated Equipment*, 2003, 501(2):418 – 462.
- [86] Abe K, et al. Calibration of the Super-Kamiokande Detector. *Nucl. Instrum. Meth.*, 2014, A737:253–272.
- [87] Nakahata M, Fukuda Y, Hayakawa T, et al. Calibration of super-kamiokande using an electron linac. *Nuclear Instruments and Methods in Physics Research Section A: Accelerators, Spectrometers, Detectors and Associated Equipment*, 1999, 421(1):113 – 129.
- [88] Blaufuss E, et al. N-16 as a calibration source for Super-Kamiokande. *Nucl. Instrum. Meth.*, 2001, A458:638–649.
- [89] Smy M. Low Energy Event Reconstruction and Selection in Super-Kamiokande-III. *Proceedings, 30th International Cosmic Ray Conference (ICRC 2007): Merida, Yucatan, Mexico, July 3-11, 2007, volume 5, 2007. 1279–1282.*
- [90] Conner Z. A study of solar neutrinos using the super-kamiokande detector[博士学位论文]. Maryland: University of Maryland, 1997.
- [91] Desai S. High energy neutrino astrophysics with super-kamiokande[博士学位论文]. Boston: University of Boston, 2004.
- [92] Li S W, Beacom J F. First calculation of cosmic-ray muon spallation backgrounds for MeV astrophysical neutrino signals in Super-Kamiokande. *Phys. Rev.*, 2014, C89:045801.
- [93] Shiozawa M. Search for proton decay  $p \rightarrow e + \pi^0$  in a large water cherenkov detector[博士学位论文]. Tokyo: University of Tokyo, 1999.
- [94] Cokinos D, Melkonian E. Measurement of the 2200 m/sec neutron-proton capture cross section. *Phys. Rev. C*, 1977, 15:1636–1643.
- [95] Agostinelli S, et al. GEANT4: A Simulation toolkit. *Nucl. Instrum. Meth.*, 2003, A506:250–303.
- [96] Watanabe H, et al. First Study of Neutron Tagging with a Water Cherenkov Detector. *Astropart. Phys.*, 2009, 31:320–328.
- [97] Irvine T J. Development of neutron-tagging techniques and application to atmospheric neutrino oscillation analysis in super-kamiokande[博士学位论文]. Tokyo: University of Tokyo, 2014.

- [98] Speckmayer P, Hocker A, Stelzer J, et al. The toolkit for multivariate data analysis, TMVA 4. *J. Phys. Conf. Ser.*, 2010, 219:032057.
- [99] Honda M, Kajita T, Kasahara K, et al. Calculation of atmospheric neutrino flux using the interaction model calibrated with atmospheric muon data. *Phys. Rev.*, 2007, D75:043006.
- [100] Honda M, Kajita T, Kasahara K, et al. Improvement of low energy atmospheric neutrino flux calculation using the JAM nuclear interaction model. *Phys. Rev.*, 2011, D83:123001.
- [101] Richard E, et al. Measurements of the atmospheric neutrino flux by Super-Kamiokande: energy spectra, geomagnetic effects, and solar modulation. *Phys. Rev.*, 2016, D94(5):052001.
- [102] Ferrari A, Sala P R, Fasso A, et al. FLUKA: A multi-particle transport code (Program version 2005). 2005..
- [103] Battistoni G, Ferrari A, Montaruli T, et al. The atmospheric neutrino flux below 100-MeV: The FLUKA results. *Astropart. Phys.*, 2005, 23:526–534.
- [104] Agency I A E. <http://www.iaea.org/>, 2015.
- [105] Rolke W A, Lopez A M, Conrad J. Limits and confidence intervals in the presence of nuisance parameters. *Nucl. Instrum. Meth.*, 2005, A551:493–503.
- [106] Brun R, Rademakers F. ROOT: An object oriented data analysis framework. *Nucl. Instrum. Meth.*, 1997, A389:81–86.
- [107] Sekiya H. Supernova neutrinos in SK-Gd and other experiments. *J. Phys. Conf. Ser.*, 2017, 888(1):012041.
- [108] Abe K, et al. Letter of Intent: The Hyper-Kamiokande Experiment — Detector Design and Physics Potential —. 2011..
- [109] Langanke K, Vogel P, Kolbe E. Signal for supernova muon-neutrino and tau-neutrino neutrinos in water Cherenkov detectors. *Phys. Rev. Lett.*, 1996, 76:2629–2632.
- [110] Beacom J F, Vogel P. Mass signature of supernova muon-neutrino and tau-neutrino neutrinos in Super-Kamiokande. *Phys. Rev.*, 1998, D58:053010.
- [111] Kolbe E, Langanke K, Vogel P. Estimates of weak and electromagnetic nuclear decay signatures for neutrino reactions in Super-Kamiokande. *Phys. Rev.*, 2002, D66:013007.
- [112] Hayato Y. A neutrino interaction simulation program library NEUT. *Acta Phys. Polon.*, 2009, B40:2477–2489.
- [113] Ueno K. Study of neutral-current de-excitation gamma-rays with the T2K neutrino beam[D]. The University of Tokyo, 2012.
- [114] Huang K. Measurement of the Neutrino-Oxygen Neutral Current Quasi-elastic Interaction Cross-section by Observing Nuclear De-excitation  $\gamma$ -rays in the T2K Experiment[D]. Kyoto University, 2016.
- [115] Benhar O, Farina N, Nakamura H, et al. Electron- and neutrino-nucleus scattering in the impulse approximation regime. *Phys. Rev.*, 2005, D72:053005.
- [116] Bradford R, Bodek A, Budd H S, et al. A New parameterization of the nucleon elastic form-factors. *Nucl. Phys. Proc. Suppl.*, 2006, 159:127–132. [,127(2006)].
- [117] Kobayashi K, et al. De-excitation gamma-rays from the s-hole state in N-15 associated with proton decay in O-16. 2006..

- [118] Brun R, Bruyant F, Maire M, et al. GEANT3. 1987..
- [119] Zeitnitz C, Gabriel T A. The GEANT - CALOR interface and benchmark calculations of ZEUS test calorimeters. Nucl. Instrum. Meth., 1994, A349:106–111.
- [120] Smy M. Low Energy Event Reconstruction and Selection in Super-Kamiokande-III. Proceedings, 30th International Cosmic Ray Conference (ICRC 2007): Merida, Yucatan, Mexico, July 3-11, 2007, volume 5, 2007. 1279–1282.
- [121] Watanabe H, et al. First Study of Neutron Tagging with a Water Cherenkov Detector. Astropart. Phys., 2009, 31:320–328.
- [122] Abe K, et al. Measurement of the inclusive charged current cross section on carbon in the near detector of the T2K experiment. Phys. Rev., 2013, D87(9):092003.
- [123] Abe K, et al. First measurement of the muon neutrino charged current single pion production cross section on water with the T2K near detector. Phys. Rev., 2017, D95(1):012010.
- [124] Aguilar-Arevalo A A, et al. Measurement of Neutrino-Induced Charged-Current Charged Pion Production Cross Sections on Mineral Oil at  $E_\nu \sim 1$  GeV. Phys. Rev., 2011, D83:052007.
- [125] McGivern C L, et al. Cross sections for  $\nu_\mu$  and  $\bar{\nu}_\mu$  induced pion production on hydrocarbon in the few-GeV region using MINERvA. Phys. Rev., 2016, D94(5):052005.
- [126] Ou I, et al. Measurement of  $\gamma$ -rays from Giant Resonances of  $^{16}\text{O}$  and  $^{12}\text{C}$  with Application to Supernova Neutrino Detection. JPS Conf. Proc., 2016, 12:010048.
- [127] Wan L, Hussain G, Wang Z, et al. Geoneutrinos at jinping: Flux prediction and oscillation analysis. Phys. Rev. D, 2017, 95:053001.
- [128] Enomoto S. Experimental study of geoneutrinos with KamLAND. Neutrino geophysics. Proceedings, Conference, Neutrino Sciences 2005, Honolulu, USA, December 14-16, 2005, 2005. 131–146.
- [129] Ludhova L, Zavatarelli S. Studying the Earth with Geoneutrinos. Advances in High Energy Physics, 2013, 2013:425693.
- [130] Laske G, Masters G, Ma Z, et al. Update on CRUST1.0 - A 1-degree Global Model of Earth's Crust. Geophys. Res. Abstracts, 2013, 15(Abstract):EGU2013–2658.
- [131] Sramek O, Roskovec B, Wipperfurth S A, et al. Revealing the Earth's mantle from the tallest mountains using the Jinping Neutrino Experiment. Scientific Reports, 2016, 6(33034):33034.
- [132] Olive K A. Review of Particle Physics. Chin. Phys., 2016, C40(10):100001.
- [133] Birks J B. Scintillations from organic crystals: Specific fluorescence and relative response to different radiations. Proceedings of the Physical Society. Section A, 1951, 64(10):874.
- [134] Lebanowski L, Wan L, Ji X, et al. An efficient energy response model for liquid scintillator detectors. Nucl. Instrum. Meth., 2018, A890:133–141.
- [135] Li M, Guo Z, Yeh M, et al. Separation of Scintillation and Cherenkov Lights in Linear Alkyl Benzene. Nucl. Instrum. Meth., 2016, A830:303–308.
- [136] Huber P. On the determination of anti-neutrino spectra from nuclear reactors. Phys. Rev., 2011, C84:024617. [Erratum: Phys. Rev.C85,029901(2012)].
- [137] Mueller T A, Lhuillier D, Fallot M, et al. Improved predictions of reactor antineutrino spectra. Phys. Rev. C, 2011, 83:054615.

- [138] Baldoncini M, Callegari I, Fiorentini G, et al. Reference worldwide model for antineutrinos from reactors. *Phys. Rev. D*, 2015, 91:065002.
- [139] Beacom J F, et al. Physics prospects of the Jinping neutrino experiment. *Chin. Phys.*, 2017, C41(2):023002.
- [140] Herndon J M, Edgerley D A. Background for terrestrial antineutrino investigations: Radionuclide distribution, georeactor fission events, and boundary conditions on fission power production. Submitted to: *Proc. Roy. Soc. Lond. A Math. Phys. Eng. Sci.*, 2005..
- [141] Read A L. Presentation of search results: the cl s technique. *Journal of Physics G: Nuclear and Particle Physics*, 2002, 28(10):2693.
- [142] Cicenias B, Solomey N. The HANOHANO Detector and Ongoing Research and Development. *Phys. Procedia*, 2012, 37:1324–1331.
- [143] Shimizu I. Directional measurement of anti-neutrinos. *Nucl. Phys. Proc. Suppl.*, 2007, 168:147–149.
- [144] Tanaka H, Watanabe H. (6)Li-loaded directionally sensitive anti-neutrino detector for possible geo-neutrino-graphic imaging applications. *Scientific Reports*, 2014, 4:4708.
- [145] Leyton M, Dye S, Monroe J. Exploring the hidden interior of the Earth with directional neutrino measurements. *Nature Commun.*, 2017, 8:15989.
- [146] Wang Z, Chen S. Reveal the Mantle and K-40 Components of Geoneutrinos with Liquid Scintillator Cherenkov Neutrino Detectors. 2017..

## Acknowledgement

First, I would like to express my gratitude to my supervisor Prof. Shaomin Chen. He introduced me to field of neutrino physics and the collaboration of Super-Kamiokande. He has always been supportive and understanding during the entire course of my graduate study. Without his valuable comments and detailed suggestions, I would have accomplished much less.

I am grateful to Masayuki Nakahata-san, the spokesperson for the SK collaboration, who inspired me with his physics insight. I would like to acknowledge Michael Smy and Takeuchi-san. From the numerous email exchanges and comments, I acquired a much deeper understanding of LOWE group analysis. I also wish to thank Moriyama-san, Mine-san, and Luis Labarga for their advisorship when I started my analysis in SK from calibration group. I benefitted significantly from discussions with Motoyasu Ikeda-san, Yasuhiro Nakajima-san, Yoshinari Hayato-san, Yusuke Koshio-san, and Lluís Martí. There are more names to list, and I would like to thank all the collaborators at SK and all the staffs at the Kamioka Observatory.

Many thanks go to the professors and colleagues at the High Energy Physics Center at Tsinghua University. The guidance and supervision from Prof. Zhe Wang and other teachers showed me the essences to perform a physics analysis independently. I appreciate Dr. Hanyu Wei, Dr. Xiangpan Ji, Dr. Logan Lebanowski, and many colleagues for our academic discussions as well as our friendship.

Besides, I would like to acknowledge Ondrej Sramek, Yufei Xi, and William F. McDonough for leading me into the field of geoneutrinos. Thanks to Prof. Ling-Fong Li for the chance to systemize my knowledge, and thanks to Benda Xu for the help and inspiration during my stay at Kamioka Observatory.

My friends and family have been supporting me during the long journey. Owing to the easy atmosphere they created, I was able to concentrate on my interest and fulfill my goal. I enjoyed their company so much.

## Declaration

本人郑重声明：所呈交的学位论文，是本人在导师指导下，独立进行研究工作所取得的成果。尽我所知，除文中已经注明引用的内容外，本学位论文的研究成果不包含任何他人享有著作权的内容。对本论文所涉及的研究工作做出贡献的其他个人和集体，均已在文中以明确方式标明。

签 名： 马林松 日 期： 2018.12.19

## Resume and Publications

### 个人简历

1991年10月9日出生于湖南省常德市。

2009年9月考入清华大学工程物理系工程物理专业，2013年7月本科毕业并获得工学学士学位。

2013年9月免试进入清华大学工程物理系攻读物理学博士学位至今。

### 发表的学术论文

- [1] Linyan Wan, et al., *Geoneutrinos at Jinping: Flux prediction and oscillation analysis*, Phys. Rev. D **95**, 053001 (2017).
- [2] Linyan Wan for Jinping Collaboration, *Jinping Neutrino Experiment*, J. Phys. Conf. Ser. **888**, 012058 (2017).
- [3] Linyan Wan, et al., *Hands on Nuclear Emulsion Detectors: Scanning with Automatic Microscopes and Data Analysis*, PoS GSSI **14**, 012 (2015).
- [4] Super-Kamiokande Collaboration, *Search for Neutrinos in Super-Kamiokande Associated with the GW170817 Neutron-star Merger*, Astrophys. J. **857**, (2018).
- [5] Logan Lebanowski, Linyan Wan (contact author), et al., *An efficient energy response model for liquid scintillator detectors*, Nucl. Instrum. Meth. A. **890**, 133-141 (2018).
- [6] Jinping Collaboration, *Physics prospects of the Jinping neutrino experiment*, Chin. Phys. C, **41**, 023002 (2017).
- [7] Super-Kamiokande Collaboration, *Search for Neutrinos in Super-Kamiokande associated with Gravitational Wave Events GW150914 and GW151226*, Astrophys. J. L. **830**, 1 (2016).
- [8] Super-Kamiokande Collaboration, *Solar Neutrino Measurements in Super-Kamiokande-IV*, Phys. Rev. D **94**, 052010 (2016).